RELATING OVERTURNS TO MIXING AND BUOYANCY FLUX

By

Peter S. Galbraith

DALHOUSIE UNIVERSITY

DEPARTMENT OF

DEPARTMENT OF OCEANOGRAPHY

The undersigned hereby certify that they have read and recommend to the Faculty of Graduate Studies for acceptance a thesis entitled "**Relating Overturns to Mixing and Buoyancy Flux**" by **Peter S. Galbraith** in partial fulfillment of the requirements for the degree of **Doctor of Philosophy**.

Dated: August, 1992

External Examiner: _____
William Crawford

Research Supervisor: _____
Daniel E. Kelley

Examing Committee: _____
Denis Lefaivre

_____
C. J. R. Garrett

_____
Barry R. Ruddick

_____
Neil S. Oakey

_____
Glen Lesins

DALHOUSIE UNIVERSITY

Date: **August, 1992**

Author: **Peter S. Galbraith**

Title: **Relating Overturns to Mixing and Buoyancy Flux**

Department: **Department of Oceanography**

Degree: **Ph.D.**   Convocation: **Fall**   Year: **1992**

_____
Signature of Author

To Katia,

who kept me going through it all.

Contents

List of Tables

List of Figures

Abstract

Oceanic mixing occurs at molecular diffusion and viscous scales, called the Batchelor and Kolmogorov scales, although it has signatures at larger scales. For example, the rate of creation of temperature fluctuations by overturning against a mean temperature gradient is balanced by the rate of dissipation at the Batchelor scale. In potential energy terms, buoyancy flux accumulates into a standing crop of available potential energy of the fluctuations (APEF), which in turn decreases due to the potential energy dissipation term, raising the mean potential energy of the water column. If a steady-state exists, then both the buoyancy flux and potential energy dissipation rate are equal to the APEF divided by a suitable decay time.

This parameterisation of mixing is separated in two turbulence cases: growing isotropic overturning scales and steady-state overturning scales with balanced inertial and buoyancy forces. The decay time is shown to be inversely proportional to overturn-scale shear and proportional to overturning time; this becomes proportional to the buoyancy period for turbulence in inertial-buoyancy balance, whether it be isotropic or not. Buoyancy flux is estimated from overturning scale quantities, which are much easier to measure than mixing at the smaller viscous and diffusive scales. Predictions of buoyancy flux and mixing efficiency compare favourably with laboratory turbulence data and to lake and oceanic data, provided that salinity-compensated intrusions can be excluded from the analysis. Overturn scales are subsequently used in the St. Lawrence estuary to estimate mixing rates; data suggest that solitons create more mixing at the head of the Laurentian channel than does the larger scale internal tide.

List of Symbols

α Coefficient of thermal expansion [$°C^{-1}$].

χ_θ Rate of diffusive dissipation of temperature fluctuations or variance [$°C^2 \ s^{-1}$].

γ Strain due to soliton.

γ_{mix} Degree of homogenisation of an overturning layer.

Γ Mixing efficiency $\Gamma = J_b/\epsilon$.

ϵ Rate of dissipation of turbulent kinetic energy [$W \ kg^{-1}$].

η Isopycnal displacement [m].

κ_T Molecular diffusivity for heat [$m^2 \ s^{-1}$].

ν Kinematic viscosity [$m^2 \ s^{-1}$].

ξ Available Potential Energy of the Fluctuations [$J \ kg^{-1}$].

ω Frequency [s^{-1}].

c_n Eigenvalue for nth vertical modes of internal tide oscillation.

C_x One-dimensional Cox number $C_x = \overline{(\partial T'/\partial z)^2}/(\partial \overline{T}/\partial z)^2$.

$E(k)$ Kolmogorov turbulent kinetic energy spectrum $E(k) \propto \epsilon^{2/3} k^{-5/3}$

Fr_t Turbulent Froude number $Fr_t = u'/NL_T$.

$(Fr_t)_{iso}$ Turbulent Froude number restricted to isotropy ($L_h = L_T$);
$$(Fr_t)_{iso} = (L_O/L_T)^{2/3}.$$

$(Fr_t)_{IB}$ Turbulent Froude number restricted to inertial-buoyancy balance ($L_h = L_O$);
$$(Fr_t)_{IB} = L_O/L_T.$$

$(Fr_t)_{isoIB}$ Empirical value of the turbulent Froude number at isotropy and inertial-buoyancy balance.

Fr_h Turbulent Froude number based on horizontal length scales; quantifies degree of inertial-buoyancy balance. $Fr_h = u'/NL_h$.

g, g' Gravitational constant $g = 9.8$ m s^{-2}, and reduced gravitational constant $g' = g\,\rho'/\overline{\rho} \approx N^2 L_T$

J_b Buoyancy flux $J_b = (g/\rho)\overline{w'\rho'}$ [J kg^{-1}].

K_ρ Eddy diffusivity for mass $K_\rho = -\overline{w'\rho'}/(\partial\overline{\rho}/\partial z)$ [m^2 s^{-1}].

K_{heat} Eddy diffusivity for heat $K_{\text{heat}} = \chi_\theta/(2[\partial\overline{T}/\partial z]^2)$ [m^2 s^{-1}].

K_m Eddy viscosity $K_m = -\overline{u'w'}/(\partial\overline{u}/\partial z)$ [m^2 s^{-1}].

L_B Buoyancy scale $L_B = (J_b/N^3)^{1/2}$ [m].

L_h Horizontal turbulent length scale [m].

L_O Ozmidov scale $L_O = (\epsilon/N^3)^{1/2}$ [m].

L_t Turbulent displacement scale $L_t = \overline{\rho_e'^2}^{1/2}/(\partial\rho_o/\partial z)$ [m].

L_T Thorpe scale (rms average of Th) [m].

M_2 Semi-diurnal tidal frequency [s^{-1}].

N Buoyancy frequency (usually calculated on re-ordered profile).

R_f Flux Richardson number $R_f = J_b/-\overline{u'w'}(\partial\overline{u}/\partial z)$.

Re Reynolds number $Re = u'L_t/\nu$

Re_w Reynolds number based on vertical turbulent velocity $Re_w = w'L_t/\nu$

Ri_g Gradient Richardson number $Ri_g = N^2/(\partial U/\partial z)^2$.

$(Ri_g)_{cr}$ Empirical value of the critical gradient Richardson number for overturning.

Ri_t Turbulent Richardson number $Ri_t = N^2 L_t^2/u'^2$.

$(Ri_t)_{cr}$ Empirical value of the critical turbulent Richardson number for overturning (isotropic inertial-buoyancy balance value).

$(Ri_t)_{iso}$ Turbulent Richardson number restricted to isotropy $(L_h = L_T)$;
$(Ri_t)_{iso} = (L_T/L_O)^{4/3}$.

$(Ri_t)_{IB}$ Turbulent Richardson number restricted to inertial-buoyancy balance $(L_h = L_O)$;
$(Ri_t)_{IB} = (L_T/L_O)^2$.

t_o Decay time of the turbulent kinetic energy by ϵ [s].

T, ρ Temperature and density.

$\overline{T}$, $\overline{\rho}$ Mean temperature or density.

T_o, ρ_o Re-ordered temperature and density profile.

T', ρ' Thorpe fluctuation at a point, $T' = T - T_o$.

T_e', ρ_e' rms fluctuation at a point defined as difference between observation and mean state. Includes internal waves.

Th Thorpe displacement [m].

TKE Turbulent kinetic energy $= u'^2 + v^2 + w'^2 \approx q^2$ [m^2 s^{-2}].

u', v', w', q Turbulent velocity fluctuations; $q^2 = 2\,u'^2 + w'^2$.

Acknowledgments

I must first thank my father, Don Galbraith, for telling me I should apply for a summer job in a Canadian lab. I must then thank Denis Lefaivre and Steve Peck for hiring me in a Canadian lab! During my first three summers there, I worked for Pierre Larouche. I thank him for getting me interested in oceanography. I'm looking forward to working with him again. Denis Lefaivre helped me get my foot in the door at Dalhousie, and for that I am grateful; but I'm much more thankful to Denis for the generous supply of ship time he managed to get for me to do my measurements.

The story at Dalhousie continued with Chris Garrett. He has always been demanding enough to make me work hard, yet distant enough to let me drift into my own thesis project. Since Chris was my supervisor, he's both my 'father' and 'grandfather' in academia! Barry Ruddick has a habit of asking questions from left field at critical moments during committee meetings; fear keeps you on edge! Thanks Barry! I thank Neil Oakey for sharing his data with me, and for all his comments on thesis drafts. Glen Lesins also suffered through drafts; I owe you all a great deal. Thanks are also extended to Bill Crawford, for his great job as external (he passed me didn't he?).

This brings me to Dan Kelley. Dan is the nicest guy I know; he also happens to be a great scientist who spent many hours with me talking about science and about 'other' interesting subjects. His friendship means a lot to me. I was glad to be his first grad student.

Chapter 1

Introduction

Interest in oceanic turbulence and mixing is maintained by the need to parametrize eddy viscosity and diffusivity. Applications come from many areas: for example, ocean circulation models require a formulation of subgrid-scale diapycnal mixing in terms of grid-scale variables. Buoyancy budgets and fluxes of passive tracers such as nutrients are important issues on continental shelves and in estuaries.

Recent direct measurements of diapycnal buoyancy flux J_b used a vertical sampling pitot tube to measure w' (Moum, 1990) or a conventional air-foil probe sampling horizontally (Yamazaki and Osborn, 1992). However, most J_b measurements are made indirectly, usually inferred from the rate of diffusive smoothing of temperature fluctuations, χ_θ, or from the rate of dissipation of turbulent kinetic energy, ϵ. The idea behind the inference of buoyancy flux from measurements of the rate of dissipation of temperature variance is that buoyancy flux produces temperature fluctuations, and that if there is a steady-state then the dissipation of the potential energy associated with that variance must equal the buoyancy flux. Measurements of χ_θ and ϵ are made at millimeter to centimeter scales, where molecular diffusion and viscous dissipation occur. The measurements are technically difficult to execute, and have yet to become routine; for example, microstructure measuring intruments are not installed on CTDs.

In this thesis, I shall discuss the use of 'overturn-scale' quantities to infer mixing rates. Quantities such as Thorpe scales, L_T, describing the size of overturning eddies,

and the Available Potential Energy of the density Fluctuations (APEF), describing the potential energy of the overturns, have been related to mixing rates (Ozmidov, 1965; Thorpe, 1977; Dillon, 1982; Crawford, 1986; Dillon and Park, 1987). These quantities can be measured much more easily than dissipation scale quantities. They are called Thorpe variables, because overturns are obtained by comparing a measured profile to its re-ordered counterpart; a technique pioneered by Thorpe (1977).

Traditional thought is that the turbulent energy cascade relates the energy-containing Thorpe scales to the dissipative ones (Ozmidov, 1965); from this was born the idea that Thorpe scales L_T should be related to the rate of dissipation of turbulent kinetic energy ϵ through the Ozmidov scale $L_O = (\epsilon/N^3)^{1/2}$ (Thorpe, 1977).

This 'traditional' model is by no means the only point of view on the relation of overturn scales to dissipative ones, but it is widespread. For example, Ivey and Imberger (1991) interpreted the varying mixing efficiency of grid turbulence in terms of a turbulent Froude number (discussed in Appendix B), a new approach, yet interpret the results using the traditional model by assuming that oceanic mixing occurs at a balance between inertial and buoyancy forces where turbulent kinetic energy is only sufficient to overturn against stratification; this defines the inertial-buoyancy balance (The turbulent Froude number $Fr_t = u'/NL_T$ is approximately equal to unity). This view is also consistent with kinematical models of breaking internal waves, where the size and frequency of breaking events determines the effective diffusivity of the water column (Garrett, 1989), because it is typically assumed that these events (or puffs) occur at inertial-buoyancy balance due to the K-H instability creating them. Ivey and Imberger's (1991) view is that this occurs with maximal mixing efficiency.

The kinematical model associated with the traditional link of $L_T \approx L_O$ is that of the occasional breaking of internal waves due to superposition of waves such that the gradient Richardson number is critical. If this occurs as isolated events (Gregg, 1987), then each overturn evolves individually, as described by Thorpe (1973) (discussed in section 2.3.1). The energy balance leading to models such as the Osborn-Cox model (Osborn and Cox, 1972) is then unclear because of time evolution and unknown

redistribution terms; it is hoped that ensemble averaging of multiple profiles takes care of these variations (Gregg, 1987).

A simple picture of mixing events is nevertheless as follows: overturning at large scales of the inertial sub-range brings dense waters up and lighter waters down through the water column. As overturned water is buoyantly forced back to its equilibrium position, it is also entrained by the possibly stronger inertial forces (if $Fr_t > 1$ such that turbulent velocities are greater than the buoyancy velocity) in an assumed cylindrical motion at overturning scales. A turbulent cascade of energy ensues where turbulent velocity strain brings larger scale kinetic energy to smaller scales, and so on to viscous dissipation at the Kolmogorov scale (mentioning convective rolls and such features (Thorpe, 1984) are included as turbulent flow in this simplistic description). The smaller-scale turbulent velocities are less energetic than the outer scale overturning velocities, such that they redistribute energy, possibly inducing some restratification. This cascade drains energy at a rapid rate, within an overturning time proportional to the turbulent velocity scale divided by the length scale of the overturn. The potential energy gained from large scale overturning corresponds to positive buoyancy flux. Since the final mixed state must have lower potential energy than the overturned state, some restratification must occur by redistribution from the turbulent velocities. During this time, dissipation at the Batchelor scale diffuses temperature fluctuations (and salinity fluctuations at smaller scales) away, raising the potential energy of the water column.

Identifying Overturns

Thorpe (1977) found overturns in vertical density profile by re-ordering the density profile; the size of the overturn was characterized by the rms distance points were moved in the re-ordering. This implies that the overturn is defined in the density profile as extending as far as the density profile differs from the re-ordered profile. Dillon (1982) found continuous depth spans containing re-ordering displacements much shorther than the depth span. In this case he used the entire span as an averaging

layer, instead of individual overturns, because it wasn't clear where one started and finished. In this thesis, the extent of an overturn in a vertical density profile is defined as the smallest group of consecutive points which may be re-ordered without moving any other point in the profile. This uniquely identifies overturns even if they are found consecutively.

New Models

Two new models will be presented, with predictions similar to Ivey and Imberger (1991) and to Dillon and Park (1987), but with implicit interpretations (which follow from model assumptions) different than those of these authors. These two models do not assume random overturning, but rather continuous overturning in energetically mixed layers, with external forcing giving overturning its energy balance (or lack of balance) between inertial and buoyancy forces and isotropy characteristics, rather than internal instability leading to inertial-buoyancy balance. In these models, the Available Potential Energy of the Fluctuations (APEF) introduced by Dillon (1984) is related directly to buoyancy flux through a decay time proportional to an eddy overturning time; this time scale is the same as for the decay of the turbulent kinetic energy (TKE) by ϵ.

The description of the overturning events for these two models is similar to the above, except that initial instability leads to persistent overturning fed from Reynolds stress acting on the mean shear. Two cases occur. The first is that overturning may occur at scales smaller than inertial-buoyancy balanced scale (for example, due to bottom roughness setting the initial overturning scale). Overturning is then unrestrained by stratification and overturn scales grow as they do in unstratified grid turbulence experiments. This is described by model two, for growing isotropic turbulence (model one describes the traditional assumption that $L_T \approx L_O$).

Isotropy implies that properties of the turbulence do not depend on direction or the choice of a coordinate system. Strictly speaking, isotropy implies that there are no Reynolds stresses $\overline{u'w'}$; in this thesis, isotropy describes only the characteristic

of approximate equality of turbulent kinetic energy in all directions. Therefore, the ratio of vertical to horizontal rms velocity fluctuations w'/u' will quantify isotropy, where w' and u' are rms turbulent velocities at the largest scales of the overturn. This is consistent with observations of Gargett *et al.* (1984) who observed that vertical spectral components were disminished relative to horizontal ones for a turbulent intensity, $\epsilon/\nu N^2$, less than 200. Assuming that continuity in turbulent scales holds as $u'L_T \approx w'L_h$, where L_T and L_h represent vertical and horizontal turbulent lengthscales, isotropy will also be simply described by the ratio of vertical to horizontal turbulent lengthscales L_T/L_h approximately equal to unity. Note, however, that while L_T is obtained easily by re-ordered the vertical density profile, horizontal turbulent lengthscales are not as easily measured because of the lack of a horizontal mean gradient of a scalar property of the fluid; its use will be to provide a picture of the state of the turbulence, but the velocity component ratio can be interchanged for L_T/L_h.

In the second case for which persistent overturning occurs, external shear forces the turbulence on a vertical extent smaller than the inertial-buoyancy balanced vertical overturning scale (for example, shear from an internal tide mode may be strong on a short vertical scale). Vertical overturning scales stop growing when they reach this forcing limit, but nothing stops horizontal scales from growing further. A scaling analysis in chapter 3 shows that horizontal scales should grow to the same scale as the vertical inertial-buoyancy balance scale (the Ozmidov scale), which is greater than the vertical overturning scale. Overturning remains in this steady-state, obtaining its energy from the mean shear; mixing then erodes the stratification within the layer. Mixing efficiency may then decrease as the potential energy available to overturning is eroded away with the stratification, limiting the potential energy that can appear as buoyancy flux. Further entrainment leads to density fluctuations, measured as available potential energy and related to buoyancy flux.

This last model applies to steadily mixing layers such as surface or bottom boundary layers that tend to be well mixed. Buoyancy flux in these layers may then come

from entrainment or erosion of the adjacent pycnocline. A parameterization in terms of layer quantities describing the forcing could be used (or developed) instead of using the above approach. However this thesis is not about relating forcing directly to mixing (e.g. Gregg's (1989) model relating the rate of dissipation of TKE to 10-m internal wave shear), but rather aims at showing that measurements of the act of overturning can lead to adequate mixing estimates.

In these two new models, the persistence of the overturning is thought to lead to a steadier energy distribution between overturning potential energy and turbulent kinetic energy, as well as between kinetic and potential energy dissipation rates. The turbulent redistribution terms are still present, leading to possible mis-estimates of energy equation terms from vertical profiling through overturn events, because redistribution is not measured. However, sampling variance should be reduced relative to random overturning because of the greater degree of homogeneity of the turbulent field.

The work presented here parameterizes the average buoyancy flux of single overturns in terms of snapshot measurements of their available potential energy. To relate these results to basin-scale values of buoyancy flux or eddy diffusivity, a sufficient number of such profiles would need to be averaged to take account of the spatial and temporal distributions of the overturning events. These distributions, which must vary between locations depending on the intensity of the forcing mechanism, are not discussed in this thesis.

Dillon (1982) has probably accomplished the most in showing the relation of overturn-scale quantities to both the rate of dissipation of turbulent kinetic energy, and to buoyancy flux. He was first to validate (under limited conditions) Thorpe's (1977) idea that Thorpe scales should be related to Ozmidov scales $L_O = (\epsilon/N^3)^{1/2}$. His efforts have resulted in a more recent empirical model relating the APEF to buoyancy flux (Dillon and Park, 1987). However, the views of the L_T–L_O relation (Dillon, 1982) and of the APEF–J_b relation (Dillon and Park, 1987) are different as the first relates overturns to ϵ (through L_O) and the second relates them to

J_b. For example, Dillon *et al.* (1987) said "It is not our intention to suggest that the APEF is preferable to the Thorpe scale but rather to point out that Thorpe variables other than L_T also have physical significance." It was therefore unclear which model should be used. We will build on Dillon's results here with simple kinematical models relating overturning to buoyancy flux, and relate these concepts to Dillon's empirical results.

A suggestion that Thorpe variables can be used to infer buoyancy flux comes from recent direct measurements of buoyancy flux. The dissipation of temperature variance is a microscale quantity, but Moum (1990) measured buoyancy flux directly in the equatorial undercurrent, and found that the largest values of $\overline{w'\rho'}$ (mass flux) were at overturn-scales, rather than at dissipative scales. This is an indication that temperature variance is created at the energy-containing scales and dissipated at smaller scales. Instead of focusing on difficult microscale measurements, the buoyancy flux could be inferred from measurements of overturn-scale quantities where most of J_b occurs.

This thesis will do just that: focus on the relation of the APEF to buoyancy flux, parameterized over individual overturn measurements. Basin scale values of eddy diffusivity or buoyancy flux are obtained by further averages which are not discussed in this thesis. The outline of the thesis is as follows:

Chapter 2 reviews models used to infer mixing rates from microstructure measurements. Terminology (*e.g.* mixing layers and overturns) is established. The APEF is introduced, and approximations of it used throughout the thesis are derived and tested.

Chapter 3 reviews the assumptions made in the traditional view of linking L_T to ϵ. Alternate derivations are made, leading to 3 mixing models to be tested:

Model one: The traditional view, links L_T to ϵ. It will be emphasized that, as Dillon (1982) suggested, this is not a general result in the ocean.

Model two: Relates J_b to the dissipation of the APEF within an "overturning

period" of approximately L_T/u', where u' is the turbulent velocity associated with the overturn.

Model three: relates J_b to the dissipation of the APEF within a buoyancy period N^{-1}.

Models two and three apply in different conditions. I will show that they are preferable to model one in energetic cases.

A hypothesis is put forward that the overturning time scale L_T/u' is proportional to the inverse of the large scale shear $(\partial \overline{U}/\partial z)^{-1}$ when this shear forces the turbulence. The buoyancy flux of model two, and mixing efficiency of models two and three, could then be inferred without measurements of turbulent velocities.

Chapter 4 verifies the assumptions made in the derivation of models two and three using grid-turbulence data. The second model is also shown to work for a wide range of overturning periods; predictions for buoyancy flux and mixing efficiency are consitent with data within a factor of two. The hypothesis $L_T/u' \propto (\partial \overline{U}/\partial z)^{-1}$ is verified.

Chapter 5 uses Dillon's (1982) oceanic data to show that model one holds, but only in limited conditions, and that oceanic mixing rates are more consistent with model three. Another fresh-water data set is somewhat consistent with the second model. The buoyancy flux is related to the decay of the APEF over a decay time scale t_o for both models two and three, but both models apply for different physical circumstances. It is not inconsistent that both do well for different data sets. Model one is discarded in strongly forced mixing in favour of models two and three because the assumption of constant mixing efficiency does not generally hold in strongly mixed areas of the ocean.

Chapter 6 discusses a test case of the application of models to new data taken in Emerald basin (Van Haren, pers. communication; Oakey, 1990). It is shown

that the inferred buoyancy flux is mostly consistent with observations of ϵ. At least 40 to 60% of the water column expected to be overturning is shown to be overturning. Some of the high APEF data are inconsistent with simultanenous low measurements of ϵ; these anomalous APEF values are thought to be caused by intrusions.

Chapter 7 uses the buoyancy flux models to study mixing layers observed in the St. Lawrence estuary. It is shown that reliable use of any model requires first that intrusions be detected using T–S relations and excluded from APEF calculations. The head of the Laurentian channel is thought to be the generation point of a large internal tide, which was thought to force high mixing rates. Analysis of a few mixing layers using buoyancy flux models tested in this thesis shows that solitons in fact create more mixing than is associated with internal tide shear.

Chapter 8 provides a summary and suggestions for future work. Models two and three are appropriate for different conditions. Model two requires knowledge of turbulent velocities to infer the turbulent Froude number in order to obtain buoyancy flux; in cases where such data are not available, the buoyancy flux from model three serves as a lower bound.

Chapter 2

Microstructure Models, Overturns and Thorpe Quantities

This chapter serves three purposes

- To introduce the models used to infer buoyancy flux from microstructure measurements. Overturn-scale methods described in later chapters share some of the concepts used.

- To discuss the general notion of overturning structures that lead to mixing.

- To introduce overturn-scale quantities such as Thorpe scales and the Available Potential Energy of the Fluctuations and its approximations. These will be used throughout the thesis.

The first two sections are all a review, mostly of Gregg's (1987) own review of mixing. The third section introduces the APEF and some new key results quantifying the validity of several approximations.

2.1 Microstructure Measurements

Except for recent direct measurements of diapycnal buoyancy flux[1] $J_b = (g/\overline{\rho})\overline{\rho'w'}$ (Moum, 1990; Yamazaki and Osborn, 1992), the majority of J_b measurements are made indirectly. The buoyancy flux is usually inferred using measurements of the rate of diffusive smoothing of temperature fluctuations, χ_θ, which occurs at the Batchelor scale $(\nu\kappa_T^2/\epsilon^{-1})^{1/4}$ (for a Prandtl number ν/κ_T greater than unity, as for water) or using measurements of the rate of dissipation of turbulent kinetic energy, ϵ, which occurs at the Kolmogorov scale $L_K = (\nu^3/\epsilon)^{1/4}$.

2.1.1 Shear Microstructure

The rate of dissipation of turbulent kinetic energy, ϵ, is used, amongst other things, to determine internal wave decay rates and, by comparison with laboratory experiments, to determine whether turbulence is intense enough to produce a buoyancy flux (see appendix A for a discussion) (Gregg, 1987). It is used indirectly to determine the diapycnal flux of momentum and mass.

Both momentum and mass flux formulations start from the turbulent kinetic energy equation for a shear flow, derived below.

Turbulent Kinetic Energy Equation

The turbulent kinetic energy (TKE) equation is obtained by multiplying the Navier-Stokes equation

$$\frac{\partial \tilde{u}_i}{\partial t} + \tilde{u}_j \frac{\partial \tilde{u}_i}{\partial x_j} = -\frac{1}{\rho}\frac{\partial \tilde{p}}{\partial x_i} + \nu \frac{\partial^2 \tilde{u}_i}{\partial x_j^2} - g'\delta_{i3} \tag{2.1}$$

by $\tilde{u}_i$, where the superscript ~ represents a Reynolds decomposition into mean and turbulent parts

$$\tilde{u}_i = \overline{U}_i + u'_i \tag{2.2}$$

and the index i is for the three velocity components with summation over $j = 1, 2, 3$. The term g' represents reduced gravity $\rho'g/\rho$ associated with a density fluctuation ρ'

---

[1]The sign of J_b was chosen to be the same as mass flux, instead of negative mass flux

in a fluid of mean density ρ. Here, $\overline{U}$ may be interpreted as a time average, and u' as a fluctuation away from this average due to turbulence.

Let us assume that turbulence is confined within an 'overturn', where heavy water has overturned over overlying lighter water and turbulent motions begin, straining turbulent energy from the overturning scale to the smaller viscous scales.

The product of (2.1) with $\tilde{u}_i$ leads to an energy equation from which the kinetic energy equation of the mean flow can be subtracted (See Tennekes & Lumley (1972) for a discussion). This leaves the TKE equation

$$\frac{\partial}{\partial t}\left[\frac{1}{2}\overline{u_i'u_i'}\right] + \overline{U}_j\frac{\partial}{\partial x_j}\left[\frac{1}{2}\overline{u_i'u_i'}\right] = \frac{\partial}{\partial x_j}\left[-\frac{1}{\rho}\overline{u_j'p} + \frac{1}{2}\overline{u_i'u_i'u_j'} - 2\nu\overline{u_i's_{ij}}\right]$$
$$- \overline{u_i'u_j'}\frac{1}{2}(\frac{\partial\overline{U}_i}{\partial x_j} + \frac{\partial\overline{U}_j}{\partial x_i}) - 2\nu\overline{s_{ij}s_{ij}} - \overline{g'u_i}\delta_{i3} \quad (2.3)$$

where the quantity s_{ij} is the fluctuating rate of strain, defined by

$$s_{ij} = \frac{1}{2}\left[\frac{\partial u_i'}{\partial x_j} + \frac{\partial u_j'}{\partial x_i}\right] \quad (2.4)$$

If the turbulence is steady and homogeneous, the left-hand side terms of (2.3) vanish. The first three terms on the right hand side (within the divergence term) are transport terms by pressure-gradient work, by turbulent velocity fluctuations and by viscous stress. If the flux into a closed control volume, enclosing the turbulent overturn, is zero, these terms redistribute energy (Tennekes and Lumley, 1972). The viscous term, $2\nu\,\partial\overline{u_i's_{ij}}/\partial x_j$ is much smaller than the other two and is usually neglected; Its ratio to either of the other divergence terms is Re_t^{-1} (Tennekes and Lumley, 1972) where Re_t is a turbulent Renolds number $u'L/\nu$ and L is a turbulent length scale. Since Re_t is much greater than unity for turbulent flows, then that transport term is safely neglected. The first two redistribution term are neglected assuming that sampling of the turbulent flow is sufficient to average them out.

The term $\overline{u_i'u_j'}\frac{1}{2}(\partial\overline{U}_i/\partial x_j + \partial\overline{U}_j/\partial x_i)$ is the rate of production of TKE by Reynolds stresses acting against the rate of strain of the mean flow. For a simple vertically sheared flow, this term reduces to $\overline{u'w'}\,\partial\overline{U}/\partial z$. This is the only turbulent energy source for such a flow.

The term $2\nu\overline{s_{ij}s_{ij}}$ is often written $\nu u_i'\nabla^2 u_i'$ or $\frac{15}{2}\nu\overline{[\frac{\partial u'}{\partial z}]^2}$, used because the integrated shear spectra is directly measured with shear probes (Oakey and Elliott, 1982; Oakey, 1982) and is called the rate of dissipation of turbulent kinetic energy, ϵ. This expresses the molecular dissipation due to small-scale shears created by turbulent strain.

For a stratified sheared flow with homogeneous steady-state turbulence, the TKE equation reduces to

$$\overline{u'w'}\frac{\partial \overline{U}}{\partial z} = -J_b - \epsilon \tag{2.5}$$

where the buoyancy flux $J_b = (g/\rho)\,\overline{w'\rho'}$ is the energy sink for the TKE transfered to potential energy. The relative contribution of the buoyancy flux as an energy sink is often expressed as the flux Richardson number, defined by

$$R_f \equiv \frac{J_b}{-\overline{u'w'}(\partial \overline{U}/\partial z)} \tag{2.6}$$

Dissipation Method

The dissipation method expresses the momentum flux in terms of an eddy coefficient K_m

$$\overline{u'w'} = -K_m\frac{\partial \overline{u}}{\partial z} \tag{2.7}$$

This eddy parameterisation assumes that the flux of the quantity u', or momentum, is equal to an eddy coefficient times the gradient of that same quantity. Since the velocities fluctuations u' are transported—and even created—by overturning motions, they can be defined as overturning scale fluctuations from the mean state.

Combining (2.5) with (2.6) and (2.7) yields K_m in terms of R_f together with measurable quantities ϵ and shear.

$$K_m = \frac{\epsilon}{(1 - R_f)[\frac{\partial \overline{u}}{\partial z}]^2} \tag{2.8}$$

This parameterisation is not appropriate when internal-wave shear forces the turbulence, because then the shear evolves on the same time scale as the turbulence, N^{-1}, (Gregg, 1987) where $N^2 = (-g/\rho)\partial\rho/\partial z$ is the stability of the water column, and $2\pi N^{-1}$ is the buoyancy period. The parameterisation is appropriate when a

strong mean shear is greater than the fluctuating part due to internal waves, such as for the equatorial undercurrent or for a tidal shear (Gregg, 1987).

Osborn Model

The mass flux formulation again uses an eddy coefficient formulation (Osborn, 1980), defined by

$$\overline{w'\rho'} = -K_\rho \frac{\partial \overline{\rho}}{\partial z} \tag{2.9}$$

equivalent to

$$J_b \equiv \frac{g}{\rho} \overline{w'\rho'} = K_\rho N^2 \tag{2.10}$$

Substituting (2.6) and (2.5) into (2.10) gives the familiar form for eddy diffusivity[2]

$$K_\rho = \frac{R_f}{1 - R_f} \frac{\epsilon}{N^2} \tag{2.11}$$

2.1.2   Temperature Microstructure

The Osborn-Cox (1972) model for heat flux in a mixing fluid assumes that temperature fluctuations T' are created by turbulent overturning against a mean gradient $\partial \overline{T}/\partial z$ (Gregg, 1987). Here T' is a fluctuation from a mean state $\overline{T}$, and will be assumed later to be a Thorpe fluctuation.

The formulation starts from the temperature equation

$$\frac{\partial T}{\partial t} + u_i \frac{\partial T}{\partial x_i} = \kappa_T \frac{\partial^2 T}{\partial x_i^2} \tag{2.12}$$

where κ_T is the molecular diffusivity of heat. Velocity and temperature variations are divided into mean and turbulent fluctuation parts, similarly to the TKE derivation. The equation for the turbulent part is

$$\frac{\partial T'}{\partial t} + \overline{U}_i \frac{\partial T'}{\partial x_i} + u_i' \frac{\partial \overline{T}}{\partial x_i} + u_i' \frac{\partial T'}{\partial x_i} = \kappa_T \frac{\partial^2 T'}{\partial x_i^2} \tag{2.13}$$

---

[2]From the definitions of eddy diffusivity (2.10) and eddy viscosity (2.7), the relationship $K_m/K_\rho = Ri_g/R_f$ follows by using the definition of R_f from (2.6) and the definition of $Ri_g = N^2/(\partial U/\partial z)^2$. The often assumed equality between eddy diffusivity and viscosity implies that the gradient and flux Richardson numbers are equal as well.

Multiplying by $2T'$ and averaging yields an equation for temperature variance $\overline{T'^2}$

$$\frac{\partial \overline{T'^2}}{\partial t} + \overline{U}_i \frac{\partial \overline{T'^2}}{\partial x_i} + 2\,\overline{u_i' T'} \frac{\partial \overline{T}}{\partial x_i} + \overline{u_i' \frac{\partial T'^2}{\partial x_i}} = 2\,\overline{T' \kappa_T \frac{\partial^2 T'}{\partial x_i^2}} \tag{2.14}$$

The terms on the left-hand side are rate of change of temperature variance, advection, production by turbulent overturning against mean gradients, and turbulent redistribution. The right-hand side term can be rewritten by noting that

$$\frac{\partial}{\partial x_i}\frac{\partial}{\partial x_i}(T' \cdot T') = 2\frac{\partial}{\partial x_i}\left[T'\frac{\partial T'}{\partial x_i}\right] = 2\frac{\partial T'}{\partial x_i}\frac{\partial T'}{\partial x_i} + 2\,T'\frac{\partial^2 T'}{\partial x_i^2} \tag{2.15}$$

The right-hand side of (2.14) becomes

$$2\,\kappa_T \overline{T'\frac{\partial^2 T'}{\partial x_i^2}} = \kappa_T \frac{\partial^2 \overline{T'^2}}{\partial x_i^2} - 2\,\kappa_T \overline{\frac{\partial T'}{\partial x_i}\frac{\partial T'}{\partial x_i}} \tag{2.16}$$

The first term on the right-hand side is a redistribution term and the second is the decay term: the rate of diffusive smoothing of temperature fluctuations.

If the turbulence is steady and homogeneous, if the redistribution terms are neglected (or averaged out by adequate sampling) and if only vertical temperature gradients exists, the production of fluctuations is then balanced by their rate of diffusion, $\chi_\theta = 6\kappa_T \overline{(\partial T'/\partial z)^2}$ (where the factor of 6 comes from assuming isotropy). The temperature fluctuation equation (2.14) is then

$$2\overline{w'T'}\frac{\partial \overline{T}}{\partial z} = -6\kappa_T \overline{\left[\frac{\partial T'}{\partial z}\right]^2} \tag{2.17}$$

Like many other 'eddy' parameterisations, the transported quantity $\overline{w'T'}$, in this case temperature flux, is assumed to equal to the product of an eddy coefficient K_{heat} and of the mean gradient. This form is similar to the molecular heat transport through diffusion $\kappa_T \partial T/\partial z$ where κ_T is the molecular diffusivity of heat. The eddy coefficient formulation for the production, $\overline{w'T'} = -K_{\text{heat}}\,\partial \overline{T}/\partial z$, yields (Osborn and Cox, 1972):

$$K_{\text{heat}} = \frac{\chi_\theta}{2[\partial \overline{T}/\partial z]^2} \tag{2.18}$$

The quantity $\overline{(\partial T'/\partial z)^2}/(\partial \overline{T}/\partial z)^2$ is termed a one-dimensional Cox number, C_x, and within a constant factor is the ratio of turbulent to molecular diffusivities for heat. The eddy diffusity for heat can be simply written

$$K_{\text{heat}} = 3\,\kappa_T C_x \tag{2.19}$$

where the factor of 3 assumes full isotropy, but is sometimes replaced by 1 (layered) to 3 (isotropic).

The Osborn-Cox model is not appropriate where lateral motions, rather than overturning, create the temperature fluctuations. In that case vertical production does not balance the creation of temperature variance from overturning against a vertical temperature gradient, which is a basic assumption of the model. Thus it will fail in the presence of thermohaline intrusions (Gregg, 1987).

2.1.3 Mixing efficiency

The ratio $R_f/(1 - R_f)$ in (2.11) corresponds to the ratio of J_b/ϵ. It is referred to as the mixing efficiency $\Gamma = J_b/\epsilon$. Osborn (1980) uses an energetics argument to suggest that R_f, and therefore Γ, must be less than unity. The argument reads as follows. If shear $\partial \overline{u}/\partial z$ is the source of turbulent production, u' velocity fluctuations will first be created. Pressure velocity correlations then re-distribute the energy to v' and w' fluctuations. Viscous dissipation acts on all components of velocity fluctuations, but buoyancy flux can only come from the vertical component. The mixing efficiency must then be of the order of one third, because all three components of velocity fluctuations are dissipated by viscosity while only one participates in buoyancy flux.

Oakey (1982; 1985), having simultaneous measurements of both χ_θ and ϵ, equated K_ρ from (2.11) to K_{heat} from (2.19) to yield

$$\Gamma = \frac{(2 \pm 1)\,\kappa_T C_x N^2}{\epsilon} \tag{2.20}$$

This is equivalent to equating buoyancy flux J_b to the dissipation of potential energ in $\Gamma = J_b/\epsilon$: the assumption of the Osborn-Cox model. Oakey obtained $\Gamma = (1 \pm \frac{1}{2})\,0.24$

from 25 segments of 10 to 15 m of vertical microstructure profiles (Oakey, 1982) and $\Gamma = (1 \pm \frac{1}{2}) \, 0.265$ using 275 such segments (Oakey, 1985). The $\pm$ factor is due to the isotropy condition of (2.19), having assumed a factor of 2 which can vary from 1 (layered) to 3 (isotropic).

2.2   Overturning Scale

The microstructure methods of inferring mixing rates described above assume a Reynolds stress acting against a mean shear[3]. All used some form of eddy parameterisation. This view is compatible with steady 3-dimensional homogeneous turbulence where energy is carried through eddies from the large scale inputs to small scale where it is dissipated, consistent with the Kolmogorov TKE spectrum. Thus, there is a basis for inferring microscale mixing rates from the measurement of larger scale overturning.

2.2.1   Ozmidov Scale, L_O

In this context of steady-state turbulence, Ozmidov (1965) related ϵ to the size of the biggest isotropic eddy in a stratified fluid. The Kolmogorov energy spectrum, $E(k) \propto \epsilon^{2/3} k^{-5/3}$ (Tennekes and Lumley, 1972), gives the velocity fluctuations at an overturning length scale l as

$$\overline{u'^2} \approx k E(k) \approx (l \, \epsilon)^{2/3} \qquad (2.21)$$

assuming isotropy and using $l \approx k^{-1}$ as a scaling[4]. If stratification is added then overturning must also work against stratification. The potential energy increase tied to the overturning motion is $\approx N^2 l^2$. It increases faster with overturning size ($\propto l^2$)

---

[3]The concept of the mixing efficiency $\Gamma = J_b/\epsilon$ is still useful to describe mixing forced by internal waves rather than by production against a mean shear (as used in the definition of R_f). In such a case the generalized form of the production term in (2.3) provides the forcing term, and the redistribution terms may be more important because of the short time scale of the internal waves.

[4]Equation (2.21) will be shown to hold very well empirically in chapter 4, section 4.3.1, in the presence in stable stratification.

than the source of energy in the Kolmogorov spectrum (from (2.21), $\overline{u'^2} \propto l^{2/3}$). Therefore, there is an energy balance between the two at a length scale known as the Ozmidov scale

$$L_O = (\epsilon/N^3)^{1/2} \tag{2.22}$$

L_O corresponds to the length scale of the biggest isotropic eddy possible in the presence of stable stratification. The Ozmidov scale, depending on ϵ, is a microscale measurement of a large scale variable. It could be argued that the Ozmidov scale is actually based on a wavenumber, and that a factor of 2π should be added to (2.22). However (2.22) is widely used in the literature, and so it is left as it is.

2.2.2 Thorpe Scale, L_T

Thorpe (1977) measured temperature inversions—where density decreases with depth—which he thought to be associated with overturning turbulent eddies, called "overturns". Although these mixing events are neither continuously created nor in a steady-state, the overturning scale was thought to be correlated with the Ozmidov scale. There is a tremendous utility in this correlation, if it exists, because then the overturn size could be used to estimate microscale dissipation, and therefore overturn scale measurements might be used to infer microstructure mixing rates. The required temperature (or density) and depth resolution is discussed at the end of this chapter.

Thorpe devised an empirical method to estimate the size of overturns in a stratified flow from the inversions that they create. The method consists of rearranging the inversion-containing vertical density profile $\rho(z)$ into a unique stable monotonic profile $\rho_o(z)$. Thus $\rho_\circ(z_1) \leq \rho_\circ(z_2)$ if $z_1 > z_2$ and z is the vertical coordinate increasing upwards. The idea is that the re-ordered profile approximates the state before instabilities occurred, or equivalently the profile obtained after the gravitational collapse of all the overturns without irreversible mixing. The Thorpe displacements, Th, are defined as the distance measured points are moved during the re-ordering computation to reach their stable location; thus $\rho(z) = \rho_\circ(z + Th(z))$. The Thorpe scale L_T is the rms value of Th over all points of the overturn or any other averaging

depth span.

The size and frequency distribution of overturns are most simply conceptually linked to vertical diffusivity through $K_v = \frac{1}{12}\gamma_{\mathrm{mix}}H^2 t_e^{-1}$ (derived in Chapter 3), where H is the overturn size, t_e is the time between overturning events and perfect homogenisation leads to $\gamma_{\mathrm{mix}} = 1$ or $\gamma_{\mathrm{mix}} < 1$ if the layer is not mixed completely (Garrett, 1989). If Th varies linearly between $-H$ to $+H$ within an overturn of size H, and if the overturn persists for a time t_o, the expected squared Thorpe scale (averaged over the profile and over time) is $\langle L_T^2 \rangle = \frac{1}{3}H^2(t_o/t_e)$. Garrett (1989) uses this and $K_v = \frac{1}{12}aH^2 t_e^{-1} = \Gamma\epsilon/N^2$ to show that a $L_O/\langle L_T \rangle$ ratio close to unity is not unexpected with $\Gamma \approx 0.2$, $\gamma_{\mathrm{mix}} \approx 1$ (assuming the overturn mixes the layer completely), and $Nt_o = 0(1)$ (assuming that the natural time scale is set by buoyancy forces). Dillon (1982) was first to measure both dissipation and Thorpe scales and show the L_O/L_T ratio to be a constant near unity away from surface mixed layers. The Thorpe scale is then a fine scale measurement of microscale dissipation. This result will be reviewed in this thesis.

2.3 Mixing Structures

The kind of mixing structure present in various parts of the ocean has a bearing on the mixing intensity and efficiency and on the parameterisation of the mixing itself. In his discussion of the characteristics of the turbulence, Gregg (1987) discusses 3 types of structures observed in the thermocline: puffs, wisps and persistent mixing zones. The puffs and persistent mixing zones are outlined here because the kinematics of mixing layers and mixing events is at the foundation of the microstructure mixing models described earlier. The descriptions and discussion of the section are mostly from the reviews of Gregg (1987) and Thorpe (1973). It should be noted that many of the ideas and laboratory observations about mixing are not tested in the ocean, and we do not have a clear picture of all the mechanics of ocean mixing.

2.3.1 Puffs—K-H billows

Puffs, or isolated billows, resemble Kelvin-Helmholtz billows. In the ocean, these typically have thicknesses ≤ 1 m and a horizontal extent ≤ 200 m (Gregg, 1987).

Thorpe (1973) describes the evolution of K-H billows; a short account will be given here. Instabilities were created in the laboratory by tilting a tank containing a layer of fresh water overlying a layer of brine, with the interface thickness set by diffusion after a fixed time. After the tube is tilted, instability occurs when the gradient Richardson number $Ri_g = N^2/(\partial \overline{u}/\partial z)^2$ at the interface falls below $\approx \frac{1}{4}$. The instability has the form of waves which steepen at alternating nodes, overturning to form billows. The largest vertical velocities observed were one third of the velocity difference across the interface. Turbulence begins near the centre when the billow height is about one third of its wavelength (twice the density interface thickness). The turbulence quickly fills the billow, which then spreads vertically by entraining fluid above and below. The edges of the turbulent region spread at a rate of $\Delta U/5$, where ΔU is the velocity difference between the top and bottom layers. Growth stops at a non-dimensional time (starting at the onset of turbulence) $\tau \equiv g't/\Delta U = 1.5$

when $Ri_g = 0.37 \pm 0.12$. The decaying turbulence appears isotropic until $\tau = 3$, after which some re-stratification appears to occur.

Thorpe (1984) showed that the turbulence was due to the sidewalls of the tanks in these experiments. It seems that there is an additional condition for turbulence based on the turbulent Reynold's number. Secondary structures in the billows such as convective rolls are also thought to be important for turbulence. These highly dissipative structures may be what leads to turbulence rather than billow collapse (Thorpe, 1984), but since large scale overturning must still occur I plan to argue that overturning scale quantities may possibly be used to infer mixing rates even if these larger scales are not directly responsible for the mixing. This is the goal of this thesis, and so will be shown through simple models that neglect the small scale structures within overturns in favour of the larger scales. These models will be tested with various data sets.

Early estimates of the mixing efficiency by Thorpe (1973) from the increase in potential energy are consistent with Oakey's (1982) later oceanic result of $0.24 \times (1 \pm \frac{1}{2})$. But because Thorpe's experiments were contaminated by mixing from the sidewalls, Thorpe (1984) considered this mixing efficiency to be an upper limit for the K-H instability.

The expected L_T signature of a K-H instability, sampled with a CTD probe, varies according to the evolution stage of the overturn according to Thorpe (1973): L_T is greatest during initial overturning, and the Th profile looks like a single S-shape[5]. This denotes a single structure where heavy water overlies lighter water. As the overturn decays, the density profile is mostly stable with some density fluctuations that re-order on the scale of the billow. This changes quickly with re-stratification. At $\tau = 3.75$ the density profile has smaller amplitude fluctuations that would perhaps resemble many new smaller-scale overturns, each with an S-shape Th profile. Based on Thorpe's description, I argue that the average of many profiles should be used to infer mixing rates from overturn scale quantities.

---

[5]An idealized overturn with a Z-shaped Th profile is shown in Figure 3.2

2.3.2   Persistent Mixing Zones

The interaction of currents and bathymetry is a typical forcing found on the continental shelf and in estuaries. This may form persistent mixing layers. Large scale shears such as internal tides may be expected to have similar energetics to near-inertial mixing zones discussed by Gregg (1987) because the forcing time is much longer than N^{-1}. Gregg (1987) describes these mixing layers as having typical thicknesses from 5–10 m and horizontal extent greater than 1 km. They are energetic, with Reynolds number high enough to support buoyancy flux ($\epsilon >15$ to $25\,\nu N^2$) and marginally high enough to assume isotropic turbulence ($\epsilon > 200\nu N^2$). Overturning occurs over a sufficiently long time (hours to days) to lead to mixed layers (Gregg, 1987).

For example, completely mixing a stratified layer raises its potential energy by about $N^2H^2/12$, where N is measured using the gradient of the re-ordered overturn-containing density profile, and approximates the stratification before instability occurred. Assuming that the buoyancy flux is $\Gamma\epsilon$ with $\Gamma = \frac{1}{4}$, the time required for complete homogenization is $t = N^2H^2/12\Gamma\epsilon$. For example, a perhaps typical layer in the thermocline with $H = 5$ m, $N^2 = 10^{-4}$ s^{-2} and $\epsilon = 1.5 \times 10^{-8}$W kg^{-1} needs $t = 15$ hours to mix. If mixing persists for many hours, it thus leads to significant increase in potential energy. Osborn (1980) had this type of process in mind for his model of TKE production balancing J_b and ϵ, the same for Osborn and Cox's (1972) model for heat flux (Gregg, 1987).

These forced mixing layers can be compared to laboratory experiments of grid-generated turbulence in a shear flow (Gregg, 1987), where the shear provides the forcing for the mixing subsequent to its initial formation at the grid. After the initial growth, an inertial-buoyancy balance follows with $L_T \approx L_O$ (Rohr *et al.*, 1988).

The mixing layers under a steady forcing can also be compared to oscillating grid experiments in stratified fluids. When the grid is oscillated faster than N, turbulent intrusions are formed which spread into the interior (Thorpe, 1982; Browand and Hopfinger, 1985). Strongly mixed layers can be expected to produce such intrusions, similar to a continuous collapse. The velocity scale of such a density current is

$(g'H)^{1/2}$ where H is the intrusion thickness, g' is $g\Delta\rho/\rho$ and $\Delta\rho$ is the density difference between the intruding waters and their environment, about half of the density difference across the originating mixed layer. The shear associated with the intruding flow is $\approx (g'/H)^{1/2}$, leading to a Richardson number at the boundary of the intrusion of $N^2 H/g' \approx 1$. Thus, as the intrusions disturb the surrounding waters, they may lead to further mixing and entrainment.

2.3.3 Application to Coastal Regions, Thermocline and Abyss

In the abyssal ocean and in the thermocline, the internal wave field occasionally has breaking waves when the Richardson number becomes critical. This occurs over short time scales of order N^{-1}, which is of the same order as the turbulence time scale (say u'/L_T). In this case microstructure models of buoyancy flux may not be applicable because the assumptions of steady homogenous turbulence do not hold. It is hoped that averaging could compensate for this (Gregg, 1987). The observation of overturning events with an instrument such as a CTD is also quite difficult in the abyss because of the small overturning density fluctuation expected (shown later in this chapter) and the difficulties of sampling at depth.

Estuaries and coastal regions are mostly mixed by shears with long time scale compared to N^{-1} (for example the tidal period is long compared to N^{-1}). The Osborn model for K_ρ and the Osborn-Cox model for K_{heat} are consistent with these shear structures. Measuring overturn scales is much easier than in the abyss or oceanic thermocline because of the shallow sampling, larger overturning scales and higher density gradients. CTD sampling through energetically forced layers should thus lead to a good estimate of the mixing; this will be the focus of many chapters in this thesis. Persistent mixing layers are also found in the thermocline (Gregg *et al.*, 1986); in this case overturn measurements can possibly be used in cases of strong mixing when instrument resolution is adequate (this is briefly discussed later in this chapter).

In summary, overturn scale measurements are more likely to lead to pratical estimates of mixing rates in energetic areas than in the abyss. New models (two and three) presented in the next chapter link buoyancy flux and mixing efficiency of persistent overturning to overturn scale measurements, and are applicable to persistent mixing layers discussed here, with further restrictions to be imposed when laying down the model assumptions.

2.4 Available Potential Energy of the Fluctuations

The Available Potential Energy of the (density) Fluctuations of overturns, called the APEF and denoted ξ, is also a large scale variable linked to buoyancy flux. Its use will be extensive in the thesis, and so it is defined and explained here.

2.4.1 Definition and Alternative Formulation

Dillon (1984) defined the APEF, ξ, as the depth-averaged difference of potential energy per unit mass between a measured density profile ρ and the corresponding re-ordered profile $\rho_\circ$. We can write this as

$$\xi = \frac{1}{H}\frac{g}{\overline{\rho}}\int_0^H \rho' z \, dz \tag{2.23}$$

where g is the acceleration of gravity, H is the integrated depth, $\overline{\rho}$ is the average water density, and $\rho'(z) = \rho(z) - \rho_\circ(z)$ is the "Thorpe fluctuation", the amplitude of the density instability. The re-ordered profile $\rho_\circ$ was introduced in Section 2.2.2 because it is also used to calculate Thorpe displacements. It is the state of lowest potential energy to which the measured profile can evolve adiabatically, and so is chosen as the reference level against which density fluctuations are evaluated. For measurements uniformly spaced at depths $z(i)$, the APEF, in $\mathrm{J\,kg^{-1}}$, is[6]:

$$\xi = \frac{g}{n\,\overline{\rho}}\sum_{i=1}^{n} z(i)\,\rho'(i) \tag{2.24}$$

---

[6]Equation (2.24) is modified from Dillon (1984) where temperature was used instead of density.

The definition of ξ can be written in another form. First write (2.24) as $\sum z\rho(z) - \sum z\rho_\circ(z)$. Then, the index of the second summation is changed such that the point at $z + Th(z)$ is summed instead of that at z. This is valid as it only changes the order in which the points are summed. The APEF becomes $\sum z\rho(z) - \sum[z + Th(z)]\rho_\circ(z + Th(z))$. From the Thorpe displacement definition, this becomes: $\sum z\rho(z) - \sum[z + Th(z)]\rho(z)$ so that

$$\xi = \frac{g}{n\,\bar{\rho}}\sum_{i=1}^{n} -Th(i)\,\rho(i) \qquad (2.25)$$

This form emphasizes that ξ is the potential energy released in moving heavy water down and light water up in the re-ordering of the measured profile.

Equations (2.24) and (2.25) both sum products of fluctuations Th or ρ' and profile quantities ρ or z. These last quantities are not completely determined, in the sense that any constant can be added to them, and (2.24) and (2.25) must still hold. The summation must therefore be made over points such that $\sum Th$ or $\sum \rho'$ is zero; in that way, an added constant cancels out. This is the only restriction to evaluate ξ over depth intervals: that the $\sum Th$ or equivalently $\sum \rho'$ must be zero over the points for which ξ is evaluated. This is true, although not exclusively, when the evaluation interval encloses overturns completely.

2.4.2 Approximations

The calculation of ξ over fixed depth bins is made difficult by the requirement that fluctuation summation be done over spans that include all of a disturbance. For this reason, approximations of ξ were derived and will be shown here. Other uses for these approximations include scaling arguments and estimation of ξ from bin-averaged archived data for which ξ was not calculated. These are used in Chapters 4 and 5.

Point-by-Point Two-Point Exchange Approximation

Assume two unstable points with density difference ρ' separated by a distance Th can both be moved to their stable re-ordered position by exchanging places. The exchange involves a potential energy change per unit mass of $g\,\rho'\,Th/\overline{\rho}$, one half of which can be attributed to each point involved. If all unstable points come in such pairs, then the profile can be re-ordered by two-point exchanges where points are moved no more than once. The potential energy change at each point, called the two-point exchange APEF, is[7]

$$\xi(i) \approx -\frac{g}{2\overline{\rho}}\,\rho'(i)\,Th(i) \tag{2.26}$$

If a linear re-ordered density profile is assumed, then $\rho'(i) = Th(i)(\partial\rho_\circ/\partial z)$ in (2.26) and ξ is estimated as $\frac{1}{2}N^2 Th(i)^2$ ($= \frac{1}{2}N^2 L_T^2$ when suitably averaged) where N is the buoyancy frequency of the re-ordered density profile.

This two-point exchange formulation (2.26) is an approximation. The sum of (2.26) over the profile is different from (2.24) because inversions cannot always be re-ordered using a single series of two-point exchanges. For example, the point at $z(i)$ may get exchanged with the point at $z(j)$ to go to its re-ordered location, but then point j exchanged to depth $z(i)$ may not be in a stable re-ordered location, so it may have exchanged with some other point. The energy change in secondary exchanges is not taken into account in (2.26). Dillon and Park (1987) show that for their data the method errs by less than 2% averaged over complete profiles, increasing to 14%

---

[7]Equation (2.26) is equivalent to Equation (2) in Dillon and Park (1987)

error over individual overturns.[8]

Linear Profile Approximation

As stated after (2.26), the assumption of a linear re-ordered density profile reduces (2.26) to

$$\xi \approx \frac{1}{2}N^2 L_T^2 \tag{2.28}$$

Estimating L_T by $\overline{\rho'^2}^{1/2}/(\partial\overline{\rho_\circ}/\partial z)$

If L_T is not available, then it could be scaled from Thorpe fluctuations ρ' (e.g. in grid-turbulence experiments in chapter 4) and the mean gradient as $\overline{\rho'^2}^{1/2}/(\partial\overline{\rho_\circ}/\partial z)$ and ξ is approximated as

$$\xi \approx \frac{1}{2}\frac{g}{\overline{\rho}}\frac{\overline{\rho'^2}}{\partial\overline{\rho_\circ}/\partial z} \approx \frac{1}{2}\left[\frac{g}{\overline{\rho}}\right]^2 \frac{\overline{\rho'^2}}{N^2} \tag{2.29}$$

Local Density Gradient Approximation

Crawford (1986) finds that $\frac{1}{2}N^2 L_T^2$ over-estimates ξ by a factor of 2.8 when N^2 is calculated over a layer enclosing both overturning and non-overturning intervals. This is assumed to be caused by locally smaller N within overturns than in the layer surrounding them.

In an attempt to correct for this effect, if ξ is not directly calculated, it is now hypothesized that the mean local gradient within overturns of a layer can be estimated

---

[8]It is likely that the approximation (2.26) holds so well because it may sum to (2.24) over the profile even if the profile cannot be re-ordered using a single series of two-point exchanges. This occurs when the re-ordered density profile is linear over the span of each overturn and the sampling interval is constant. Taking ξ to be the average of (2.24) and (2.25), we get

$$\xi = \frac{1}{2}\frac{g}{\overline{\rho}}\sum(\rho' z - \rho Th) \tag{2.27}$$

The Thorpe fluctuation $\rho' = \rho - \rho_\circ$ is transformed using the definition of the Thorpe displacement, $\rho(z) = \rho_\circ(z + Th(z))$, to $\rho'(z) = \rho_\circ(z + Th(z)) - \rho_\circ(z)$. The re-ordered profile is assumed to be linear so this becomes $\rho'(z) = Th(z)[\rho_\circ(z) - \rho_\circ(0)]/z$ where $\rho_\circ(0)$ is the density at the surface. Substituting into (2.27) with summation over the complete overturn, $\rho_\circ(0)$ cancels out. This leaves $\xi = g/2\overline{\rho}\sum\rho_\circ Th - \rho Th = -(g/2\overline{\rho})\sum\rho' Th$ which is equal to (2.26).

as $\overline{\rho'^2}^{1/2}/L_T$. In this case, ξ is approximated by

$$\xi \approx \frac{1}{2}\frac{g}{\bar{\rho}}\,\overline{\rho'^2}^{1/2}\,L_T \tag{2.30}$$

resembling the two-point exchange approximation (2.26), but using layer-averaged properties.

2.4.3 A Test on CTD Data

The approximations of ξ (2.26), (2.28), (2.29), (2.30) are tested using CTD profiles sampled in the St. Lawrence estuary in July 1988. Nine consecutive CTD profiles taken at 4 minute intervals sampled a mixing layer of order 10 m thick. The CTD profiler was lowered at 50 cm s^{-1} to obtain 'oversampled' data at 2 cm intervals (the physical size of the temperature and conductivity sensors, as well as their separation, are slightly greater than this 2 cm sampling interval, such that adjacent values are expected to be correlated). The profiles are the first nine profiles of a layer discussed in chapter 7; see the boxed area in Figures 7.7 and 7.8, and temperature profiles and T–S relation in Figure 7.9.

To summarize, the approximations are based on these assumptions

- (2.26) $\xi \approx -\sum i \left[\frac{g}{2\bar{\rho}}\,\rho'(i)\,Th(i)\right]$ is half of the potential energy increase in every substitution of a point with the one located at the first's re-ordered position. Secondary exchanges are neglected. All data from the profiles are required to calculated this, there is thus little advantage in using it rather than the definition form of ξ.

- (2.28) $\xi \approx \frac{1}{2}N^2 L_T^2$ assumes that N^2 is linear and represents the density gradient of the re-ordered profile within the overturn. Bulk properties (layer averages) can be used for L_T and N.

- (2.29) $\xi \approx \frac{1}{2}\left[\frac{g}{\bar{\rho}}\right]\frac{\overline{\rho'^2}}{N^2}$ assumes that the (possibly unmeasured) Thorpe scale is well approximated by $L_T = \overline{\rho'^2}^{1/2}/(\partial\overline{\rho_\circ}/\partial z)$. Bulk properties can be used for L_T and N.

- (2.30) $\xi \approx \frac{1}{2}\frac{g}{\rho}\overline{\rho'^2}^{1/2}L_T$ assumes that the density gradient within overturns is well approximated by $\partial\overline{\rho_\circ}/\partial z = \overline{\rho'^2}^{1/2}/L_T$. The advantage is that N^2 does not enter into (2.30) to bias toward the higher values of stratification found outside of the overturns.

Figure 2.1 shows the approximations of ξ, plotted against the definition values of ξ evaluated using (2.24). In panels on the left-hand side, each data point represents a separate overturn. The rms quantities L_T, ρ'^2 and $\overline{\rho'Th}$ were calculated within each of the 346 separate overturns found[9] which consisted of more than 10 points. The stratification N^2 was also calculated only within the span of each overturn. Regressions in logarithmic space show that the slope of the approximated APEF versus ξ is never significantly different from one; therefore the regressions with forced slope of one are used. All four approximations have (unquantified) little scatter and a coefficient usually only a few percent away from one. All four approximations are judged to do very well.

Looking at the above assumptions, the success of the methods means that when evaluated and averaged over the span of a single overturn

- N^2 and therefore $(\partial\overline{\rho}/\partial z)$ within an overturn are both well approximated by a linear regression on the re-ordered density profile because (2.28) and (2.29) hold over overturns (assuming L_T would not be biased by re-ordering in any case).

- That the density gradient within an overturn is well approximated by $\overline{\rho'^2}^{1/2}/L_T$, where these rms quantities are calculated over that overturn, because (2.30) holds over separate overturns.

In the right-hand panels of Figure 2.1, the rms quantities L_T, ρ'^2 and $\overline{\rho'Th}$ were calculated over the entire depth span of the mixing layer for each overturn. This yielded only 9 averages. The stratification N^2 is also evaluated by linear regression

---

[9]Defined as the smallest group of consecutive points which may be re-ordered without moving any other point in the profile.
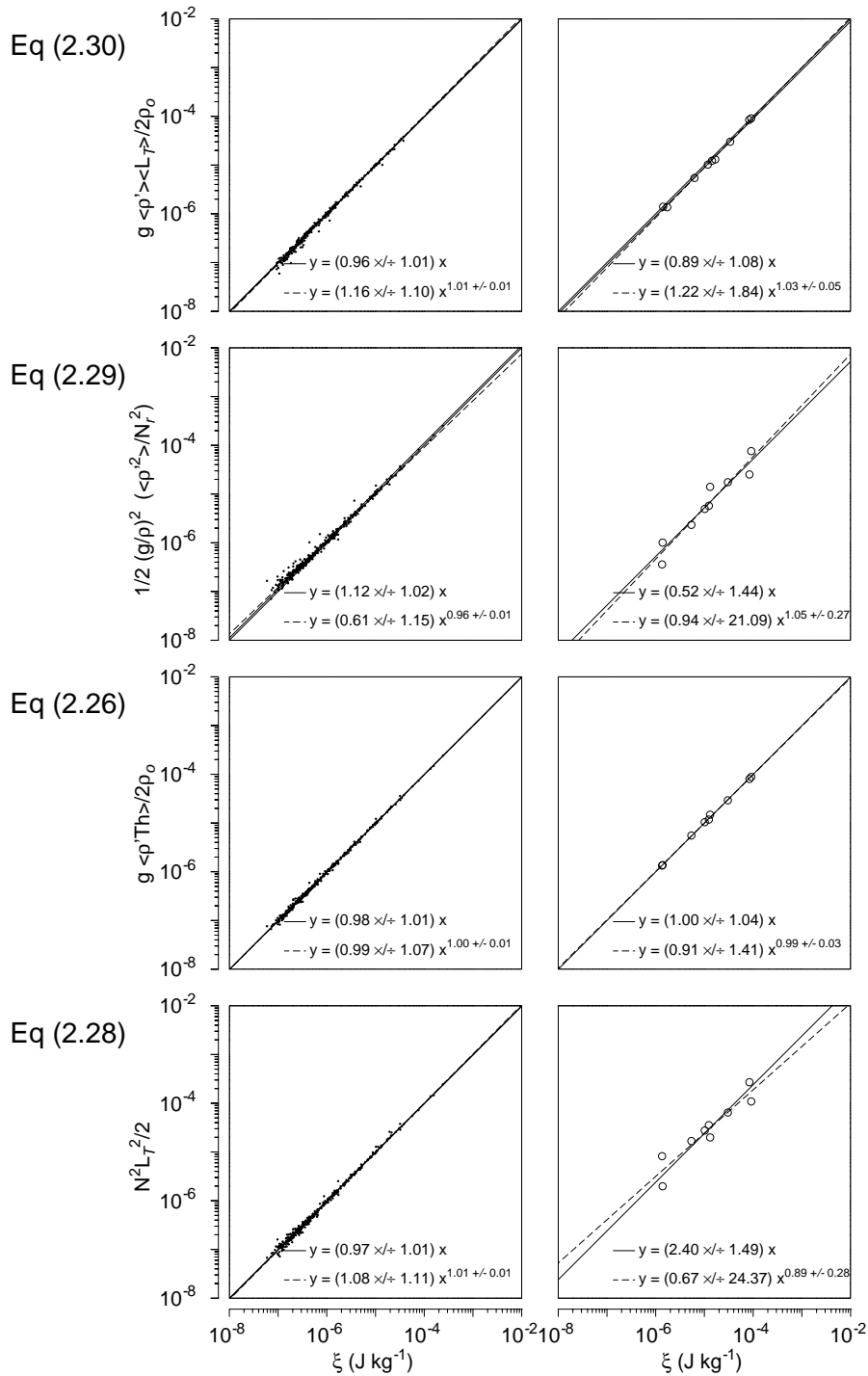
Figure 2.1: Four approximations of the APEF, ξ, are evaluated using data from 9 CTD casts in the St. Lawrence estuary. The panels on the left are calculated using statistics averaged over individual overturns; those on the right used one average per profile over the entire layer.

on the re-ordered density profile over the entire layer depth. This includes overturning and non-overturning depth spans.

Crawford (1986) found that N^2 evaluated over a layer enclosing overturns is higher than N^2 within only the overturns. This result is confirmed here. Both (2.28) and (2.29) use the density gradient in their approximations, and both are biased because of it. It is found that the density gradient within overturns is on the average 2 to 2.4 times smaller than over the entire mixing layer.

The fact that N^2 is lower within overturns than in surrounding waters could be interpreted in different ways: **i)** overturns occur preferentially where N is low; **ii)** the overturn has done some mixing and thus a lower stratification is found; **iii)** strain is associated with Kelvin-Helmholtz billows such that a vertical transect through the billow shows lower stratification than found after billow collapse (recall that in section 2.3.1, turbulence was quoted as beginning when billow height was twice the density interface thickness (Thorpe, 1973)). Since it is not easy to quantify these effects, especially for oceanic data for which the driving force is not always known, the difference in N is noted but not further explained.

Not surprisingly, the two-point exchange approximation (2.26) does almost perfectly. Recall that it is an average of products over all points of the overturns. This approximation requires that all original data is available in order to use it because $\overline{\rho' Th}$ is not usually a calculated quantity in archived data.

A New Approximation

The approximation $\xi \approx \frac{1}{2}(g/\overline{\rho}) \overline{\rho'^2}^{1/2} L_T$ is within 10% of ξ. This implies that the average density gradient within several overturns can be well estimated by $\overline{\rho'^2}^{1/2}/L_T$. This is a new and very useful result: for example, Dillon (1982) tables layer-averaged overturning data for mixing layers; he does not table ξ, but he does table both L_T and $\overline{\rho'^2}^{1/2}$ such that ξ can be approximated much better than by using $N^2 L_T^2/2$, which would have previously been used.

2.5 Requirements to Resolve Overturns

CTD profiles must have adequate density and depth resolution to measure overturns of a given energy. The noise level for ξ is estimated from (2.26) as $(g/2\overline{\rho})\,\rho'_{min}\,Th_{min}$, where ρ'_{min} and Th_{min} are the minimum measurable Thorpe fluctuation and Thorpe displacement.

Denoting depth resolution as δz and density noise as $\delta \rho$, in most cases $(g/2\overline{\rho})\delta z\,\delta \rho$ is a lower bound on the ξ noise level. There are actually two separate cases to consider: low stratification where $\delta \rho$ is the limiting factor, and high stratification where δz is the limiting factor.

High Stratification

Assume that stratification is high enough that the density difference between two consecutive points in the re-ordered density profile is greater than the noise level $\delta \rho$. This condition is expressed as $\delta \rho / \delta z < \partial \rho_o / \partial z$. In this case, depth resolution limits the minimum measurable Thorpe fluctuations and Thorpe displacements to $\delta z(\partial \rho_o/\partial z)$ and δz respectively. The minimum APEF measurable is then

$$\xi_{\text{noise}} = \frac{g}{2\overline{\rho}}\,\frac{\partial \rho_o}{\partial z}\,(\delta z)^2 \tag{2.31}$$

Low Stratification

Assume now that stratification is low, such many consecutive density points of the re-ordered profile are not significantly different. This condition is expressed as $\delta \rho / \delta z > \partial \rho_o / \partial z$. In this case, density resolution limits the minimum measurable Thorpe fluctuations and Thorpe displacements to $\delta \rho$ and $\delta \rho/(\partial \rho_o/\partial z)$ and respectively. The minimum APEF measurable is then

$$\xi_{\text{noise}} = \frac{g}{2\overline{\rho}}\,(\frac{\partial \rho_o}{\partial z})^{-1}\,(\delta \rho)^2 \tag{2.32}$$

Minimum Measurable APEF

Listing (2.31) and (2.32) together, the minimum measurable APEF is

$$
\begin{aligned}
\xi_{\text{noise}} &= \frac{g}{2\rho} \left(\frac{\partial\rho_o}{\partial z}\right)^{-1} (\delta\rho)^2 && \text{if } \frac{\delta\rho}{\delta z} > \frac{\partial\rho_o}{\partial z} \\
\xi_{\text{noise}} &= \frac{g}{2\rho} \frac{\partial\rho_o}{\partial z} (\delta z)^2 && \text{if } \frac{\delta\rho}{\delta z} < \frac{\partial\rho_o}{\partial z}
\end{aligned}
\tag{2.33}
$$

If stratification $(\frac{\partial\rho_o}{\partial z})$, depth resolution (δz) and noise level $(\delta\rho)$ are known, (2.33) gives the minimum ξ that can be detected. For example,

- At the base of the thermocline where $N = 0.005$ s^{-1} a density probe capable of measuring fluctuations of 10^{-3} kg m^{-3} at 1-cm intervals, will only measure overturns bigger than 0.4 m $(= \delta\rho\,(\partial\rho_o/\partial z)^{-1})$, of $\xi > 2 \times 10^{-6}$ J kg^{-1} and $\epsilon > 10^{-8}$ W kg^{-1}, using the approximate relation $\epsilon = \xi N$.

- In an energetic estuary with a high stratification of $N = 0.03$ s^{-1}, depth resolution limits the smallest measurable overturn. The error levels are then $\xi = 5 \times 10^{-8}$ J kg^{-1} and $\epsilon > 1.5 \times 10^{-9}$ W kg^{-1}.

Note that both these examples used the relation $\epsilon \approx \xi N$ which is derived from $L_O \approx L_T$; it will be shown in this thesis that this is not a general result, and is used here merely as a scaling argument. Also, the kinematical model leading to $L_O \approx L_T$ assumes that sporadic occurrences of breaking internal waves leads to overturning. The Thorpe scale is thus a time average. If overturning were to occur during only 10% of the time, then the overturning energy is ten times higher than average during overturning; noise levels set here should be compared with this latter value, if it can be approximated.

These error levels for dissipations can be related to eddy diffusivities by $K_\rho = \Gamma\epsilon N^{-2}$ (Osborn, 1980) using a mixing efficiency of $\Gamma = 0.265$ (Oakey, 1985). For the previous examples, the minimum detectable K_ρ is 10^{-4} m^2 s^{-1} for the thermocline and 4×10^{-7} m^2 s^{-1} for the estuary. The strong mixing in the estuary should be well resolved, but the thermocline example may only have sufficient density resolution to measure the likely weak mixing (estimated at $K_v = 10^{-5}$ m^2 s^{-1} (Garrett, 1984))

if overturning events occur less than 10% of the time (shorter overturning fraction implying larger and easier to measure overturns).

2.6   Summary

This chapter started with a review of microstructure models parameterising mixing, as well as a traditional view of the Thorpe scales being related to microstructure. The APEF was also introduced.

In summary, it was noted that

- Puffs are consistent with the kinematical model of occasional breaking internal waves, and less so with the mixing models used to interpret microstructure mixing measurements because of the assumptions of homogeneity and steady-state (averaging is typically assumed to overcome these requirements).

- Persistent mixing zones, and especially strong mixing found in surface and bottom boundary mixing layers, are more likely to fit mixing model assumptions, thus perhaps requiring less averaging. (Overturning scale models presented in chapter 3 will apply to these persistent mixing zones).

- Some initial scalings were presented to test whether overturning data should resolve an expected level of mixing.

The main results are

- A new APEF approximation using layer-averaged quantities was shown to hold very well. It is $\xi \approx \frac{1}{2}\frac{g}{\rho}\overline{\rho'^2}^{1/2} L_T$

- The commonly used approximation $N^2 L_T^2/2$ only holds when N^2 is representative of the density gradient of the re-ordered profile within the overturn.

- This previous assumption was shown *not* to hold using mixing-layer averages of data from the St. Lawrence estuary, in agreement with earlier findings of

Crawford (1986). In the present case, stratification within overturns is 2 to 2.4 times smaller than the layer average.

Chapter 3

Relating Buoyancy Flux And Dissipation of Turbulent Kinetic Energy To Overturn Scales

In this chapter, three models for buoyancy flux, J_b, and turbulent kinetic energy, ϵ, are derived; some derivations are old and some are new, and the new derivations lead to existing empirical models. The term 'model' is used loosely here, perhaps as Osborn's (1980) useful derivations are also coined a model. They parameterize mixing quantities in terms of simple physical mechanisms. This permits interpretation of the conditions necessary to apply them to the ocean. Figure 3.1 shows a diagram of the three models. The assumptions required for each model are listed in summary Table 3.1 (found at the end of the chapter) and will be tested in subsequent chapters.

The correspondence between the Ozmidov scale, L_O, and the Thorpe scale, L_T, yields model one. This model is not new. In fact, it is perhaps the most commonly accepted view held by the mixing community (see Crawford (1986) for a review). Model one relates overturning to the dissipation of turbulent kinetic energy. It assumes both a constant mixing efficiency, Γ, and a balance between inertial and buoyancy forces. This latter concept, called inertial-buoyancy balance, simply is discussed in this chapter. In Figure 3.1, the measurement of overturn sizes L_T is translated laterally to an
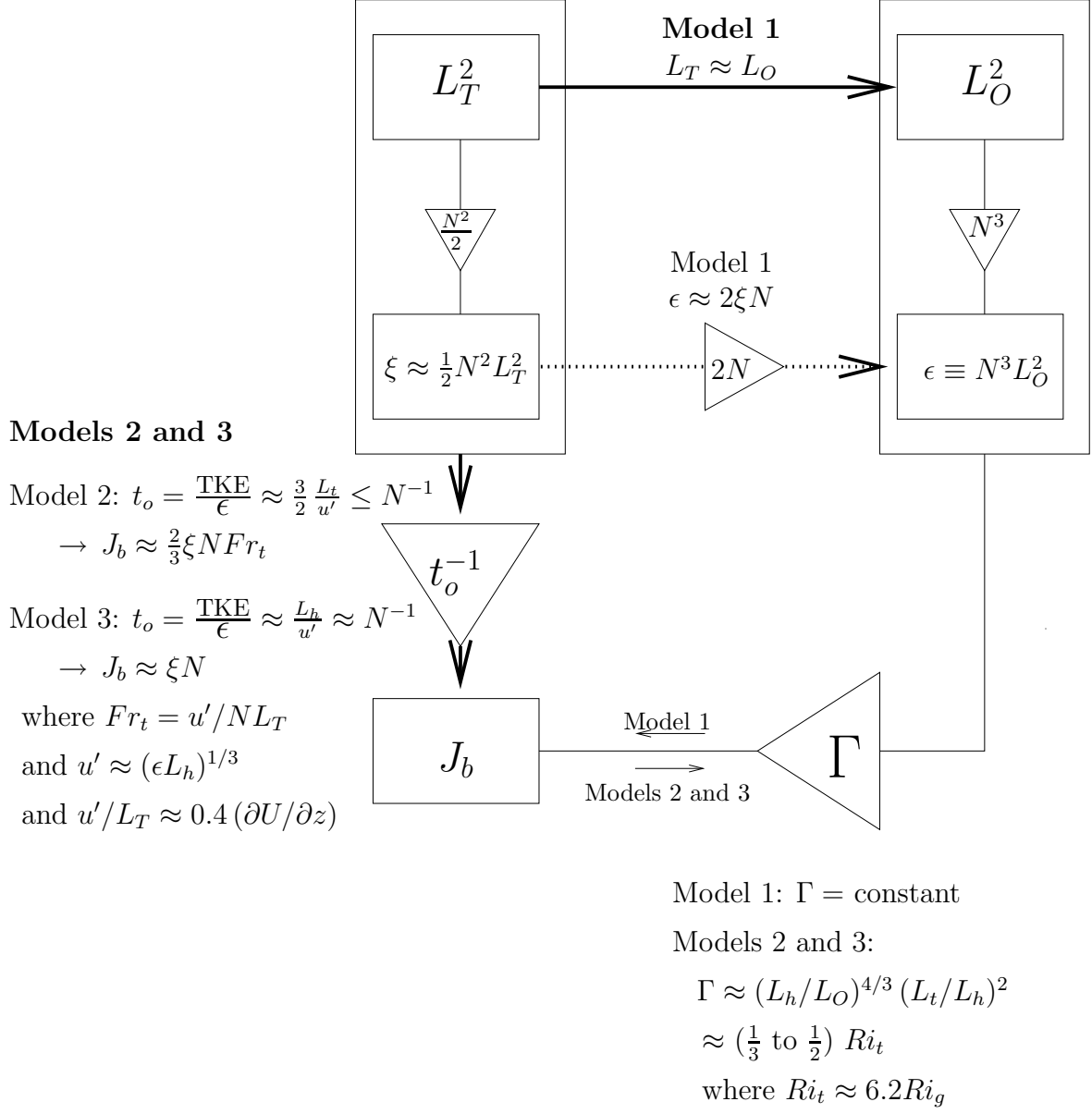
Figure 3.1: Diagram of the three models derived in this chapter. **Model one:** Traditional view linking L_T to L_O, and therefore ξ to ϵ via a decay time N^{-1}. A constant mixing efficiency is assumed; **Model two:** New model for growing isotropic turbulence, linking ξ to J_b via a decay time $\propto L_T/u' \propto (\partial \overline{U}/\partial z)^{-1}$; **Model three:** New model for anisotropic inertial-buoyancy balanced turbulence, linking ξ to J_b via a decay time N^{-1}; Mixing efficiency for models two and three depend on Ri_t, which can be inferred from Ri_g or ϵ and ξN. Boxes indicate measurable quantities, and triangles are multipliers that relate those quantities to each other.

Ozmidov scale, which is a measure of the rate of dissipation of TKE. By assuming a constant mixing efficiency Γ, the buoyancy flux is estimated from the estimate of ϵ. It will be shown in subsequent chapters that typical continental shelf mixing is not characterized by a constant mixing efficiency where this model should thus not be used. It may however be relevant to breaking internal waves in the abyss, which are thought to occur at inertial-buoyancy balance and thus at constant mixing efficiency (Ivey and Imberger, 1991).

Model two is new. It relates overturning directly to buoyancy flux for isotropic growing turbulence. Both mixing efficiency and balance between inertial and buoyancy forces depend on the character of the turbulent flow, parameterized by the turbulent Froude number, Fr_t. The results are similar to Ivey and Imberger's (1991) empirical result based on laboratory experiments (reviewed in Appendix B); the interpretation of the results differs substantially from Ivey and Imberger's. In Figure 3.1, the measurement of the potential energy of the overturns (APEF) is related directly to buoyancy flux through a turbulent Froude number dependent decay time, usually smaller than N^{-1} (where $2\pi N^{-1}$ is the buoyancy period). It will be shown that this time scale can be related to the inverse of the shear if shear drives the turbulence. Model two should apply to cases of strongly driven mixing, where overturning scales are thought to be isotropic and growing; in chapter 7, we apply this model to an apparently new mixing layer and another known to be new because it is forced by a passing soliton.

Model three is an extension of model two for the case of steady-state mixing at inertial-buoyancy balance. The inertial-buoyancy balance sets the decay time scale. The turbulence is allowed to be anisotropic, which will affect the mixing efficiency. This model makes a prediction for buoyancy flux similar to Dillon and Park's (1987) empirical result. In Figure 3.1, the multiplication of the APEF by the inverse of the decay time still equals buoyancy flux, as for model two, but the decay time is now constant and approximately equal to N^{-1} due to the inertial-buoyancy balance. The rate of dissipation of TKE can be estimated from J_b from the mixing efficiency only

if the degree of isotropy is known (because it determines mixing efficiency in model three). Model three is expected to hold for mixing layers forced for a long time, but over a vertical scale smaller than the Ozmidov scale. This includes the surface layer, perhaps the bottom boundary layer and others mixing zones forced by depth-specific shears such as internal tides.

All three models will be compared to data in various mixing regimes in latter chapters, where it will also be shown that the traditional view—the first model—is a special case in the other two models. The latter two models apply in different circumstances, but it is difficult to differentiate between them with the oceanic data sets presented in this thesis.

These models do not offer a complete view on mixing. For example, recent work by Gregg (1989) attempts to quantify mixing directly as a function of the forcing shear. In contrast, work presented here relates an overturn scale mixing signature to small scale mixing; measurements of the these signatures (APEF) are required for the parameterization. The methods presented here are still useful because provide mixing rates and yet are simpler to execute than microscale measurements of mixing.

The mixing is parameterized over individual overturn measurements. The quest for a basin value of eddy diffusivity or buoyancy flux is then an exercise in averaging which is not discussed in this thesis. Work on the size and frequency of overturns in various mixing regimes would complement the parameterisations presented here.

3.1   Model One; Overturning Related to Dissipation of Turbulent Kinetic Energy

Garrett's (1989) derivation, showing the link between Ozmidov and Thorpe scales, was overviewed in the previous chapter. It is presented again in detail because the required assumptions lead into the second model in the next section. The first two models will be contrasted using the following derivations.

If a 'perfect' overturn is created as in Figure 3.2A and mixes to completion as in

Figure 3.2C, then the potential energy per unit mass of the water column within the overturn is raised by $N^2 H^2/12$. This is equal to the time-integrated buoyancy flux within the overturn. The buoyancy flux $J_b = \frac{g}{\rho}\overline{w'\rho'}$ is, related to the vertical eddy diffusivity K_ρ through the definition of K_ρ

$$J_b = K_\rho N^2 \tag{3.1}$$

Garrett (1989) linked the size and frequency distribution of overturns to K_ρ through

$$K_\rho = \frac{1}{12}\gamma_{\text{mix}}H^2 t_e^{-1} \tag{3.2}$$

where H is the overturn size or layer thickness, t_e is the time between overturning events and perfect homogenisation leads to $\gamma_{\text{mix}} = 1$ or $\gamma_{\text{mix}} < 1$ if mixing is incomplete (Note that the 'mixing efficiency' γ_{mix} is different from $\Gamma = J_b/\epsilon$ because no assumption is made of the relative quantity of kinetic to potential energy dissipation).

Garrett's use of (3.2) shifts from the mixing done by a single overturn to a time-average, suitable to the entire thermocline. Garrett then relates the layer thickness H to the Thorpe scale, a quantity measured in the field. The Thorpe displacement, shown in Figure 3.2B, varies linearly between $-H$ to $+H$ for a single overturn. The squared Thorpe scale is the rms value of that, and is equal to $L_T^2 = H^2/3$. If the water column is sampled many times between successive overturning events, the time-averaged Thorpe scale becomes $\langle L_T^2\rangle = (H^2/3)\,t_o/t_e$ where t_o is the decay time of the overturn. The brackets on $\langle L_T^2\rangle$ indicate time-averaging. The subtle difference between space and time averaging is briefly discussed in Section 3.2.1.

Combining the expression for $\langle L_T^2\rangle$ into (3.2), the time between events cancels out, leaving

$$K_\rho = \frac{1}{4}\,\gamma_{\text{mix}}\,\langle L_T^2\rangle\,t_o^{-1} \tag{3.3}$$

This kinematical expression for K_ρ can be equated to the Osborn model $K_\rho = \Gamma\epsilon/N^2$, after substituting $\epsilon = L_O^2 N^3$, yielding

$$K_\rho = \Gamma L_O^2 N = \frac{1}{4}\,\gamma_{\text{mix}}\,\langle L_T^2\rangle\,t_o^{-1} \tag{3.4}$$
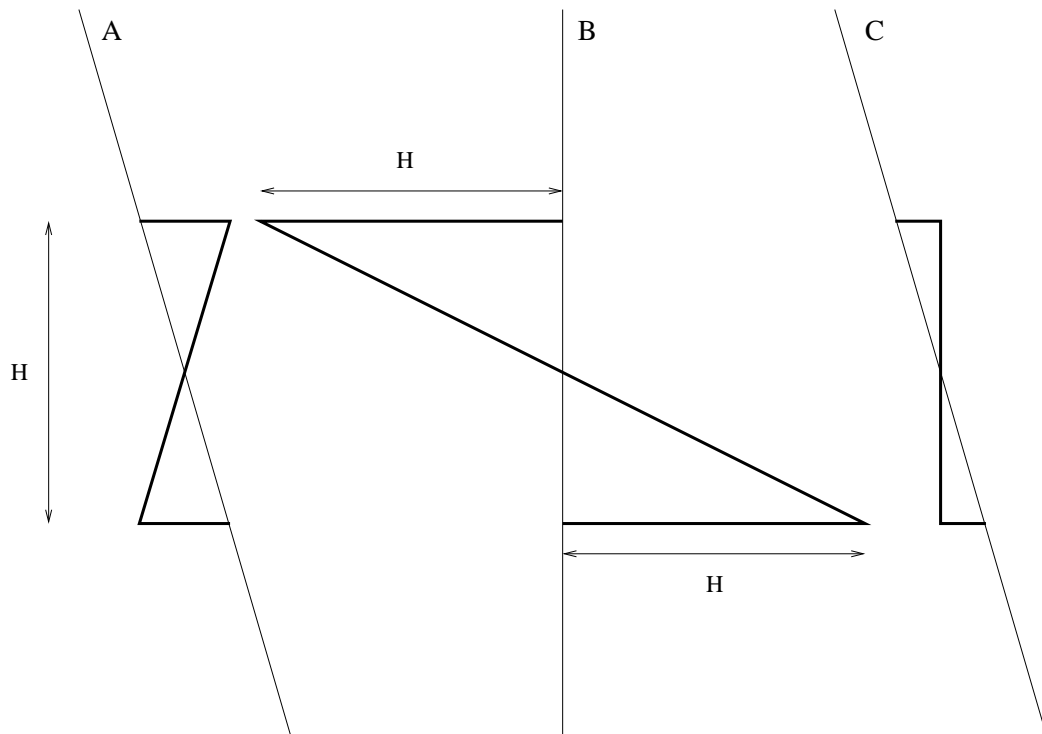
Figure 3.2: Idealized overturn creating a mixed layer. **A-** Density profiles before (thin line) and during (thick line) the overturn. Potential energy difference between profiles is $H^2N^2/6$; **B-** Thorpe displacement profile through the overturn. The rms squared Thorpe displacement is $H^2/3$; **C-** density profiles before overturn (thin line) and after complete homogenisation of the layer by mixing (thick line). Potential energy difference between profiles is $H^2N^2/12$.

If mixing efficiency is a constant of approximately $\Gamma \approx \frac{1}{4}$, as found by Oakey (1982; 1985)[1], if the decay time of an overturn scales with buoyancy as $t_o \approx N^{-1}$, and if mixing is complete ($\gamma_{\mathrm{mix}} \approx 1$), then the averaged Thorpe scale should be equal to the Ozmidov scale $\langle L_T^2 \rangle \approx L_O^2$.

Formulation of Model One

The above arguments lead to model one, equating L_T to L_O. While assumptions of turbulence homogeneity and steady-state (as well as no redistribution terms) are typically made in microstructure models (inconsistently with the kinematic model of sporadic K-H instabilities forced by random superposition of internal waves), Garrett's (1989) derivations show that time averaging suitable to the entire thermocline leads to $L_O \approx L_T$ even assuming that overturning is not homogeneous nor in a steady-state. The model implies a link between overturn size and dissipation of turbulent kinetic energy as

$$\epsilon \approx L_T^2 N^3 \tag{3.5}$$

Note that since the Available Potential Energy of the Fluctuation, ξ, is approximately equal to $N^2 L_T^2 / 2$, the first model can also be written as $\epsilon \approx 2\,\xi N$.

3.2 Background of Models Two and Three: Overturns Linked to Buoyancy Flux

Model one links overturn scales L_T or ξ to the rate of dissipation of kinetic energy. The usual kinematical model for this model is of random superposition of internal waves leading to breaking at critical Richardson number.

In this section the basis for new models is shown. I argue here that these overturn scale quantities are related directly to buoyancy flux, rather than to ϵ. The APEF

---

[1]Oakey (1982; 1985) did not assume full isotropy; doing so increases his mixing efficiency by 50%. He also assumed that unmeasured buoyancy flux was equal to measured potential energy dissipation, which is the assumption of the Osborn-Cox model

is shown to be related to J_b via a suitable decay time. Models two and three are end members of this new approach; they will be differentiated by the decay time and isotropy conditions.

The physical concepts behind these two models will constrain their application to a few types of turbulence: energetic, isotropic growing turbulence, and energetic anisotropic steady-state turbulence. These can only apply to shear-forced mixing layers where overturning is expected to be continuously extracting energy from the mean shear. The view is not of random internal waves breaking at a balance between inertial and buoyancy forces (inertial-buoyancy balance), but rather of the evolution of a uniform mixing layer much more homogeneous and steady, where the balance between potential and kinetic energy associated with isotropic inertial-buoyancy balance is not guaranteed.

In this section, the parent relation $J_b = \xi/t_o$ to both models two and three is established by re-examining Garrett's (1989) assumption of constant mixing efficiency, and also by looking at the temperature variance equation.

3.2.1   First Line of Argument: Garrett's Derivation Revisited

Garrett's argument relating L_T (and thus ξ) to ϵ is easily modified to relate ξ to buoyancy flux instead of to ϵ.

Garrett relates (3.3) to ϵ through $K_\rho = \Gamma\epsilon/N^2$ using a constant mixing efficiency. Instead, from (3.1) and (3.3) and by assuming $\gamma_{\mathrm{mix}} = 1$, one could write

$$J_b = \frac{1}{4}\left\langle L_T^2 \right\rangle N^2 t_o^{-1} \approx \frac{1}{2}\left\langle \xi \right\rangle t_o^{-1} \tag{3.6}$$

where $\langle \xi \rangle$ is a time-averaged quantity, approximately $\frac{1}{2}N^2\langle L_T^2 \rangle$. This relates a time-averaged buoyancy flux directly to ξ through a decay time t_o.

Alternatively, one may start at the beginning of Garrett's derivations. The form for K_ρ as (3.2) assumes that the integrated buoyancy flux is responsible for the increase in mean potential energy of the water column within the overturn. It is then simpler to relate the buoyancy flux directly to the change in mean potential energy

during the time between overturning events t_e. The APEF of the overturn in Figure 3.2A is twice the potential energy change observed between the final mixed state and initial state in Figure 3.2C. Thus the formulation in terms of K_ρ can be skipped and, using the half of the APEF to quantify the final increase in potential energy of the water after complete mixing of the overturn, the following expression for buoyancy flux can be written directly as

$$J_b = \frac{1}{2}\xi t_e^{-1} \tag{3.7}$$

The difference between (3.6) and (3.7) is the averaging method. The first divides an average potential energy by the true decay time of an event. The second considers only the energy of a single event and divides by the time separating events. Both yield the same averaged buoyancy flux. If one uses $J_b = \frac{1}{2}\xi\, t_o^{-1}$, using ξ from one overturn, then this becomes the buoyancy flux from that particular overturn. An ensemble average of many such overturns, including profiles where none were observed, would yield the same average as the other forms.

3.2.2 Second Line of Argument: Temperature Variance Equation

Let us now consider the temperature variance equation to argue for (3.7) without scaling arguments.

Suppose that density fluctuations are directly proportional to temperature fluctuations, so that buoyancy flux can be written as $J_b = -\alpha g \overline{w'T'}$. The temperature variance equation is (Tennekes and Lumley, 1972; Osborn and Cox, 1972; Dillon, 1982)

$$\frac{\partial}{\partial t}\overline{T'^2} = -2\,\overline{w'T'}\frac{\partial \overline{T}}{\partial z} - \chi_\theta \tag{3.8}$$

where the divergence terms have been neglected (an ensemble average is required to assume this); Further assumptions include isotropy and that no horizontal gradients exist (Dillon, 1982). While the time-derivative term is also usually neglected, it is kept here to show the connection of the APEF to the dissipation of potential energy

in a later derivation.

Definition of Turbulent Fluctuations

The turbulent fluctuations T' and w' in (3.8) require a definition. Dillon (1982) used the re-ordered profile as the base state for temperature fluctuations. In such a case, T' (or ρ') in temperature variance equations or turbulent kinetic energy equations refer to Thorpe fluctuations. The temperature variance $\overline{T'^2}$ is guaranteed to be zero for this choice of a base state when there are no overturns to create fluctuations. Also, profile averages through an overturn have $\overline{T'} = 0$ using Thorpe fluctuations. The notation used so far is thus appropriate, as it is consistent with Thorpe fluctuations used in the rest of the thesis.

If temperature and density fluctuations are defined as overturn-scale variables, then so too must turbulent velocities be, as their cross-correlation determines the buoyancy flux. This is consistent with the Kolmogorov turbulent kinetic energy spectrum, where the energy-containing scale is the size of the overturn (Tennekes and Lumley, 1972). In typical CTD sampling, turbulent velocities w' are not measured; therefore these will be infered from other measurements, but are assumed to be of overturn scale.

Comparison of Terms

Dillon (1982) showed that the turbulence is active rather than 'fossil', a term used by Gibson (for example, Gibson (1982)) to describe signatures of old turbulence no longer mixing. To do so, Dillon compared the terms $\partial \overline{T'^2}/\partial t$ and χ_θ in (3.8) to assess the importance of gravitational collapse in the temperature variance equation, choosing N^{-1} as a re-stratifying time scale[2]. The comparison is then between χ_θ and $N\overline{T'^2}$ and is shown in Figure 3.3. The data series in Figure 3.3 are explained in section C.1.

---

[2]Dillon calculated N^2 on the re-ordered profile as an average over a layer which encloses several overturns. This is discussed in depth in chapter 5, as it is likely to over-estimate N^2 by a factor of 2 to 3 (*e.g.* Crawford's (1986) factor and the factor of 2.4 to 2.8 introduced in chapter 2).

Dillon interpreted this figure for the combined series A B and C as

$$\chi_\theta = (3 \text{ to } 10) \, N\overline{T'^2} \tag{3.9}$$

indicating that the destruction of temperature variance from turbulent diffusion is much faster than what is expected from gravitational re-stabilization[3]. Dillon's assumption is then that additional fluctuations must be continually produced from the production term in (3.8) to balance their dissipation by χ_θ because the restratification time scale (and therefore the rate of change of temperature variance) is most certainly greater $N^{-1}/3$. Gibson's argument that temperature fluctuations survive after the turbulence is incompatible with Dillon's result that temperature variance is created and dissipated in a time much smaller than N^{-1}.

Potential Energy Equation

Equation (3.8) can be easily transformed into a potential energy equation. Thorpe fluctuations were shown to be related to ξ in chapter 2, as ξ is the measure of the potential energy contained within those fluctuations. In addition, χ_θ is related to the dissipation of potential energy. Multiplying (3.8) by $\alpha g/(2\partial T_o/\partial z)$, where T_o is the re-ordered temperature profile used to obtain the gradient, a potential energy equation is obtained as (Dillon, 1984)

$$\frac{\partial}{\partial t}\left[\frac{\alpha g \overline{T'^2}}{2\frac{\partial T_o}{\partial z}}\right] = -\alpha g \, \overline{w'T'} - \frac{\alpha g \chi_\theta}{2\frac{\partial T_o}{\partial z}} \tag{3.10}$$

The term on the left of (3.10) approximates the rate of change of ξ assuming $L_T \approx \overline{T'^2}^{1/2}/(\partial T_o/\partial z)$ (See section 2.4.3). The first term on the right is the rate of production of potential energy (the buoyancy flux) and the second is the rate of dissipation of potential energy, equal to $3N^2\kappa_T C_x$ (Dillon, 1984).

---

[3]Figure 3.3 also indicates data for which I have calculated that $\overline{T'^2}^{1/2}/(\partial T_o/\partial z) < 0.2L_T$. These data are circled in Figure 3.3. The first term in (3.10) under-estimates ξ by a factor of 5 or more for these points. The proportionality relation must hold even better between ξN and J_b than Figure 3.3 shows.
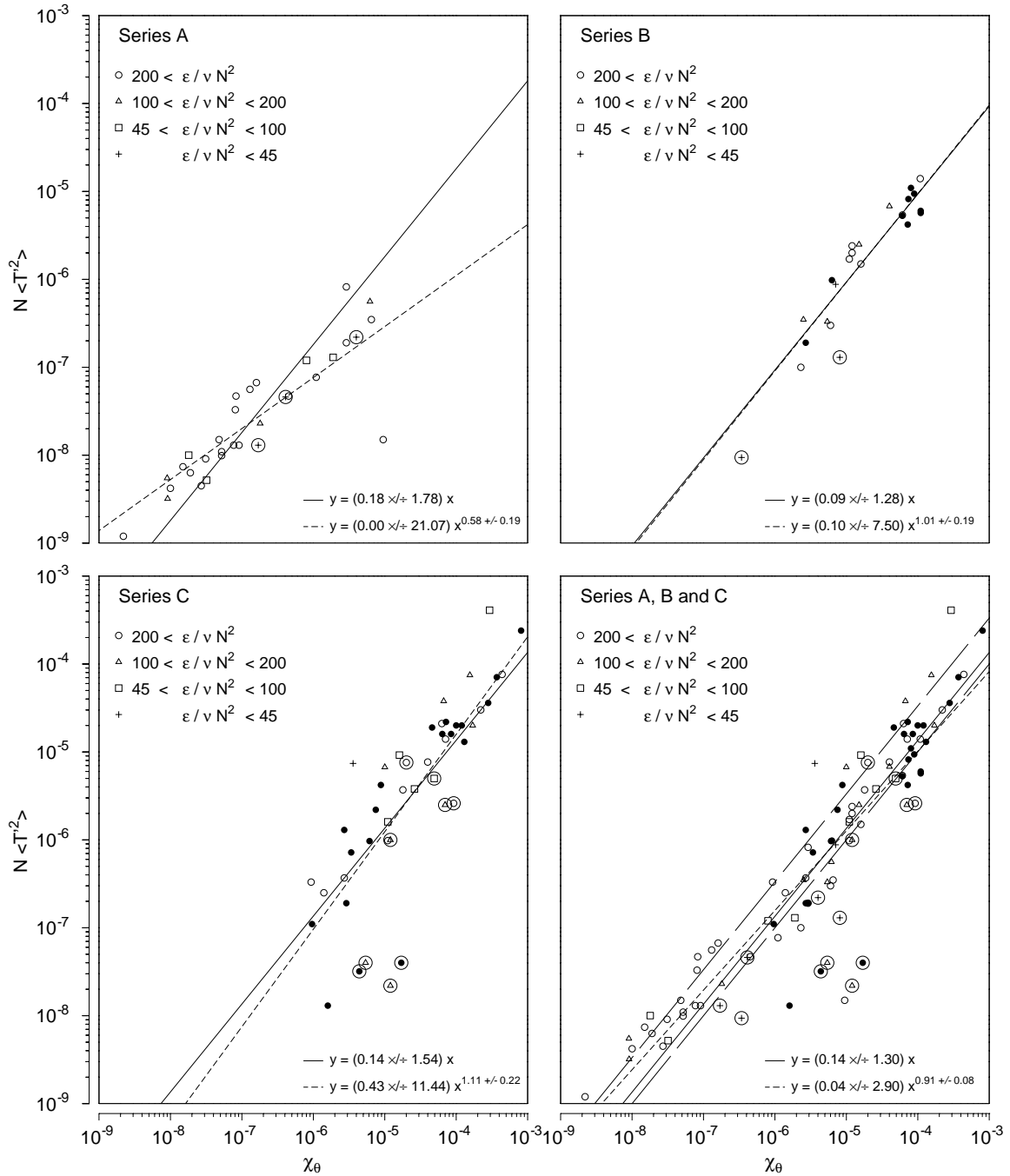
Figure 3.3: Comparison of $N\overline{T'^2}$ vs χ_θ. The long-dashed lines in the series A, B and C panel are $N\overline{T'^2} = 3\chi_\theta$ and $N\overline{T'^2} = 10\chi_\theta$, quoted from Dillon as the range of the scatter. Regressions are on data with $\epsilon/\nu N^2 > 200$. Data are coded according to turbulent intensity according to the legend; open symbols are well resolved data, filled symbols are marginally resolved; circled data have $(\overline{T'^2}^{1/2}/L_T)/(\partial\overline{T}/\partial z) < 0.2$. Data are from tables in Dillon (1982); both axes are in $^\circ C^2$ s^{-1}. This figure corresponds somewhat to Figure 7 in Dillon (1982).

In a steady-state, the rate of change of ξ is zero. This results in the familiar Osborn-Cox formulation for the heat flux $J_b = -\alpha g \overline{w'T'} = -3N^2\kappa_T C_x$, where $C_x = \overline{(\partial T'/\partial z)^2}/(\partial \overline{T}/\partial z)^2$ is the one-dimensional Cox number.

Relevance to Buoyancy Flux Model

Although (3.10) and (3.8) are linked through a constant, my interpretation of (3.10) differs from Dillon's interpretation of (3.8). Dillon wanted to show that the rate of change of temperature variance (assuming a buoyancy time scale) must be slower than the dissipation time scale; my following argument aims to show that the rate of change of potential energy—without yet specifying the time scale—is tied to buoyancy flux and dissipation of potential energy at both ends of the size spectrum, and that the equilibrium implies a proportionality between the potential energy (APEF) and the in and out fluxes.

Imagine an impossible case where no dissipation of potential energy occurs. Then, the buoyancy flux, equivalent to throwing heavy particles of water up into the water column, must accumulate into APEF. No mixing occurs which would permanently raise the center of mass of the water column and reduce the APEF; mixing can only occur through the dissipation term. The rate of change of the APEF is therefore J_b. Imagine now that buoyancy flux is cut off, and that dissipation begins. The stock of accumulated APEF feeds into dissipation of potential energy, raising the potential energy of the water column, and the rate of change of the APEF is therefore the dissipation of potential energy.

If both buoyancy flux and dissipation of potential energy occur, I argue that buoyancy flux is an overturn-scale quantity and does not feed into dissipation of potential energy directly; the flow of density fluctuations must go through a pool of APEF. This is somewhat like a hose filling a punctured swimming pool. If the pool is filled faster than it empties, the water level increases until the pressure is sufficient to make the outflow as big as the inflow. A steady-state ensues. If both buoyancy flux and dissipation exist in a steady-state, the stock—the APEF—must be proportional

to the flows, in this case buoyancy flux and the rate of dissipation of potential energy, through a suitable decay time t_o.

Since (3.8) and (3.10) are related by a constant, a proportionality relation also exists between ξ and J_b with an assumed timescale apparently proportional to (but much shorter than) N^{-1}, but which is presumably the same time scale t_o used in (3.6)[4].

It is assumed that this is valid for single 'overturns' in a steady forced mixing layer where energy comes from production against the mean shear, although it could be argued that ensemble averaging is required to obtain an average of the APEF, as this may vary throughout the evolution of the overturning. The application to puffs (individual K-H instabilities that lead to overturning, mixing and decay) is unclear because the APEF may only be high in the initial instants of overturning, before dissipation starts. However, this should not matter to the parameterisation of mixing because the APEF should nevertheless be representative of the increase in potential energy of the water column after mixing has completed, regardless of the moment's lack of balance between terms. Ensemble averaging simply gives a more stable values of the APEF.

---

[4]Dillon's argument that the re-stratifying term is small in (3.8) is not necessarily consistent with my interpretation. What if restratifying time were 3 to 10 faster than N^{-1}? Considering that Dillon did not find simply that χ_θ were much greater than the $\overline{T'^2}N^{-1}$, but that they were in fact proportional, this indeed points to a physical relation between the two terms. However, this does not prove that restratification actually occurs. Restratification, if it did occur, could simply be measured as negative buoyancy flux. The time-averaged buoyancy flux would then be reduced. My point is that if buoyancy flux and dissipation of potential energy are physically related to the APEF via a time scale of N^{-1}, Dillon would have observed a coefficient of unity in (3.9) and might have wrongly assumed that re-stratification is important. It will be argued in chapter 5 that Dillon's values of χ_θ may in fact be a factor of 3 too high such that $\chi_\theta \approx \overline{T'^2}N^{-1}$, in which case Dillon's argument is not quite as convincing.

3.2.3 Summary of Arguments Linking Overturns to Buoyancy Flux

Both Garrett's revised derivations leading to (3.6) and the potential energy equation leading to $J_b = \xi/t_o$ suggest that

$$J_b = \left[\frac{3}{4} \pm \frac{1}{4}\right] \frac{\xi}{t_o} \tag{3.11}$$

where t_o is the time scale over which (half of) the potential energy ξ decays into the dissipation of potential energy, or equivalently the rate at which ξ is supplied by the buoyancy flux. A definition for t_o in terms of the TKE will follow shortly. The range given in (3.11) comes from the fact that in one instance the buoyancy flux is assumed to provide all the energy difference between the re-ordered and overturned state ($H^2N^2/6$), and in the second instance the buoyancy flux is assumed to equal the dissipation of potential energy, the sum total of which is the difference between the overturned state and the well-mixed state ($H^2N^2/12$). These two views differ by a factor of 2, but it is usually assumed that buoyancy flux equals the rate of dissipation of potential energy. Thus, uncertainty in the physical model itself leads to the factor of two; the coefficient can be settled-on empirically.

In these models, the APEF represents the potential energy available to the buoyancy flux and to the dissipation of potential energy. The buoyancy flux is thus limited by the potential energy available for mixing: a completely mixed layer cannot support a buoyancy flux.

To equate the buoyancy flux term and dissipation of potential energy term to the decay of the APEF over a time t_o, it is assumed that the turbulent energy redistribution terms can be neglected through ensemble averaging. It is also assumed that temperature fluctuations are created from overturning against a mean vertical gradient such that horizontal temperature gradients must be small.

3.3 Model Two: Growing Isotropic Turbulence

Assuming that buoyancy flux is equal to the dissipation of ξ over a decay time scale, then what is the time scale? Dillon (1982; 1984) and Dillon and Park (1987) suggest using $t_o \approx N^{-1}$. This might seem a natural time scale to choose because it is the buoyancy time scale: the time it takes for water to bob up and down (within a factor of 2π). It is argued next using the total energy equation that the overturning time scale provides a better choice for the decay time scale. This results in model two, linking ξ to J_b.

3.3.1 Derivation of the Decay Time

The APEF, TKE and buoyancy flux are linked by the total energy budget, obtained by first considering the turbulent kinetic energy equation

$$\frac{1}{2}\overline{\frac{\partial}{\partial t} u_i' u_i'} = S - \epsilon - J_b \tag{3.12}$$

where the overbar denotes volume averaging over overturns and S is the rate of supply of kinetic energy due to shear production, turbulent and mean advection and pressure-velocity correlations (Dillon, 1982). This equation can be added to (3.10) to obtain a total energy equation for the turbulent flow (Dillon, 1984)

$$\frac{3}{2}\frac{\partial}{\partial t}\overline{u'^2} + \frac{\partial \xi}{\partial t} = S - \epsilon - 3N^2 \kappa_T C_x \tag{3.13}$$

where isotropy was assumed for the turbulent velocities.

Since the turbulent velocity fluctuations are determinant in both the buoyancy flux $\overline{g'w'}$ and the TKE, the decay time of both the APEF and TKE is assumed to be the same. Recall the discussion in section 2.1.3 that mixing efficiency $\Gamma = J_b/\epsilon$ is expected to be of the order of one third or so. This implies that the TKE terms in (3.13) are expected to be bigger than the potential energy terms because even if the kinetic energy in the vertical axis equals the potential energy (APEF), there is three times that amount of kinetic energy in total. The decay time of the TKE

can therefore be used for the potential energy decay time, because the kinetic energy may be bigger than the potential energy. It is also parameterizable in terms of the turbulence. The decay time of ξ is given by

$$t_o = \frac{\text{TKE}}{\epsilon} \tag{3.14}$$

by neglecting the smaller J_b sink to the TKE. This equation is taken as the definition of t_o.

Assuming the Kolmogorov turbulent kinetic energy spectrum, $E(k) \propto \epsilon^{2/3} k^{-5/3}$, the TKE at any scale k in the sub-range is approximately $u'(k)^2 \approx k\, E(k) \approx \epsilon^{2/3} k^{-2/3}$. Also, since the Kolmogorov spectrum assumes that dissipation is independent of the length scale, dissipation must therefore scale like $\epsilon \approx u'^3/L$, from $u'^2 \approx \epsilon^{2/3} k^{-2/3}$ where $u' = u'(k)$ varies with scale and L is the length scale associated with the turbulent velocities. Since the TKE of the Kolmogorov spectrum is greatest at the overturning scale, the largest turbulent velocities measured within an overturn must be associated with the length scale of the overturn. Therefore, the energy-containing scales provide a scaling for dissipation. In the case of isotropic turbulence, this becomes $\epsilon \approx u'^3/L_T$ where L_T is the largest overturning scale. This provides a scaling to relate usually unmeasured turbulent velocities to the rate of dissipation of turbulent kinetic energy. This scaling will be shown to hold very well in chapter 4 for grid turbulence.

Using $\epsilon \approx u'^3/L_T$ in (3.14) yields

$$t_o \approx \left[\frac{3}{2} u'^2 \right] \Big/ \left[\frac{u'^3}{L_T} \right] \approx \frac{3}{2} \frac{L_T}{u'} \approx \frac{3}{2}\, Fr_t^{-1}\, N^{-1} \tag{3.15}$$

where

$$Fr_t = \frac{u'}{N L_T} \tag{3.16}$$

Thus, the decay time scale is dependent on the character of the turbulence[5], parameterized by Fr_t. This is in contrast to the assumption that $t_o \approx N^{-1}$ in model one

---

[5]If the turbulence is not isotropic, it is characterized by $w' < u'$ and $L_T < L_h$, where L_h is the horizontal length scale of the turbulence. Since the energy-containing scales provide the dissipation scaling u'^3/L, then

$$\epsilon \approx u'^3/L_h$$

because the horizontal lengthscale L_h is associated with the energy containing horizontal velocities

(Dillon, 1982; Dillon and Park, 1987; Garrett, 1989)Model 1 coincides with model 2 only for the special case of $Fr_t \approx 1$ (the inertial-buoyancy balance, discussed shortly).

3.3.2 Formulation of Model Two: Buoyancy Flux for Growing Isotropic Turbulence

Combining the simple model for buoyancy flux (3.11) with the expression for the decay time (3.15) yields the buoyancy flux for isotropic growing turbulence as

$$J_b \approx \left[\frac{3}{4} \pm \frac{1}{4} \right] \frac{2}{3} \xi \, N \, Fr_t \tag{3.17}$$

using (3.15) for t_o and assuming isotropy.

The turbulent Froude number is important because it affects the buoyancy flux in model two, but it is typically not measured in the ocean. However, Fr_t will be shown to depend on the ratio of ξ/TKE or $\xi N/\epsilon$, and later even on Ri_g, such that it can be inferred from other measurements. After a brief discussion on the turbulent Froude number, it will be made clear why this model applies to growing turbulence.

3.3.3 Interpretation of the Turbulent Froude Number: Isotropic Case

In the isotropic case, the horizontal and vertical overturning scales are the same ($L_T = L_h$, where L_h is the horizontal length scale of the turbulence), so the turbulent Froude number Fr_t is the same as one based on horizontal scales (u'/NL_h). The following discussion applies to the isotropic case only.

The turbulent Froude number is the ratio of the horizontal inertial velocity (u') to the vertical buoyancy velocity (NL_T). Assuming isotropy, if this ratio is very high then the effects of buoyancy on the turbulence can be assumed to be very low. If the

---

for the anisotropic case. This form conserves the Kolmogorov spectrum and the energy flux across scales is equal to ϵ. This is taken as the more general result. Although it does not apply to the isotropic model two, it will apply to the anisotropic model three. This dissipation scaling will be verified in a later chapter. The decay time t_o would be written using a turbulent Froude number based on horizontal scales $t_o = \frac{3}{2} (u'/NL_h)^{-1} N^{-1}$.

turbulence has only enough kinetic energy to overcome stratification, then a balance $w' \approx NL_T$ exists, where w' is the vertical turbulent velocity scale. In this case, the turbulent Froude number is of order unity, assuming isotropy ($u' = w'$). We call this state "inertial-buoyancy balance".

At inertial-buoyancy balance, the decay time $(3/2)\, L_h/u'$ is approximately equal to the buoyancy time scale N^{-1}. In this case (3.17) is simply written $J_b \approx \left[\frac{3}{4} \pm \frac{1}{4}\right]\xi N$. Thus, (3.17) is only especially useful away from inertial-buoyancy balance, where turbulence does not feel buoyancy effects and must therefore be growing as it does in laboratory experiments. That is why (3.17) relates specifically to growing turbulence, although it is valid for any isotropic turbulence (if the turbulence is still isotropic at inertial-buoyancy balance, then $Fr_t \approx 1$ and $t_o \approx N^{-1}$).

Turbulent Richardson Number—Mixing Efficiency

The turbulent Richardson number is also related to Fr_t. It is defined as

$$Ri_t = \frac{N^2 L_T^2}{u'^2} = Fr_t^{-2} \tag{3.18}$$

which could be written

$$Ri_t = \frac{N^2 L_T^2/2}{u'^2/2} \approx \frac{3\,\xi}{\text{TKE}} \tag{3.19}$$

using the approximation $\xi \approx N^2 L_T^2/2$, valid if N is evaluated over the re-ordered density profile within an overturn. A test in chapter 2 and Crawford (1986) showed that $N^2 L_T^2/2$ may over-estimate ξ by a factor of 2 to 3 when N is over scales larger than the overturns[6]. However, even in the worst case scenario of using layer averages for N^2, the approximation (3.19) holds within a factor of two. The turbulent Richardson number can be interpreted as the ratio of the APEF to the TKE in one dimension.

Using the ξ/TKE ratio, buoyancy flux for model two can also be written

$$J_b = \left[\frac{3}{4} \pm \frac{1}{4}\right]\frac{\xi}{\text{TKE}}\,\epsilon \approx \left[\frac{3}{4} \pm \frac{1}{4}\right]\frac{Ri_t}{3}\,\epsilon \tag{3.20}$$

---

[6]If we wish to define Ri_t using N evaluated at a larger scale, then the factor of 3 in (3.19) should be replaced by a factor of 6 or possibly more.

using (3.19), assuming that the ξ approximation is valid. This is useful because it gives the mixing efficiency directly from $\Gamma = J_b/\epsilon$ as

$$\Gamma \approx \left[\frac{3}{4} \pm \frac{1}{4}\right] \frac{Ri_t}{3} \tag{3.21}$$

The turbulent Richardson number Ri_t quantifies the relative contribution of the energy equations (3.10) and (3.12) to the sum (3.13). This in turn affects the mixing efficiency. This relation will be tested in chapter 4.

Relative Effects of ϵ and ξN on J_b

Since both ξN and ϵ affect J_b from (3.17) and (3.20), an expression for J_b as function of ξN and ϵ can be written to see which of ξN or ϵ is more determinant to J_b. Assuming that the scaling relation $\epsilon \approx u'^3/L_h$ holds, Ri_t is written

$$Ri_t = \frac{N^2 L_T^2}{u'^2} \approx \frac{N^2 L_T^2}{(\epsilon L_h)^{2/3}} \approx \left[\frac{2\,\xi\,N}{\epsilon}\,\frac{L_T}{L_h}\right]^{2/3} \tag{3.22}$$

if ξ is well approximated by $\frac{1}{2}N^2 L_T^2$. Assuming isotropy ($L_T \approx L_h$ such that $\epsilon \approx u'^3/L_T$), this becomes

$$(Ri_t)_{iso} \approx \left[\frac{2\,\xi\,N}{\epsilon}\right]^{2/3} \tag{3.23}$$

Buoyancy flux can then be written

$$J_b \approx \left[\frac{3}{4} \pm \frac{1}{4}\right] \frac{2}{3}\,\xi\,N \left[\frac{\epsilon}{2\,\xi\,N}\right]^{1/3} \approx \left[\frac{3}{4} \pm \frac{1}{4}\right] 0.53\,(\xi\,N)^{2/3}\,\epsilon^{1/3} \tag{3.24}$$

It is seen here that ξN is more determinant to J_b than is ϵ.

Relation of Ri_t to a Ratio of Length Scales

Assuming that $\epsilon \approx u^3/L_h$ holds and using $L_O \equiv (\epsilon N^{-3})^{1/2}$, the turbulent Richardson number can be written

$$Ri_t = \frac{N^2 L_T^2}{u'^2} \approx \frac{N^2 L_T^2}{(\epsilon L_h)^{2/3}} \approx \frac{L_T^2}{L_O^{4/3} L_h^{2/3}} \tag{3.25}$$

which, in the isotropic case, reduces to

$$(Ri_t)_{iso} \approx \left[\frac{L_T}{L_O}\right]^{4/3} \tag{3.26}$$

Thus Ri_t (for isotropy) is determined by the ratio of the size of the overturns to the maximum vertical scale that overturns can evolve to in the presence of stratification (the Ozmidov scale). The ratio L_T/L_O is often used to describe the degree of inertial-buoyancy balance in isotropic turbulence (Stillinger *et al.*, 1983; Itsweire *et al.*, 1986).

3.3.4 Description of Model Two

Let us now describe an imaginary experiment similar to real turbulent flow created by advecting it through a grid and advected downstream. This imaginary experiment differs from reality in the assumption that the flow evolves with its turbulent kinetic energy level (the Kolmogorov spectrum) remaining constant through time. Let us assume that production of turbulence from Reynolds stresses acting against a mean shear could provide the sustaining energy. This is simply to allow scaling of various quantities without introducing the effect of variations of the TKE and of ϵ.

The idea of such real experiments is that downstream evolution of the turbulence may mimic time variation of turbulence created by strong shears in the field, if turbulence is not created already at inertial-buoyancy balance (as it is thought to be from K-H instability). Turbulence is created at small overturning scales behind the grid and grows towards inertial-buoyancy balance as it is advected downstream.

Turbulent length scale evolution and the effect of that length scale on mixing efficiency and buoyancy flux will be described below. This is useful because it illustrates how buoyancy flux and mixing efficiency vary with the growth stage, quantified by Fr_t, in model two.

In this case, the TKE equation is

$$\overline{U}\frac{\partial}{\partial x}\frac{3}{2}\overline{u'^2} = -\overline{u'w'}\frac{\partial \overline{U}}{\partial z} - J_b - \epsilon \tag{3.27}$$

with the added growth-advection of the TKE at a mean velocity[7] $\overline{U}$, and the production term.

Overturns are created as water passes through the grid; the initial overturn scale will be related to the grid spacing or the thickness of the bars (the ratio of spacing to thickness was kept constant in real experiments). This scale can be made very small. With constant dissipation of the TKE through time and length scales, the scaling $\epsilon \approx u'^3/L_h$ suggests that turbulent velocities will be smallest at first. The turbulence is isotropic and does not feel the effect of buoyancy because velocities are greater than NL_T. This implies that L_T is much smaller than the Ozmidov scale, and that $Fr_t \gg 1$. Density fluctuations are proportional to the overturn size and are small at this stage. They cannot contribute much to buoyancy flux. The mixing efficiency is thus low.[8]

Initially, L_T grows at the same rate regardless of the stratification, as in unstratified experiments[9]. As the overturn scale grows, so do density and velocity fluctuations and buoyancy flux. The potential energy required for overturning increases as L_T^2 (e.g. $\xi \approx \frac{1}{2}N^2L_T^2$), but the TKE only increases as $L_T^{2/3}$ (e.g. $k\,\mathrm{E}(k) \propto L_T^{2/3}$). While overturning velocities are increasing, the overturning period (and decay time) L_T/u' increases as $L_T^{2/3}$. Dissipation is constant despite the increasing TKE because of the increasing decay time. This overturning time scale eventually reaches the buoyancy time scale N^{-1}, and the vertical component of the TKE equals the potential energy. At that point, L_T has reached the maximum size allowed by the energy source in the presence of stable stratification. It has reached the Ozmidov scale $L_O = \epsilon/N^3$.

---

[7]The mean advection velocity is assumed to be much greater than turbulent velocities, simplifying the advection term as turbulent-advection can safely be neglected

[8]From (3.21), the mixing efficiency (using the upper bound of the factor of 2) is approximately $Ri_t/3$; the degree of the approximation depending only on the APEF approximation $\frac{1}{2}N^2L_T^2$. At low values of Ri_t the potential energy is much less than the TKE. Mixing efficiency is low because turbulent fluctuations carry much kinetic but little potential energy. The kinetic energy is dissipated as usual but buoyancy flux is limited by the little amount of density fluctuations carried by the turbulent flow.

[9]In this description of isotropic growing turbulence, the buoyancy flux can only be about equal to the dissipation of temperature fluctuations (which occurs at the Batchelor microscale $(\nu\kappa_T^2/\epsilon)^{1/4}$, which is of order 1 mm) if the rate of change of the potential energy ξ is much less than J_b. It is unclear how the $\propto t^{0.3}$ length scale growth observed in lab experiments affects this assumption.

Steady-state ensues.

It is expected that the ratio of L_T/L_O at the inertial-buoyancy balance steady-state will be of order unity. Its exact value is important because it determines the maximum mixing efficiency of the turbulence.[10]

While turbulence is growing, both velocity and density fluctuations increase $\propto L_T^{1/3}$ and $\propto L_T$ respectively. This leads to a cross-correlation for $\overline{\rho'w'}$ (and therefore buoyancy flux) increasing as $\propto L_T^{4/3}$. Thus mixing efficiency increases proportionately with $L_T^{4/3}$ (e.g. combining (3.21) and (3.26)).

The previous description (summarized in Figure 4.1 in the next chapter) shows how overturning grows from small scales, fast decay time and low mixing efficiency to largest overturning scales $\approx L_O$, lowest decay times $\approx N^{-1}$ and maximum mixing efficiency.

3.4 Model Three: Inertial-Buoyancy Balance Anisotropic Case

The model just described interpreted high turbulent Froude numbers, $Fr_t \gg 1$, as isotropic turbulence that does not feel the effects of buoyancy. In this section, situations where turbulence is not growing, yet has $Fr_t \gg 1$ are considered. This will lead to the third model considered in this thesis, relating buoyancy flux to anisotropic, yet energetic, steady-state turbulence.

The description of turbulence in model three affects assumptions made in the formulation. For this reason, this description is discussed next.

---

[10]The determination of the value of L_T/L_O at inertial-buoyancy balance has been a goal for many investigators studying grid turbulence (Stillinger *et al.*, 1983; Itsweire *et al.*, 1986; Rohr *et al.*, 1984) and of others interested in oceanic values (Dillon, 1982; Crawford, 1986) because it determines the constant between ϵ and ξN in model one.

3.4.1 Description of Model Three

Imagine a mixing layer driven by a locally strong shear, say by an internal tide, but only over a layer of thickness smaller than L_O, outside which the shear falls off. The vertical overturning scale grows to the mixing layer thickness and remains there in a steady state. Although in a steady state, the vertical scale of the overturns is smaller than L_O and, like the growing overturns in the lab, the overturns do not feel the effects of buoyancy. Another case is a wind-forced layer for which the overturning scale has out-grown the layer thickness. While mixing may slowly erode the pycnocline at the bottom of the layer, the vertical turbulent scale is limited to the layer thickness. In both these cases, nothing prevents the horizontal scale of the turbulent velocity fluctuations from growing further.

It could be argued that if a layer is (close to) well-mixed, then we need only worry about entrainment, and so an entrainment model as a function of forcing parameters would be necessary. The overturn scale method suggested in this chapter does not attempt to quantify mixing from the observed forcing, but rather from the intermediate result of overturning which leads to mixing. If stratification is nearly gone, then entrainment would presumably be observed in one particular profile as some APEF (the re-ordered density gradient would then be non-zero). In this case, the well developed TKE field will transport the potential energy to small scales and dissipate it as described in model three.

The Ozmidov scale $L_O = (\epsilon/N^3)^{1/2}$ is interpreted as the largest still isotropic eddy size in the presence of stable stratification (Ozmidov, 1965). A new discussion is given next, showing that it can also be interpreted as the horizontal turbulent length-scale derived from Kolmogorov scaling from the minimum turbulent velocity fluctuation against a stable stratification.

The vertical component of the TKE is limited by inertial-buoyancy balance and can be no less than the potential energy gained by a parcel of water travelling upwards a distance L_T. Assuming that this energy balance is characterized at isotropy by a constant turbulent Froude number, $(Fr_t)_{isoIB}$, which is expected to be of order unity,

one can write (e.g. (3.16))

$$w' \approx (Fr_t)_{isoIB} NL_T \tag{3.28}$$

for the vertical turbulent velocity at inertial-buoyancy balance, which is the minimum vertical velocity allowed by buoyancy forces. The inertial-buoyancy value $(Fr_t)_{isoIB}$ can be written at isotropy because $w' = u'$; if the turbulence is not isotropic, we cannot expect $Fr_t = (Fr_t)_{isoIB}$, but we still expect (3.28) to hold for vertical turbulent velocities at inertial-buoyancy balance.

The horizontal and vertical turbulent velocities are assumed to be related by

$$u' L_T \approx w' L_h \tag{3.29}$$

implying some sort of continuity on turbulence, where L_T and L_h are vertical and horizontal overturning scales respectively (The second horizontal component is neglected in this continuity scaling).

Combining (3.28) and (3.29), the horizontal velocity scale becomes

$$u' \approx w' L_h/L_T \approx (Fr_t)_{isoIB} NL_h \tag{3.30}$$

regardless of isotropy.

Since, by assumption of model 3, the horizontal overturning scales are much greater than in the vertical ($L_h \gg L_T$), there is turbulent energy at those larger scales. The Kolmogorov scaling of the turbulent energy cascade must scale with the more energetic horizontal scales as

$$\epsilon \approx u'^3/L_h \tag{3.31}$$

such that ϵ is still conserved at all scales, if the Kolmogorov spectrum $E(k) \propto \epsilon^{2/3} k^{-5/3}$ still holds.

Using (3.30), Kolmogorov scaling reduces to $\epsilon \approx (Fr_t)^3_{isoIB}(NL_h)^3/L_h$ and the horizontal length-scale becomes $L_h \approx (Fr_t)^{3/2}_{isoIB}(\epsilon N^{-3})^{1/2} \approx L_O$.

If $(Fr_t)_{isoIB}$ is close to unity, then, even if the turbulence is not isotropic, it can be argued that in steady-state turbulence the horizontal length-scale L_h should be of

the order of the Ozmidov scale L_O. In model three, turbulence is at inertial-buoyancy balance ($L_h \approx L_O$ and $u' \approx N L_h$) but is allowed to be anisotropic if the vertical scale is limited by the layer to be smaller than the horizontal scale ($L_T < L_h$)

3.4.2 Derivation of the Decay Time

As in the second model, the buoyancy flux model equates J_b to the dissipation of the APEF over the decay time of the TKE from ϵ.

For $L_h = L_T$, the decay time was argued to be $t_o \approx \frac{3u'^2/2}{u'^3/L_T} \approx \frac{3}{2}L_T/u'$. However, inertial-buoyancy balance is now assumed, such that $L_h = L_O$. The decay time becomes

$$t_o \approx \frac{u'^2}{u'^3/L_h} \approx \frac{L_h}{u'} \approx (Fr_t)_{isoIB} \, N^{-1} \tag{3.32}$$

using (3.30) and assuming that the TKE is $\frac{2}{2} u'^2 = u'^2$ instead of $\frac{3}{2} u'^2$ from neglecting the smaller vertical component. This decay time can be safely approximated as $t_o \approx L_O/u' \approx N^{-1}$ for $(Fr_t)_{isoIB}$ close to unity.

The decay time is the overturning time. In the isotropic case, the turbulent length scale determines this time scale. In the inertial-buoyancy balance case, the relevant horizontal length scale is set by buoyancy forces such that the decay time is the buoyancy period.

3.4.3 Formulation of Model Three; Buoyancy Flux for Anisotropic Inertial-Buoyancy Balanced Turbulence

The buoyancy flux $J_b = \left[\frac{3}{4} \pm \frac{1}{4}\right] \frac{\xi}{t_o}$ is simply

$$J_b \approx \left[\frac{3}{4} \pm \frac{1}{4}\right] \xi \, N \tag{3.33}$$

This result is similar to Dillon *et al.*'s (1987) empirical result (see chapter 5 and Appendix B).

3.4.4 Interpretation of the Turbulent Froude Number: Inertial-Buoyancy Case

In the context of energetic anisotropic turbulence at inertial buoyancy balance, a turbulent Froude number based on horizontal scales will by definition be equal to the inertial buoyancy value ($Fr_h = u'/(NL_h) = (Fr_t)_{isoIB}$). The turbulent Froude number Fr_t may still vary, and is therefore not interpreted as a measure of the ratio of inertial to buoyancy forces. It will be shown that Fr_t can be interpreted as a ratio of vertical to horizontal overturning length scales: a measure of anisotropy. This will also be related to mixing efficiency.

Turbulent Richardson Number—Mixing Efficiency

The turbulent Richardson number, defined as (3.18), can be written

$$Ri_t = \frac{N^2 L_T^2/2}{u'^2/2} \approx \frac{2\,\xi}{\text{TKE}} \tag{3.34}$$

for the reduced TKE, using the approximation $\xi \approx N^2 L_T^2/2$.

Similarly to model two, buoyancy flux can be written

$$J_b = \left[\frac{3}{4} \pm \frac{1}{4}\right] \frac{\xi}{\text{TKE}} \epsilon \approx \left[\frac{3}{4} \pm \frac{1}{4}\right] \frac{Ri_t}{2} \epsilon \tag{3.35}$$

such that the mixing efficiency is

$$\Gamma \approx \left[\frac{3}{4} \pm \frac{1}{4}\right] \frac{Ri_t}{2} \tag{3.36}$$

from $\Gamma = J_b/\epsilon$, with the quality of the approximation depending only on the approximation $\xi = \frac{1}{2}N^2 L_T^2$. As it did for model two, Ri_t quantifies the relative amounts of potential to kinetic energy, which affects mixing efficiency.

Relation of Ri_t to a Ratio of Length Scales

Assuming that horizontal length and velocity scales provide the Kolmogorov scaling $\epsilon \approx u'^3/L_h$, the turbulent Richardson number

$$Ri_t \approx \frac{L_T^2}{L_O^{4/3} L_h^{2/3}} \tag{3.37}$$

becomes

$$(Ri_t)_{IB} \approx \left[\frac{L_T}{L_O}\right]^2 \tag{3.38}$$

for $L_h = L_O$, instead of (3.26) obtained for the isotropic case $L_T = L_h$. Equivalently, we can write $Fr_t = L_O/L_T$.

Since mixing efficiency is $Ri_t/2$, the anisotropy factor $L_T/L_O \approx (Ri_t)_{IB}^{1/2}$ determines mixing efficiency. This is to be expected. An isotropic layer at inertial-buoyancy balance has maximum mixing efficiency. If the layer gets thinner, it is still dissipating its TKE on horizontal scales. However, at a given stratification the contribution to buoyancy flux of the density fluctuations is limited by the vertical overturning scale.

This model is consistent with what is thought to occur in wind mixed layers. As the mixing persists, stratification is lowered and can no longer support a buoyancy flux when completely mixed. In this case, the mixing efficiency is very low. This models predicts this from the low APEF in the mixing layer, limiting the energy that can ever go to buoyancy flux.

3.5 Relating the turbulent parameters to the large scale

The second and third models presented both have a mixing efficiency uniquely determined by the turbulent Richardson number. This is subject to the condition that the turbulence is sufficiently intense to produce a buoyancy flux ($\epsilon/\nu N^2 > 15$; see Appendix A). The turbulent parameters Ri_t and $\epsilon/\nu N^2$ describe the turbulence, but these are not easily measured. The models provide a useful framework, but yet seem to require too much knowledge about the state of the turbulence to be very useful.

The hypothesis is put forward that the turbulent parameter Ri_t can be related to the larger scale forcing as described by the gradient Richardson number $Ri_g = N^2/(\partial\overline{U}/\partial z)^2$.

Assuming that turbulent velocity fluctuations originate from overturning over a scale L_T against the large scale shear $\partial\overline{U}/\partial z$, the turbulent velocity fluctuations

should be (geometrically) proportional to both as

$$u' = a\, L_T \frac{\partial \overline{U}}{\partial z} \tag{3.39}$$

where a is an as-yet undefined constant, then Ri_t is related to Ri_g by

$$Ri_t = \frac{N^2 L_T^2}{u'^2} = \frac{N^2 L_T^2}{a^2 L_T^2 (\partial \overline{U}/\partial z)^2} = \frac{1}{a^2}\, Ri_g \tag{3.40}$$

The highest value of Ri_t that can sustain turbulence is at inertial-buoyancy balance, and is of order unity. The maximum gradient Richardson number which can create shear-instabilities is of order $1/4$. The constant a is thus expected to be about $1/2$, and must be less than unity (turbulent velocities cannot be larger than their source).

The turbulent velocities in the Kolmogorov spectrum scale with overturn size as $\propto L_h^{1/3}$ (see Section 3.3.4). If the shear provides a velocity proportional to L_T, it must be assumed that this is only valid for the largest energy-containing scales. Smaller scales will have higher turbulent velocities than the $\propto L_T$ shear-scaling, and will follow the Kolmogorov spectrum.

If turbulent velocities come from the shear as $\propto L_T(\partial \overline{U}/\partial z)$, then this must scale the largest velocities between u' and w' if they are anisotropic. The choice of u' in (3.39) is thus the appropriate choice. This relation should also hold for anisotropic turbulence (Third model).

Equation (3.39) will be tested in a later chapter for isotropic turbulence. If it is correct, a larger scale forcing parameter such as the gradient Richardson number can be related to the turbulent parameter Ri_t, which is believed to quantify mixing efficiency and buoyancy flux. Thus, relating Ri_g to Ri_t, measurements of Ri_g and ξ would be sufficient to determine ϵ, J_b and Γ.

3.6 Summary

This chapter introduced three models to the thesis, relating overturn-scale quantities to buoyancy flux or to the dissipation of turbulent kinetic energy. Some of the model

predictions, as well the assumptions made to derive them, will be tested in later chapters. The models, assumptions and predictions are summarized in Table 3.1. Some predictions are functions of Fr_t or Ri_t which depend on turbulent velocity fluctuations u', which are not usually measured in the ocean. Table 3.2 summarizes proposed methods to infer the turbulent velocities to obtain Fr_t or Ri_t.

First Model

The first model is the 'traditional' view of overturning and relates the dissipation of TKE, ϵ, to the overturning length scale L_T via the Ozmidov scale $L_O = (\epsilon/N^3)^{1/2}$.

The main assumptions are

- The mixing efficiency Γ is constant.

- The decay time of an overturn is approximately equal to N^{-1}, implying a balance between inertial and buoyancy forces.

The prediction is that dissipation is related to overturning by $\epsilon \approx L_T^2 N^3$, and buoyancy flux is given by assuming a constant mixing efficiency (usually $\Gamma \approx \frac{1}{4}$) as $J_b = \Gamma \epsilon$.

Since this model converges with model two and three at isotropic inertial-buoyancy balance, it is expected to hold for mixing created at inertial-buoyancy balance. This presumably occurs when the gradient Richardson number is slowly lowered to a critical value and instability occurs. Overturning then has only sufficient kinetic energy to overcome stratification and an inertial-buoyancy balance insues. If mixing is not driven more strongly by a shear, then all phases of mixing may be at inertial-buoyancy balance such that a constant, and maximal, mixing efficiency should result. This should be the case for breaking internal waves in the abyss and thermocline.

Second Model

By simplifying the arguments leading to the first model, a second model relating buoyancy flux to the dissipation of the available potential energy of the overturn over

Model	Result	Assumptions	Comments
1	$\epsilon \approx L_T^2 N^3$	$\Gamma = \frac{1}{4}$ (or constant) Inertial-buoyancy balance	May apply to breaking internal waves.
2	$J_b \approx \left[\frac{3}{4} \pm \frac{1}{4}\right] \frac{2}{3} \xi N Fr_t$ $\Gamma \approx \left[\frac{3}{4} \pm \frac{1}{4}\right] Ri_t/3$	Isotropy ($L_T = L_h$) $\epsilon \approx u'^3/L_h$ or $\epsilon \approx u'^3/L_T$ $\xi \approx \frac{1}{2}N^2 L_T^2$	An approximation of $\epsilon \approx u'^3/L_h$ is shown to hold (see below). May be overestimate by factor 2-3 using layer-N rather than overturn-N.
3	$J_b \approx \left[\frac{3}{4} \pm \frac{1}{4}\right] \xi N$ $\Gamma \approx \left[\frac{3}{4} \pm \frac{1}{4}\right] Ri_t/2$	Inertial-buoyancy balance $\epsilon \approx u'^3/L_h$ $u'L_T \approx w'L_h$ $\xi \approx \frac{1}{2}N^2 L_T^2$	The combination $\epsilon = u'^3/(L_T u'/w')$ is shown to hold in average sense in ch. 4 for grid turbulence. May be overestimate by factor 2-3 using layer-N rather than overturn-N.

Table 3.1: Summary of models with predictions, assumptions and comments. Model one describes traditional thought linking L_T to L_O; Model two describes growing isotropic turbulence and should apply to strongly forced mixing layers for which overturning scale are thought to be still growing; Model three describes steady-state anisotropic turbulence and should apply to strongly forced mixing layers thought to have been mixing sufficiently long such that L_T approaches the layer thickness and horizontal turbulent scale may be larger than L_T.

Result	Assumptions	Comments
$u' \approx (\epsilon L_T)^{1/3}$	Isotropy $(L_T = L_h)$ $\epsilon \approx u'^3/L_h$	Allows estimation of u' in Model two to obtain Fr_t, if ϵ is measured.
$u' \approx 0.4 L_T \, (\partial \overline{U}/\partial z)$ $(Ri_t \approx 6.2 \, Ri_g)$		Allows estimation of u' for both Models two and three to obtain u' from large scale shear, and to infer Γ from Ri_t relations.
$Ri_t \approx (L_h/L_O)^{4/3} \, (L_T/L_h)^2$	$\epsilon \approx u'^3/L_h$	General form for Ri_t (related to Γ) for models two and three as a function of length scales.

Table 3.2: Summary of methods to infer u' and Ri_t from large scale shear or from measurements of ϵ and L_T (for model two).

a suitable decay time was derived as

$$J_b = \left[\frac{3}{4} \pm \frac{1}{4} \right] \frac{\xi}{t_o}$$

The decay time t_o was argued to be the same as for the turbulent kinetic energy. This decay time is implicit to the Kolmogorov spectrum.

$$t_o = \frac{\text{TKE}}{\epsilon}$$

If shear is driving the turbulence and creating the turbulent velocity fluctuations, then the turbulence decay time is proportional to $(\partial \overline{U}/\partial z)^{-1}$, if the hypothesis that $u' = a L_T \partial \overline{U}/\partial z$ holds.

This model is expected to describe isotropic growing turbulence with sufficiently intense turbulence to generate a buoyancy flux ($\epsilon/\nu N^2 > 15$ to 25).

The assumptions are that

- That Kolmogorov scaling of the turbulent velocities holds: $\epsilon \approx u'^3/L$, where L

is the turbulent length scale (isotropic). This permits obtaining a useable form of the decay time as $t_o \approx (3/2)Fr_t^{-1}N^{-1}$ and the relation $(Ri_t)_{iso} \approx (L_T/L_O)^{4/3}$.

- That ξ is well approximated by $N^2 L_T^2/2$. This is used to obtain $\Gamma \approx \left[\frac{3}{4} \pm \frac{1}{4}\right] Ri_t/3$. There is an extra factor of two of uncertainty, depending on how N^2 is calculated, because the gradient within overturns is smaller than outside the overturns.

The predictions of the model are:

- Buoyancy flux is given by: $J_b \approx \left[\frac{3}{4} \pm \frac{1}{4}\right] \frac{2}{3} \xi N Fr_t$.

- Mixing efficiency is: $\Gamma \approx \left[\frac{3}{4} \pm \frac{1}{4}\right] Ri_t/3$ to within the extra factor of two mentioned above if a layer-N is used, where Ri_t describes the ratio of potential to kinetic energy ($Fr_t = Ri_t^{-1/2}$ describes the ratio of inertial to buoyancy forces) or the degree of inertial-buoyancy balance.

This model should apply to growing isotropic mixing, especially away from inertial-buoyancy balance. This will obviously be the case in grid-generated turbulence, but I argue that it should also apply to boundary layers (surface or bottom) at an early stage when turbulence is still growing. Periodic forcing shears such as associated with tides could cause this. This model should also hold when it is clear that turbulence has only recently started, away from inertial-buoyancy balance. This could be the case in internal tide flow or when a passing soliton is known to force a recent mixing layer. It is not clear how mixing evolves in these cases. If the layer starts through K-H instability, then we could argue that $Fr_t \approx 1$ (inertial-buoyancy balance holds) and that the mixing should all occur at maximum mixing efficiency. However, strong shear can presumably drive mixing to higher turbulent Froude number, forcing overturning scales to grow. Little is known about the length scale evolution in the ocean.

Third Model

The third model describes energetic turbulence with vertical overturning scales limited to a layer thinner than the buoyancy length scale L_O. The turbulence becomes anisotropic as the scales grow horizontally.

The model is similar to the second, in that buoyancy flux is given by the decay of the potential energy of the overturns. However the decay time is approximately N^{-1} because of the balance of inertial and buoyancy forces.

The assumptions are that

- Kolmogorov scaling of the turbulent velocities holds using horizontal velocity and length scales, even if anisotropic ($L_h > L_T$): $\epsilon \approx u'^3/L_h$. This permits obtaining the decay time as $t_o \approx N^{-1}$, the relation $(Ri_t)_{IB} \approx (L_T/L_O)^2$, and the primary prediction that $L_O \approx L_h$

- Continuity holds on turbulent scales: $u'L_T \approx w'L_h$

- ξ is well approximated by $N^2 L_T^2/2$, with the same factor of two of possible error described for the second model. This is used to obtain $\Gamma \approx \left[\frac{3}{4} \pm \frac{1}{4}\right] Ri_t/2$.

The predictions of the model are:

- Buoyancy flux is given by $J_b \approx \left[\frac{3}{4} \pm \frac{1}{4}\right] \xi N$

- Mixing efficiency is $\Gamma \approx \left[\frac{3}{4} \pm \frac{1}{4}\right] Ri_t/2$, to within the extra factor of two, where $Fr_t = Ri_t^{-1/2}$ is approximated by the ratio of the horizontal turbulent scale L_h to vertical turbulent scale L_T ($Fr_t \approx L_h/L_T$).

- The horizontal turbulent scale L_h is approximately equal to the Ozmidov scale $L_O = (\epsilon/N^3)^{1/2}$

This model should apply in strongly forced shear layers thinner than the Ozmidov scale, such as boundary layers. In a steady state, the horizontal turbulent scale is then argued to outgrow the vertical extent of the layer out to the Ozmidov scale L_O. Thus this model should be most appropriate for layers with steady-state energetic mixing, for which the vertical overturning scale nearly equals the layer thickness.

Isotropy Effect on Mixing Efficiency

The second and third model are contrasted by their interpretation of the turbulent Richardson number Ri_t, which is proportional to mixing efficiency.

- In the second model, it was stated that Ri_t describes the ratio of potential to kinetic energy or the degree of inertial-buoyancy balance.

- In the third model, Ri_t describes the ratio of the horizontal turbulent scale L_h to vertical turbulent scale L_T, or the degree of isotropy.

In fact, both are related. The general interpretation is that Ri_t describes the ratio of potential to kinetic energy. The potential energy is limited by the buoyancy flux, and the amount of kinetic energy present limits the dissipation ϵ. This is what determines the mixing efficiency.

The second model assumed isotropy. If turbulence departs slightly from isotropy (say by a factor of 2), the relation $\Gamma \approx Ri_t/3$ still holds if Kolmogorov scaling using horizontal scales is valid ($\epsilon \approx u'^3/L_h$). The effect is that the TKE stays about the same, but $\xi \approx N^2 L_T^2/2$ decreases proportionally to the square of the degree of isotropy ($\propto L_T^2/L_h^2$).

Both models are then consistent; mixing efficiency is determined by the ratio of potential to kinetic energy in both. The $(Ri_t)_{iso} \approx (L_T/L_O)^{4/3}$ dependence of the second model describes how variations in L_T/L_O affect the energy ratio when the turbulence is isotropic and follows the Kolmogorov spectrum; The $(Ri_t)_{IB} \approx (L_T/L_O)^2$ dependence of the third describes how departures from isotropy affect the energy ratio. Both can be combined into a generalized model.

A prediction is then

- For slight departures from isotropy, the measured Ri_t decreases $\propto L_T^2/L_h^2$ such that mixing efficiency is still given by approximately $\left[\frac{3}{4} \pm \frac{1}{4}\right] Ri_t/3$. Mixing efficiency is lower, but if $Ri_t = N^2 L_T^2/u^2$ is the measured quantify there is no extra adjustment to make for isotropy.

- The generalized form of Ri_t in terms of length scales combines both the inertial-buoyancy balance L_h/L_O and isotropy L_T/L_h factors as

$$Ri_t \approx (L_h/L_O)^{4/3} (L_T/L_h)^2 \tag{3.41}$$

(using $\epsilon \approx u'^3/L_h$)

Relating Gradient Richardson Numbers to Turbulent Richardson Numbers

The turbulent parameter Ri_t, which determines the mixing efficiency in both the second and third models, is not presently a measured quantity in the ocean. A hypothesis is put forward that the turbulent parameter Ri_t can be related to the larger scale gradient Richardson number Ri_g if turbulent velocities are produced from the mean shear.

The hypothesis is

$$u' = a \, L_T \frac{\partial \overline{U}}{\partial z}$$

or equivalently

$$Ri_t = \frac{N^2 L_T^2}{a^2 L_T^2 (\partial \overline{U}/\partial z)^2} = \frac{1}{a^2} Ri_g$$

where a is expected to be less than unity, possibly around $1/2$.

This model would allow the turbulent character of the flow to be established from simultaneous measurements of shear with an ADCP and density profile with a CTD profiler.

Applicability to the Ocean

The first model is actually within the domain of the other two models. If indeed the APEF is primarily linked to buoyancy flux, and mixing efficiency is about $1/4$ at the inertial-buoyancy balance, then it follows that there will also be a relation between dissipation of the turbulent kinetic energy and the overturning scale through $J_b = \Gamma \epsilon$.

Even if the second model is correct, it may not be an important distinction if the mixing efficiency in the ocean is constant. The second model will differ significantly

from the traditional view of a L_T–L_O link if there is a wide range in mixing efficiency in the ocean. This issue will be addressed in the next chapters.

Another issue to address is the value of $(Fr_t)_{isoIB}$, the value of the turbulent Froude number at the inertial-buoyancy balance. The second model predicts a rise in mixing efficiency with Ri_t, but does not predict the value of the maximum mixing efficiency, which is found at the inertial-buoyancy balance.

Consideration will also be given to difficulties in making these overturn-scale measurements in energetic ocean flows. Intrusions of water masses along isopycnals are likely to occur at or near intense mixing regions. These are known to cause problems with the measurement of density using a conventional CTD profiler. The mismatch between temperature and conductivity sensors often causes what is referred to as spiking. Intrusions make the CTD's task more difficult.

Another sampling problem is combining density profiles from CTD measurements with shear profiles from an ADCP to obtain gradient Richardson numbers on a useful scale. This will also be addressed.

A Recipe for the Use of the Models

Later chapters will show that mixing efficiency is not constant in the energetically stirred parts of the ocean, such that we may do much better to estimate buoyancy flux using model two or three than using model one. Model one may still apply to the kinematical model of breaking internal waves upon superposition of waves; this is thought to lead to sporadic K-H instability occurring at inertial-buoyancy balance. Both models two and three should be used instead in more energetic areas where strong shears are thought to force persistent mixing layers, not just random instabilities. Each of these two models applies in different circumstances, such that they do not invalidate each other. Model two should be used when the overturning scales are thought to be growing and isotropic (unfortunately, this is difficult to determine from standard CTD measurements alone). Such a case is presented in chapter 7 where a layer is observed to start mixing. Model three should be used for

layers that have been mixing for a longer period, such that overturning scales have grown to steady-state at inertial-buoyancy balance. This is typical of wind-mixed layers, or layers that have been mixing for a long time relative to the buoyancy period. The vertical overturning scale should perhaps approach the layer thickness (although this would imply that the layer becomes quickly nearly well mixed). This would be a good indicator that steady-state has been reached and that horizontal turbulent scales may be larger than in the vertical, causing anisotropy. If no indication of the state of the turbulence is available, or if the turbulent Froude number cannot be inferred, then one should use the buoyancy flux formulation of model three as a lower bound.

Chapter 4

Grid-Generated Turbulence

In the last chapter, three turbulence models were explored. The first reflects the most commonly held view, applicable to breaking internal waves, and the other two present a new outlook applicable to strongly mixed layers which is argued to be a more complete description of turbulence. These latter two models are based on assumptions and other models (e.g. the Kolmogorov spectrum and its scaling of turbulent velocities) which must be tested in addition to model predictions. Such tests are very difficult to undertake under uncontrolled (and logistically challenging) oceanic conditions. So, for more than a decade, laboratory experiments have been conducted to investigate turbulence. Typically, a tank is filled with salt-stratified or unstratified water. A flow is passed through a grid to create turbulence which decays downstream. The parameters ρ', (rms turbulent velocities) u', w', $\overline{\rho'w'}$, N^2 and ϵ are measured downstream. The experiments are especially useful because the buoyancy flux $g\overline{\rho'w'}/\overline{\rho}$ is measured directly. A close variant of the turbulent parameter Fr_t is also measured. These measurements are rare in the ocean.

These grid generated turbulence experiments are discussed here to give credence to the assumptions made in the derivation of turbulence models two and three in chapter 3; for example, the Kolmogorov scaling of turbulent velocities is verified empirically in an ensemble sense. The buoyancy flux and mixing efficiency of the grid-turbulence will only be compared to model two, because the turbulence is clearly

growing and nearly-isotropic over two decades of variation in L_T/L_O.

The experiments will first be briefly described. Their results will then be used to verify that (with ensemble averaging)

- The Kolmogorov scaling holds for turbulent velocity fluctuations $\epsilon \approx u'^3/L_h$, where L_h is a horizontal length scale, and to verify the conditions under which it holds (averaging).

- The (quasi) continuity equation $u'L_T \approx w'L_h$ holds on turbulent scales.

- ξ is well approximated by $N^2 L_t^2/2$, such that the mixing efficiency predicted by the isotropic growing turbulence model can be compared to lab measurements. (Here L_t is a new quantity defined in this chapter, which replaces L_T in laboratory experiments for which L_T is rarely measured.)

- The prediction for mixing efficiency $\Gamma \approx \left[\frac{3}{4} \pm \frac{1}{4}\right] Ri_t/3$ of model two is correct.

- The prediction that $\Gamma \propto Ri_t = N^2 L_T^2/2$ includes the effect of anisotropy.

- Ri_t is proportional to Ri_g

- And finally to quantify the value of Fr_t at the inertial-buoyancy balance $(Fr_t)_{isoIB}$

4.1   Description of the Experiments

In grid-turbulence experiments, growing turbulence is created at small overturning scales by passing a flow through a grid and advecting the growing turbulence downstream. The idea of such experiments is that downstream evolution of the turbulence will mimic time variation of turbulence in the field. Turbulence is created at small overturning scales behind the grid and grows towards inertial-buoyancy balance as it is advected downstream.

4.1.1 Idealized Description

Figure 4.1A summarizes the discussion of model two in section 3.3.4, describing the length scale evolution of a turbulent flow with constant rate of turbulent kinetic energy dissipation. The current case of decaying grid-turbulence is very similar; the only difference is that there is no mean shear to sustain the TKE level. The production term in (3.27) is removed; as there is no energy source, the TKE must decrease and the advection term is now positive. It feeds TKE dissipation and buoyancy flux until turbulent motions are too weak to create any mixing. The evolution of a turbulent flow in decaying grid-turbulence experiments is depicted by Figure 4.1B

As the energy level is decaying, then from the Kolmogorov spectrum $E(k) \propto \epsilon^{2/3} k^{-5/3}$, ϵ must decay also. Therefore, Figure 4.1B now shows a decreasing Ozmidov scale $L_O = (\epsilon/N^3)^{1/2}$, the maximum vertical scale that the TKE can overturn against buoyancy forces. During this decay, there is an increase of the Kolmogorov scale $L_K = (\nu^3/\epsilon)^{1/4}$—the length scale at which viscous forces equal inertial forces and viscosity dissipates energy. This decreases the bandwidth of turbulent length scales from both ends. This bandwidth, or non-dimensional dissipation, quantifies the turbulence intensity. It is often written as L_O/L_K or $\epsilon/\nu N^2$, which are related by

$$\left[\frac{L_O}{L_K}\right]^{4/3} = \frac{\epsilon}{\nu N^2} \tag{4.1}$$

The turbulent bandwidth, shown as the L_O/L_K ratio, shrinks in time in Figure 4.1B. The initial overturning length scale still grows in this case. As long as overturns are smaller than the Ozmidov scale L_O, they are not restrained by buoyancy forces. As L_T increases towards L_O, this latter length scale decays towards L_T. At some point, the overturning length scale and Ozmidov scales reaches the inertial-buoyancy balance value of the ratio of L_T/L_O. At this point, L_T decays at the same rate as L_O, such that the ratio L_T/L_O stays constant.

Gargett *et al.* (1984) have shown that turbulence departs from isotropy when the turbulent bandwidth is smaller than approximately $\epsilon/\nu N^2 = 200$. This corresponds to a ratio of $L_O/L_K = 55$. When L_O crosses the $55 L_K$ line indicated in Figure 4.1B,

A

log (L)

L_O

$\dfrac{L_O}{L_K}$ $\dfrac{L_O}{L_T}$

L_T

L_K

$L_O \sim a\,L_T \quad (a \sim 1)$

Least buoyancy effects

smallest eddies

low ξ

low Γ

high Fr_t

low u'

low t_o

$\rho' \propto L_T$

$\xi \propto L_T^2$

$TKE \propto L_T^{2/3}$

ε = constant

$\Gamma \propto L_T^{4/3}$

$t_o \propto L_T^{2/3}$

Inertial–buoyancy balance

largest eddies

highest ξ

highest Γ

lowest Fr_t

highest u' $u' \sim N L_T$

highest t_o $t_o \sim N^{-1}$

grid

log (time or x)

B

L_O

L_T

L_K

Inertial–buoyancy balance

Departure
from isotropy

$\vec{J}_b = 0$

55 L_K

$\dfrac{L_O}{L_K} \sim 55$

10 L_K

$\dfrac{L_O}{L_K} \sim 10$

log (time or x)
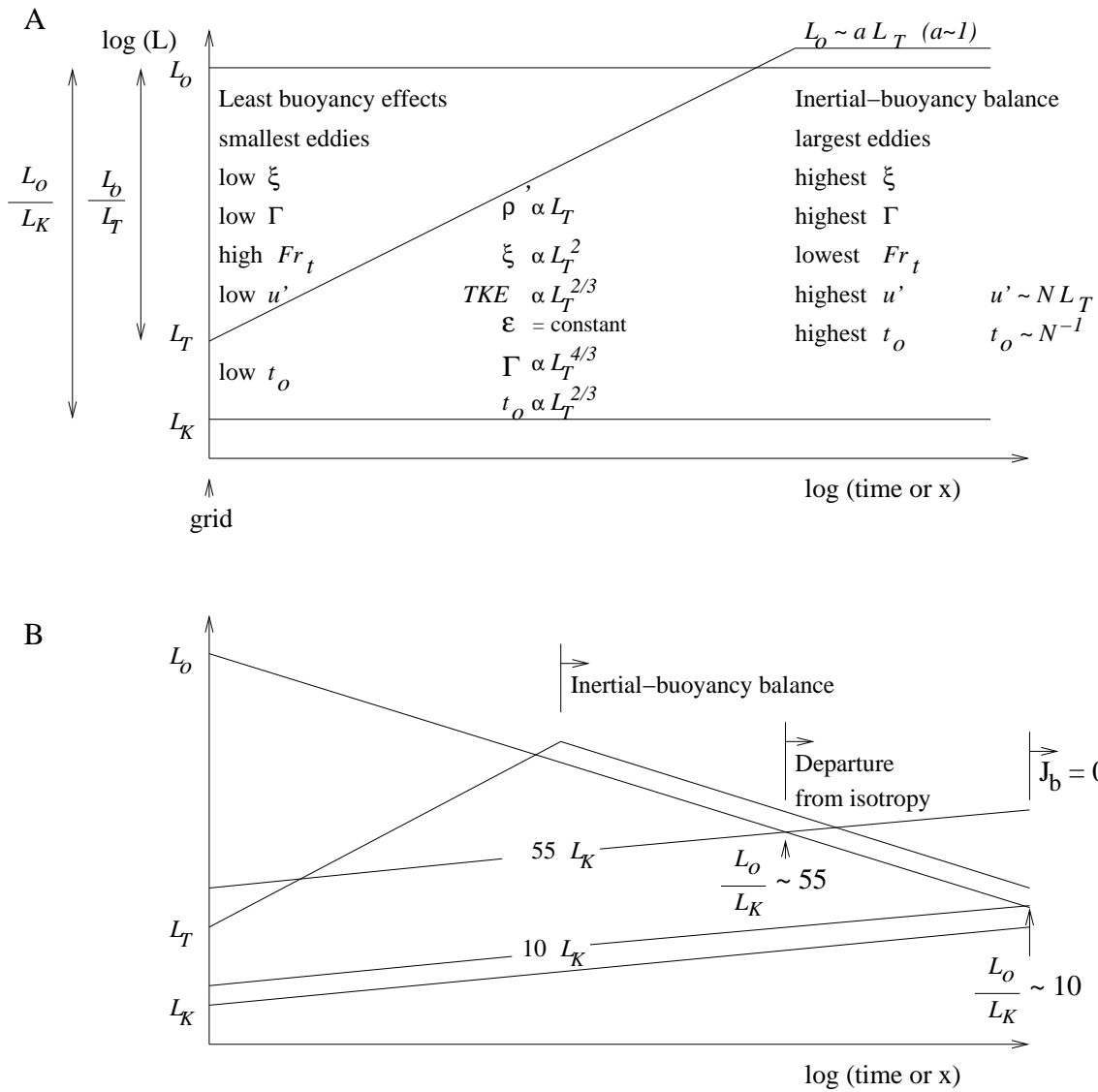
Figure 4.1: Depiction of growing isotropic turbulence. **A-** Assuming a constant energy level; **B-** Assuming no sources of energy are present such that turbulence decays.

turbulence departs from isotropy.

Laboratory experiments reviewed here have shown that when the turbulent band-width is very small (L_O/L_K from 8 to 10) turbulence can no longer sustain a buoyancy flux. This threshold is indicated in Figure 4.1B by a line at $10L_K$; Approximately when L_O crosses the $10L_K$ line, buoyancy flux is thought to stop (Itsweire *et al.*, 1986).

4.1.2   Experiment Description

Figure 4.2 shows the evolution of L_t, L_K and L_O for experiments by Stillinger *et al.* (1983), denoted SHV, and three experiments by Itsweire *et al.* (1986), denoted IHV[1]. Note that many experiments with various stratification are shown together in each panel (the stratification is indicated by symbols in the legend).

The panels in Figure 4.2 are similar to Figure 4.1B, showing the relevant turbulent length-scales as a function of non-dimensionalized distance from the grid. The mean flow velocity is $\overline{U} = 25$ cm s^{-1}, much greater than the highest turbulent velocity. The TKE equation describing the flow is (3.27), excluding the production term. All other terms in (3.27) were measured in the experiments, and they balanced to within 5% (Itsweire *et al.*, 1986).

There are two differences between Figure 4.2 and Figure 4.1B. The first is that Thorpe scales L_T obtained from re-ordering vertical density profiles were not measured in these experiments. The overturning length scale is instead inferred by density measurements as

$$L_t = \rho'_e / \frac{\partial \overline{\rho}}{\partial z} \tag{4.2}$$

where ρ'_e is the rms density difference from the mean value at a fixed point and $\partial \overline{\rho}/\partial z$ is the mean density gradient. Note that ρ'_e includes fluctuations from internal waves

---

[1]Data from Rohr, Itsweire & Van Atta (1984) are not included here because their large and small grid experiment are nearly identical to IHV experiments R36 and R52 respectively (Itsweire *et al.*, 1986). Although the experiments pre-dates the IHV work, IHV extended the tank to allow sampling the decay for longer periods.
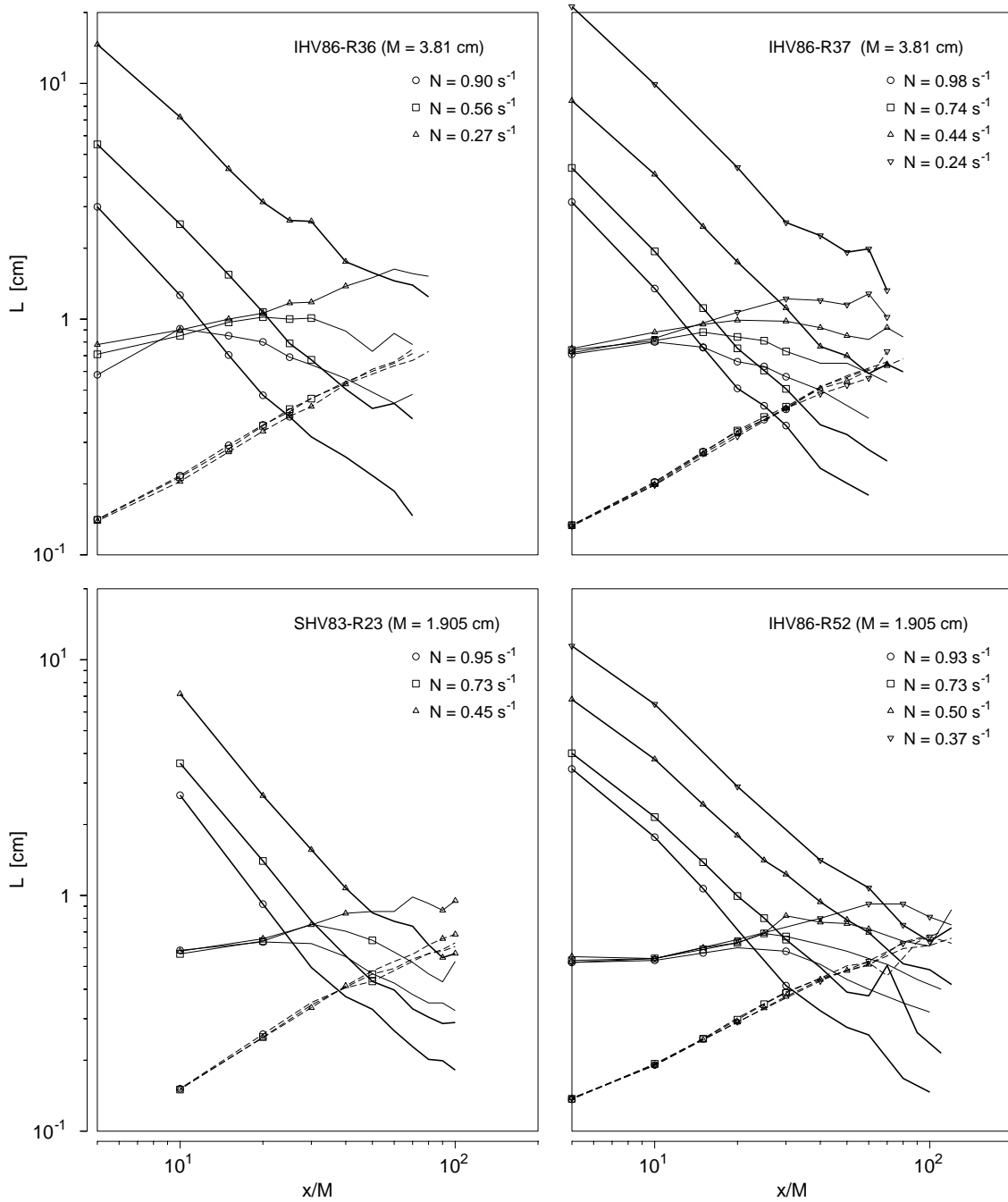
Figure 4.2: Evolution maps of turbulent length-scales for SHV and IHV experiments. Position is downstream of grid, non-dimensionalized by the grid mesh size M equal to 1.905 cm for R23 and R52 and 3.81 cm for R36 and R37. Group of lines are, from top to bottom, L_O (thick), L_t (thin) and $7.63\,L_K$ for R36 and R37 and $9.86\,L_K$ for R23 and R52 (dashed). Symbols were plotted only for data meeting the criterion $q < 2.2(\epsilon L_t)^{1/3}$ explained in the text. Experiments evolve from left to right.

as well as turbulent fluctuations associated with overturning, so that L_t may not be an accurate measure of overturning.

The ratio of Ozmidov to Kolmogorov scales where the measured buoyancy flux falls to zero (as described for Figure 4.1B) has been estimated by IHV as 7.63 ± 0.45 and 9.86 ± 0.48 for small (1.905 cm) and large (3.81 cm) grid mesh size respectively. These ratios correspond to normalized transition dissipation rates $\epsilon/\nu N^2$ where turbulence cannot maintain a buoyancy flux. Using (4.1), the L_O/L_K ratios are converted as

$$
\begin{aligned}
\epsilon_{tr} &= (15 \pm 1.2)\,\nu N^2 \quad \text{for } M = 1.905 \text{ cm} \\
\epsilon_{tr} &= (21 \pm 1.4)\,\nu N^2 \quad \text{for } M = 3.81 \text{ cm}
\end{aligned}
\tag{4.3}
$$

Values of 7.63 L_K and 9.86 L_K are shown on Fig. 4.2 so that they may be related to L_O to show the possible extinction of buoyancy flux. The second difference between Figure 4.1B and Fig. 4.2 is that the L_K line is not shown, nor is the $\epsilon/\nu N^2 = 200$ line for departure from isotropy (Gargett *et al.*, 1984). Note how odd it is that different grid sizes yield different transition dissipation rates; this is discussed in appendix A, but the reader may wish to read a later section on internal waves in the tank before venturing into appendix A.

4.2   The Turbulent Length Scale L_t

The overturning scale is not measured using Thorpe scales in these experiments. This raises two questions if L_t is to be used to test our model predictions from chapter 3. The first is how does L_t compare to L_T in the absence of internal waves? The second is how can it be confirmed that what are thought to be overturning scales are not, in fact, internal waves? This is a recurring concern. Itsweire *et al.* (1986) argued that internal wave motions observed during the late stages of decay were in fact present near the grid and predominate further downstream when turbulent motions have been dissipated.

4.2.1 Relating the Turbulent Length Scale L_t to Thorpe Scales

In a related experiment using the same facility, Itsweire (1984) showed L_t to be about equal to L_T in the absence of internal waves. His figure is reproduced as Figure 4.3. The points on the left-hand side for $N = 0.98$ s^{-1} which have $L_T/L_t < 1$ have dissipation levels too low to maintain a buoyancy flux ($\epsilon < \epsilon_{tr}$). The high values of L_t are said to be caused by internal wave motion (Itsweire, 1984). Figure 4.3 shows that L_T/L_t varies from less than 1 to more than 1.2, discounting internal waves and low dissipation levels. Itsweire *et al.* (1986) interpreted this figure as $L_T/L_t = 1.2$.

The highest values of L_T/L_t could be caused by an under-estimation of L_t from using a layer-averaged density gradient. In chapter 2, layer-averaged density gradients were observed to over-estimate the re-ordered density gradient within the overturns. Since L_t is inversely proportional to $\partial \overline{\rho}/\partial z$, using a layer-averaged density gradient would under-estimate L_t if such were the case here. Density gradients in these experiments are full-depth averages. Because the data are not tabled and therefore cannot be further analysed, and because the range of variations is small, the simplest interpretation of Figure 4.3 is to say that $L_T/L_t \approx 1$.

4.2.2 Internal Waves Contamination of L_t

To ensure that density fluctuations due to internal wave motions in the tank do not make L_t an over-estimate of overturning scales, let us attempt to separate the turbulence from the internal wave motions. In doing so, the Kolmogorov scaling of turbulent velocities will also be verified, at least for the isotropic case.

Itsweire *et al.* (1986) attempt to separate the internal wave component of the motion by noting that a buoyancy length scale $L_B = w'/N$ was related to L_O by a power law of the form $L_O = cL_B^b$, and that the slope b changed at a given point presumably because of the internal wave contributions to L_B. The failings of the method are that it has no theoretical basis and that the power law changes from one
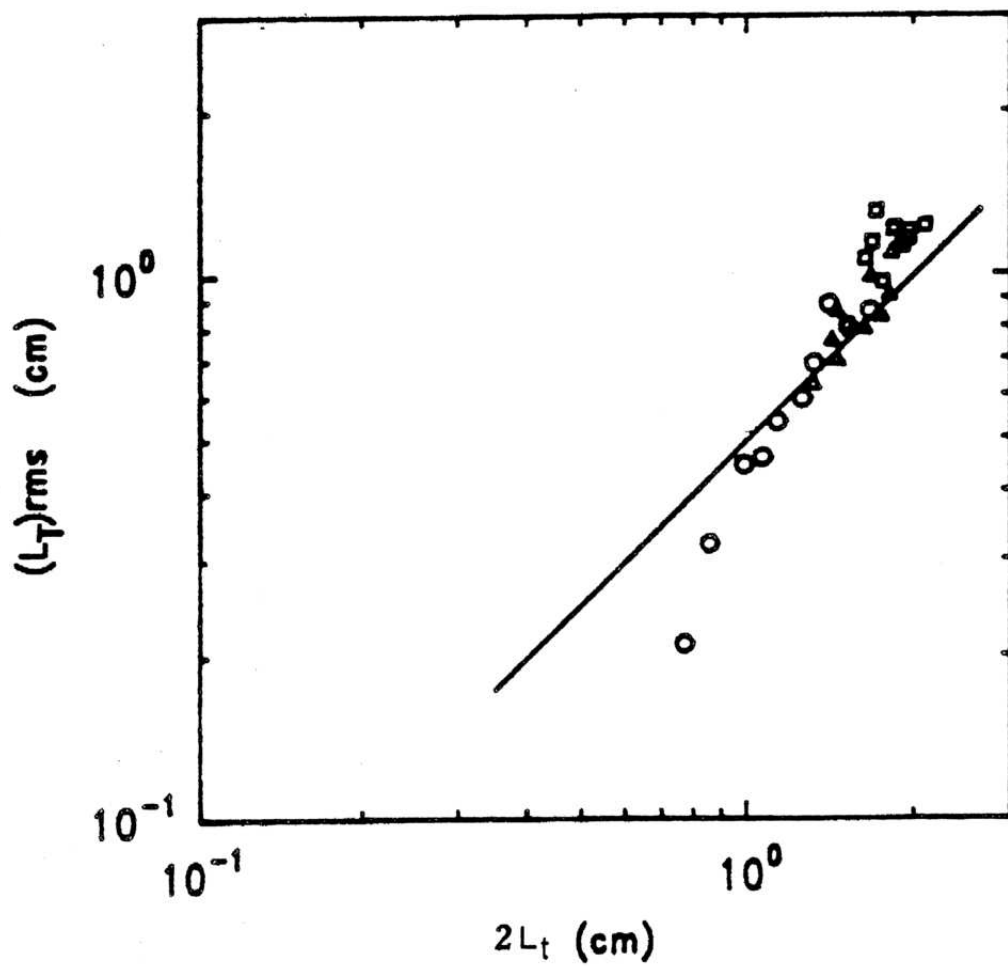
Figure 4.3: Thorpe scale L_T versus L_t for a grid turbulence experiment where both were measured. $N = 0.98$ s^{-1} ($\circ$), 0.67 s^{-1} ($\triangle$), 0.45 s^{-1} ($\square$). Figure reproduced from Itsweire (1984) (Figure 3). Note that the horizontal scale is $2L_t$, not L_t. This is due to a different definition of L_t used by Itsweire.

data set to another. Also, it can be shown, assuming isotropy and $u' \approx (\epsilon L_t)^{1/3}$, that $L_O \propto Ri_t^{-1/4} L_B$. Since there is a large change in Ri_t during the growth, this may cause the $L_O = cL_B^b$ power law to have a varying slope unrelated to internal waves.

A Method To Detect Internal-Waves In Grid-Turbulence

The internal wave and turbulence separation scheme that I propose uses differences in the expected behaviour of the ratio $(3u'^2)^{1/2}/(\epsilon L_t)^{1/3}$ versus L_t/L_O for both turbulence and internal waves.

For the nearly isotropic turbulence in the grid-generated turbulence, Kolmogorov scaling of turbulent velocities gives $\epsilon \approx u'^3/L_t$. For now, let us assume isotropy so that the TKE is $q^2 = 3u'^2$. The relation $q/(\epsilon L_t)^{1/3} \approx 3^{1/2}$ is then expected for turbulent motions at all times in the turbulence evolution (assuming $L_T = L_t$, i.e. no internal waves). Since the turbulence is decaying, the downstream evolution maps to an evolving ratio of L_O/L_t. The relation

$$\frac{q}{(\epsilon L_t)^{1/3}} \approx 3^{1/2} \tag{4.4}$$

is expected to hold for all values of L_O/L_t for turbulence without internal waves.

The small internal waves in the tank have a velocity scale $q \approx NL_t$ when density fluctuations ρ'_e are caused by internal waves, such that $L_t = \rho'_e/(\partial\overline{\rho}/\partial z)$ yields the wave amplitude and N^{-1} scales like the period. In this case, turbulent velocities should be greater than the Kolmogorov spectrum can account for in terms of ϵ. The relation

$$\frac{q}{(\epsilon L_t)^{1/3}} \approx \left[\frac{L_t}{L_O}\right]^{2/3} \tag{4.5}$$

is expected to hold for internal wave motions.

Figure 4.4 shows $q/(\epsilon L_t)^{1/3}$ versus L_t/L_O for the SHV and IHV data sets. Data with $L_t/L_O \ll 1$ follow (4.4), the Kolmogorov velocity scaling expected for turbulence. Note that a ratio of $L_t/L_O \approx 1$ and $\epsilon \approx u'^3/L_t$ implies a low turbulent Richardson number, Ri_t, from (3.26). In turn, this means that the inertial velocity u' is much

greater than the buoyancy velocity NL_t such that internal waves cannot exist; this range of data in Figure 4.4 are unambiguously classified as turbulence.

Around $L_t/L_O = 1$, data diverge and follow the scaling (4.5), expected for internal waves. These internal wave data follow a slope close to 2/3. Data with $q/(\epsilon L_t)^{1/3} \gg 3^{1/2}$ have more TKE than the Kolmogorov sprectrum can account for from the level of dissipation of TKE. The energy cannot have cascaded from larger turbulent scales.

To establish our desired criterion for distinguishing internal waves from turbulence, data with

$$q/(\epsilon L_t)^{1/3} > 2.2 \tag{4.6}$$

are judged by eye to better fit the internal wave scaling (4.5) than the turbulence scaling (4.4). Many points around $L_t/L_O \approx 1$ which could be classified as internal waves (because $u' \approx NL_t$ suitable for internal waves at $L_t \approx L_O$ and because data at $L_t \approx L_O$ fall along both classifying slopes) have been left as turbulence, because they cannot be unambiguously eliminated using this criterion.

Using the above criterion, L_t can be used interchangeably with L_T for the grid turbulence data shown because internal waves can be detected and excluded from analysis. For example, in Figure 4.2, only data not identified as internal waves are plotted with symbols. For nearly all experiments there are few turbulent data points during the inertial-buoyancy balanced decay, where L_t is expected to decay in constant proportion to L_O. Thus, in the evolution of turbulence depicted in Figure 4.2, the late decay stage contains significant internal wave energy such that $L_t > L_T$. This is why L_t decays slower than L_O, contrary to expectations shown in Figure 4.1B.

4.3 Checking The Assumptions of the Models

The following assumptions were made to derive the second model, which describes isotropic growing turbulence

- That Kolmogorov scaling of the turbulent velocities holds: $\epsilon \approx u'^3/L$, where L is the turbulent length scale (isotropic). This permits obtaining a usable form
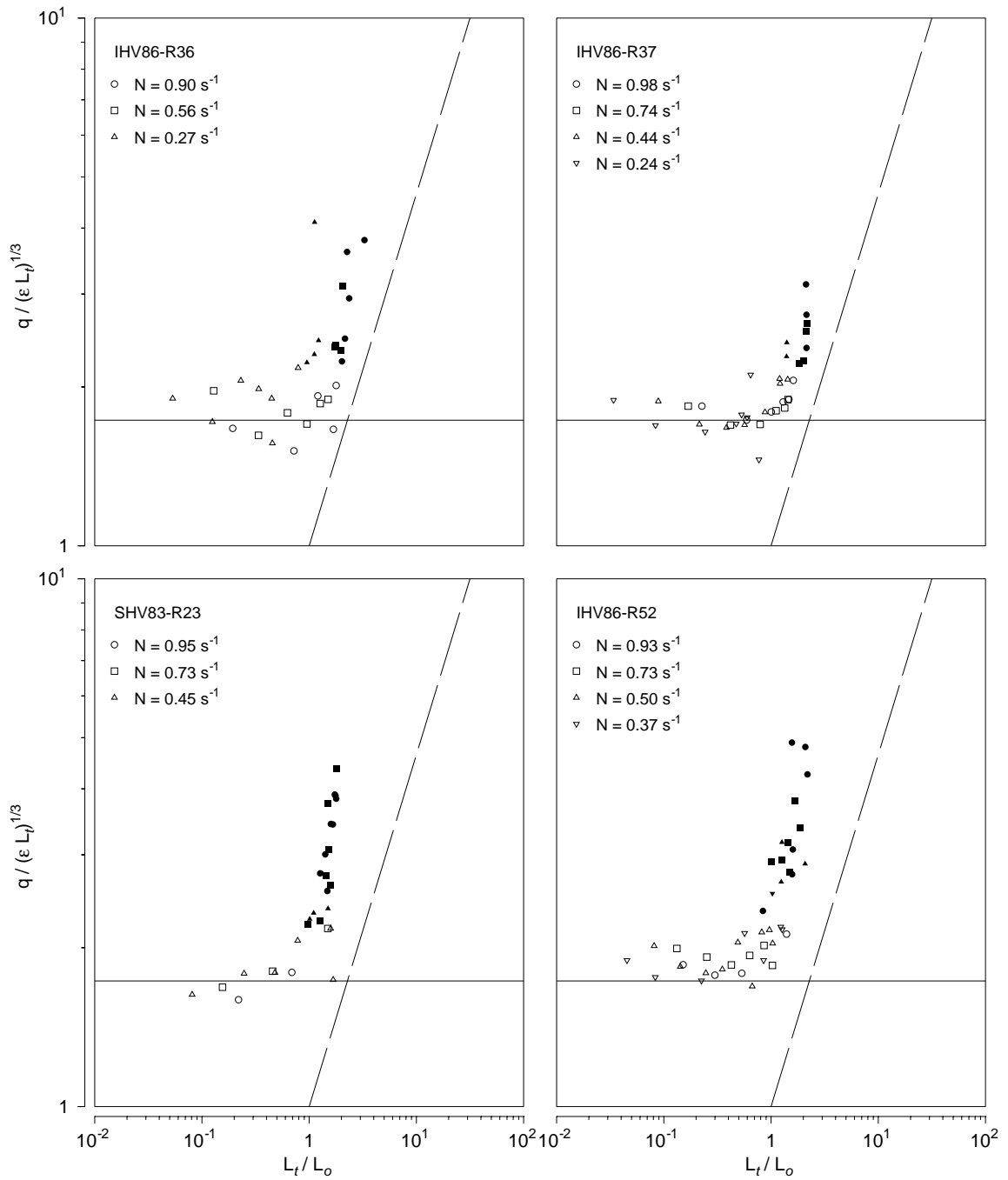
Figure 4.4: Internal waves detection criterion showing $q/(\epsilon L_t)^{1/3}$ vs L_t/L_O for all data from SHV and IHV experiments. The horizontal line is $q/(\epsilon L_t)^{1/3} = 3^{1/2}$ which is approximately expected for isotropic turbulence. The dashed line is $q/(\epsilon L_t)^{1/3}$ vs $(L_t/L_O)^{2/3}$, a relation expected for internal wave motions. Data with $q/(\epsilon L_t)^{1/3} \geq 2.2$ (filled symbols) are identified as internal waves because they resemble the $q/(\epsilon L_t)^{1/3} \propto (L_t/L_O)^{2/3}$ criterion expected for internal waves rather than $q/(\epsilon L_t)^{1/3} \approx 3^{1/2}$ expected for turbulence. Experiments evolve from left to right.

of the decay time as $t_o \approx (3/2)Fr_t^{-1}N^{-1}$ and the relation $(Ri_t)_{iso} \approx (L_T/L_O)^{4/3}$.

- That ξ is well approximated by $N^2L_T^2/2$ (Used to obtain $\Gamma \approx \left[\frac{3}{4} \pm \frac{1}{4}\right] Ri_t/3$).

In addition, other assumptions were necessary to derive the third model, which describes steady-state anisotropic turbulence at inertial-buoyancy balance

- That Kolmogorov scaling of the turbulent velocities holds using horizontal scale specifically (anisotropic): $\epsilon \approx u'^3/L_h$. This permits obtaining the decay time as $t_o \approx N^{-1}$, the relation $(Ri_t)_{IB} \approx (L_T/L_O)^2$, and the primary prediction that $L_O \approx L_h$.

- That continuity holds on turbulent scales: $u'L_T = w'L_h$.

- That ξ is well approximated by $N^2L_T^2/2$ (Used to obtain $\Gamma \approx \left[\frac{3}{4} \pm \frac{1}{4}\right] Ri_t/2$).

These will now be discussed in turn.

4.3.1 Kolmogorov Scaling and the Continuity Assumption

The verication of the assumption of Kolmogorov scaling of turbulent velocity fluctuations, *i.e.* $\epsilon \approx u'^3/L_h$, presents difficulties. The horizontal turbulent scale is not measured in the experiments. The isotropy ratio, measured from the ratio of rms velocity fluctuations w'/u', varies from 0.7 to 1. This is much less variation than could result from the third model of turbulence where $L_h \approx L_O$. Therefore, the $\epsilon \approx u'^3/L_h$ relation can only be verified empirically for "nearly isotropic" turbulence with the current data. (Note that, contrary to my interpretation, Gargett (1988) interprets these experiments as evolving anisotropically with $L_h \approx L_O$. This is discussed in appendix B where new evidence is shown to counter her claim.)

The scaling $\epsilon \approx u'^3/L_t$ was shown to hold in Figure 4.4 for data unaffected by internal waves. Unfortunately, I cannot show that both the assumption that $\epsilon \approx u'^3/L_h$ and that $u'L_T = w'L_h$ hold independently because L_h is not measured. However, combinations of these two assumptions can be verified, in particular the

L_t/L_O–Ri_t relation, which depends on the Kolmogorov scaling. It was shown that $Ri_t \approx (L_T^2 L_O^{4/3})/L_h^{2/3}$ in (3.25). For the isotropic case of $L_T = L_h$, this reduces to $(Ri_t)_{iso} \approx (L_T/L_O)^{4/3}$. This $(Ri_t)_{iso}$ relation would be a general result for Ri_t if Kolmogorov scaling is really $\epsilon \approx u'^3/L_t$ instead of $\epsilon \approx u'^3/L_h$. If the turbulence is slightly anisotropic, the general result $Ri_t \approx (L_T^2 L_O^{4/3})/L_h^{2/3}$ should hold better than $Ri_t \approx (L_T/L_O)^{4/3}$ if Kolmogorov scaling should be done using L_h rather than L_t. Let us combine (3.25) with the assumption $u'L_T = w'L_h$ and verify if

$$Ri_t \approx \frac{N^2 L_t^2}{(\epsilon L_h)^{2/3}} \approx \frac{L_t^{4/3}}{L_O^{4/3}} \left[\frac{L_t}{L_h}\right]^{2/3} \approx \left[\frac{L_t}{L_O}\left(\frac{w'}{u'}\right)^{1/2}\right]^{4/3} \tag{4.7}$$

holds as well or better than $Ri_t \approx (L_T/L_O)^{4/3}$.

This scaling comparison is done in Figure 4.5. The reader is reminded that experiments evolved from low to high values of Ri_t. Data identified as internal waves contribute to most of the error in the scalings (by definition, since that is how internal waves were detected). The identification of internal waves in the grid-turbulence data is thus a significant contribution.

Regressions in this and other log–log figures are performed in logarithmic space. The confidence interval on the mean is expressed as $10^{a \pm ci} = 10^a \,^\times\!/_\div\, 10^{ci}$. Regressions are performed minimizing variance in the ordinate for both the slope and the multiplicative coefficient. Regressions are also shown with the slope set to that expected from scaling arguments, letting the multiplicative coefficient be determined by minimizing variance.

Least-squares regressions in logarithmic space with the slope undetermined yield the predicted 4/3 slope for both cases. If the isotropy-adjusted scaling ($\epsilon \approx u'^3/L_h$) is wrong, the error should increase at the higher values of L_t/L_O where anisotropy is strongest (up to $w'/u' \approx 0.7$) because of the decaying turbulence. It does not (visually, ignoring the internal wave data). Also, note that the coefficient for the isotropy-adjusted scaling is closer to unity than the unadjusted scaling.

Both assumptions $\epsilon \approx u'^3/L_h$ and $u'L_T = w'L_h$ are very consistent with the data, although it would be difficult to show that scaling turbulent velocities with L_h is
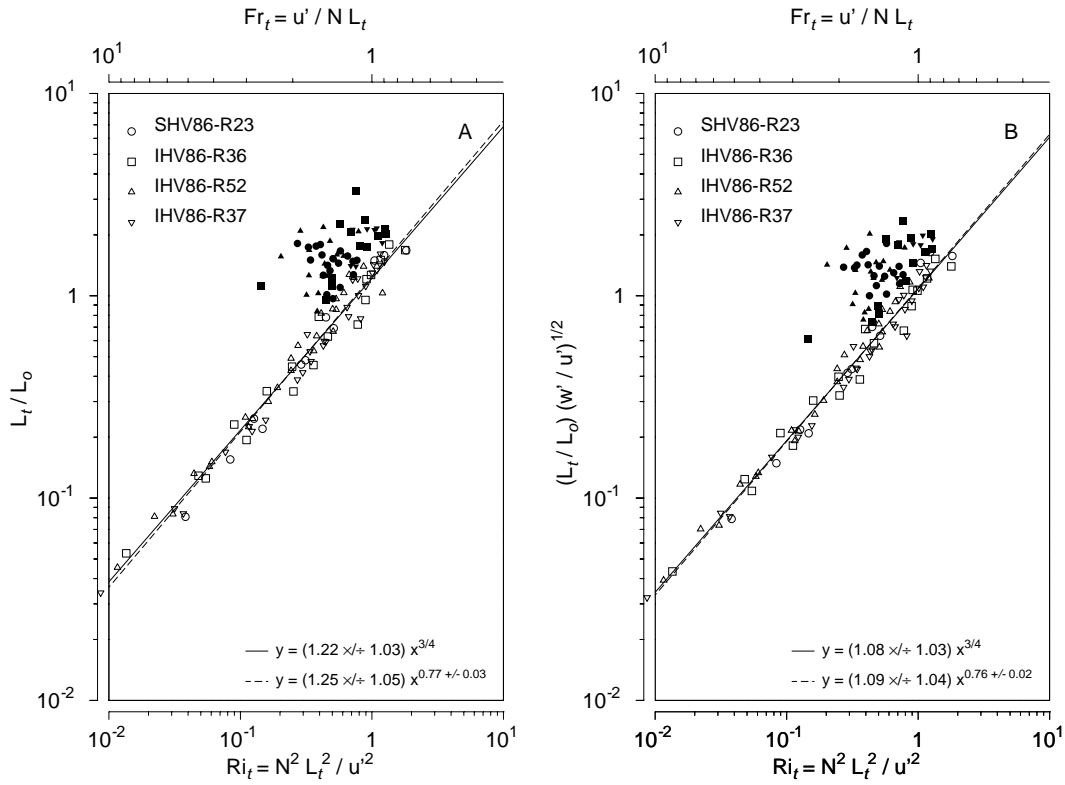
Figure 4.5: Ratio of overturning to Ozmidov length scales L_t/L_O versus turbulent Richardson number Ri_t **A:** L_t/L_O vs Ri_t. Data are coded according to experiments, open symbols for $q/(\epsilon L_t)^{1/3} < 2.2$ and solid symbols for $q/(\epsilon L_t)^{1/3} \geq 2.2$. The least-squares regressions are shown for $q/(\epsilon L_t)^{1/3} < 2.2$ data in log space; the first forces the slope, the second has the slope determined by the fit. **B:** Same as (A), but a correction for anisotropy is included which is expected to make the 4/3 scaling better. Experiments evolve from left to right.

significantly different than using L_t for this data because of the small departure from isotropy (*i.e.* $(0.7)^{2/3} \approx 0.8$ is a small factor to detect).

4.3.2 APEF Approximation

In order to derive forms of the mixing efficiency for the models, the APEF is approximated by $N^2 L_T^2/2$. In chapter 2, this was shown to be an over-estimate by a factor of 2 to 3. The reason is that the average value of N^2 over a depth span larger than an overturn tends to be higher than N^2 calculated on the re-ordered density profile within the overturn. The laboratory estimate of ξ is not subject to this same over-estimation. Since L_T is estimated from density fluctuations as $L_t = \rho'_e/(\partial\overline{\rho}/\partial z)$, the approximation of the APEF is

$$\xi \approx \frac{N^2 L_t^2}{2} \approx \frac{1}{2} \frac{-g}{\rho} \frac{\partial\overline{\rho}}{\partial z} \left[\frac{\rho'_e}{\partial\overline{\rho}/\partial z}\right]^2 \approx -\frac{1}{2} \frac{g}{\rho} \frac{(\rho'_e)^2}{\partial\overline{\rho}/\partial z} \tag{4.8}$$

Thus $N^2 L_t^2/2$ is inversely proportional to the density gradient. If the bulk density gradient is higher than within overturns, the APEF will be under-estimated. This was also shown to be true for (2.29) in Figure 2.1 using bulk averages that over-estimate N^2.

Is the Density Gradient Over-Estimated?

If the density gradient is over-estimated, then the growing turbulence model's predicted mixing efficiency $\Gamma = Ri_t/3$ (within a factor of 2) could be under-estimated. The only evidence available is the comparison of L_t to L_T in Figure 4.3. As previously discussed, it shows $L_t \approx L_T$. In chapter 2 in a test of (2.29), it was shown that the equality $L_T = \overline{\rho'^2}^{1/2}/(\partial\overline{\rho}/\partial z)$ holds if $\partial\overline{\rho}/\partial z$ is equal to the gradient *within* overturns. Since there should be a one-to-one correspondence between $\overline{\rho'^2}^{1/2}$ and the fixed-point measurement ρ'_e, then it appears that the density gradient quoted for the lab experiments is indeed representative of the re-ordered density profile within the overturns, at least to within 20% or so (much better than the factor of 2 to 3 for oceanic data in chapter 2).

The APEF should be well approximated by ξ, and $Ri_t/3$ should correspond to the predicted mixing efficiency of the isotropic growing turbulence model, because the density gradient quoted for lab experiments appears to be representative of that within overturning (using the re-ordered density profile)[2].

4.3.3 Summary of Assumptions

Excluding the internal wave energy-dominated data, the assumption of Kolmogorov velocity scaling was shown to be valid (with time-averaging performed at sample locations along the tank). The approximation of ξ as $N^2 L_t^2/2$ was also shown to be valid, based on Itsweire's (1984) experiment. Thus the scaling assumptions made to derive the isotropic growing turbulence model in chapter 3 are verified to the best of our ability using the grid turbulence data. The model can now be compared to the grid-turbulence data.

It must be noted here that the assumptions and predictions are only tested here using averaged data, such that redistribution terms of the TKE and temperature variance equations can also be neglected. These results cannot be readily generalized to individual overturns. Likewise, the turbulence found past grids may not resemble a K-H billow in its finer details, nor can we assume that a constant turbulent Froude number can characterise the entire evolution of a K-H billow. However, the turbulence found here is argued to resemble the steadily forced mixing layers in mind for models two and three, such that these results should be relevant to shallow sea mixing (continental shelfs, estuaries, straits), but not to abyssal mixing due to breaking internal waves unless forced by a long-lasting (relative to overturn period) shear.

---

[2]It is unclear how N^2 evolves following the flow because the length of the tank is sampled sequentially, not simultaneously.

4.4 Mixing Efficiency as Function of Ri_t

The model prediction for mixing efficiency is

$$\Gamma \approx \left[\frac{3}{4} \pm \frac{1}{4}\right] \frac{Ri_t}{3} \tag{4.9}$$

Figure 4.6 shows the flux Richardson number R_f as a function of Ri_t (or Fr_t as both coordinates are shown). The flux Richardson number is closely related to $\Gamma = J_b/\epsilon$. It is defined as the ratio of buoyancy flux to the production of TKE. In the absence of production, it is determined as the ratio of buoyancy flux to all other sink terms. It is written as

$$R_f = \frac{J_b}{\epsilon + J_b} = \frac{\Gamma}{1 + \Gamma} \tag{4.10}$$

The flux Richardson number is sometimes referred to as the mixing efficiency. I have referred to Γ as the mixing efficiency instead. Note that $R_f \approx \Gamma$ at small values.

The upper limit of the prediction (4.9) is shown in Figure 4.6. The fit to data is improved when internal wave data are removed in Figure 4.6B. It matches data at low turbulent Richardson numbers well within a factor of 2.

The prediction of the second model for maximum mixing efficiency is only that it must occur at the balance between inertial and buoyancy forces. The value of the mixing efficiency or of turbulent Richardson number at the inertial-buoyancy balance was not predicted. At first glance, Figure 4.6 suggests $Ri_t = 0.7$ (equivalent to $Fr_t = 1.2$) and $\Gamma = 0.23$ (Ivey and Imberger, 1991) for maximum mixing efficiency at inertial-buoyancy balance. I believe this suggestion to be incorrect, but its discussion will wait until further evidence for the inertial-buoyancy value of Ri_t is presented.

4.5 Slight Departures From Isotropy

The following predictions were made about the effect of slight anisotropy on Ri_t and mixing efficiency:

- The measured Ri_t decreases $\propto L_T^2/L_h^2$ such that mixing efficiency is still given
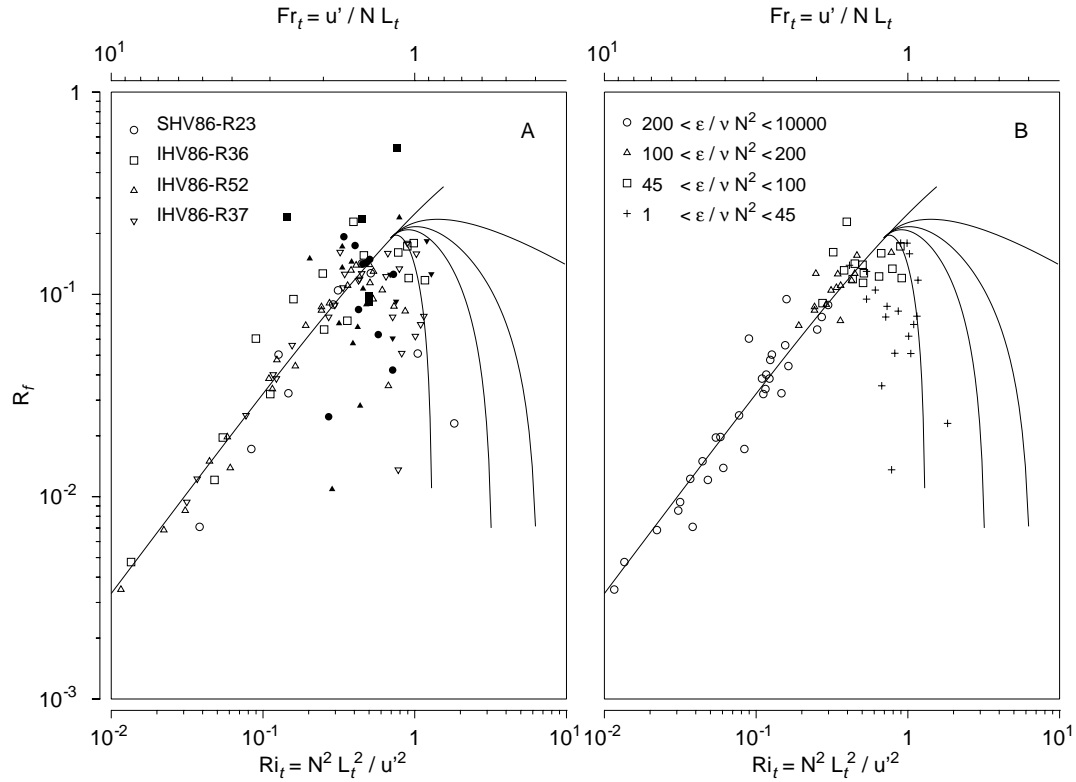
Figure 4.6: Flux Richardson number R_f vs turbulent parameters Fr_t or Ri_t with only data with $R_f > 0$ shown (not re-stratifying). Solid line on left is (4.9) extended to $Fr_t = 0.8$. Other curves for $Fr_t < 1.2$ are Ivey & Imberger's (1991) predictions for $Re_t = 50000, 100, 50$ and 20 from top to bottom. Results of Ivey & Imberger (1991) are discussed in appendix B. Experiments evolve from left to right; **A:** Data are coded according to experiments, open symbols for $q/(\epsilon L_t)^{1/3} < 2.2$ and solid symbols for $q/(\epsilon L_t)^{1/3} \geq 2.2$. **B:** Only data with $q/(\epsilon L_t)^{1/3} < 2.2$ are shown, a criterion which eliminates most data with high internal wave energy. Data are coded by values of $\epsilon/\nu N^2$.

approximately by $\left[\frac{3}{4} \pm \frac{1}{4}\right] Ri_t/3$. There is no extra adjustment to make on $\Gamma \approx \left[\frac{3}{4} \pm \frac{1}{4}\right] Ri_t/3$ for isotropy.

- The generalized form of Ri_t in terms of length scales combines both the inertial-buoyancy balance and isotropy factors as $Ri_t \approx (L_h/L_O)^{4/3} (L_h/L_T)^2$ (using $\epsilon \approx u'^3/L_h$)

This is an important question for ocean turbulence which can be of low intensity ($\epsilon/\nu N^2 < 200$) such that turbulence may become anisotropic (Gargett et $al.$, 1984).

The effect of turbulent intensity on isotropy is difficult to ascertain using the laboratory experiments. This might be because of the internal waves which stand out at low turbulent intensity, and cloud the evaluation of turbulent kinetic energy and its dissipation[3]. However, the effect of isotropy on the prediction of mixing efficiency as $Ri_t/3$ can be examined.

Figure 4.7 shows the ratio of measured mixing efficiency Γ to the upper bound of the expected mixing efficiency $Ri_t/3$—identical to the ratio of measured to expected buoyancy flux—versus (A) the degree of isotropy w'/u' and (B) versus turbulent intensity $\epsilon/\nu N^2$. As expected, isotropy variations of 0.7 to 1 do not affect the prediction of buoyancy flux from Ri_t. The buoyancy flux falls short of predictions only for $\epsilon/\nu N^2 < 45$ where the Ri_t model fails. It is possible that internal wave contamination is related to the observed cut-off value of $\epsilon/\nu N^2$ (see discussion in appendix A), or that viscosity effects do in fact reduce buoyancy flux below $\epsilon/\nu N^2 \approx 45$ as suggested by Figure 4.7B.

In other words, the degree of isotropy affects Ri_t where departure from isotropy is most noticeable for $\epsilon/\nu N^2 < 100$ (see Figure A.1). However, the resulting Ri_t seems to predict the correct buoyancy flux. Figure 4.5 shows that, perhaps counter-intuitively, anisotropy results in $Ri_t < (L_t/L_O)^{4/3}$. It is seen by comparing the isotropy-adjusted $Ri_t \approx (L_t/L_O)^{4/3}(L_t/L_h)^{2/3}$ to the unadjusted $(Ri_t)_{iso} \approx (L_t/L_O)^{4/3}$ which overestimates the former.

---

[3]Figure A.1 described in appendix A shows that w'/u' generally decreases for $\epsilon/\nu N^2$ less than a few hundred, except for a rise due to internal waves unrelated to turbulence.
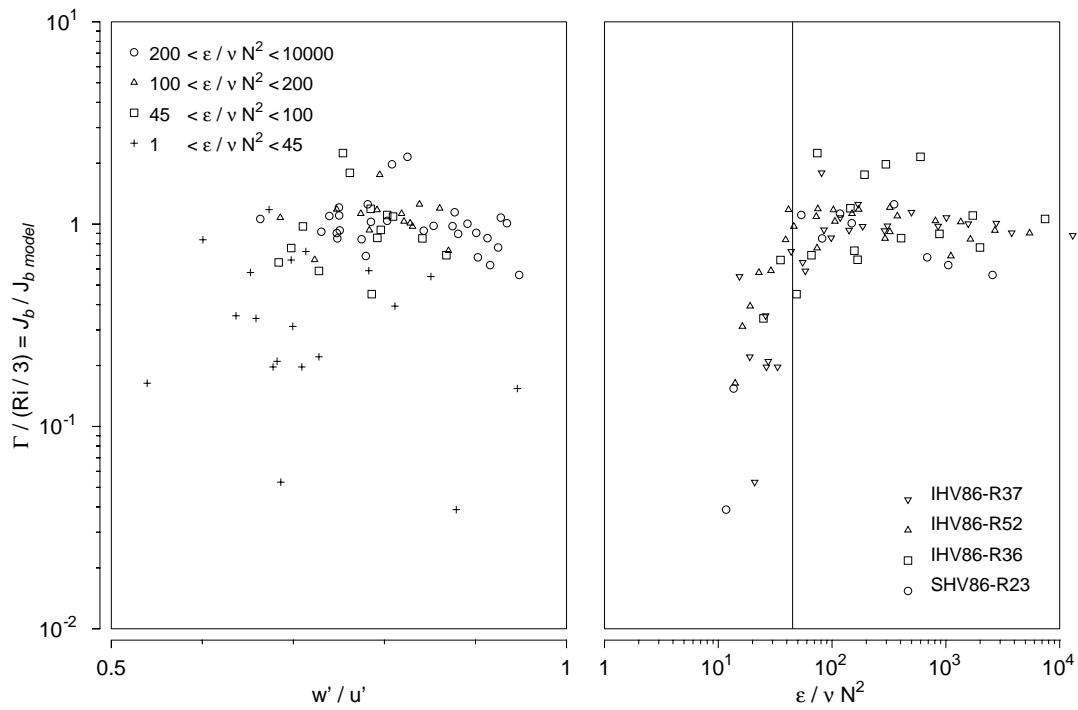
Figure 4.7: Ratio of measured to predicted mixing efficiency versus isotropy w'/u' and turbulent intensity $\epsilon/\nu N^2$. Vertical line in (B) is at $\epsilon/\nu N^2 = 45$. Experiments evolve from high to low values of $\epsilon/\nu N^2$.

4.6 Relating the turbulent parameters to the large scale

The applicability of the buoyancy flux model prediction (4.9) is limited. The turbulent parameter Ri_t, while easily obtained in the lab, is not easily measured in the ocean. The mixing efficiency parameterization in terms of Ri_t provides a useful framework, as well as my earlier discussion on the significance of Fr_t, but they may require too much knowledge about the state of the turbulence to be very useful.

In the previous chapter, it was hypothesized that Ri_t is related to the larger scale gradient Richardson number Ri_g if turbulent velocities are produced from the mean shear. The mixing efficiency could thus be inferred from measurements of Ri_g. This model is tested now. If Ri_g is a useful substitute to Ri_t, then the parameterization of Γ in terms of Ri_t allows large scale measurements to be used to infer the state of the turbulence and its mixing efficiency.

The hypothesis is that

$$u' = a\, L_T \frac{\partial \overline{U}}{\partial z}$$

or equivalently that

$$Ri_t = \frac{N^2 L_T^2}{a^2 L_T^2 (\partial \overline{U}/\partial z)^2} = \frac{1}{a^2}\, Ri_g$$

Figure 4.8 shows data from Rohr $et\ al.$ (1988)[4] and Stillinger (1981) conducted in the same tank as the SHV and IHV experiments, but with the addition of a mean shear flow.[5]

The value of L_t/L_O is shown against the gradient Richardson number $Ri_g = N^2/(\partial \overline{U}/\partial z)^2$ where $\overline{U}$ is the mean velocity, now a function of depth. Turbulence

---

[4]Data from Rohr & Van Atta (1987) at three different values of Ri_g fit on the same line as the Rohr $et\ al.$ (1988) data.

[5]The data point from Tavoularis $et\ al.$ (1981) should be disregarded. First, it is from an experiment in air (different Prandtl number). Second, they used $Ri_g = (g/\overline{T})(\partial \overline{T}/\partial z)/(\partial \overline{U}/\partial z)^2$. Substituting their tabled values for Ri_g, $\partial \overline{T}/\partial z$ and $\partial \overline{U}/\partial z$ one gets $\overline{T} = 21$. Unless these were very cold air experiments (not noted in the paper) they wrongly used temperature in degrees Celcius rather than Kelvin to calculate Ri_g. Third, the turbulence appears anisotropic. However, it should be possible to check $u' = a\, L_T\, \partial \overline{U}/\partial z$ from the original data.
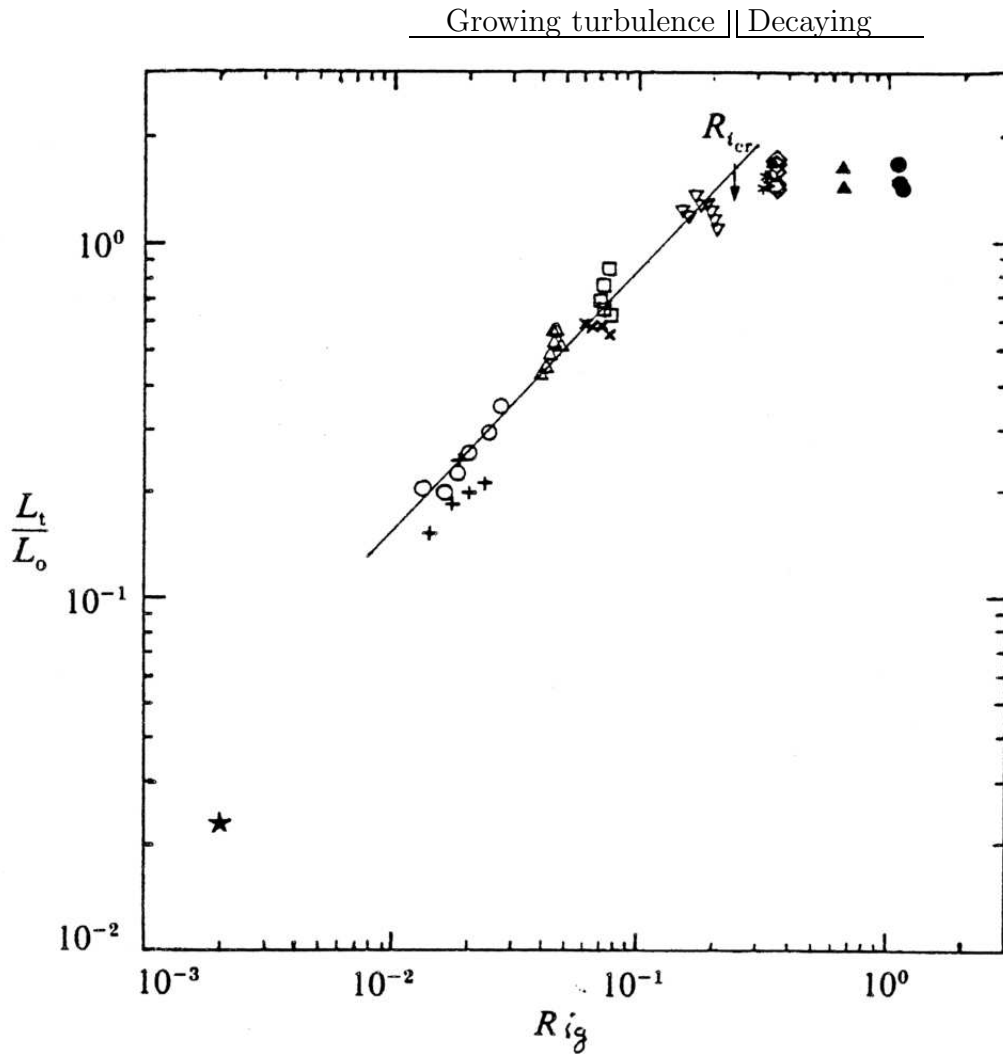
Figure 4.8: Relation of turbulent parameter L_t/L_O to gradient Richardson number Ri_g for an grid turbulence experiment with a mean shear. Includes data from Stillinger (1981) and Tavoularis & Corrsin (1981). Figure reproduced from Rohr *et al.* (1988) (Their Figure 15). Note that $(Ri_t)_{iso} \approx (L_t/L_O)^{4/3}$ for isotropic turbulence. The slope of the line is 3/4 such that $Ri_g \propto Ri_t$.

grows downstream for $Ri_g < (Ri_g)_{cr}$, where $(Ri_g)_{cr} = 0.25$. Recall that for isotropic turbulence—as expected in the presence of a driving shear—the isotropic turbulent Richardson number $(Ri_t)_{iso}$ is approximately equal to $(L_t/L_O)^{4/3}$, assuming $\epsilon = u'^3/L_T$ (this scaling was shown to hold to better than a factor of two in Figure 4.5). In Figure 4.8 it is shown that for $Ri_g < (Ri_g)_{cr}$ in growing turbulence, the gradient Richardson number is proportional to $(L_t/L_O)^{4/3}$, which is equal to $(Ri_t)_{iso}$

The gradient Richardson number can therefore be related to the turbulent parameter Ri_t or Fr_t, which quantifies mixing efficiency in our model and in the grid experiments discussed earlier. Thus, measurements of Ri_g, ξ and N are sufficient to determine values of ϵ, J_b and R_f.

If models two and three were proved to be wrong, the fact that Ri_g is proportional to $(L_t/L_O)^{4/3}$ and that $L_t \approx L_T$ means that measurements of Ri_g and L_T in the ocean would yield indirect measurements of ϵ (but no indication of mixing efficiency).

The proportionality coefficient a will be discussed in the following sections.

4.6.1 Link Between the Ri_g–Ri_t Relation and Inertial-Buoyancy Balance

The interpretation of Figure 4.8 implies a connection between the Ri_g–Ri_t relation and the value of the turbulent Froude number at the inertial-buoyancy balance, $(Fr_t)_{isoIB}$.

The Ri_g–$(Ri_t)_{iso}$ proportionality ends at $(Ri_g)_{cr}$ because gradient Richardson numbers greater than $(Ri_g)_{cr}$ do not lead to instabilities and may not provide sufficient shear to completely drive turbulence. Runs with $Ri_g > (Ri_g)_{cr}$ result in decaying turbulence not unlike unsheared experiments, and the correlation between Ri_g and Ri_t disappears. The value of Ri_t at $Ri_g \geq (Ri_g)_{cr}$ is thus the inertial-buoyancy value: the maximum value of Ri_t allowed in a turbulent flow, where the vertical kinetic energy can just overcome buoyancy force.

The value of Ri_t at $Ri_g \geq 0.25$ and the value $Ri_t = a^{-2}\,(Ri_g)_{cr}$ should be identical, and represent the inertial-buoyancy balance values. They are identical within the error bounds of Figure 4.8. Thus the proportion, a, of the velocity available to the

overturn from the shear, $L_T(\partial \overline{U}/\partial z)$, that is converted to turbulent velocities, u', determines the inertial-buoyancy value of Ri_t at $Ri_g = (Ri_g)_{cr}$. An empirical value for a then follows from the inertial-buoyancy value of Ri_t, dicussed in the next section.

4.7 Inertial-Buoyancy Balance Value of Ri_t

The values of Ri_t and L_t/L_O at the inertial-buoyancy balance are of interest for three reasons: *i*) To determine the proportionality constant between Ri_g and Ri_t such that the more commonly measured Ri_g can determine the state of the turbulence; *ii*) To determine the maximum mixing efficiency predicted by the proposed model two as $\approx Ri_t/3$; *iii*) To compare oceanic measurements of L_T/L_O to laboratory results in relation to inertial-buoyancy balance values.

There is scatter in the $Ri_g \propto (L_t/L_O)^{4/3}$ relation of Figure 4.8, ranging from $(L_t/L_O)^{4/3} = 5.6\, Ri_g$ to $(L_t/L_O)^{4/3} = 10.4\, Ri_g$ (These values are taken by eye from Figure 4.8 because the data were not tabulated). The corresponding 'critical' turbulent Richardson numbers are $(Ri_t)_{cr} \approx 1.4$ to 2.6. For the decaying turbulence at inertial-buoyancy balance ($Ri_g > 0.25$) in Figure 4.8, we find $L_t/L_O \approx 1.45$–1.7, corresponding to $Ri_t \approx 1.65$ to 2.03. The range of critical values of Ri_t is rather large due to observational errors, but these seem to agree that it is greater than unity.

Maximum Mixing Efficiency in Grid Experiments

Returning to Figure 4.6, the maximum mixing efficiency expected at inertial-buoyancy balance occurs at $Ri_t = 0.7$, much lower than anticipated from the experiments with shear described above. There is thus an inconsistency to be resolved between these data sets. The interpretation found in the original papers is described in appendix B.

With this inconsistency, one might wonder if the description in section 4.1.1 of the evolution of the experiment is correct about the inertial-buoyancy balance decay with constant ratio of L_T/L_O. Figure 4.6 suggests that mixing efficiency reaches a peak before the decay stage, instead of thereafter remaining constant.

Figure 4.9 shows the downstream evolution of Thorpe scales L_T and Ozmidov scales L_O in a grid-turbulence experiment without a mean shear. The experiment evolves from right to left on the figure. Nearly a decade of inertial-buoyancy balance decay was measured with constant L_T/L_O. There is again a lot of scatter, but I find approximately $L_T/L_O \approx 1.5$ during the decay, corresponding to $(Ri_t)_{cr} \approx 1.7$.

Thus the initial discussion in section 4.1.1 is consistent with other data, but not with Figure 4.2, where all data in the late decay stage are contaminated by internal waves. This helps to resolve the inconsistency. While it is possible that $\overline{w'\rho'}$ correlations are affected by internal waves, it is also possible that that my classification of these data as internal waves and the mixing efficiency decrease are both symptoms of turbulent kinetic energy extinction. If the internal waves were generated at the grid, they would only become apparent when the initially much stronger turbulent energy has decayed. Figure 4.10 shows the parameter space L_t/L_O versus $\epsilon/\nu N^2$ covered for the SHV and IHV data. The parameter space L_t/L_O–$\epsilon/\nu N^2$ is highly correlated; high intensity turbulence has low Ri_t and the reverse. It is difficult to separate the effects of one parameter from the other on the turbulence, which could explain the misinterpretation of decreasing mixing efficiency as related to L_t/L_O, while it could be due to low $\epsilon/\nu N^2$ values.

Data not identified as internal waves ($q/(\epsilon L_t)^{1/3} < 2.2$) in Figure 4.10 have a wide range of $\epsilon/\nu N^2$, but when the turbulence has evolved to an inertial-buoyancy balance ($L_t/L_O \approx 1.4$) it can barely sustain a buoyancy flux, with $\epsilon/\nu N^2$ in the range 15 to 25.[6] As discussed in section 4.5, it is possible that viscosity effects reduce buoyancy flux below $\epsilon/\nu N^2 \approx 45$ as suggested by Figure 4.7B. This is a lower turbulent intensity than Gargett *et al.* (1984) reported for departure from isotropy. Perhaps anisotropy occurs first during the decay, followed later by a reduction in mixing efficiency also due to the effects of viscosity.

---

[6]The exact value of $\epsilon/\nu N^2$ needed to sustain a buoyancy flux is discussed in appendix A. Also, data with $10 < \epsilon/\nu N^2 < 100$ fall in both categories of turbulence and internal waves, suggesting that $\epsilon/\nu N^2$ is not the critical parameter to classify data as internal waves. As an additional test, the ratio $q/(\epsilon L_t)^{1/3}$ was plotted against $\epsilon/\nu N^2$ and no value of $\epsilon/\nu N^2$ could consistently separate turbulence from internal waves for all experiments
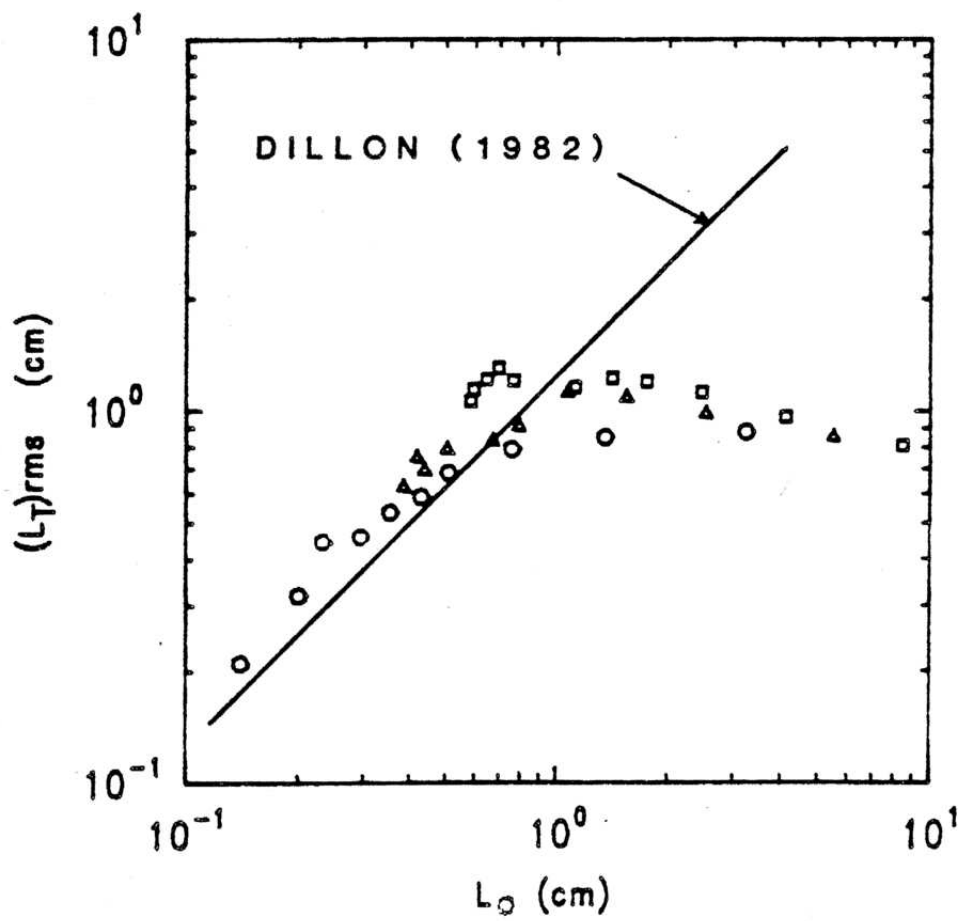
Figure 4.9: Thorpe scale L_T versus Ozmidov scale L_O evolution in a grid-turbulence turbulence experiment where both were measured. $N = 0.98$ s^{-1} ($\circ$), 0.67 s^{-1} ($\triangle$), 0.45 s^{-1} ($\square$). Experiments evolve from right to left. Figure reproduced from Itsweire (1984) (His Figure 4).
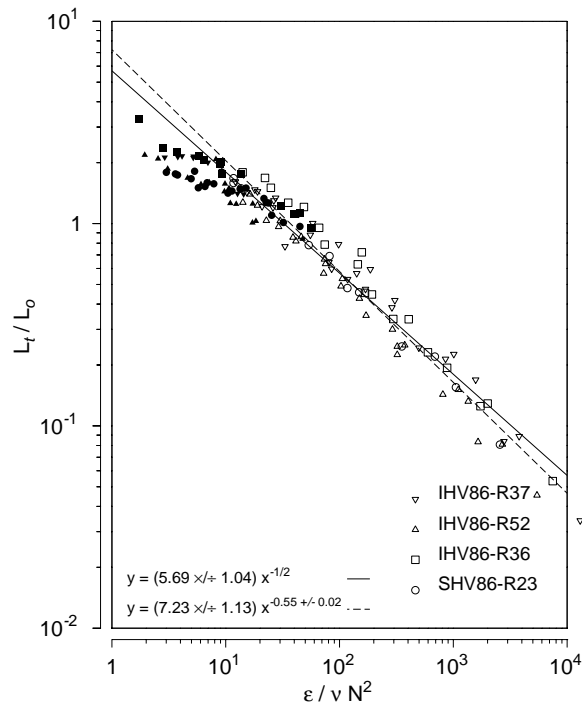
Figure 4.10: Turbulent parameter space L_t/L_O vs $\epsilon/\nu N^2$ for $q/(\epsilon L_t)^{1/3} \geq 2.2$ (filled symbols) and $q/(\epsilon L_t)^{1/3} < 2.2$ (open symbols). The $L_t/L_O \propto (\epsilon/\nu N^2)^{-1/2}$ fit (on data with $q/(\epsilon L_t)^{1/3} < 2.2$) is predicted for Gargett's (1988) theory of low vertical Reynolds number turbulence, which is discussed in appendix B. Experiments evolve from right to left.

Thus, in summary, data sets from SHV and IHV cannot provide information about the mixing efficiency during the inertial-buoyancy balanced decay because of the very low turbulent intensity at that stage of the evolution (e.g. Figure 4.2). Other sketchy data from Figure 4.8 from Rohr *et al.* (1988) and Stillinger (1981) and from Figure 4.9 reproduced from Itsweire (1984) indicate that the inertial buoyancy balance value of Ri_t is in the range of 1.4 to 1.7. Taking a middle ground value of 1.55, one obtains a maximum mixing efficiency of $\Gamma \approx Ri_t/3 \approx 0.52$ using the upper bound of (4.9). In terms of turbulent Froude number, this becomes

$$(Fr_t)_{isoIB} \approx 0.8 \tag{4.11}$$

The relation between velocity fluctuations and shear is thus given approximately by

$$u' \approx 0.4\, L_T \frac{\partial \overline{U}}{\partial z} \tag{4.12}$$

where the factor of 0.4 comes from $Ri_t = \frac{1}{a^2}\, Ri_g$ using critical values to determine a from $\frac{1}{a^2} \approx 1.55/0.25 \approx 6.2$; This factor is only known approximately. Equivently, the gradient and turbulent Richardson numbers are related approximately by

$$Ri_t \approx 6.2\, Ri_g \tag{4.13}$$

4.8 Summary and Discussion

The main results of this chapter are that

- The Kolmogorov scaling for turbulent velocity fluctuations $\epsilon \approx (u'^3/L_t)(w'/u')$, where L_t is $\rho'_e/(\partial \overline{\rho}/\partial z)$ and where $L_t\,(u'/w')$ is used to approximate the horizontal turbulent length scale, was shown to hold (to much better than a factor of two), at least for slight isotropy (w'/u' varied from 0.7 to 1). Note that turbulent velocities and length scales, buoyancy flux and TKE dissipation rates are all time-averages at various locations behind the grid. It is not obvious how these results can be extrapolated to individual overturns, or even to individual profile measurements of a steadily forced mixing layer.

- ξ is well approximated by $N^2 L_t^2/2$ in the laboratory experiments.

- Mixing efficiency was well within a factor of two modelled by $Ri_t/3$, the upper limit of the expected result for model two.

- Even though anisotropy reduces Ri_t, possibly as a result of viscosity at $\epsilon/\nu N^2 < 200$ (Gargett *et al.*, 1984), the resulting Ri_t still models the mixing efficiency well until about $\epsilon/\nu N^2 < 45$. This later value of mixing intensity is an upper limit (The actual cutt-off value could be lower), as the lab data may contain internal wave energy at this turbulent intensity. This implies that dividing the measured APEF by a decay time would be a good estimate of buoyancy flux for turbulent intensities as low as $\epsilon/\nu N^2 \approx 45$

- Large and turbulent scales are related in the following way:

  - $Ri_t \approx \frac{1}{a^2} Ri_g$, from a model relating turbulent velocity fluctuations to the mean shear and overturning scale as $u' \approx a\, L_T(\partial \overline{U}/\partial z)$, where a is a constant.

  - The constant a was shown to be related to the inertial-buoyancy balance of Ri_t, which in turn determines the maximum mixing efficiency of the model.
  The relation is such that $(Fr_t)^{-2}_{isoIB} = (Ri_t)_{cr} \approx \frac{1}{a^2}(Ri_g)_{cr}$, where $(Ri_t)_{cr}$ is the inertial-buoyancy value and $(Ri_g)_{cr} = 0.25$

  - The value of $(Ri_t)_{cr}$ is uncertain with current data, but seems to be approximately 1.55 (at best within a factor of two).
  The corresponding turbulent Froude number at isotropic inertial-buoyancy balance is $(Fr_t)_{isoIB} \approx 0.8$ This corresponds to $a \approx 0.4$ using $(Ri_g)_{cr} = 0.25$.
  This corresponds to $Ri_t \approx 6.2\, Ri_g$

The above results tend to substantiate the major assumptions and predictions of the second model of chapter 3 for isotropic growing turbulence, for which buoyancy

flux is given by ξ divided by a timescale set by turbulent overturning. This is true at least for averaged data, where redistribution of kinetic and potential energy can also be neglected. The extrapolation to single sampling profiles of a mixing layer is unclear.

Another implication is that model one, which assumes a constant mixing efficiency, would over-estimate buoyancy flux by 2 orders of magnitude in the early stages of growth in these laboratory experiments. Model one would have to be set aside if mixing efficiency (and Fr_t) is found to vary likewise in the ocean (not always at inertial-buoyancy balance), although it is likely to hold for breaking internal waves in the ocean interior.

The determination of the inertial-buoyancy balance value of Ri_t is problematic. The lab experiments are not well designed for this purpose. The initial overturn size, mostly determined from the grid mesh size, is too small relative to the Ozmidov scale $L_O = (\epsilon/N^3)^{1/2}$, which is fairly close to the final overturn size at the end of growth. Turbulent intensity falls off before turbulence fully evolves to inertial-buoyancy balance. A proper parameter range would show a knee in Figure 4.10: the increase of L_t/L_O would stop, while values of $\epsilon/\nu N^2$ would continue to decrease. The flat L_t/L_O range would correspond to the inertial-buoyancy balanced decay.

Future experiments should focus on the inertial-buoyancy balance to better quantify $(Ri_t)_{cr}$. The parameter is important because it determines the maximum mixing efficiency possible. Perhaps more importantly, $(Ri_t)_{cr}$ also determines the proportionality coefficient between the gradient Richardson number and the turbulent Richardson number.

However, these considerations assume that these results are relevant to the ocean. Questions must be answered before this can be assumed. Does the ocean mix at a wide range of turbulent Richardson numbers leading to a range in mixing efficiencies? Or does the ocean mixing layers quickly evolve to steady-state isotropic turbulence at inertial-buoyancy balance? If so, can my predicted inertial-buoyancy balance mixing

efficiency (for isotropic turbulence) of 0.5 be reconciled with Oakey's (1985) result[7] of 0.40. These questions is will addressed in the next 2 chapters.

---

[7]Oakey(1985) obtains $\Gamma = 0.265$ assuming a factor of 2 (partial) rather than 3 (full) for isotropy.

Chapter 5

Comparison of the Mixing Models in the Ocean

In this chapter, oceanic and fresh water turbulence data reported by Dillon (1982) and used again by Dillon (1984) and Dillon *et al.* (1987) are used with the following purposes in mind:

- To test the 3 models put forward in chapter 3 with oceanic data.

- To compare Dillon's models to each other. Dillon *et al.* (1987) put forward an empirical relation between buoyancy flux and ξN, but never compared it to earlier relations between the buoyancy flux and L_T and between the dissipation of turbulent kinetic energy and L_T (Dillon, 1982).

- To determine the value of the turbulent Froude number Fr_t at isotropic inertial-buoyancy-balance . This value is important because it determines the maximum mixing efficiency and the constant relating Ri_t to Ri_g.

- To determine the range of Fr_t and Γ values for oceanic turbulence to see if model two and three are really any different from model one in oceanic conditions.

The Dillon data set is divided in cases called A, B and C in this chapter. The reader is referred to appendix C for a description of the cases, and of Dillon's results. The

data were obtained at Ocean Station P during the MILE experiment (Series A and B) and at Green Peter Reservoir (Series C). All of Dillon's data are mostly temperature-stratified such that temperature Thorpe fluctuations T' will be used instead of using density fluctuations ρ' (see appendix C). The turbulent Froude number Fr_t was not measured by Dillon, but layer-averages for ϵ, N, and L_T will make it possible to extract Fr_t and to calculate the buoyancy flux predicted by the models. Measurement of the dissipation of temperature variance χ_θ are also available for the layers. These can be related easily to the potential energy dissipation. The approximation that this term equals J_b is made throughout this chapter. Buoyancy flux predictions can then be compared to overturn-scale observations.

5.1   Calculation of N^2

The APEF must be evaluated to compare model predictions for J_b from chapter 3 to observations. Dillon first defined the APEF in his 1984 paper; it is not tabulated in his 1982 paper along with other layer-averaged quantities. An approximation must therefore be made using the stratification against which work is done by overturning. However, this stratification definition may differ from the large scale stratification used, for example, in parameterizing mixing rates in terms of K_ρ. Dillon's layer averages are examined here to determine if his tabled values of N^2 are large scale parameterization or representative of the overturns.

In Chapter 2, it was shown that ξ was well approximated by $N^2 L_T^2/2$ when $N^2 = (g/\overline{\rho})\,\partial\rho/\partial z$ is calculated by a least-squares fit on the re-ordered density profile of an overturn. However, a larger-scale parameterization with N obtained over a span containing non-overturning portions led to overestimating ξ by a factor of 2 to 2.4 for the layer, since the stratification is lower within overturns[1]. Dillon calculated N^2 over 50 cm segments of the re-ordered profiles, and averaged together the segments associated with overturns, sometimes enclosing 25–50 cm outside of the overturns.

---

[1]Crawford (1986) does a similar analysis and finds that ξ is overestimated by a factor of 2.8 when bulk stratification is used.

When the span of an individual overturn was not obvious, parameters were averaged over a depth span of similar statistical distributions. Thus the averaging spans of data tabled by Dillon (1982) should be somewhere in between overturn spans and a large-scale parameterization.

In chapter 2, it was shown that if $L_T \approx \overline{T'^2}^{1/2}/(\partial \overline{T_o}/\partial z)$ then $\partial \overline{T_o}/\partial z$ was representative of overturns instead of larger scales (In chapter 2, density fluctuations were used instead of temperature). Figure 5.1[2] tests this, using values of $\partial \overline{T_o}/\partial z$, L_T and T'. There is little scatter for the two oceanic cases A and B, with an average on the mean of $\partial \overline{T_o}/\partial z = 1.85\,\overline{T'^2}^{1/2}/L_T$. (from $\overline{T'^2}^{1/2}/L_T = 0.54\,\partial \overline{T_o}/\partial z$, since regressions were performed minimizing variance in the ordinate) In Chapter 2 statistics on a mixing patch in the St. Lawrence estuary yielded $\partial \overline{T_o}/\partial z = 0.93\,\overline{T'^2}^{1/2}/L_T$ when $\partial \overline{T_o}/\partial z$ was evaluated over distinct overturns, and $\partial \overline{T_o}/\partial z = 2.14\,\overline{T'^2}^{1/2}/L_T$ when $\partial \overline{T_o}/\partial z$ was evaluated over spans enclosing many overturns. Thus the data in Series A and B seem to have been evaluated over spans which include sharper gradients than those found within the overturns. Series C, the fresh water case, has many points with $\partial \overline{T_o}/\partial z$ greatly exceeding $\overline{T'^2}^{1/2}/L_T$. This can lead to great errors in the models put forward in this chapter, as well as in the estimated measured buoyancy flux $\alpha g \chi_\theta/2(\partial \overline{T}/\partial z)$.

Because N^2 is representative of larger scales than overturns, the APEF approximation $N^2 L_T^2/2$ is expected to over-estimate by a factor of 2 (from the above comparison of $\overline{T'^2}^{1/2}/L_T = 0.54\,\partial \overline{T_o}/\partial z$). Verifying the buoyancy flux models from chapter 3 using this approximation would result in extra scatter. The only APEF approximation using larger scale averages that was shown to work in chapter 2 is $\xi \approx (1/2)(g/\overline{\rho})\overline{\rho'^2}^{1/2}L_T$. We will show in the next section that this relation does in fact lead to less scatter compared to buoyancy flux.

---

[2]The regressions shown in Figure 5.1, as well as in all log–log figures in this chapter, are performed in logarithmic space. The confidence interval on the mean is expressed as $10^{a \pm ci} = 10^a \,{}^\times\!/_{\div}\, 10^{ci}$.
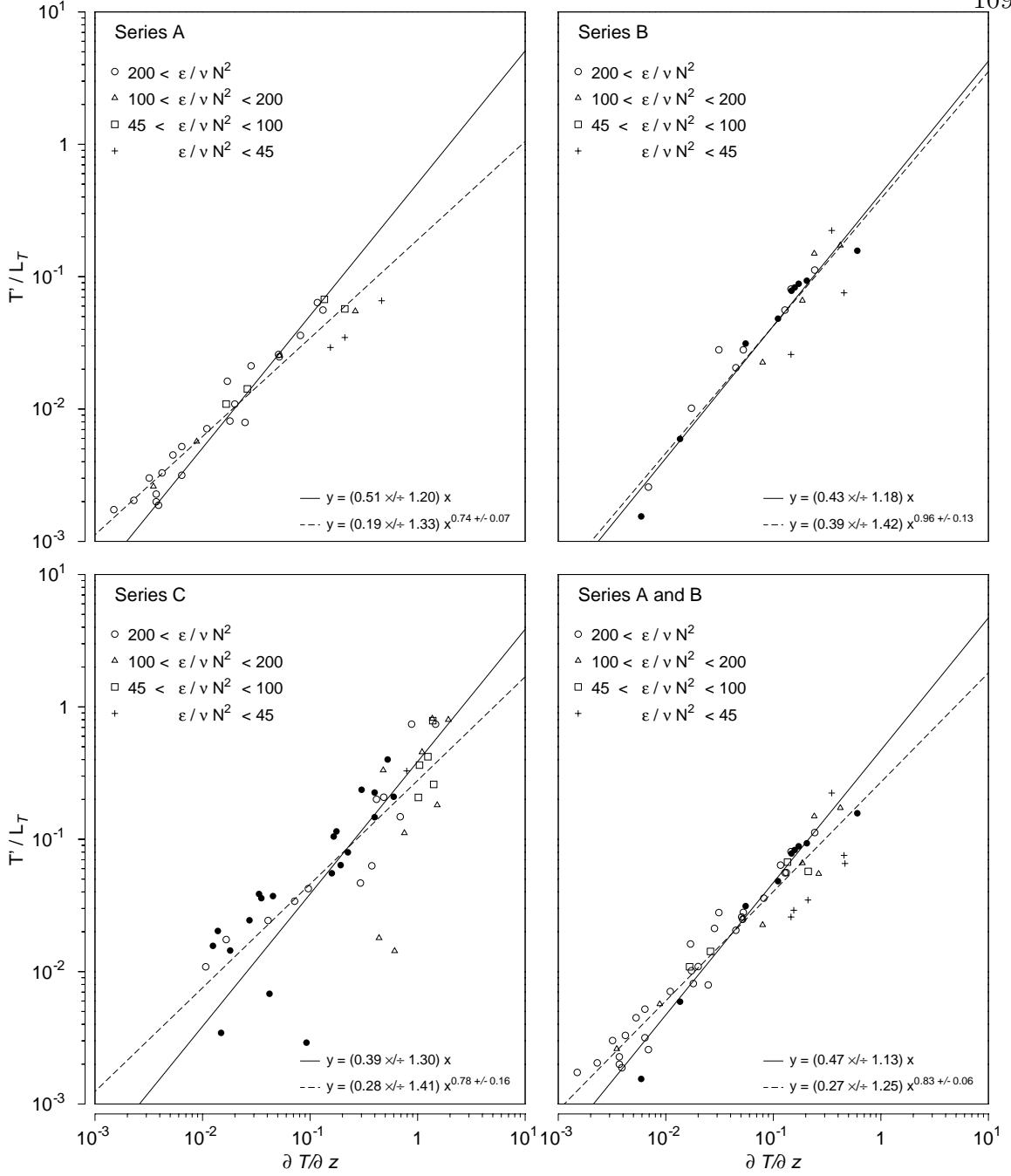
Figure 5.1: Comparison of estimated temperature gradient within overturns $\overline{T'^2}^{1/2}/L_T$ to measured gradient $\partial \overline{T_o}/\partial z$ for two oceanic cases (Series A and B) and a fresh water reservoir (Series C). The gradient $\partial \overline{T}/\partial z$ is evaluated on the re-ordered profile over overturn-containing spans; $\overline{T'^2}^{1/2}/L_T$ is an estimate of the local gradient within the overturns and is found to be lower than $\partial \overline{T_o}/\partial z$. Data are classified by turbulent intensity $\epsilon/\nu N^2$. Open symbols are well resolved; filled symbols are marginally resolved. Regression are on points with $\epsilon/\nu N^2 > 200$. Data are from tables in Dillon (1982).

5.2 Dillon's Relations

In this section, the models inferred from Dillon's relations L_T–L_O and L_T–L_B (explained in appendix B) are examined more closely and discussed. Dillon compared the L_T–L_O and L_T–L_B relations, but did not compare his later $J_b = 4.8\,\xi\,N$ model to the first two. His first two models are related to the APEF and its commonly used approximation $N^2 L_T^2/2$.

The results of chapter 2 will be confirmed, showing that the density gradient within overturns is well approximated by bulk properties as $\overline{\rho'^2}^{1/2}/L_T$, such that the APEF approximation $N^2 L_T^2/2$ works well by substituting that gradient into the expression for N^2. Also confirmed will be that $N^2 L_T^2/2$ over-estimates ξ by a factor of two if a bulk N^2 is used.

Of Dillon's relations, the one that best matches his data will be determined, such that it can be related to and compared to the models from chapter 3.

5.2.1 Relationship Between ϵ and L_T

The relation $L_T/L_O = 1.17$ was found to hold for oceanic series B (see appendix B, Figure C.1) Substituting the definition of $L_O = (\epsilon/N^3)^{1/2}$ leads to

$$\epsilon \approx 0.7 L_T^2 N^3 \tag{5.1}$$

using N^2 calculated over a larger scale than that of the overturns.

This is identical to the first model from chapter 3 (apart from the coefficient): the traditional view relating overturns to mixing.

5.2.2 Buoyancy Flux Relation to Thorpe Scale

Dillon's relation $L_T/L_B = 1.23$, where $L_B = (J_b/N^3)^{1/2}$ leads to

$$J_b \approx 0.65 L_T^2 N^3 \tag{5.2}$$

Comparing (5.1) to (5.2), the combined data sets have an average mixing efficiency $\Gamma = J_b/\epsilon$ of order unity. This high value compared to other oceanic observations of Γ (e.g. Oakey (1985)) will be discussed in section 5.5.

Both relations inferred from Dillon are compared in the top two panels of Figure 5.2. Comparing top and middle panels suggests that the Thorpe scale is a better predictor of buoyancy flux than of dissipation, especially for Series A and C where the mixing efficiency is much lower. The L_O–L_T relation seems to depend on a constant mixing efficiency, as Dillon suggested (See appendix C).

5.2.3 Test of the Models

The term $L_T^2 N^3$ in (5.2) could be interpreted as $2\xi N$ since ξ is often approximated as $L_T^2 N^2/2$. We would now like to test which of $J_b \propto L_T^2 N^3$ or $J_b \propto \xi N$ results in a better description of the data, as $J_b \propto \xi N$ corresponds to our model three and Dillon *et al.*'s (1987) empirical result. Dillon did not table values of ξ, so that an approximation must first be chosen. The actual coefficients in the models will be discussed later.

Bulk stratification N^2 greatly over-estimates overturn stratification for points with $(\overline{T'^2}^{1/2}/L_T)/(\partial\overline{T}/\partial z) < 0.2$ in the middle panels of Figure 5.2.[3] For these points, $L_T^2 N^3$ consistently over-estimates J_b (middle panels) because N appears to a higher power then in the lower panels. This implies that the stratification local to the overturns is a more relevant factor. The approximation of ξ in the lowest panels of Figure 5.2 uses $\xi = N^2 L_T^2/2$ with a local stratification N^2 estimated as $N^2 = \alpha g \overline{T'^2}^{1/2}/L_T$. The approximation is $\xi = (\alpha g/2)\overline{T'^2}^{1/2} L_T$, shown in chapter 2 to be best for layer averaged Thorpe quantities.

Consistent with the results of chapter 2, the estimated APEF from $L_T^2 N^2/2$ is 1.9 times higher than from $(\alpha g/2)\overline{T'^2}^{1/2} L_T N$ by comparing the middle and lower panels of Figure 5.2. To see which of the two approximations is accurate, at

---

[3]The ratio $(\overline{T'^2}^{1/2}/L_T)/(\partial\overline{T}/\partial z)$ is not affected by a reduction in L_T by averaging overturns along with non-overturning regions, because $\overline{T'^2}^{1/2}$ is reduced in exactly the same manner.
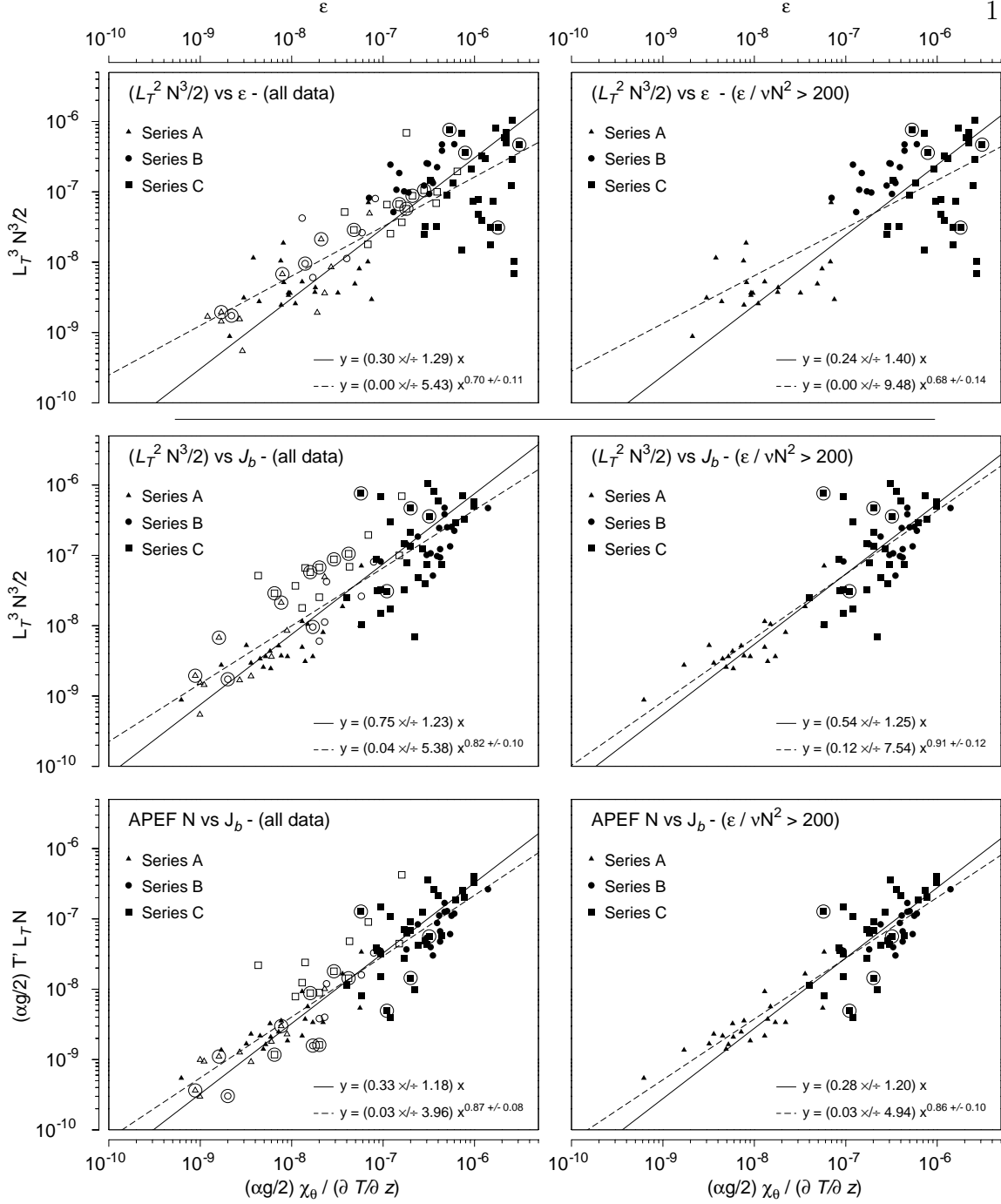
Figure 5.2: Comparison of models inferred from Dillon's results. The top two panels compare $(L_T^2 N^3/2)$ to ϵ. The middle two compare $(L_T^2 N^3/2)$ to the estimated buoyancy flux. The bottom two compare (ξN) to estimated J_b approximating ξ as $(\alpha g/2)\overline{T'^2}^{1/2} L_T$. Data are coded by the data set, by turbulent intensity (open symbols have $\epsilon/\nu N^2 < 200$; solid symbols have $\epsilon/\nu N^2 > 200$) and circled data have $(\overline{T'^2}^{1/2}/L_T)/(\partial \overline{T}/\partial z) < 0.2$. The left-hand side panels include all data and the right-hand side ones include only data with $\epsilon/\nu N^2 > 200$.

least in an average sense, we compare it to Dillon *et al.*'s (1987) calculation of a mean $(\alpha g \chi_\theta / 2 \partial \overline{T} / \partial z) / (\xi N)$ ratio, using the definition form of the APEF. Here I am assuming that buoyancy flux equals the dissipation of potential energy $J_b = (\alpha g / 2) \chi_\theta / (\partial \overline{T} / \partial z)$ (e.g. Equation (3.10) assuming that the time-derivative is zero); Dillon *et al.* (1987) did not require this assumption, comparing ξN to the dissipation of potential energy without assumptions about J_b. Dillon *et al.* (1987) found $J_b / (\xi N) = 4.8$ (replacing the dissipation of potential energy by simply J_b in the notation, whereas a similar calculation in linear space yields $J_b / (\alpha g / 2) \overline{T'^2}^{1/2} L_T N$ $= 4.38$. This indicates that $(\alpha g / 2) \overline{T'^2}^{1/2} L_T$ is a good approximation of ξ, and that $N^2 L_T^2 / 2$ is an over-estimate by a factor of two, as predicted from Figure 5.1.

Comparing the middle and lower panels of Figure 5.2 tests which of $J_b \propto L_T^2 N^3$ or $J_b \propto \xi N$ results in the better fit. Note that even in the ξN panel, there is a slight bias toward over-estimating J_b for data with $\epsilon / \nu N^2 < 200$, although this is mostly true in Series C, the fresh water case. Those data have been removed from the least squares fit regression in the right-hand panels. Since data with $(\overline{T'^2}^{1/2} / L_t) / (\partial \overline{T} / \partial z) < 0.2$ yield a better fit in the lower panels of Figure 5.2 than in the middle panels, and that the fit for all data appears (judged by eye only, as the statistics only yield confidence errors on the mean, not information on the variance explained by the regression) to be generally better in the lower panels, we conclude that using a better approximation of ξ appears to result in a better fit to J_b using a decay time of N^{-1} for the APEF.

Dillon *et al.*'s (1987) last relation for buoyancy flux from the APEF, as $J_b = 4.8 \, \xi N$ is then his best fitting for buoyancy flux. The L_T–L_O relation is incidental. It requires that the mixing efficiency is constant, which is not a general result (see Appendix C and Figure 5.4 for details).

5.3 Comparison of Models Two and Three to Dillon's Data

Dillon's best-fitting relation to his data is $J_b = 4.8\,\xi\,N$ (assuming that the buoyancy flux equals the potential energy dissipation). Except for the coefficient, this is my third model, describing turbulence at inertial-buoyancy where the horizontal turbulent length scale has evolved to the Ozmidov (inertial-buoyancy) length scale L_O.

Let us now compare Dillon's data to both my second and third models. The aim is to see if one is preferable to the other for Dillon's data.

As just discussed, the third model is written as

$$J_b = \left[\frac{3}{4} \pm \frac{1}{4}\right] \xi\,N = \left[\frac{3}{4} \pm \frac{1}{4}\right] \frac{\alpha g}{2}\overline{T'^2}^{1/2} L_T\,N \tag{5.3}$$

The discrepancy between the model's coefficient and that of Dillon *et al.*'s (1987) result of $J_b = 4.8\,\xi\,N$ will be discussed later.

5.3.1 Model Two Re-derived

To compare data with model two, it must be written in a form which minimizes approximations. Recall that the second model describes growing isotropic turbulence. It is written as

$$J_b = \left[\frac{3}{4} \pm \frac{1}{4}\right] \frac{2}{3} \xi\,N\,Fr_t \tag{5.4}$$

Unfortunately, the turbulent Froude number is not (usually) a measured quantity in the ocean, nor was it in Dillon's data. Since ϵ was measured and ξ can be approximated, a form such as (3.23) could be used to infer Fr_t and yield (3.24) as the second model's buoyancy flux. However, the derivation of (3.23) assumed that ξ was well approximated by $N^2 L_T^2/2$ which has be shown not to be true for this data set.

A buoyancy flux prediction for the second model is now derived using approximations that best employ the data available. Using the scaling $\epsilon \approx u^3/L_T$ which

has been shown to hold quite well for grid-turbulence (this model assumes isotropy, $L_T = L_h$), the tubulent Froude number can be written

$$Fr_t = \frac{u'}{NL_T} = \frac{\epsilon^{1/3}}{NL_T^{2/3}} \tag{5.5}$$

such that the APEF approximation $N^2 L_T^2/2$ usually used is avoided. Combining (5.4) and (5.5), and using the better APEF approximation $\xi = (\alpha g/2)\overline{T'^2}^{1/2}L_T$, we obtain an expression for the buoyancy flux of the second model as[4]

$$J_b = \left[\frac{3}{4} \pm \frac{1}{4}\right] \frac{\alpha g}{3} \overline{T'^2}^{1/2} L_T^{1/3} \epsilon^{1/3} \tag{5.6}$$

5.3.2 Comparisons of the Models

The grid-turbulence experiments agreed with the upper bound of the second model in chapter 4. In that case, the turbulence was obviously growing because it is created at small scales by a grid. In the ocean, the state of the turbulence is *unknown* and either the isotropic growing turbulence model, or the steady-state inertial-buoyancy balance model could hold.

The upper bound of the buoyancy flux predictions (5.3) and (5.6) are compared to the measured potential energy dissipation in Figure 5.3. Differences are subtle, especially if only high turbulent intensity data are considered (see right hand panels). It would be difficult to convince anyone to use one model rather than the other with the slight gains that would be afforded. It is possible that the dynamics of the mixing layers is sometimes appropriate to the second model (growing turbulence) and some other times appropriate to the third (steady-state). Data from case C appear to have less scatter in the the second model ($J_b \propto \xi N Fr_t$). The next section investigates model differences further.

---

[4] The N cancels out by combining (5.4) and (5.5) to obtain (5.6), but in fact it never enters the equation when it is considered using the decay time. Starting with $J_b = \left[\frac{3}{4} \pm \frac{1}{4}\right] \xi t_o^{-1}$, where $t_o = (3u'^2/2)/\epsilon$, the same substitution used in (5.5) gives $t_o^{-1} = (2/3)L_T^{2/3}\epsilon^{-1/3}$. Buoyancy flux is then given by (5.6) without ever using N. This means that (5.6) is not sensitive to large scale parameterisation of $N^2 = \alpha g(\partial \overline{T}/\partial z) \neq \alpha g(\overline{T'^2}^{1/2}/L_T)$.
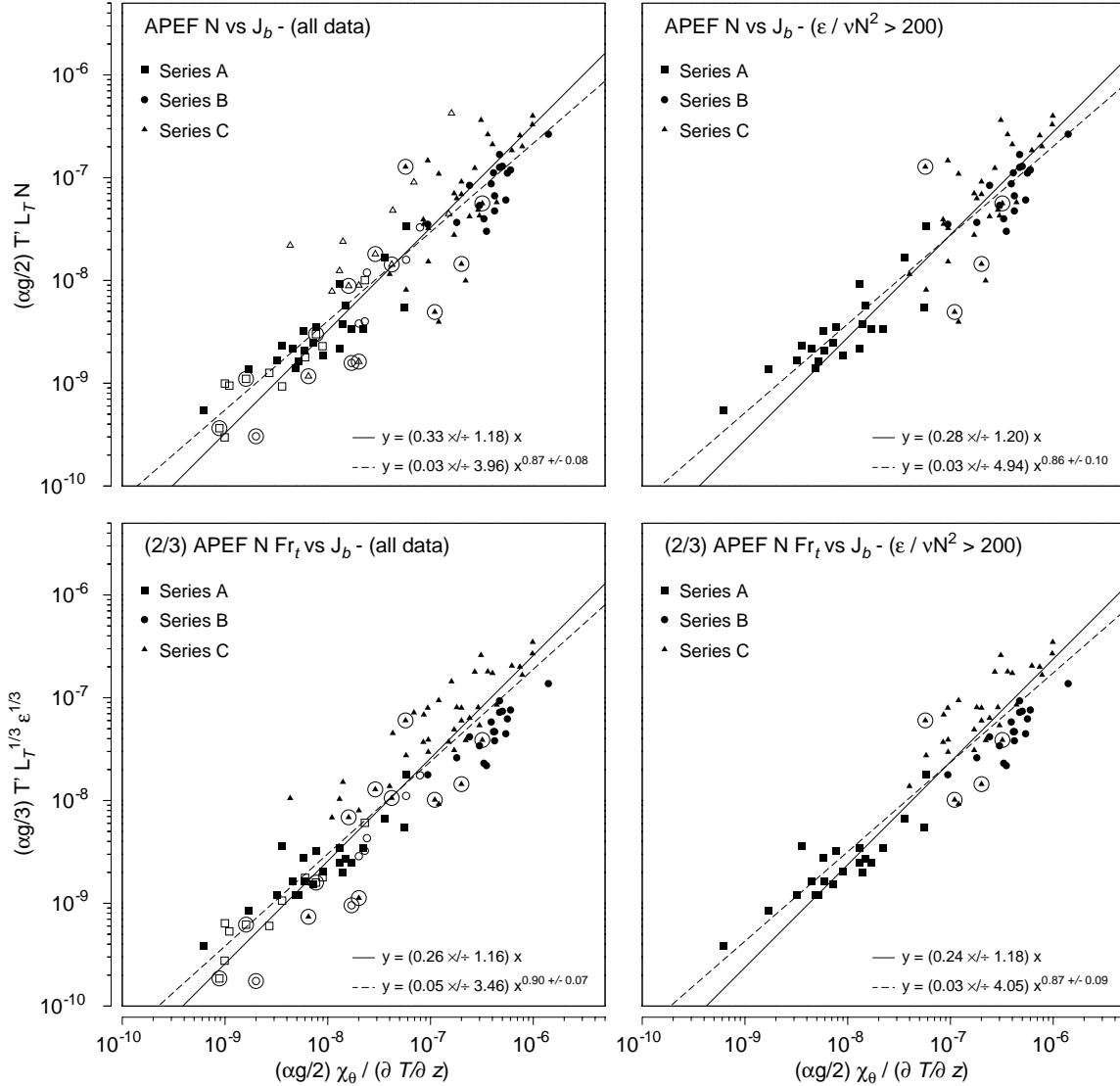
Figure 5.3: Comparison of two derivations of the buoyancy flux models from Chapter 3. The top two panels compare (ξN) to J_b approximating ξ as $(\alpha g/2)\overline{T'^2}^{1/2}L_T$ (and J_b is approximated by the dissipation of potential energy in all panels). The bottom panels compare $((2/3)\xi N Fr_t)$ to J_b, where $(2/3)\xi N Fr_t$ is best approximated by $(\alpha g/3)\overline{T'^2}^{1/2}L_T^{1/3}\epsilon^{1/3}$ for Dillon's tabled data. Data are coded by the data set, by turbulent intensity (open symbols have $\epsilon/\nu N^2 < 200$; solid symbols have $\epsilon/\nu N^2 > 200$) and circled data have $(\overline{T'^2}^{1/2}/L_T)/(\partial\overline{T}/\partial z) < 0.2$. The left-hand side panels include all data and the right-hand side ones include only data with $\epsilon/\nu N^2 > 200$.

5.4 Comparison of Mixing Efficiencies

The main difference in the predictions between the isotropic growing turbulence model (5.4) and the anisotropic fully developed turbulence model (5.3) is that the first is dependent on Fr_t and the other is not; this translates to one being dependent on ϵ in (5.6) and the other not in (5.3). The models predict similar buoyancy fluxes only where physics converges: at inertial-buoyancy balance and at isotropy. Both of these parameters determine the ratio $L_T^2/(L_O^{4/3}L_h^{2/3})$ which quantifies the mixing efficiency for both models. Comparison of the mixing efficiencies predicted by the two models with the measured mixing efficiency should highlight any differences between models.[5]

Model 2; Isotropic Case

For the isotropic model, the predicted mixing efficiency is written as

$$\Gamma = \left[\frac{3}{4} \pm \frac{1}{4}\right] \frac{\alpha g}{3}\overline{T'^2}^{1/2}L_T^{1/3}\epsilon^{-2/3} \tag{5.7}$$

using $\Gamma = J_b/\epsilon$ and (5.6).

Model 3; Steady-State Case

For the steady-state inertial-buoyancy balance model, the predicted mixing efficiency is

$$\Gamma = \left[\frac{3}{4} \pm \frac{1}{4}\right] \frac{\alpha g}{2}\overline{T'^2}^{1/2}L_T\, N\, \epsilon^{-1} \tag{5.8}$$

using (5.3).

---

[5]If the $L_O = (\epsilon/N^3)^{1/2}$ parameterisation were done using N local to overturns, two relations for mixing efficiency could easily be compared: $\Gamma = (L_T/L_O)^{4/3}/3$ for the isotropic case and $\Gamma = (L_T/L_O)^2/2$ for the non-isotropic case. Unfortunately, a correction must be made because $\partial\overline{T}/\partial z \neq \overline{T'^2}^{1/2}/L_T$. The analysis becomes complicated and, as it turns out, is not conclusive. It is therefore not included here.

5.4.1 Predicted Mixing Efficiency Comparison

In Figure 5.4, the model predictions are compared to the measured mixing efficiency. The regressions have large confidence intervals on the slopes, and so were also performed by least squares on the abscissae as well as on the usual ordinates. The geometric mean of the two slopes yields the 'geometric mean of the function regression of the ordinate on the abscissa', also called the GM regression (Ricker, 1973). It represents a better estimate of the slope if errors exist in both the abscise and the ordinate.

The predicted and measured mixing efficiency have a GM regression power law very close to unity for the combined series A and B using the third model (Figure 5.4D, highlighted). Using this criterion, the steady-state model three is a better predictor for those data. Forcing a power law of unity, the best fit is

$$\Gamma_{\text{model 3}} = (0.28^{\times}/_{\div} 1.21)\, \Gamma_{\text{measured}} \tag{5.9}$$

However, series C is not well fitted by either model. The model coming closest to a one-to-one power law is the isotropic model (Figure 5.4A, highlighted). The GM regression is a power law of 1.2. Forcing a power law of unity, the best fit for series C is

$$\Gamma_{\text{model 2}} = (0.31^{\times}/_{\div} 1.27)\, \Gamma_{\text{measured}} \tag{5.10}$$

In conclusion, Series A and B are quite different from Series C. Oceanic series A and B are found to marginally match predictions for the buoyancy flux model derived from the APEF dissipated in a time scale N^{-1}, at least within a multiplicative constant. Fresh water series C data have more scatter, and could be marginally associated with the isotropic turbulence model of growing turbulence.

In both cases, the predicted mixing efficiency is 3 times lower than the measured mixing efficiency. This is discussed next.
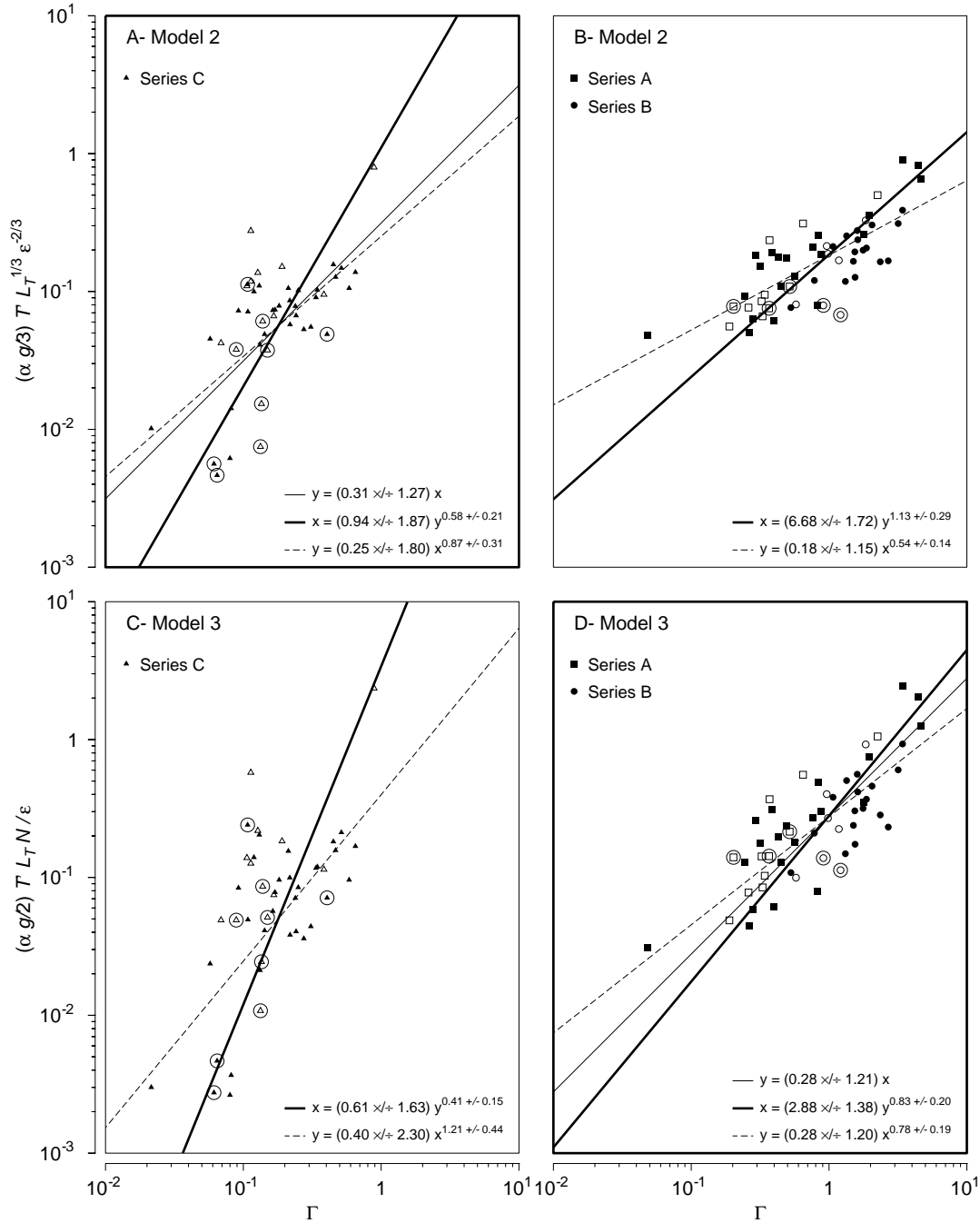
Figure 5.4: Mixing Efficiency compared to Models. **A-** Second model mixing efficiency prediction versus measure mixing efficiency for series C. GM regression has $\Gamma_{model} \propto \Gamma^{1.2}$; **B-** Second model for series A and B. GM regression has $\Gamma_{model} \propto \Gamma^{0.7}$; **C-** Third model for series C. GM regression has $\Gamma_{model} \propto \Gamma^{1.7}$; **D-** Third model for series A and B. GM regression has $\Gamma_{model} \propto \Gamma^{0.97}$; All regression are on data with $\epsilon/\nu N^2 > 200$. Thick lines are x regressed on y; thin lines are y regressed on x, solid lines have forced slope and dashed lines have best fitting slopes. Highlighted panels A and D indicate best fitting model.

5.5 Possible Bias in the Dillon Data Set

If both the buoyancy flux and mixing efficiency of Dillon's data are much higher than predicted by either the second or third model, then either the models are wrong or the data set is biased. While the mean mixing efficiency of the data set is close to unity, many individual values are above 1. In fact, 24 of the 56 data points of Series A and B have $\Gamma > 1$.

Oakey (1985) obtains Γ from simultaneous measurements of both χ_θ and ϵ in 275 10–15 m blocks. He finds values ranging from 0.01 to 1, with a mean of 0.265 (assuming a log-normal distribution) and one standard deviation confidence interval as $0.066 < \overline{\Gamma} < 0.436$.[6] Thus, Dillon's mixing efficiency seems high in comparison.

Possible bias could come from errors in $\partial\overline{T}/\partial z$, ϵ or χ_θ. These will be considered in turn, although it must be emphasized that there is no proof that any of Dillon's data are biased; they simply do not match models shown here, and have unusually high mixing efficiencies.

5.5.1 Possible Bias in $\partial\overline{T}/\partial z$

The stratification $N^2 = \alpha g(\partial\overline{T}/\partial z)$, averaged over a layer containing many overturns, has been shown to over-estimate the re-ordered density gradient within overturns, such that $\overline{T'^2}^{1/2}/L_T > \partial\overline{T}/\partial z$. An APEF approximation insensitive to this error was used, but a multiplication by an uncorrected N remains in the third model expression for mixing efficiency (5.8).

A rationale for the better APEF approximation used is as follows: if overturning statistics are averaged within a bin, but the APEF comes from one overturn within that bin, then using $\overline{T'^2}^{1/2}/L_T$ to approximate the overturn's density gradient makes

---

[6]Oakey uses a lower isotropy coefficient, namely $J_b = (\alpha g/3)\chi_\theta/(\partial\overline{T}/\partial z)$ such that his values should be multiplied by 1.5 to be compared with Dillon's. Alternatively, Dillon's values could be adjusted to Oakey's. We choose here to assume full isotropy for consistency with earlier derivations which assumed it also.

more sense than using $\partial \overline{T}/\partial z$. The same argument could be used for the the dissipation of potential energy. If all the temperature fluctuation variance is dissipated within that overturn as well, then the dissipation of potential energy $\propto (\partial \overline{T}/\partial z)^{-1}$ should be better approximated substituting $\overline{T'^2}^{1/2}/L_T$ for $\partial \overline{T}/\partial z$.

Unfortunately, if $\overline{T'^2}^{1/2}/L_T$ is used in place of $\partial \overline{T}/\partial z$ in the calculation of the dissipation of potential energy and the buoyancy flux expression of the third model (5.3), then the discrepancy increases further between (5.3) and the dissipation of potential energy. This correction could not bring Dillon's data in line with models two and three.

5.5.2 Possible Bias in ϵ

Let us consider the possibility that dissipation of turbulent kinetic energy is underestimated. The buoyancy flux prediction from the third model (5.3) is not a function of ϵ. Therefore, ϵ adjustments have no effect on fits with observations, either in terms of buoyancy flux or mixing efficiency.

On the other hand, the buoyancy flux of the second model (5.6) is proportional to $\epsilon^{1/3}$. The model's buoyancy flux must be increased by a factor of three to fit the observations. This requires an increase of ϵ by a factor 27, and would make mixing efficiencies 27 times lower. This is such a large factor that it is unlikely that Dillon's observed mixing efficiency can be brought into line with the models by presuming that a bias in ϵ exists.

5.5.3 Possible Bias in χ_θ

Changes in χ_θ have no bearing on predictions of buoyancy flux or mixing efficiency for either model. Therefore, all observations of buoyancy flux and mixing efficiency would be consistent with the models, and with Oakey's observations of mixing efficiency, by reducing χ_θ by a factor of 3.

Dillon (1982) approximates his error level in χ_θ as 30%. This is of course not compatible with my suggestion that χ_θ is over-estimated by a factor of 3. Nevertheless,

for Dillon to be correct about both χ_θ and ϵ implies that he has measured a mean mixing efficiency of order unity and measured maximum values of ≈ 4. These numbers are unusually high (*e.g.* Oakey (1985) obtains Γ from 0.01 to 1, with a mean of 0.265). Note that Marmorino (1991) plotted observations of L_T versus $(\kappa_T C_x/N)^{1/2}$, equivalent to showing $\frac{1}{2}L_T^2 N^3$ versus $N^2 \kappa_T C_x$, and obtained values of $N^2 \kappa_T C_x$ from half to a tenth of the values of Dillon. These arguments taken together suggest that Dillon's measurements of χ_θ are over-estimated by a factor of 3. If this were the case, series A and B would then be consistent with my third model, and series C would be marginally consistent with my second model.

5.6   Summary

In this chapter, the buoyancy flux models of chapter 3 were tested on Dillon's data sets consisting of two oceanic cases (Series A and B) and one fresh water reservoir (Series C). The results are summarized as follows:

- Dillon's (1982) verification of the Ozmidov scale L_O relation to the Thorpe scale L_T holds only for series B. In that case the turbulent Froude number Fr_t, and therefore the mixing efficiency, does not vary much. This is equivalent to model one discussed in chapter 3, relating the rate of dissipation of turbulent kinetic energy to ξN. It is not a general result because it fails in series A and C, with surface mixed layer data. This is not a new result as Dillon (1982) noted this, but it is included here to contrast model one with models two and three.

- Dillon's layer averages were shown to include non-overturning parts of the water column. The stratification listed by Dillon over-estimates stratification local to overturns. The APEF approximation $N^2 L_T^2/2$ is an over-estimate by a factor of 2 to 3 for this data.

  - As a corollary, the ratio of L_T/L_O is ambiguous even when used to quantify

the inertial-buoyancy balance value; this usage was discussed for grid-turbulence. The reason is that the value of $L_O = (\epsilon/N^3)^{1/2}$ obtained depends on how N^2 is evaluated. In this case, N^2 is a layer-average (see section 5.1). For the lab experiments, it measured the stratification that overturns worked against. This makes comparisons difficult.

- Dillon *et al.*'s (1987) empirical relation $J_b = 4.8\xi N$ better fits his data than earlier models $\epsilon \propto L_T^2 N^3$ and $J_b \propto L_T^2 N^3$. In the second case, it is because $N^2 L_T^2/2$ only approximates ξ. Dillon *et al.*'s (1987) empirical relation is consistent with the third model, except for a much higher coefficient used by Dillon *et al.* (1987).

- Dillon's series A and B are consistent with the third model, which assumes inertial-buoyancy balance. The Ozmidov scale L_O is the horizontal turbulent length scale L_h, generally greater than the Thorpe scale L_T representing the vertical turbulent length scale. The buoyancy flux is related to the decay of the APEF over a time scale N^{-1}.

- Dillon's fresh water series C is somewhat consistent with the second model. It describes growing isotropic turbulence. The buoyancy flux is related to the decay of the APEF over a time scale $(3/2)L_T^{-2/3}\epsilon^{1/3}$.

- While both models are consistent with different parts of the data, the predicted buoyancy flux for both models is a factor of 3 smaller than the observations. The mean mixing efficiency is of order unity, much higher than is normally observed. It is suggested here that his values of χ_θ are too high by a factor of 3. It is suggested that Dillon *et al.*'s (1987) relation not be used until this possibility is clarified because it is based on this likely over-estimate. The decay time of models two and three cannot be increased by a factor of three to accommodate Dillon's data because it is set equal to the decay time of the turbulent kinetic energy, and there is no physical basis for such an increase. Also, the decay time used in model two matches grid-turbulence results.

- Figure 5.4 shows that measured mixing efficiency (even if 3 times too high) varies by 2 orders of magnitude over the 3 series. This suggests that the first model $L_T \approx L_O$ should generally not be used for oceanic turbulence in strongly forced cases.

  The great range of mixing efficiencies found from Dillon's data can be mostly explained not by a lognormal distribution and some form of intermittency, but rather by the effect of Fr_t on the turbulence. It would be very interesting to see if Oakey's (1985) observed variations could also be explained by this model.

  - With over 2 decades of variations of mixing efficiency observed in Figure 5.4, the turbulent Froude number varies by one decade. The difference between the buoyancy fluxes of the second and third models is then a factor of 10 (see Figure 5.3, series C for models two and three).

- The maximum turbulent Froude number (at isotropic inertial-buoyancy balance) cannot be easily extracted from Dillon's data. Buoyancy flux estimates are possibly too high by a factor of 3, and model predictions have a lot of scatter versus observations. The maximum mixing efficiency could be greater than 1, indeed greater than expected in chapter 4 (≈ 0.50). It is clear that most data are not at inertial-buoyancy balance, making it more difficult to determine its value, and a better proportionality coefficient between Ri_t and Ri_g (see chapter 4).

The data presented here show that model one is not a general result and should be discarded in strongly mixed oceanic regimes. It may still apply to internal wave breaking through K-H instability, although no such example is clearly shown in this thesis. Without an indication of the state of the turbulence, it is difficult to determine which of model two or three should be used. Using the wrong one introduces errors in the estimation of buoyancy flux, but none as great as assuming a constant mixing efficiency of one quarter since it varies by two orders of magnitude.

Chapter 6

Emerald Basin: A Test Case

An oceanic test case for the buoyancy flux model was shown in chapter 5 using Dillon's tabled results (Dillon, 1982). A few unanswered questions are briefly tackled in this chapter using data from Emerald basin made available by Hans Van Haren from the Dawson 90014 Boundary Layer Study (Oakey, 1990).

Dillon's data were averaged within mixing layers where both overturning scales and dissipation were well resolved. Interpretation of the results is limited in a few ways:

- Dillon's averaging depth spans included non-overturning spans where stratification is greater than within the overturns. Thus, the amount of data averaging is uncertain. Does averaging over single overturns compare well with 10-m averages (similar to what Dillon tabulated)?

- Finestructure and microstructure parameters were only compared by Dillon in layers where both were resolved (for obvious reasons). Yet if measurements of overturning are to replace microstructure measurements (in energetic cases) it must be known how successfully they can be interpreted without a-priori knowledge of the dissipation. Two questions address this issue:

  How much of the rate of dissipation of TKE is accounted for by overturning?

  How much of the overturning is accounted for by the rate of dissipation of TKE?

This kind of 'negative' information, telling us how well the methods fair globally, is very useful because it quantifies how well one quantity maps to the other.

- Are there any difficulties in identifying overturns? Dillon's tabulated data were already layer-averages; I have not yet shown an application where I have identified overturns and discussed difficulties.

The last point about difficulties in identifying overturns concerns mainly sampling problems. Indeed, temperature is often used instead of density to measure overturning events. This is because measuring temperature requires only one sensor, while the calculation of density requires the combination of temperature and conductivity data. To get an accurate density reading, the temperature and conductivity must be measured as close together in space and time as possible, so that the temperature of the water in the conductivity cell is as close as possible to that measured by the temperature sensor. Also, the frequency response of the sensors must also be closely matched. For these reasons, density is more difficult to measure within overturning events where spatial gradients of temperature and density are enhanced. Thus temperature is often used instead, presuming a tight T–S relation exists. But if the T–S relation is not tight, stable temperature inversions can be falsely interpreted as overturns. These concerns will be addressed briefly in this chapter, and in greater details in chapter 7.

6.1   Emerald Basin Microstructure Data

The Emerald Basin experiment was conducted October 9th to 16th 1990 to study boundary layer mixing processes on the western edge of Emerald Basin. The site was chosen for its bottom slope of between 1 and 2% and little along-isobath variability (Oakey, 1990). It is shown in Figure 6.1.

The rate of dissipation of turbulent kinetic energy and the temperature were measured using the vertical profiler EPSONDE in series of consecutive profiles from the drifting ship. An uninterrupted series of EPSONDE drops taken while drifting
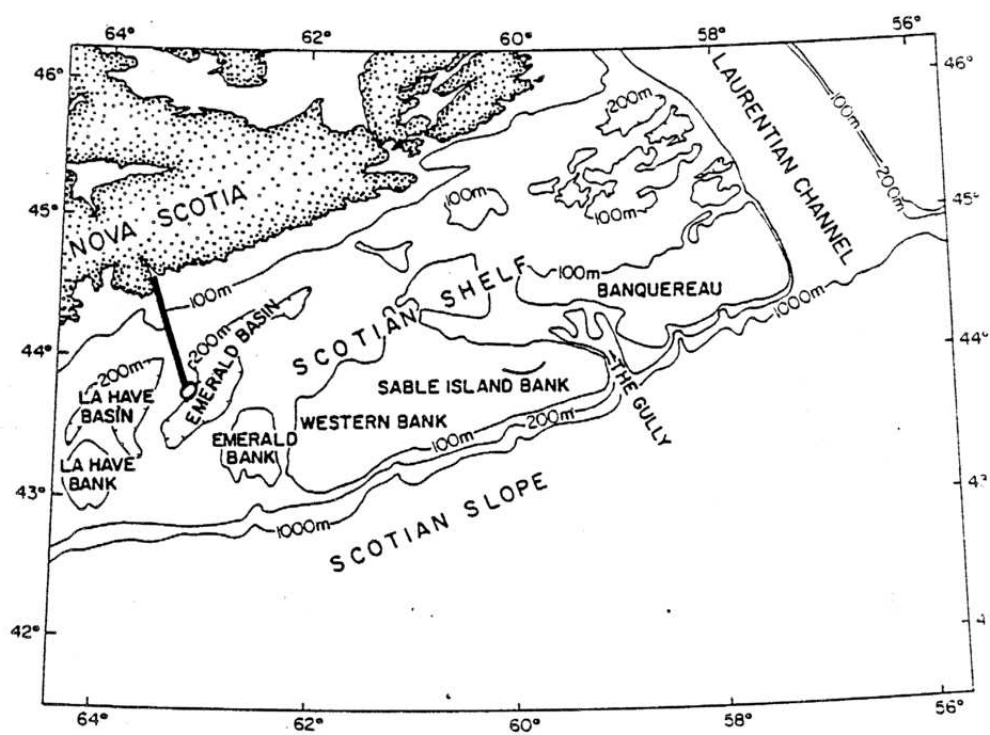
Figure 6.1: Sampling Site shown as the circle on the edge of Emerald basin. Reproduced from Oakey (1990)

will be is called a sequence in this chapter. The 190 profile locations are shown in Figure 6.2.

The dissipation data were obtained using direct measurements of vertical shear to dissipation scales averaged over vertical bins of approximately 3.4 m using the EPSONDE profiler. Temperature was also recorded by EPSONDE at approximately 2 cm intervals, although a version of the data with 40 cm intervals is used here.

The advantage of this data is that dissipation and temperature are measured from the same instrument. If the instrument falls through a dissipative overturning event then both the dissipation and the APEF should be high. If the sensors were not on the same vehicle, many profiles would have to be averaged together to allow comparisons between dissipation and finestructure because different profilers would not likely pass through exactly the same mixing and finestructure conditions. Another advantage is that dissipation is measured directly; in Dillon's data, dissipation was obtained indirectly from the temperature spectra using the Batchelor method.

It is unfortunate that the best data set available was not used for this chapter as data with 2 cm resolution exists (versus 40 cm used here). Data were obtained second-hand and this resulted in my misunderstanding of the full data set. Sooner presentation of my results to the principal investigator, Neil Oakey, would have resulted in an earlier detection of this. Data analyses were completed with the alternate data set before I learned that a better data set existed. In particular, dissipation of temperature variance (χ_θ) data are available, taken simultaneously with ϵ data used here. I was not aware of this. Future analyses of that data could be done to infer the dissipation of potential energy and compare it directly with the overturning models two and three for buoyancy flux. This would yield a much better comparison than the one presented here against ϵ only, where the two models cannot be differentiated.

The interpretation of the data set is thus not without problems. The temperature sampling interval of 40 cm is large to sample overturns; however, the largest overturns found are many meters in size such that they are still well resolved. Overturn detection is theoretically limited to those bigger than the sampling interval, but in practice it
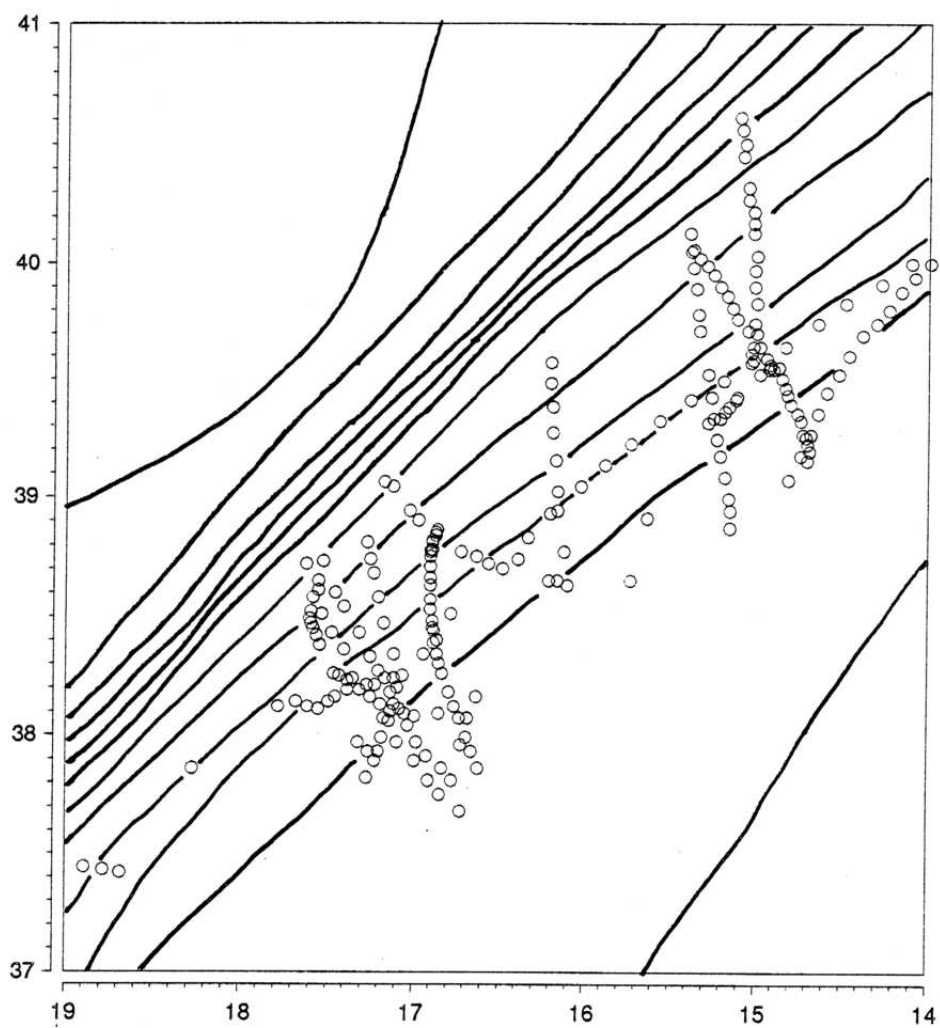
Figure 6.2: EPSONDE Sampling Stations. In all, 190 profiles of good quality were made. Line are bathymetry at 10 m interval, starting with 100 m at the upper left corner to 210 m at the lower right.

is preferable to resolve an overturn with many points. This is both to assure that the overturn is real, and to reduce the error in evaluating APEF. Also, the temperature least count is 0.001°C (the instrument resolution is 0.0015°C; data were saved with 0.001°C least count), which is not over-sampled, such that there are few noise-related inversions (although the temperature gradient data from EPSONDE has much greater resolution than this). This may sound good, but it prevents the use of a statistical method, briefly described in appendix D, to determine the temperature sensor noise level. These two factors, instrument least count and especially sampling interval, combine to make the noise level of the finestructure-estimated buoyancy flux very high, especially in high stratification (this will be quantified later).

6.2 $T–S$ Characteristics

When temperature is re-ordered to find overturns, it is assumed that temperature inversions are not salinity-compensated. The $T–S$ relation of the water column becomes a very important tool to determine the presence of salinity-stabilized inversions and intrusions.

The water column in Emerald basin (as everywhere else on the shelf, the Gulf of St. Lawrence and up into the estuary) is characterised by salinity monotonically increasing with depth, and by a mid-depth temperature minimum. CTD casts made during the cruise have a temperature minimum of 4.5°C between 30 to 50 m depth (not shown). EPSONDE profiles are recorded from about 8 m below the surface to the bottom, but will only be shown here below 60 m to compare with temperature data below the temperature minimum.

The temperature at 60 m is always below the temperature minimum such that temperature usually increases with depth and the salinity gradient controls the density gradient. Thus, instead of worrying about unstable temperature inversions being compensated-for by salinity, a harder assumption must be made. Since the temperature gradient is by itself statically unstable, it must be assumed that an overturn

appears as a stable temperature gradient, yet statically unstable because of an *un-measured* salinity gradient.

To make this assumption, a one-to-one relation is required between temperature and density. The relation does not need to be linear, but it must be tight, so that temperature differences can be interpreted as density differences.

The T–S characteristics were not available from the EPSONDE profiler[1] but CTD casts were made before and after each sequence of profiles for the first half of the cruise (until winch problems prevented CTD sampling). Figure 6.3 shows the T–S diagram obtained from all the CTD data available from the cruise (taken over 4 days, with 2 days of overlap with the EPSONDE data). At first inspection, the T–S is straight although it is wide. This presents a problem in the interpretation because the slope of the main T–S line is close to isopycnal: an isopycnal line intersects with a range of ≈ 0.15 °C in temperature due to the scatter of the T–S line. This means that temperature inversions up to 0.15 °C observed within the scatter may be isopycnal changes instead of diapycnal. There is thus danger that intrusions will be mistaken as overturns. Still, no obvious deformations of the T–S line are observed, so we will proceed, using temperature as a surrogate for density in our overturn detection.

6.3   Temperature Noise Level

The APEF is calculated by re-ordering the temperature profile obtained from EP-SONDE (density was not measured). However, some of the temperature inversions may be created by noise. In order to discard these overturns from the comparison, and also to determine the noise level of the estimated buoyancy flux, the noise level of the temperature sensor must be estimated.

A new technique for doing so is described in appendix D. Unfortunately, the technique relies on having over-resolved temperature measurements such that noise

---

[1] Temperature and conductivity were both measured from EPSONDE, but an apparent calibration problem gave a T–S curve in disagreement with the CTD. T–S gradients have not been explored (Oakey, Pers. Communication).
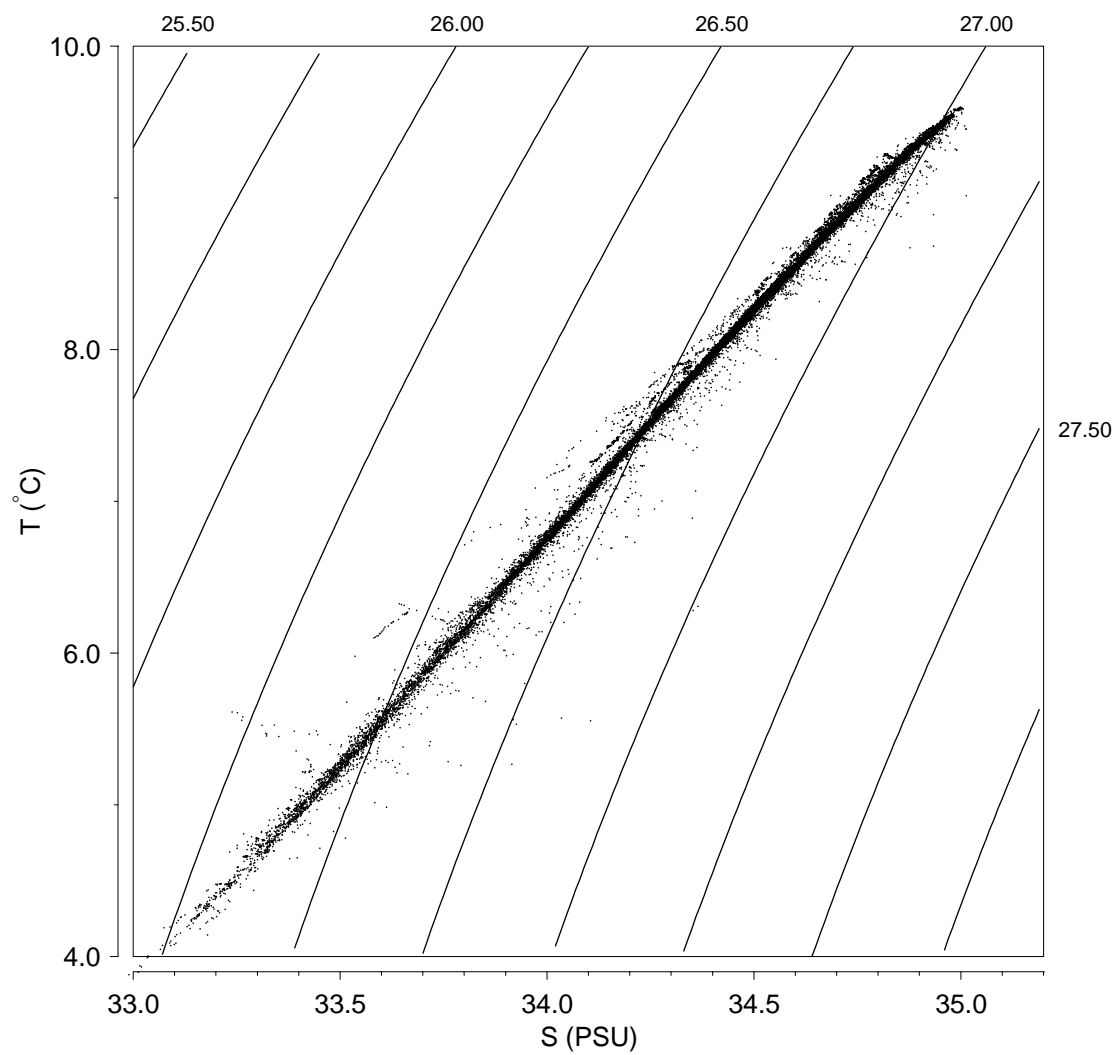
Figure 6.3: T–S diagram for all CTD data available from the cruise. In all 34445 points from 66 profiles are shown. Isopycnals $\sigma_t = 25.5$ to 28.0 are indicated.

creates inversions, which are then separated from overturning signatures using run-length statistics. The technique cannot be used with the current 40 cm sampling and $0.001°C$ least count data.

While the same CTD used here but with a lower least count and finer vertical sampling would probably yield a lower noise level, a conservative stance is taken and the noise level is estimated as $\delta T = 0.003°C$ (3 times the least count). Overturns with rms Thorpe fluctuations less than that are rejected. Further, overturns consisting of 3 points or less are also rejected.

6.4   Results

In chapter 3, buoyancy flux models were derived relating the decay of the APEF, ξ, over a time scale of N^{-1} on one hand, and a decay time function of the turbulent Froude number, Fr_t, on the other. The Fr_t-dependent decay time is shorter than N^{-1} when there is much more turbulent kinetic energy than potential energy in the turbulence (TKE $\gg 3\xi$).

Since I have compared overturning measurements to ϵ instead of directly to χ_θ, it is not possible to verify the buoyancy flux estimates. Therefore J_b will be estimated as ξN, the upper bound of model three prediction (3.33), but the the lower J_b estimate between model two and three at high Turbulent Froude number. Diagrams of ξN versus ϵ will be shown, on which the ratio of $\xi N/\epsilon$ is inferred as representing both the mixing efficiency of model three and an indicator of Fr_t for model two. From $Fr_t = Ri_t^{-1/2}$ and (3.22), the turbulent Froude number is

$$Fr_t = \left[\frac{\epsilon}{2\,\xi\,N}\,\frac{L_h}{L_T}\right]^{1/3} \tag{6.1}$$

Note that this assumes $\xi = N^2 L_T^2/2$ (e.g. (2.28)). This approximation did not hold for Dillon's tabulated data (in chapter 5) because his layer averages were shown to overestimate N^2 within overturns, but it is expected to hold here because the density gradient is evaluated separately over the depth interval of each overturn.

A given $\xi N/\epsilon$ ratio implies two different values of Fr_t (or Ri_t) depending on the assumption made for the unknown value of L_h in (6.1). In model two, isotropy sets $L_h = L_T$ such that the L_h/L_T ratio cancels out, leaving

$$(Fr_t)_{iso} = \left[\frac{\epsilon}{2\,\xi\,N}\right]^{1/3} \tag{6.2}$$

In model three, inertial-buoyancy balance sets $L_h = L_O$. The L_h/L_T ratio becomes L_O/L_T which can be written $(\epsilon/2\xi N)^{1/2}$ (again using $\xi = N^2 L_T^2/2$). Thus, if inertial-buoyancy balance conditions of model three hold, the relation between Fr_t and $\xi N/\epsilon$ becomes

$$(Fr_t)_{IB} = \left[\frac{\epsilon}{2\,\xi\,N}\right]^{1/2} \tag{6.3}$$

Values of $\xi N/\epsilon$ correspond directly to the mixing efficiency of the third model, $\Gamma_3 = \xi N/\epsilon$ (from $J_b = \xi N$ and $\Gamma = J_b/\epsilon$). From (6.2) and (6.3), a given value of $\xi N/\epsilon$ (or Γ_3) corresponds to different values of Fr_t at isotropy and inertial-buoyancy balance such that $(Fr_t)_{iso} = (Fr_t)_{IB}^{2/3}$[2]. Since efficiencies in both models are proportional to Ri_t (or Fr_t^{-2}), the mixing efficiency of model two can be obtained from $\xi N/\epsilon$ (or Γ_3) as

$$\Gamma_2 = \frac{\frac{2}{3}\xi\,N\,(Fr_t)_{iso}}{\epsilon} = \frac{1}{3}\left[\frac{2\xi\,N}{\epsilon}\right]^{2/3} \approx 0.53\left[\frac{\xi\,N}{\epsilon}\right]^{2/3} \tag{6.4}$$

by noting that $J_b = (2/3)\xi N Fr_t$ in model two.

The mixing efficiency of the second model can thus be obtained directly from the mixing efficiency of the third model for given values of $\xi N/\epsilon$ on plots of ξN versus ϵ. Mixing efficiencies for both models will be presented on a single ξN versus ϵ diagram.

6.4.1 Expected Outcome

The expected outcome is a good correlation between ξN and ϵ if at isotropic inertial-buoyancy balance (where $Fr_t \approx 1$), and $\xi N \ll \epsilon$ in well mixed layers or growing turbulence (where $Fr_t \gg 1$). Since the measurements were taken to the bottom

---

[2]This discussion is identical to the general form of $Ri_t = (L_T^2/L_O^{4/3}L_h^{2/3})$ in terms of length scales being written as either $(Ri_t)_{iso} = (L_T/L_O)^{4/3}$ or $(Ri_t)_{IB} = (L_T/L_O)^2$.

where mixing is expected to be more intense, it is likely that some well-mixed layers will be sampled and that a mix of conditions will be found. The ξN versus ϵ diagram should then resemble the $L_T^2 N^3$ versus ϵ panel in Figure 5.2.

6.4.2 Data Sub-set—Sequence 10

The finestructure data is first compared to microstructure for the sequence of EP-SONDE drops numbers 10018 to 10026. Ship drift was slow during this sequence. The temperature field and a qualitative comparison between TKE dissipation and ξN for overturns are shown in Figure 6.4 where the gray scale represents ϵ and the boxes represent overturns; the depth span of the boxes coincides with the overturn sizes, and the half-widths are values of ξN evaluated over distinct overturns. The depth span of an overturn is defined as the smallest group of consecutive points which may be re-ordered without moving any other point in the profile.

While qualitative agreement is found between high levels of ϵ and ξN, there are very few overturns in regions of high temperature gradients, especially in the 60–90 m range. The noise level for ξN (not shown) affects how much finestructure should be found, and will be shown to be responsible for these quiet areas (where ϵ is low anyway). Note that I do not have temperature profiles down to the bottom coinciding with the lower-right region of high dissipation, so that the absence of overturns is not a failure of the models.

6.4.3 Finestructure Noise Level

The noise level for $J_b = \xi N$ is determined by the minimum resolvable ξ and the value of N. Recall that the APEF noise level was discussed in chapter 2; it is the higher of the two values from (2.33). In this case, temperature is translated to density using $\delta\rho = 0.12\,\delta t$, so $\partial\rho_o/\partial z = 0.12\,\partial T_o/\partial z$, where the gradient of the re-ordered profile is calculated by centered first-difference over an interval of ± 4 data points.

Temperature, dissipation, ξN and the noise level of ξN profiles are shown in Figure 6.5 for sequence 10018–10026. Dissipation should only be compared with the
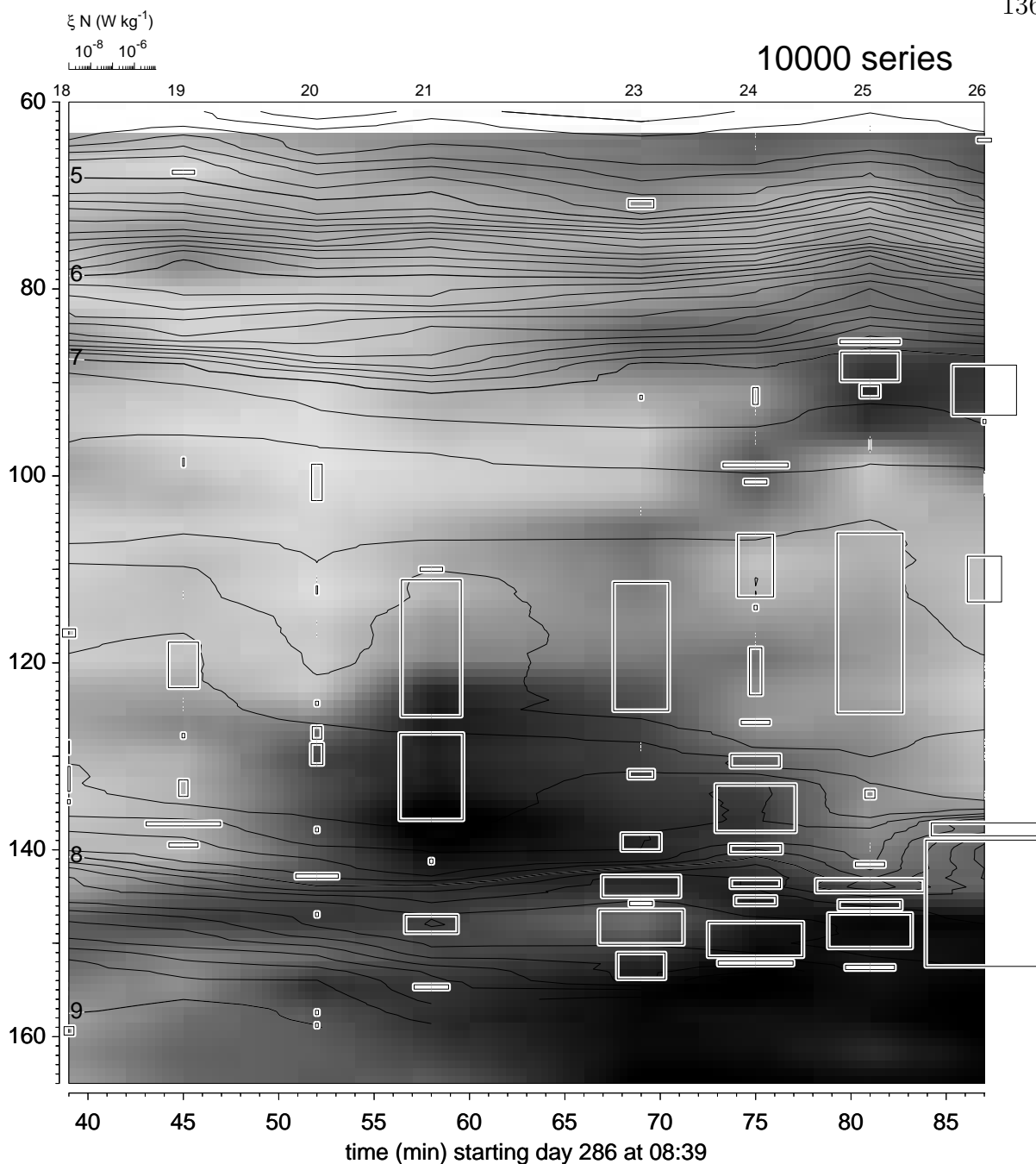
Figure 6.4: EPSONDE 10018 to 10026 sequence are qualitatively compared with overturning events and isotherms. The contours show the temperature field. The gray scale represents ϵ with white equal to 10^{-9} W kg^{-1} and black equal to 3.1×10^{-7} W kg^{-1}. Each box identifies an overturn: the vertical extent of the box shows the vertical extent of the overturn and the half-width of the box represents the value of ξN of the overturn from the scale on the upper left. Thus, a half-width of zero cm on the page means that $\xi N < 10^{-9}$ W kg^{-1}.

estimated buoyancy flux ξN in depth intervals where dissipation is greater than the buoyancy flux noise level. This is the least severe criterion that can be applied because the mixing efficiency is expected to be less than unity. In a mixed layer of high Fr_t, the mixing efficiency is expected to be much lower, say 0.1. In this case the buoyancy flux would be 10 times lower and dissipation should only be compared to ξN where the noise level is 10 times lower than ϵ.

The determination of the temperature noise level is therefore important because it determines the fraction of the water column in which buoyancy flux should be resolved by the finestructure. Note that since the ξN noise level increases with stratification (See Figure 6.5) finestructure cannot resolve overturning in the thermocline above 90 m or so, where no overturns are observed in Figure 6.4.

6.4.4 Averaging in 10-m Bins

The finestructure and microstructure for sequence 10018–10026 are averaged in 10 m bins in Figure 6.6. Values of ξN are plotted only for bins in which ξN is higher than the noise level. Note that the averages are of ξN, using N and ξ within each overturn; values of N are not 10-m averages in this case.

By comparing Figures 6.5 and 6.6, it is seen that most energetic overturns have thickness scales of the order of the bin size (10 m), such that the bin-averaging ξN does not affect their values. The averaging affects ϵ much more, removing many high wavenumber variations.

There are 49 10-m bins for which ϵ is greater than the ξN noise level. The average mixing efficiency Γ_3 for these 49 bins, calculated as the average ratio of $\xi N/\epsilon$, is 0.69 (corresponding to $\Gamma_2 = 0.51$). There are 43 bins for which ϵ times 0.69 (representing an average buoyancy flux) is greater than the noise level of ξN, the buoyancy flux for model three; perhaps this better represents the number of bins (43) in which values of ξN greater than noise level are expected to be measured. However, there are only 17 10-m bins for which ξN is greater than its noise level, compared to the expected number of 43. Thus the distribution of resolved buoyancy flux by overturning is
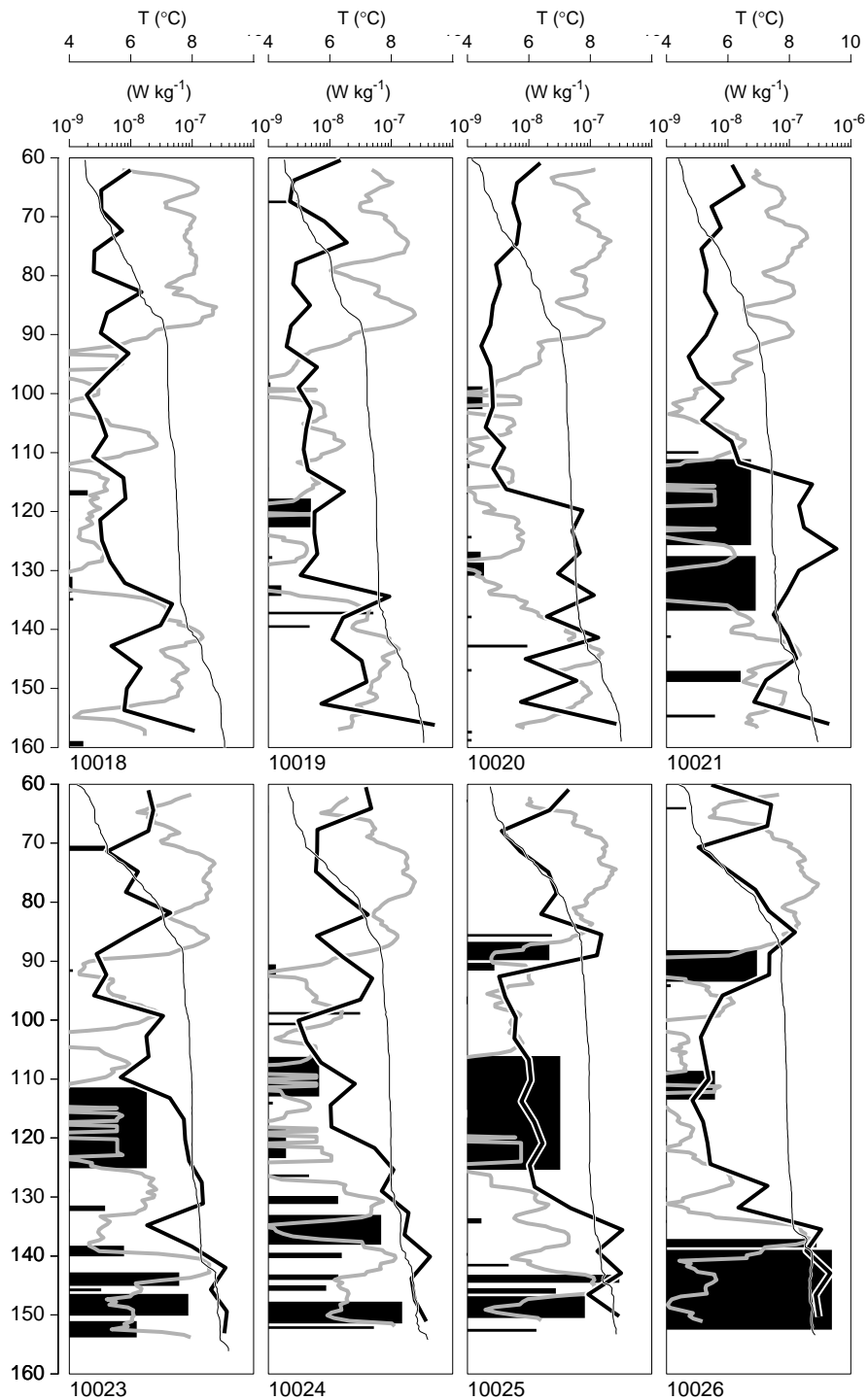
Figure 6.5: Noise level for ξN in 10018–10026 sequence. The thick gray line is the noise level for ξN. The thick black line is ϵ. Overturns are not expected to be observed if ϵ is less than the noise level. The black rectangles span the depth of overturns and their width represents ξN for the overturn. These quantities are on a logarithmic scale of 10^{-9} to 10^{-6} W kg^{-1}. The temperature profile is also plotted (thin line).
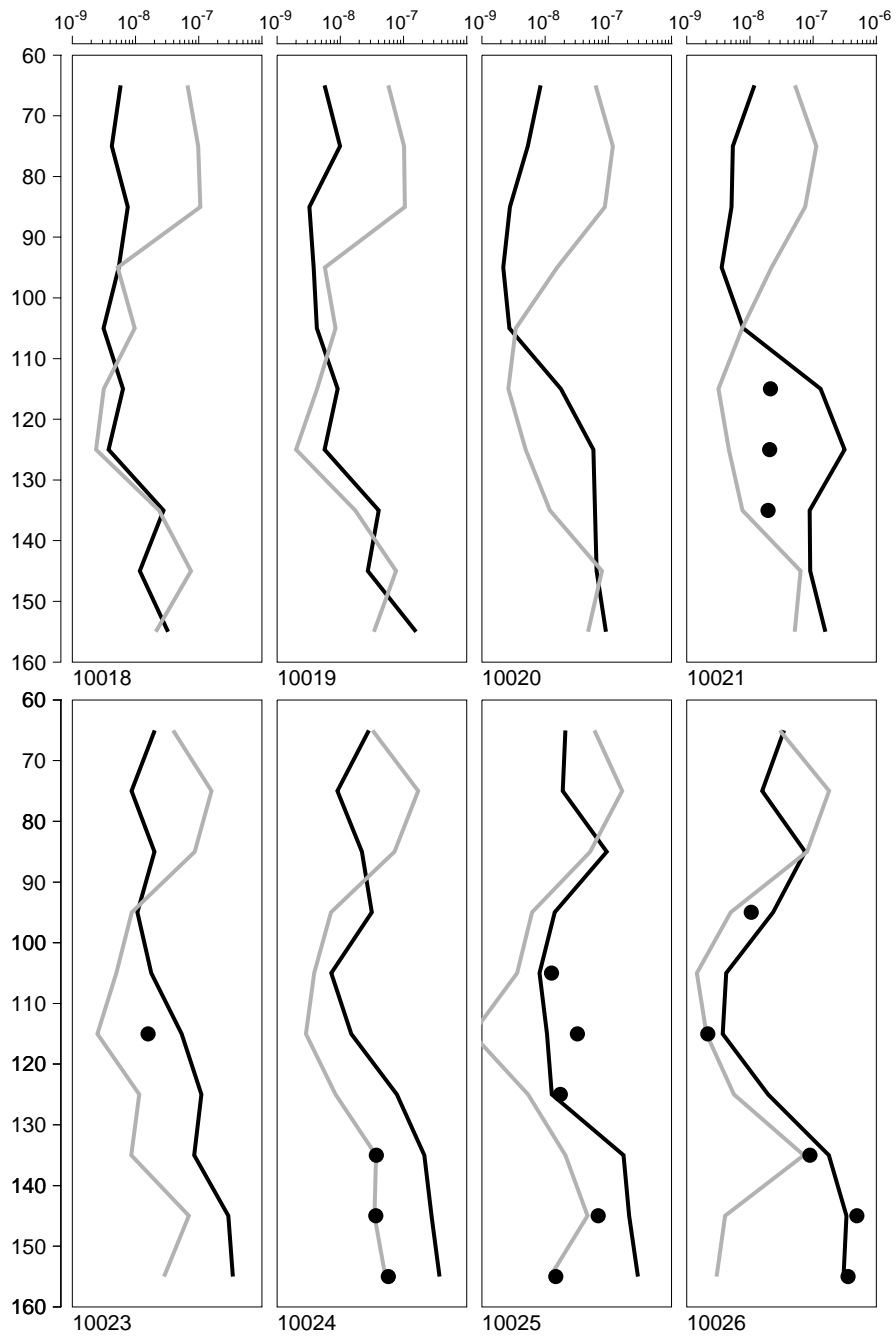
Figure 6.6: Averages in 10 m bins for ξN and ϵ in 10018–10026 sequence. The thick gray line is the noise level for ξN and the thick black line is ϵ. Symbols are averaged values of ξN for each 10 m bin, and are only plotted if greater than the noise level of the bin. All quantities are on a scale of 10^{-9} to 10^{-6} W kg^{-1}.

lower than expected from TKE dissipation rate measurements; overturning (and its modelled buoyancy flux) is found only in about 40% of the 10 m bins in which it should be resolved.

In Figure 6.7, ξN is plotted against ϵ for both overturn values of Figure 6.5 and averages of Figure 6.6. For Figure 6.7, overturn values for dissipation are simply the average ϵ measured within the span of the overturn. Only overturns consisting of more than 3 points and with rms Thorpe fluctuations greater than 0.003°C are shown. If the overturn does not vertically overlap with any dissipation sample point, it is compared to the closest dissipation measurement (so it is only an average for large overturns, greater than about 3.4 m).

While the ξN versus ϵ distributions in Figure 6.7 are slightly different for the averaged and non-averaged cases, it is difficult to say if 10-m averaging is necessarily better than taking overturn values, having no other estimates of buoyancy flux to compare with (from χ_θ, for example). It is clear that the overturn-averages do not yield results dramatically different from 10-m averages; this is probably due to the fact that most energetic overturns have length scales similar to 10 m. This large size would not be true of Dillon's observations discussed in chapter 5.

6.4.5 Analysis on Entire Data Set

Here, the above comparison is repeated on the entire data set. In Figure 6.8, ξN is compared to ϵ for each overturn in the data set resolved by more than 3 data points and for which $\overline{T'^2}^{1/2} > 0.003$°C. A plot showing the same result in terms of $\xi^{1/2} N^{-1}$ vs L_O is also shown (where multiplying $\xi^{1/2} N^{-1}$ by $2^{1/2}$ approximates L_T) because L_T–L_O diagrams are often seen in the literature to compare finestructure to dissipation.

Obviously, the comparison is not very good when all data are considered in the plot of ξN versus ϵ. The expected result is similar to Figure 6.7, where points of maximum ξN for all ϵ values falls along a line of constant mixing efficiency $\Gamma = \xi N/\epsilon$. The cloud of data below this line is expected for well mixed layers or intense, growing turbulence
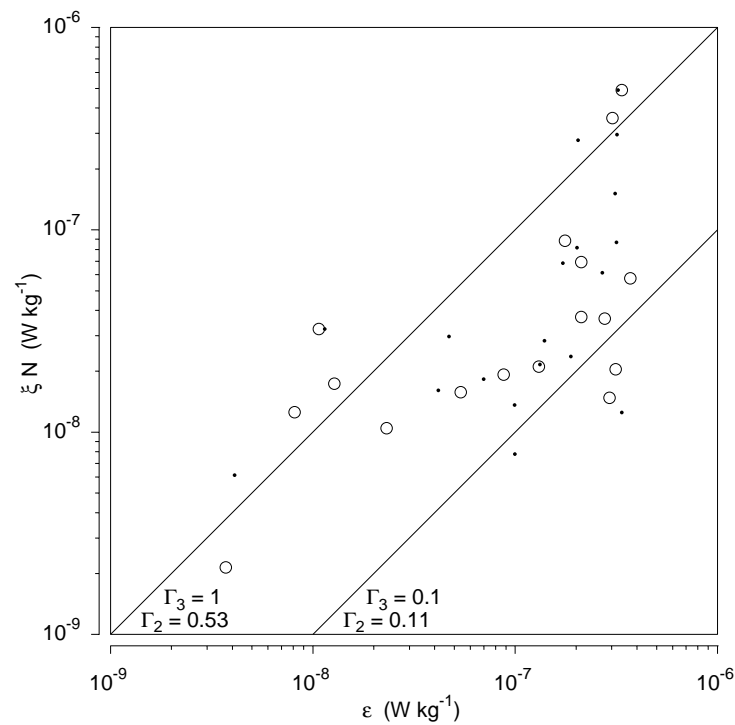
Figure 6.7: Buoyancy flux estimate ξN versus dissipation ϵ in 10018–10026 sequence. The dots are averages over the span of each overturn (from Figure 6.5). Only overturns consisting of more than 3 points and with rms Thorpe fluctuations greater than 0.003°C are shown. The circles are 10-m bin averages (from Figure 6.6). Only bins with ξN greater than noise level are shown. The oblique lines are mixing efficiencies with the indicated values for the second and third models.
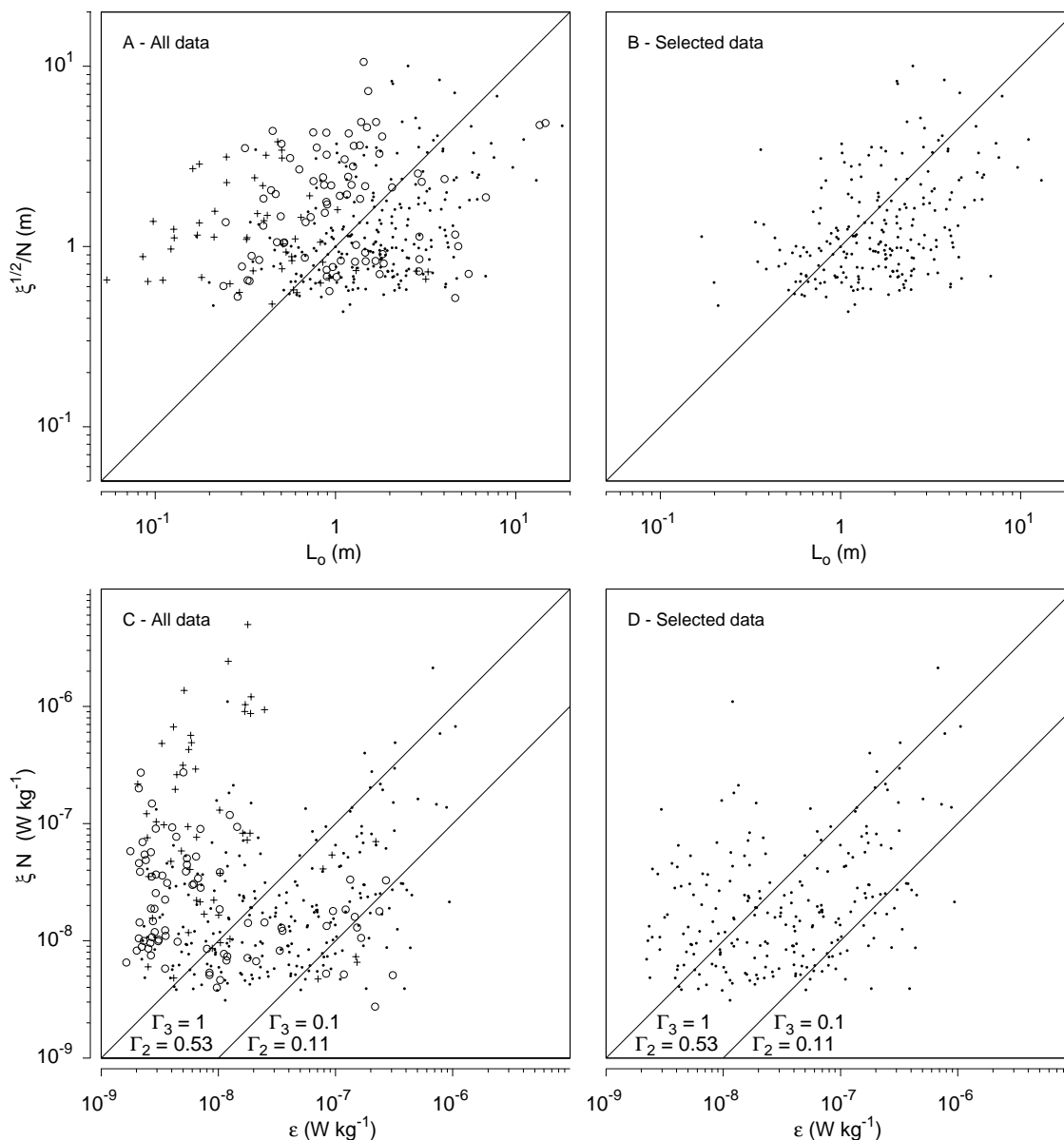
Figure 6.8: Buoyancy flux estimate ξN versus dissipation ϵ, and $\xi^{1/2}N^{-1}$ vs L_O for depth spans of well-resolved overturns, for all data set. In **A** and **C**, all data are plotted but are coded as: (+) shallower than 65 m; (○) between 8.6 and 9°C. Dots are all other data. In **B** and **D**, only dots from **A** and **C** are plotted (deeper than 65 m, yet not between 8.6 and 9°C). These well resolved data are have $\overline{T'^2}^{1/2} > 0.003$°C and more than 3 points per overturn. Note that $\xi^{1/2}N^{-1}$ approximates $0.707\,L_T$. The oblique line in **A** and **B** is a one-to-one line. The oblique lines in **C** and **D** are mixing efficiencies with the indicated values for the second and third models.

where high Fr_t turbulence has low mixing efficiency. The data with high value of ξN and low values of ϵ are 'anomalous' in the models. We will use this qualifier for now to designate them because the models cannot account for mixing efficiencies much greater than unity.

It is found that most of these 'anomalous' data are selected using two criteria. The first group are between 60 and 75 m, but have no special temperature other than they usually fall within 4 to 7°C. The second group are in the temperature range of 8.6 to 9°C. These data are removed in Figure 6.8B and D. The result is much better, more like Figure 6.7 with a triangle of values with $\epsilon \gg \xi N$ allowed (low mixing efficiency) but not the reverse. This 'filter' is to say the least Ad Hoc; it is only used now as a signature to help determine what is different about these selected data. This will be examined later in this chapter.

6.5   Discussion

Let us now review what this data analysis has revealed about the unanswered questions enumerated at the beginning of the chapter.

6.5.1   Does Averaging Over Single Overturns Compare Well With 10-m Averages?

The comparison of ξN and ϵ yield slightly different results in Figures 6.7. The biggest difference observed is an apparent decrease in dissipation variance with depth (seen mostly by comparing Figure 6.5 to Figure 6.6).

Here, we would ideally wish to compare estimates of the buoyancy flux obtained from overturning to the true buoyancy flux within the overturn, in order to estimate the importance of the redistribution terms of kinetic and potential energy in the governing turbulent equations. But we do not know the true buoyancy flux, nor even an estimate (although further work could use χ_θ measurements). We have a measurement of the rate of dissipation of TKE from single profiles, for which the

same redistribution terms usually force us to ensemble average many profiles. The best that can thus be done is to see if estimates of buoyancy flux from single overturns are as consistent with the dissipation of TKE averaged over those overturns, as they are using larger scale 10-m averaging.

The averaging on 10-m bin is typical of what is usually done. For instance, Dillon's (1982) data are for mixing layers which may hold many overturns. A major difference remains: the finestructure buoyancy flux models were not evaluated here by using a layer-averaged N, but rather with an N evaluated over each overturn and then averaged. The bias introduced in Dillon's analysis is not present here. Here, N is calculated by regression on the re-ordered temperature profile over the span of each individual overturn.

It is encouraging that the results are not dramatically different than those using 10-m bin averaging, however it must be noted that most of the more energetic overturns are of this size anyway, such that 10-m averaging should not be expected to be dramatically different.

Note that it is not known if the overturns are evolving K-H billows (puffs). overturning may be occurring in more persistent mixing layers such that initial overturning with high ξ but little ϵ (which could be observed in K-H billows) is not expected. This is because the shear forcing is likely to be steady in the boundary layer, as evidenced by many subsequent profiles with overturning near the bottom.

6.5.2 How Much of the Rate of Dissipation of TKE is Accounted for by Overturning?

If the mean mixing efficiency (for sequence 10018–10026) of $\Gamma_3 = 0.69$ is used, then it could be assumed that bins with ϵ greater than 0.69 times the buoyancy flux noise level should contain resolved overturns. Only 40 percent of them do. In particular, station 10023 has a high dissipation relative to buoyancy flux noise level for 10-m averages, and yet has very little overturning. If the expected mean mixing efficiency is reduced by half to 0.35, then 60 percent of the bins where overturns are expected

to be resolved do contain overturns.

Note that the average mixing efficiency is biased because not all bins have overturns, and those without overturns were not included in the calculation of mixing efficiency. Therefore, that number should not be used outside of the loose context in which it was introduced.

It is unclear why overturns are not observed in many of the bins for which overturning is expected. An hypothesis is that mixing efficiency is very low where overturns were not observed, such that overturning is below the noise level. This cannot be tested without estimates of Fr_t or measurements of χ_θ. However, Figure 6.7 shows that the highest $\xi N/\epsilon$ ratio, occurring consistently at all values of ϵ, has a value greater than unity, corresponding to a high maximum mixing efficiency in models two and three (the higher still values of $\xi N/\epsilon$ which occur only at low values of ϵ will be discussed separately). This perplexing result could be an averaging problem, or partly due to a changing T–S water mass line changing the conversion from temperature difference to density difference[3]. Note that such high mixing efficiencies were also observed in Dillon's data set, but that I have argued that they might be due to errors in χ_θ. Therefore, it seems unlikely that very low mixing efficiency occurs adjacent to very high values.

Thus, no clear answer to this question may be given here.

6.5.3 How Much of the Overturning is Accounted for by the Rate of Dissipation of TKE?

If overturning is observed (and models consequently predict high buoyancy flux) when the rate of dissipation of TKE is low and cannot account for any buoyancy flux, this would not be seen in comparisons done using only data where both ϵ was well resolved and overturning occurred (e.g. Dillon's analysis). The present data have

---

[3]Because the T–S line is fairly close to isopycnal, small differences could account for large changes. Up to a 30% reduction in the temperature to density conversion results in changing from the main T–S line to a secondary line shown in upcoming Figure 6.10

such occurrences. In the next section, I will try to convince the reader that these are intrusions and not overturning events; they should therefore be discounted from the comparison with the rate of dissipation of TKE. The presence of intrusions is in fact the major difficulty with the interpretation of this data, and possibly many data sets with energetic mixing.

6.6   Intrusions and Water Masses

The main problem with the interpretation of the data are those 'overturns' with very high ξN and very low rates of dissipation of TKE. Most of these anomalous data were found to be either between the depths of 60 and 75 m or between the temperature of 8.6 and 9.0°C.

The two groups of anomalously high ξN data are not spread about equally in all the data set. Figure 6.9 shows the overturn-averaged ξN versus ϵ for each time sequence of EPSONDE drops from the drifting ship. Note that not all sequences suffer from these points, and those that do often have many such points (which are spread over many profiles).

The T–S properties of the CTD data are re-examined in Figure 6.3 to identify what is different about the data between 60 and 75 m and also about those between 8.6 and 9.0°C. Upon close inspection, one can discern different water masses in Figure 6.3. In Figure 6.10, two water mass families are shown which appear to be the extremes found in the CTD data. It is possible, and likely, that these two water masses may interleave and also mix together since both these masses were sampled in close proximity.

CTD casts were taken between EPSONDE sequences for the first part of the cruise (until they experienced winch problems). There are two sequences for which CTD data is available which have anomalous ξ data characterised by 8.6–9.0°C water. These are stations 13 and 14, and the T–S diagrams are shown in Figure 6.11. It is seen that sampling in stations 13 and 14 started in one water mass and finished in
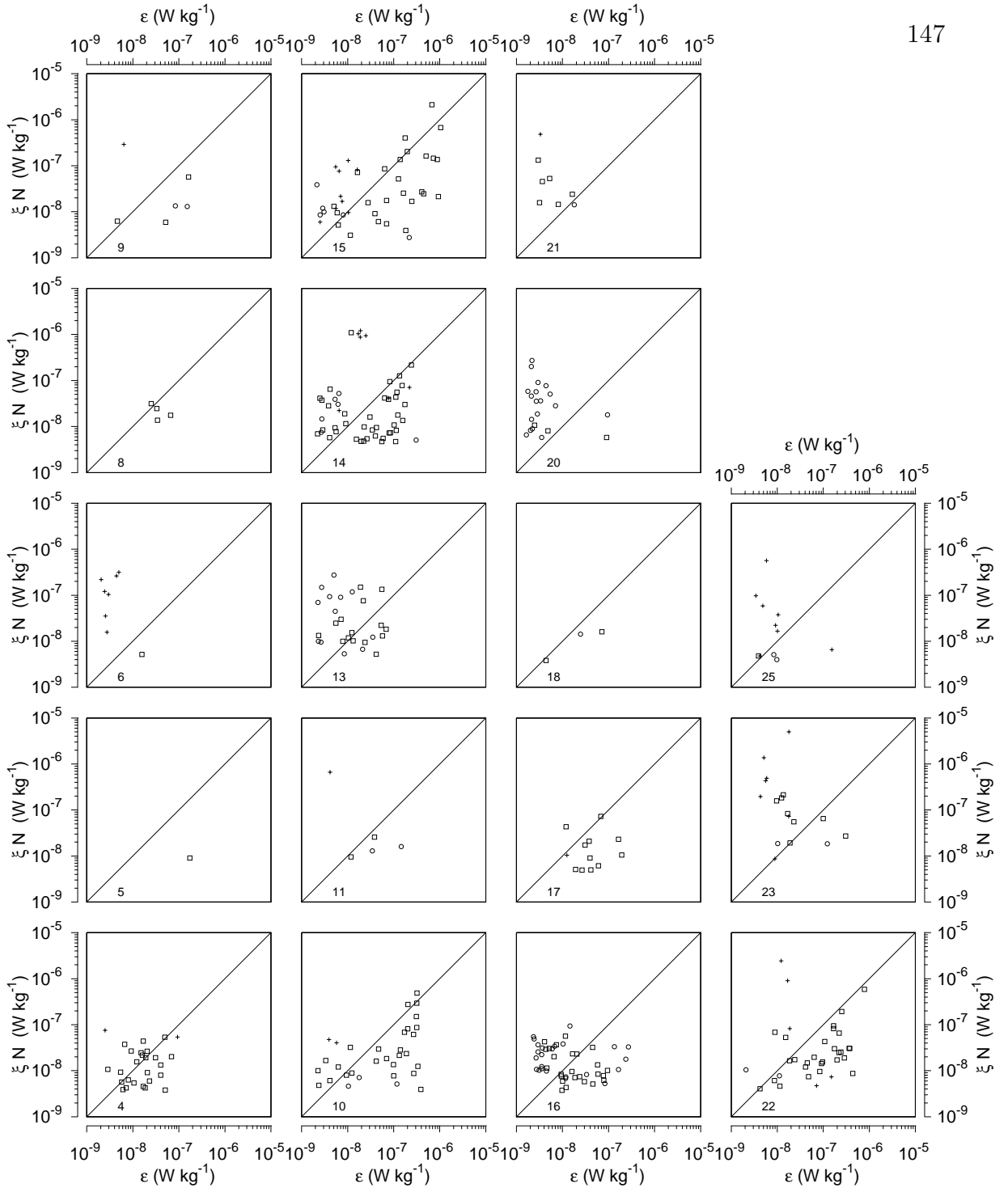
Figure 6.9: Overturn-averages of ξN vs ϵ for individual EPSONDE sequences. ($+$) shallower than 65 m; ($\circ$) between 8.6 and 9°C; ($\square$) all other data. Sequence number indicated in upper left corner of each panel. Oblique line is mixing efficiency $\Gamma_2 = 0.53$ or $\Gamma_3 = 1$.
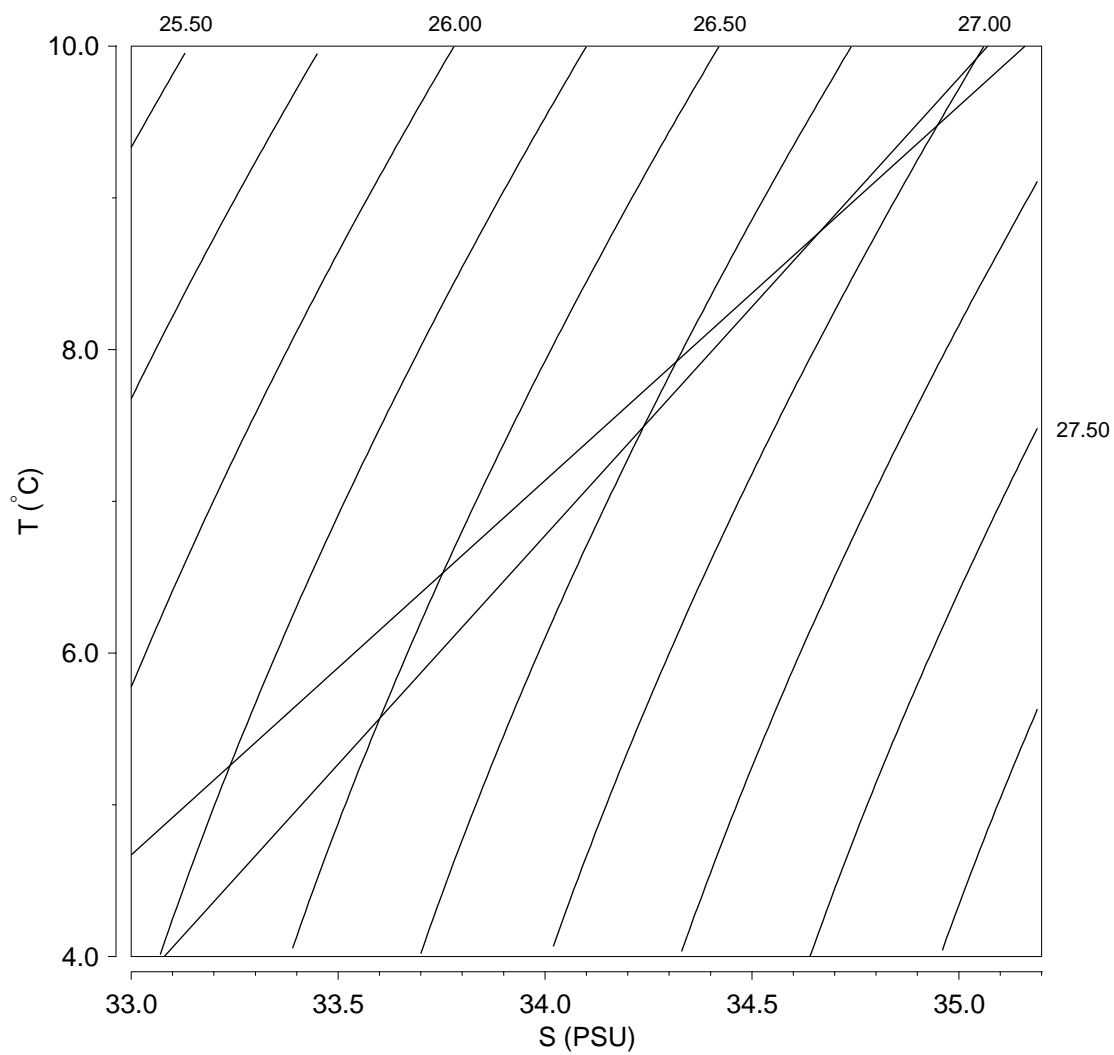
Figure 6.10: Water masses found on T–S relation. The two lines represent the extreme water masses found on the T–S relation in Figure 6.3.

the other. The temperature at the intersection of these two water masses is in the range of the observed high ξN (8.6–9.0°C). Possibly, an intrusion was occurring close to the intersection temperature of the two water masses.

The EPSONDE data characterised by depths between 60 and 75 m ('plus' symbols on Figure 6.9) cannot be found on all T–S diagrams of Figure 6.11 made from CTD casts. For example, T–S diagrams for sequences 6 and 9 are not shallow enough to observe characteristics found in this depth range (although this is merely due to a cut-off depth chosen for the CTD files given to me because the region of interest was the bottom boundary layer (Van Haren, Pers. Communication)). For this reason, we will again look to EPSONDE station 14 to explain the high ξN found in depths between 60 and 75 m (Different points within the profiles than those found between 8.6 and 9.0°C).

In sequence 14, there is a possibility that a mixture of both water masses in Figure 6.10 is intruding along an isopycnal into the sampling drift track. This stable intrusion has a different temperature for its density than would otherwise be seen. When EPSONDE enters or leaves the intrusion, the the temperature gradient would reverse and create an apparent overturn.

Figure 6.12 shows the drift track of sequence 14, as well as the positions of the pre-ceeding and following CTD casts. The time evolution is also shown, with time against the latitude position. The drift and sampling were fairly regular. Supported by this, the temperature at a chosen isopycnal is plotted linearly between the preceeding and following CTD cast position in the third panel of Figure 6.12. The temperature was observed to decrease by 0.5°C at that isopycnal during the time span of the sequence, from 7.1 to 6.6°C (in less than 6 hours). The 'overturns' with high ξN centered between 60 and 65 m (for this sequence, generally these points are between 60 and 75 m) are only found during the first five stations of sequence 14. They are shown as black dots in Figure 6.12. The minimum and maximum temperatures for each of the 'overturns' are connected and shown in the third panel. They show that the decrease in temperature of that 'overturn' throughout the sequence of profiles is consistent
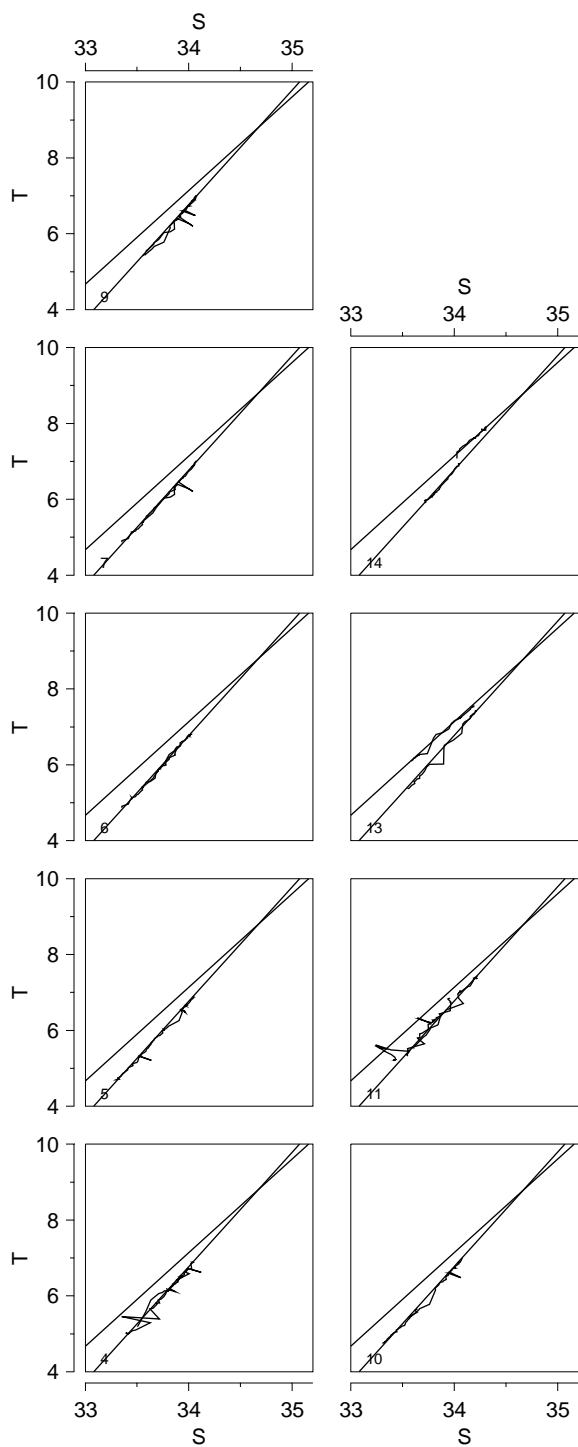
Figure 6.11: T–S diagram for all EPSONDE sequences preceeded and followed by a CTD cast. The two lines are water masses traced on Figure 6.10. Sequence number indicated in upper left corner of each panel. Note that the finestructure density measurements in these CTD casts is unreliable; none of the apparent density inversions should be believed. In certains sequences, two end water masses are found at the start and end, such that intrusions could be present during the sequence. These intrusions, not observed in any way in this figure, could be seen as overturns by EPSONDE using only temperature profiles.

with the observed temperature decrease at an isopycnal going through the 'overturn'. This suggests that the 'overturns' are in fact temperature signatures of an intrusion of both end water masses.

The origin of the mixed intrusion is unclear. It occurs at the same depth, yet different temperatures, in many profiles. In particular sequence 6 has an apparent intrusion at the same depth, but this time between 4 and 5°C instead of around 7°C. Through 6 consecutive profiles, the intrusion temperature decreases by 0.6°C. There are no sills at a depth of 60 to 70 m close by. The closest is Emerald bank, 70 to 80 m in depth, at over 20 km away from these stations.

6.7 Summary

In this chapter, microstructure data from Emerald Basin were used as a test case of the finestructure models for estimating buoyancy flux from overturns. The temperature data used have low vertical resolution for overturn detection (40 cm resolution was used here, but 2 cm resolution data exist) and so areas of high stratification were not resolved by the method. However, overturning was often on such large vertical scales (≈ 10 m) that even the 40 cm vertical sampling resolves them easily.

The main results were

- The buoyancy fluxes obtained from the overturn finestructure were consistent with the dissipation measurements even if data are averaged over the vertical extent of separate overturns (See Figure 6.5 and Figure 6.7). To my knowledge, this is the first time that these quantities have been compared on such small averaging spans. However, the large overturning size limits the applicability of this result to less energetic mixing layers.

- About 40 to 60% of 10-m bins in which overturning was expected were observed to contain overturns.

- The maximum mixing efficiency observed is fairly high ($\Gamma_3 \approx 2$). Low mixing
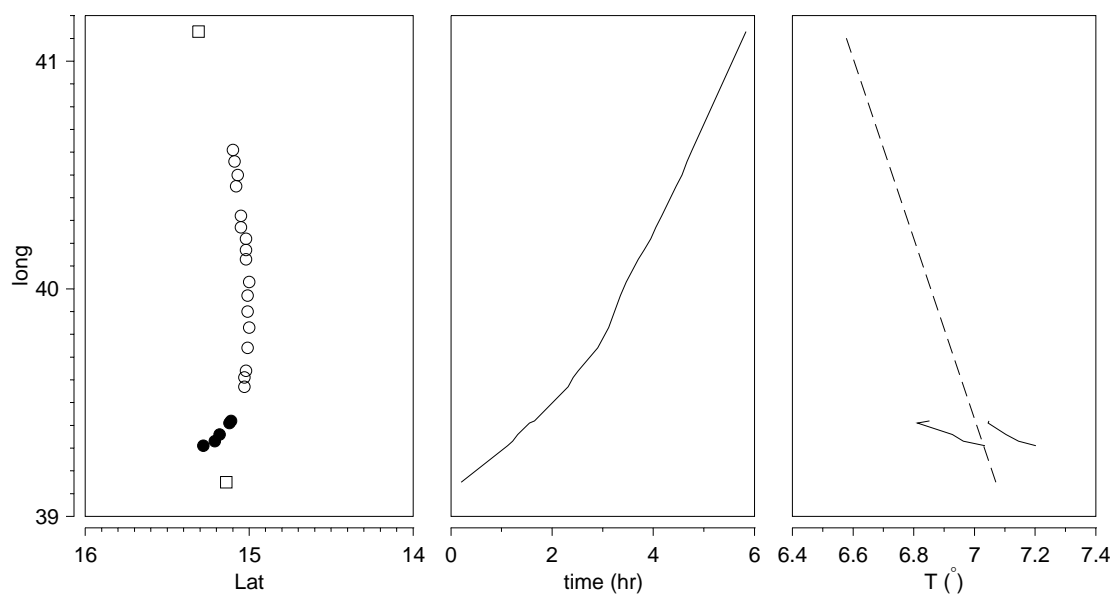
Figure 6.12: Drift Track of Sequence 14. The first panel shows the position of the CTD casts made before and after the sequence (□) and the position of each EPSONDE drop (○). The time and temperature panels are explained in the text.

efficiencies were $\Gamma_3 < 0.1$ using the third model (or $\Gamma_2 < 0.04$ using the second model). Note that these mixing efficiencies come from buoyancy flux models using the upper bound of the factor of two of their coefficient ($\left[\frac{3}{4} \pm \frac{1}{4}\right]$). Regardless of this factor, there is a range of about 2 decades in observed mixing efficiency (not counting bins where no overturns were observed), but the instrument resolution limits this range. This implies that the data are incompatible with model one, which assuming a constant mixing efficiency. The same was said of Dillon's data sets A and C.

- Temperature was used as a density tracer to identify and compute the potential energy of the overturning events. A tight T–S relation is required for this to work properly. In regions where ξN was much higher than ϵ, it was shown that the sequence started in one water mass and finished in another. Persistent apparent overturns warmed from profile to profile consistently with isopycnal changes between the two end water masses. This strongly suggests that the high ξN anomalies were in fact intrusions.

- This is perhaps the most important point: If dissipation data had not been available, and only finestructure were used to estimate mixing, all data where the T–S varied greatly would not be used because of the possibility of misinterpreting intrusions as overturns. It is therefore recommended that salinity always be measured if it can affect density in a significant amount. Even if density measurements cannot resolve overturning events sufficiently to reorder the profiles to find overturns, it is probably good enough to help identify inversions caused by intrusions. These often have uncommonly high values of ξN.

Chapter 7

Application to the St. Lawrence Estuary

Microstructure measurements have yet to be taken in the St. Lawrence estuary, yet many authors have discussed the strong mixing that occurs at the head of the Laurentian channel (Steven, 1974; Forrester, 1974; Ingram, 1975; Therriault and Lacroix, 1976; El-Sabh, 1979; Gagnon and El-Sabh, 1980; Ingram, 1983). It is thought that mixing occurs predominantly at the head of the channel (Steven, 1974), and that large shears associated with an internal tide provide the forcing (Forrester, 1974). This internal tide appears to be generated at the slope where bathymetry shallows from 350 m to 50 m in less than 15 km (Forrester, 1974), but the exact mechanism is not confirmed[1]

In this chapter, CTD and ADCP data sampled at the head of the channel are used in conjunction with the buoyancy flux models discussed in this thesis to estimate mixing rates.

---

[1]While it can be argued that a critical slope at the head can reflect some tidal energy and create the internal wave, at least one author has proposed otherwise. Blackford (1978) constructed a 2-layer generation model without rotation whereby continuity dictates that the flow over the sill must be greater than seaward. A Bernoulli depression over the sill accelerates the flow by generating a pressure gradient in the surface layer. Since there is no flow in the bottom layer seaward of the sill, the interface must tilt to compensate the pressure gradient in the top layer. The periodic tidal flow over the sill thus creates a wave at the interface which propagates seawards.

This chapter serves three purposes. First, it illustrates what is known about the hydrodynamic conditions in the area, hopefully adding to that knowledge and identifying some weak points. This includes discussions of the internal tides, intrusions and solitons. Second, an attempt is made to quantify mixing, to show what forces it, and to determine its range of turbulent Froude number Fr_t. The Froude number will be estimated from the larger scale gradient Richardson number Ri_g. No further comparison can be made between mixing models presented in earlier chapters because microstructure quantities (ϵ, χ_θ) were not measured here. Third, the overturning will be related to the shear forcing by comparison with Gregg's (1989) model which links shear to dissipation levels.

7.1   CTD and ADCP Data Set

During a preliminary cruise on the Petrel V in the fall of 1987, density inversions thought to be overturning events were measured using a conventional GuildLine CTD. A longer, second cruise took place in late June of 1988 on the C.S.S. L.-M. Lauzier. During the last three days of the cruise, an R&D Instruments 1200-KHz ADCP was graciously lent to us for demonstration purposes by David Stewart of Dasco Equipment Inc. The ADCP sampled velocity vectors in 1-m bins and 2-minute averages from 3 to 32 m. The velocities are measured relative to the surface bin because the sea floor was beyond the bottom-tracking range of the ADCP.

7.1.1   Gradient Richardson Numbers

The gradient Richardson number, Ri_g, is an indicator of the dynamic stability of the water column. It has been shown to be related to the turbulent Froude number, Fr_t, in a previous chapter, by

$$Fr_t^{-2} = Ri_t \approx 6.2\, Ri_g \qquad (7.1)$$

However, gradient Richardson numbers can be evaluated at different vertical scales. A brief outline of the methodology used for this data set follows.

Relative horizontal velocities are measured from an ADCP using 1-m bins. Its acoustic sampling results in the convolution of a sound train with each 1-m bin of water column. The end effect is a 2-m thick triangular filter imposed on velocity observations. The velocities are externally further smoothed with a $(\frac{1}{4},\frac{1}{2},\frac{1}{4})$ vertical moving average, and then first-differenced to obtain shear. The horizontal components of shear are squared and added to yield the total shear squared.

Stratification was estimated using CTD profiles sampled about 10 or 15 m away from the ADCP. These are the same profiles used to find overturning events. Density was averaged in 1-m bins using a 2-m thick triangular moving average, designed to mimic the implicit filtering in the acquisition of velocity data with the ADCP. These data are further filtered with the same three point moving-average used on the ADCP bins, and are first-differenced to yield $\partial\rho/\partial z$ and thereafter N^2.

Richardson numbers are then obtained from the ratio of N^2 to shear squared. Both shear and stratification are averaged vertically on a similar scale, but shear is also a volume average of acoustic return signals.

7.2 T–S Properties, Intrusions and Circulation

Before any CTD measurements of overturning events are discussed, it is important to describe the T–S properties of the area. A tight T–S relation is preferred to rule out the possibility of intrusions, since it is intended to use temperature instead of density to find overturns (as in chapter 6).

Figure 7.1 shows T–S properties sampled at four stations located near the head of the Laurentian channel. Station locations are shown on Figure 7.2. Each station was sampled for many hours, often over a semidiurnal tidal cycle.

There are dramatic gradients in T–S properties along isopycnals which appear related to the circulation. Ingram (1979) showed that tidal-residual circulation during the Spring season is approximately 17 cm s^{-1} up-channel at station 21 in the top 125 m. The residual circulation is down-channel on the South side, at stations 14 and
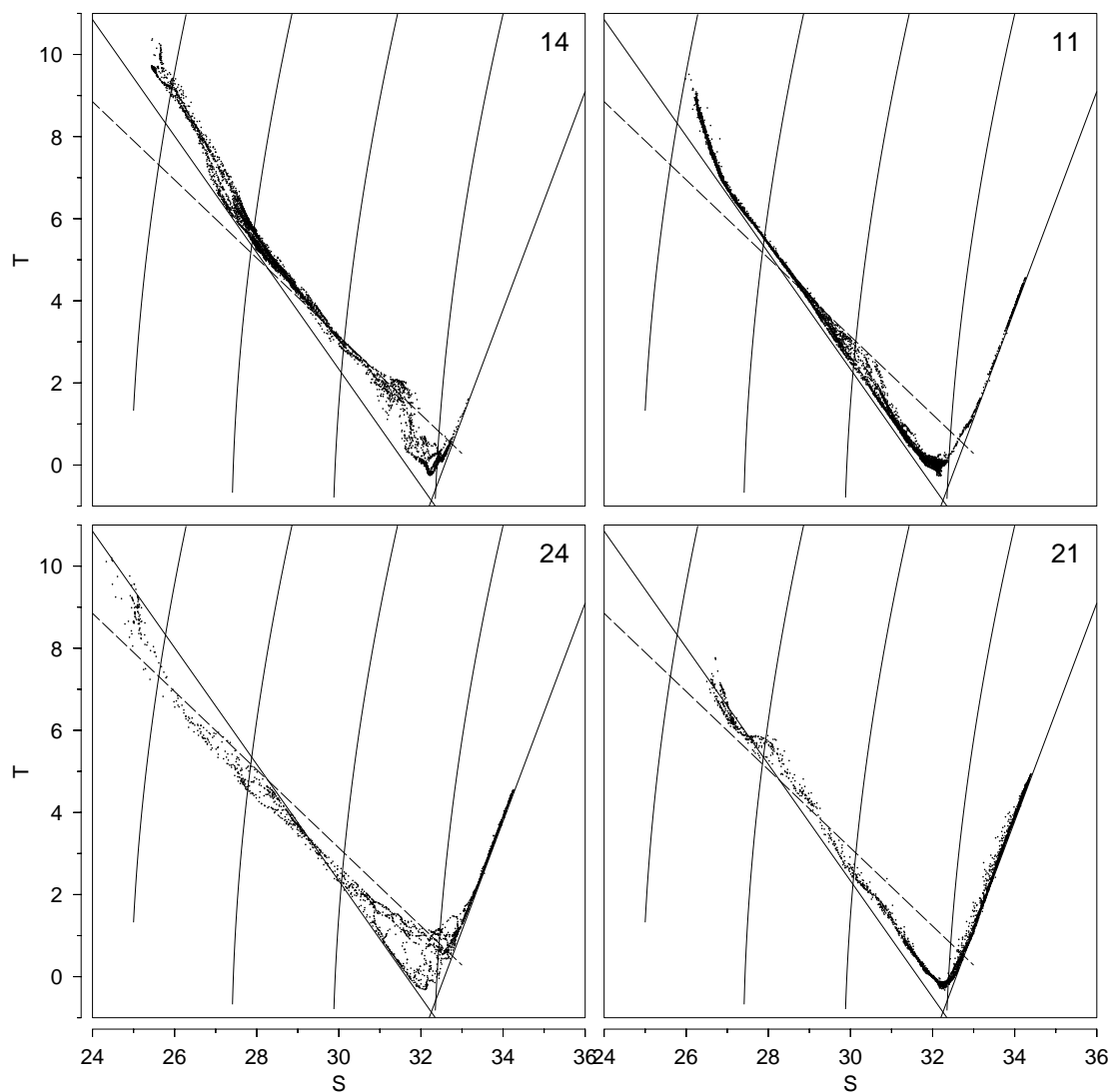
Figure 7.1: Temperature–Salinity Properties at the head of the Laurentian channel. Stations indicated in upper-right corner of each panel. Station locations are shown in Figure 7.2. Station 21 was sampled to 200 m every hour starting June 27 1988 15:01 EDT to June 28 04:58 EDT. Station 24 was also sampled to 200 m every hour, on June 29 from 14:01 to 22:59 EDT; Winds increased from very low to 25 knots at the end of the day. Station 14 was sampled to 50 m on July 4 from 04:50 to 14:04 EDT in 15 knot winds. Station 11 to 50 m was sampled from July 4 14:57 to July 5 02:45 in light winds. The last 3 profiles were taken to 235 m. See text for explanation of water mass lines.
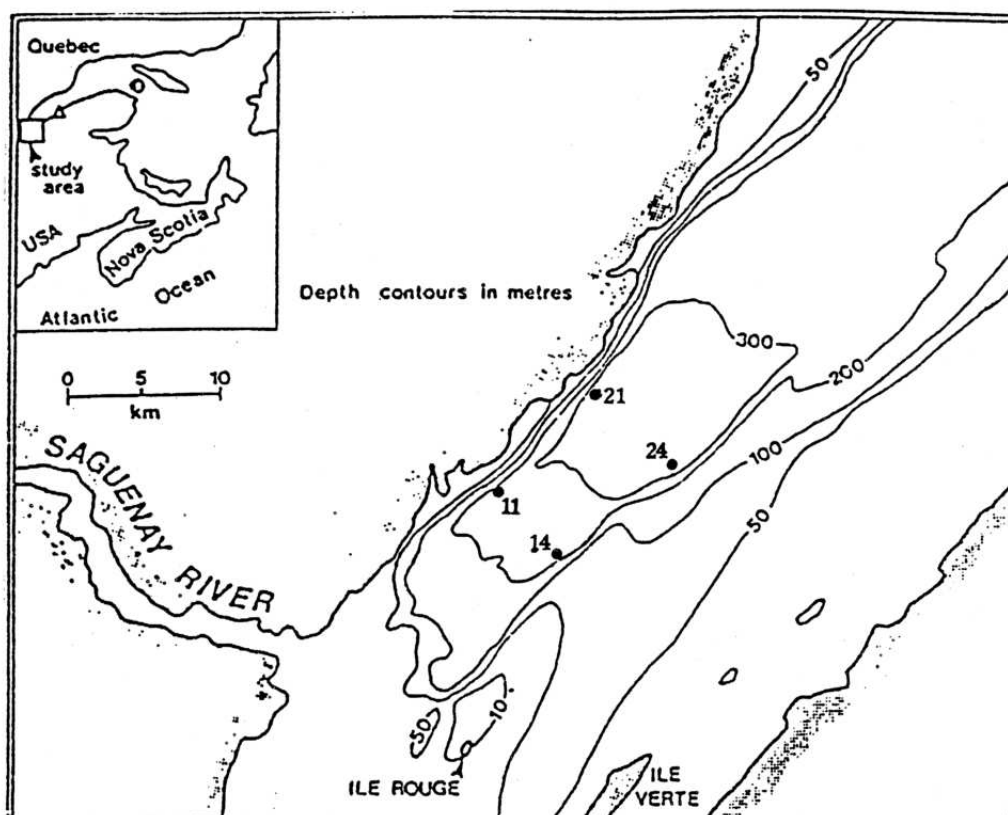
Figure 7.2: Study area in the Lower St. Lawrence estuary. Adapted from Ingram (1979).

24.

The V-shaped solid lines added to Figure 7.1 indicate the main water masses found, except for some surface cooling at stations 21 and 24, and surface warming at station 11 and, to a lesser extend, station 14. The deepest waters have a uniform T–S distribution for all stations. The T–S relation above the temperature minimum is tightest for Station 11 and 21, consistent with advection of undisturbed water into what is assumed to be a stronger mixing region.

Ingram (1979) found that the temperature minimum increased by less than 1°C between May 1973 at Gaspé and July 1973 near station 21. This 3-month interval corresponds to the advection time between the two locations. He used a simple advection-diffusion model of the temperature minimum to estimate mixing along the Laurentian channel. He could explain half of the temperature change by using $K_\rho \partial^2 T/\partial z^2 = 10^{-7}$°C s^{-1} and $K_\rho = 2 \times 10^{-5}$ m^2 s^{-1}. Ingram obtained these mixing rates from internal tide modes (Forrester, 1974) and an eddy diffusivity parameterization in term of the gradient Richardson number (Jones, 1973).

Since the minimum temperature at station 24 varies by more than 1°C, it is noteworthy that 3 months of diffusion along the Laurentian channel is overwhelmed within a time which could be presumed to be a few tidal cycles at most. This is presumed to occur here because of the larger internal tides combined with the poorly understood circulation at the slope of the head of the channel, or between the channel and the South bank of the lower estuary. Water masses which do not usually come into contact probably meet, and their mixing results in the various water masses forming the temperature minimum at station 24. Several profiles at station 24 contained intrusions between the two end water masses between $\sigma_t = 24$ and $\sigma_t = 26$.

All profiles at station 14 have an anomalous water mass corresponding to the dashed line shown on Figure 7.1. The water mass ends on its dense side with an isopycnal intrusion around $\sigma_t = 25$. If the water mass is extended to $\sigma_t = 26$, it corresponds more or less to the upper temperature minimum of station 24. Thus the end points of this water mass could be at $\sigma_t = 22$ and $\sigma_t \approx 26$ on the main T–S lines

described by the 'V'.

The water mass on the dashed line is usually found on the South side of the channel, where circulation is down-channel. However, it appears at lower densities at station 11 some of the time.

The intrusions might result from 'horizontal' spreading of mixed layers formed by mixing light waters with dense water heaved over the sill by the large isopycnal displacement of the internal tide. The intrusions provide clues to the circulation and mixing at the head of the channel; they also complicate the sampling of overturning events. It would be preferable to use temperature alone from the CTD to identity overturns because temperature is easier to measure accurately within overturns than density (*e.g.* one sensor instead of combining both temperature and conductivity within the enhanced gradients of overturns). It is possible to use temperature alone for most of the profiles of station 11 where the T–S relation is very tight. Yet in many cases intrusions can be falsely interpreted as overturns. The combined use of conductivity and temperature in the demanding environment of overturns must then be used if overturns are to be identified. In known intrusions, no attempt will be made to identify any overturns.

7.3   Internal Tide Description

If the mixing at the head of the channel is thought to be forced mostly by the shear associated with the internal tide, then analytic expressions of the internal tide could potentially be used to compare expected Ri_g to observed Ri_g and overturning events, and to fill the gaps where and when no data were taken.

In this section, I will briefly discuss how my observations differ from the literature on the internal tide, and why using previous results and analytical expressions of the internal tide have very limited application in predicting mixing. Work presented here is by no means the final word, but should serve as a useful guide for future work.

Forrester (1974) provided a description of the internal tide in the Laurentian channel from current-meter measurements from nine moorings, located from the head of the channel to over 100 km toward the mouth of the estuary. He fitted the observations to modes associated with internal Kelvin and Poincaré modes of various tidal frequencies, obtaining the vertical modal structure from a mean density profile. Data were consistent with an internal Poincaré wave in the second vertical mode (one zero-crossing of isopycnal displacements at 72 m; the first vertical mode is evanescent in a 25 km channel width using Forrester's density profile) and first lateral mode, at frequency M_2 and wavelength of 60 km, propagating toward the Gulf in a channel of 320 m depth and 25 km width. Forrester also found some evidence for the presence of a Kelvin wave at diurnal frequency, also propagating out of the estuary. Since most of the energy is found at semidiurnal frequency in the lower estuary, the Poincaré mode is addressed specifically here.

This section will address the following points:

- Effect of the mean density profile on modal shapes, showing that small changes in the profile lead to different modal shapes (mostly in the depth of the node for the second vertical mode).

- Comparison of two possible modal shapes with data, showing that an alternate choice than Forrester's leads to a more representative node depth for the second vertical mode.

- Restrictions on vertical modes from channel width, due to the dispersion relation, showing that the channel may be too narrow at the head to support the second vertical mode, even though it is observed.

- Comparison of observed shears to second vertical mode, showing that the variability of the shears could not be adequately modelled as simple internal tides to obtain analytical forms for Ri_g to compare against observed mixing. The observed shear will thus be compared to mixing, but no attempt will be made

to use analytical forms of Ri_g to predict where mixing should occur, and how much it should mix.

7.3.1 Mean Density Profile in Present Data Set—Effect on Modal Shape

In Forrester (1974), the mean density profile was approximated by the wholly empirical formula

$$\rho(z) = \rho_o e^{-a/(z+b)} \tag{7.2}$$

where ρ_o was set to 1028 kg m^{-3}, $a = 0.2016$ m and $b = 29.29$ m.

This density profile yielded the vertical modes of the wave, $\eta(z)$, as the eigenfunctions of

$$\eta_{zz} + \left[\frac{N^2 - \omega^2}{c_n^2}\right]\eta = 0 \tag{7.3}$$

where η is isopycnal displacement, subscript z indicates differentiation with respect to z, N^2 is the stability—a function of $\rho(z)$—and ω is the wave frequency (M_2 tidal).

Application of the surface and bottom boundary conditions $\eta(0) = \eta(H) = 0$ to the solution of (7.3), neglecting ω^2 with respect to N^2, sets the eigenvalues c_n for the n vertical modes of oscillation.

Figure 7.3A compares the density profile chosen by Forrester to profiles of the present data set at stations 21 and 24, covering about a tidal cycle at each station. The stations are located on either side of the channel (see Figure 7.2). Water on the North side is saltier then on the South side because of the sideways estuarine circulation. Flow on the North side is mostly up the estuary, and barely reverses on ebb flow. The fresher outflow is mostly restricted to the South side.

Figure 7.3B shows the rms difference in density between observations and the best fitting profiles for various values of a and b (choosing ρ_o at each a–b pair to minimize the difference). Forrester's choice is shown with a dot, as well as an alternate choice at $a = 0.03$ m, $b = 2$ m. While Forrester's choice results in slightly less error, and arguably a much better fit at depth (See panel A), the alternate choice
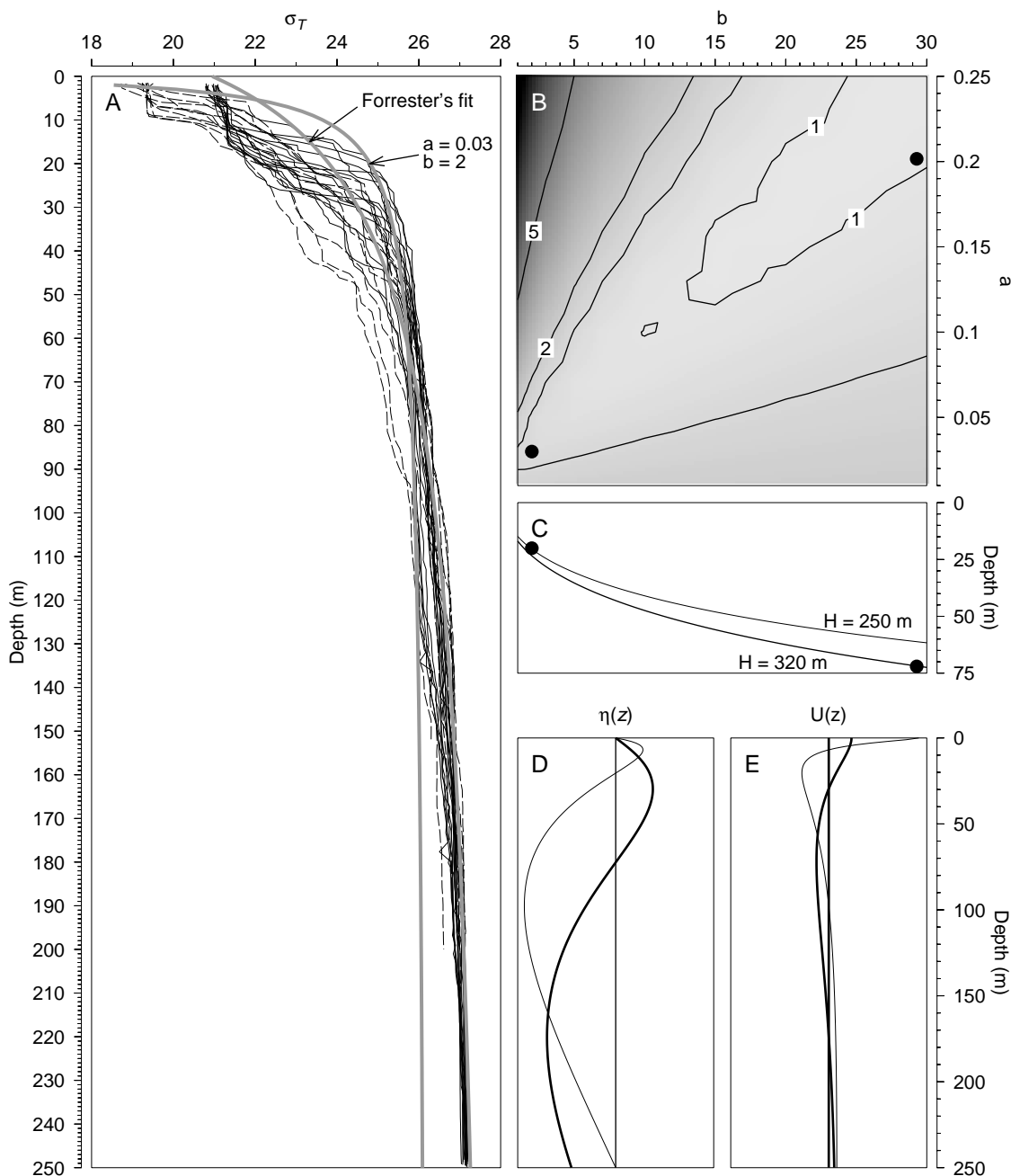
Figure 7.3: Mean density profile and its effect on node depth. **A-** Observed density profiles over nearly a tidal cycle at station 21 (solid) and 24 (dash) compared to Forrester's fit and an alternate fit; **B-** rms difference between observations and best fitting density profiles of a–b pairs. Dots shows a–b values for profiles in A; **C-** Depth of node of the second vertical mode for a channel of depth 320 m (thick) and 250 m (thin) as function of b; **D-** Eigenfunction for isopycnal displacements, η, of the second vertical mode for Forrester's fit (thick) and $b = 2$ m (thin); **E-** Eigenfunction for velocity, $d\eta/dz$, of the second vertical mode for Forrester's fit (thick) and $b = 2$ m (thin).

perhaps approximates the steppiness of shallow observations better, although only very crudely with a sharper pycnocline. Forrester's choice may be a smoothed best fit to an average that is never observed[2]. In any case, the selection of a mean profile is not very sensitive to the parameter b.

In panel C, the depth of the node of the second vertical mode is shown. It depends only on the parameter b and the depth of the channel. Forrester used a depth of 320 m, suitable for the channel as a whole; A curve for $H = 250$ m is also shown because it is more representative of the depth at our stations near the head of the channel. Note that Forrester's density profile results in a node at 72 m in a channel of 320 m depth. The node is much shallower (20 m) for $b = 2$, with not much dependence on the depth of the channel.

In panels D and E, the vertical modes for isopycnal displacements (D) and velocity (E) are shown for both $b = 29.29$ m (thick line) and $b = 2$ m (thin line). In conclusion to Figure 7.3, very different vertical modes are obtained with two mean density profiles of slightly different errors with respect to observations. Forrester's mean profile may thus lead to wrong modes. The alternate choice for b will be shown shortly to qualitatively better match observations. Perhaps future work should select modes by fitting to isopycnal displacements rather than to density profiles.

7.3.2   Comparison of Modal Shapes With Present Data Set

Figure 7.4A shows isopycnal displacements for station 21 and 24 versus tidal phase (same data as in Figure 7.3A). Sampling at station 24 started 47 hours after sampling commenced at station 21, but the data are plotted versus barotropic tidal phase such that they can be compared, with Station 24 repeated. In panel B, the isopycnal displacements predicted from $b = 2$ m in Figure 7.3D are shown for comparison.

There appears to be a phase lag with depth of the observed isopycnal motions, with deeper isopycnals moving later. More importantly, there is no node at 72 m as

---

[2]The time-average at every depth is influenced by the heaving due to the internal tide, because this motion was not removed before the mean density profile before it was fitted
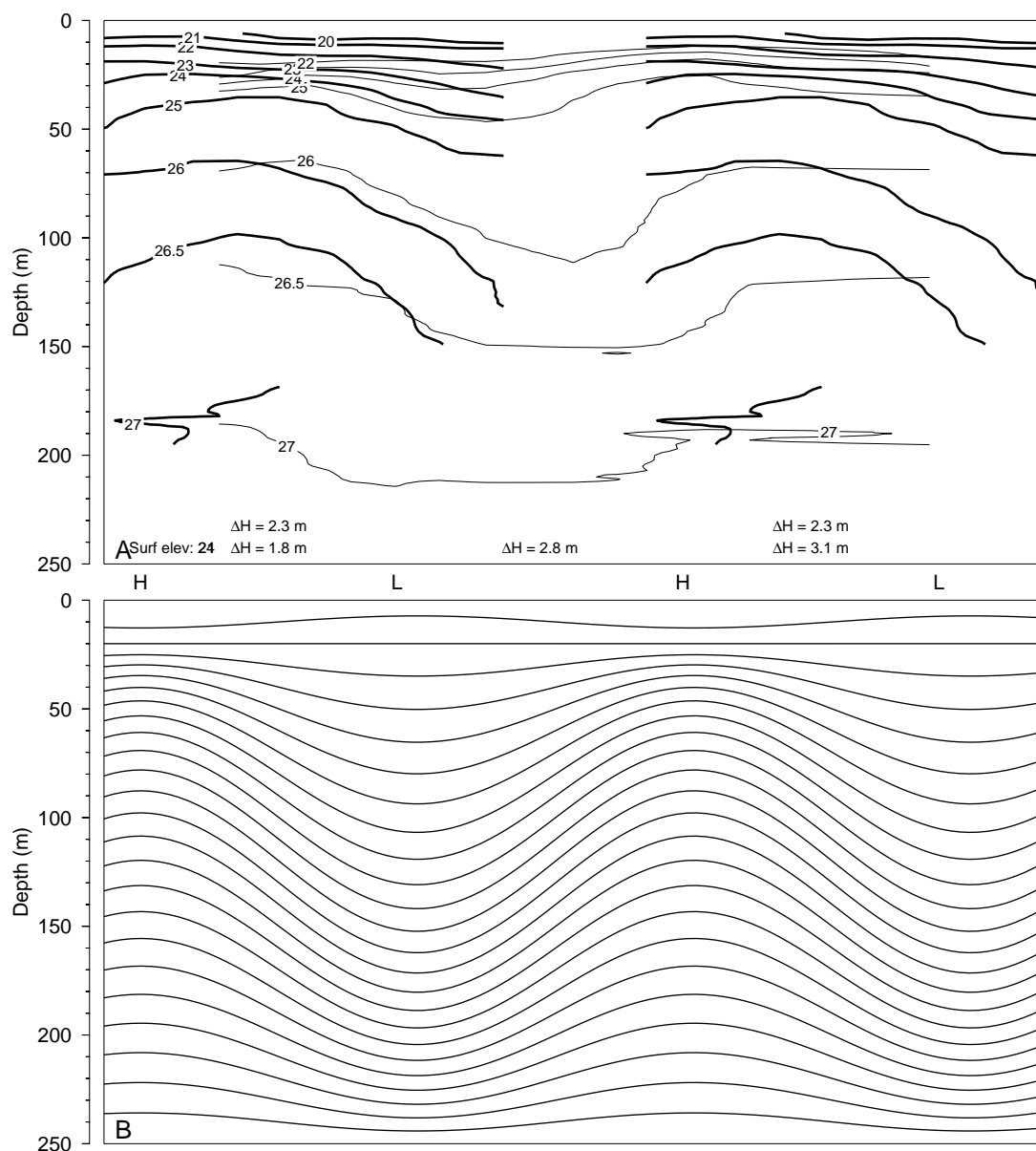
Figure 7.4: **A-** Isopycnal displacements for station 21 (thin line) and 24 (thick line) *vs* tidal phase. Station 24 is shown twice to better compare it with station 21. The tidal elevations indicated are surface elevation differences between high and low tides. High tide is indicated by H, low tide by L; **B-** Theoretical isopycnal oscillations for the second vertical mode with density profile described by (7.2) with $b = 2$ m. The phase with respect to the barotropic tide is not determined, and can be offset in panel A. The inversions on both series at high tide is due to overturning in both cases.

Forrester's fit predicted. On the data shown here, there is only a hint of isopycnal motion near the surface to indicate whether the second mode exists at all. If it does, its node is much shallower that predicted by Forrester (See also Figure 7.7B for a more evident node at 20 m at station 11). It appears that the modes obtained using $a = 0.03$ m and $b = 2$ m represent our data better than those chosen by Forrester.

7.3.3 Restrictions on Vertical Modes And Along-Channel Structure of the Internal tide

The non-uniformity of the channel brings about a problem when the possibility of existence of various vertical modes is considered. The dispersion relation for Poincaré waves in the nth vertical mode and mth lateral mode is

$$k_{nm}^2 = \frac{\omega^2 - f^2}{c_n^2} - \lambda_m^2 \tag{7.4}$$

where k_{nm} is the along-channel wavenumber, f is the Coriolis parameter and $\lambda_m = m\pi/W$ is the cross-channel wavenumber in a channel of width W.

Forrester used an average channel width of $W = 25$ km. Substituting this value into (7.4), the first vertical mode is not possible because k_{11} is imaginary. Thus Forrester looked for a fit against the second and higher modes. However, setting W to the channel width at the head of the channel, approximately 7.5 km, makes λ_1 increase over 3-fold. In this case, only the sixth and higher vertical modes are possible in this linear theory. Obviously, the observed isopycnal motions in Figure 7.4A are not in such a high mode.

An imaginary wavenumber translates to a non-propagating wave with an along-channel decay length-scale of k^{-1}: an evanescent mode. The wavenumber, describing a propagating or evanescent wave, can be explored for various values of a and b. Substituting the density profile (7.2) into the governing equation (7.3), and using the boundary conditions $\eta(0) = \eta(H) = 0$, the following expression for c_n is obtained

$$c_n^2 = \frac{ga}{\frac{1}{4} + \left[\frac{n\pi}{\ln((H+b)/b)}\right]^2} \tag{7.5}$$

Location	Geometry	$a = 0.03$ $b = 2$	$a = 0.2019$ $b = 29.29$
Far-field (Forrester)	$W = 25$ km $H = 320$ m	$2\pi/k_{21} = 35$ km (wave)	$2\pi/k_{21} = 60$ km (wave)
St. 21–24	$W = 13.5$ km $H = 320$ m	$k_{21}^{-1} = 10$ km (decay)	$k_{21}^{-1} = 6$ km (decay)
St. 11–14	$W = 7.5$ km $H = 250$ m	$k_{21}^{-1} = 2.8$ km (decay)	$k_{21}^{-1} = 2.6$ km (decay)

Table 7.1: Summary of wavenumber k_{nm} for the two sets of a and b values considered, at three locations along the channel.

Substituting this into the dispersion relation (7.4) yields

$$k_{nm}^2 = \frac{8.065 \times 10^{-9} \text{s}^{-2}}{ga} \left(\frac{1}{4} + \left[\frac{n\pi}{\ln((H+b)/b)} \right]^2 \right) - \left(\frac{m\pi}{W} \right)^2 \qquad (7.6)$$

at tidal frequency and 48° Latitude North[3]. This form of the dispersion relationship is used to construct Figure 7.5, describing k_{21} versus parameters a and b for 3 cases of channel sizes H and W. The wavenumber is very dependent on the parameter a. Figure 7.5 is summarized in Table 7.1 for the two sets of a and b parameters chosen thus far.

It is unclear from conflicting isopycnal data (not shown) whether the amplitude of the internal tide is reduced from stations 11–14 to 21–24. However, as shown in Table 7.1, the channel widens quickly such that the decay length-scale for the second vertical mode grows quickly from 3 km to 10 km at the head of the channel. It is thus possible that the observed second mode at the head of the channel is evanescent, but that some or even most of the energy leaks out as the channel widens.

---

[3]Neglecting the small contribution from the $\frac{1}{4}$ term, an nth vertical mode is possible if

$$\ln(1 + \frac{H}{b}) < 2.869 \times 10^{-5} \frac{n}{m} \frac{W}{a^{1/2}}$$

where a, b, H and W are in meters. Using Forrester's a and b values but local values of $H = 250$ m and $W = 7.5$ km, the first possible mode is the sixth. Using $a = 0.03$ m, $b = 2$ m, $H = 250$ m and $W = 7$ km, the first possible mode becomes the fourth.
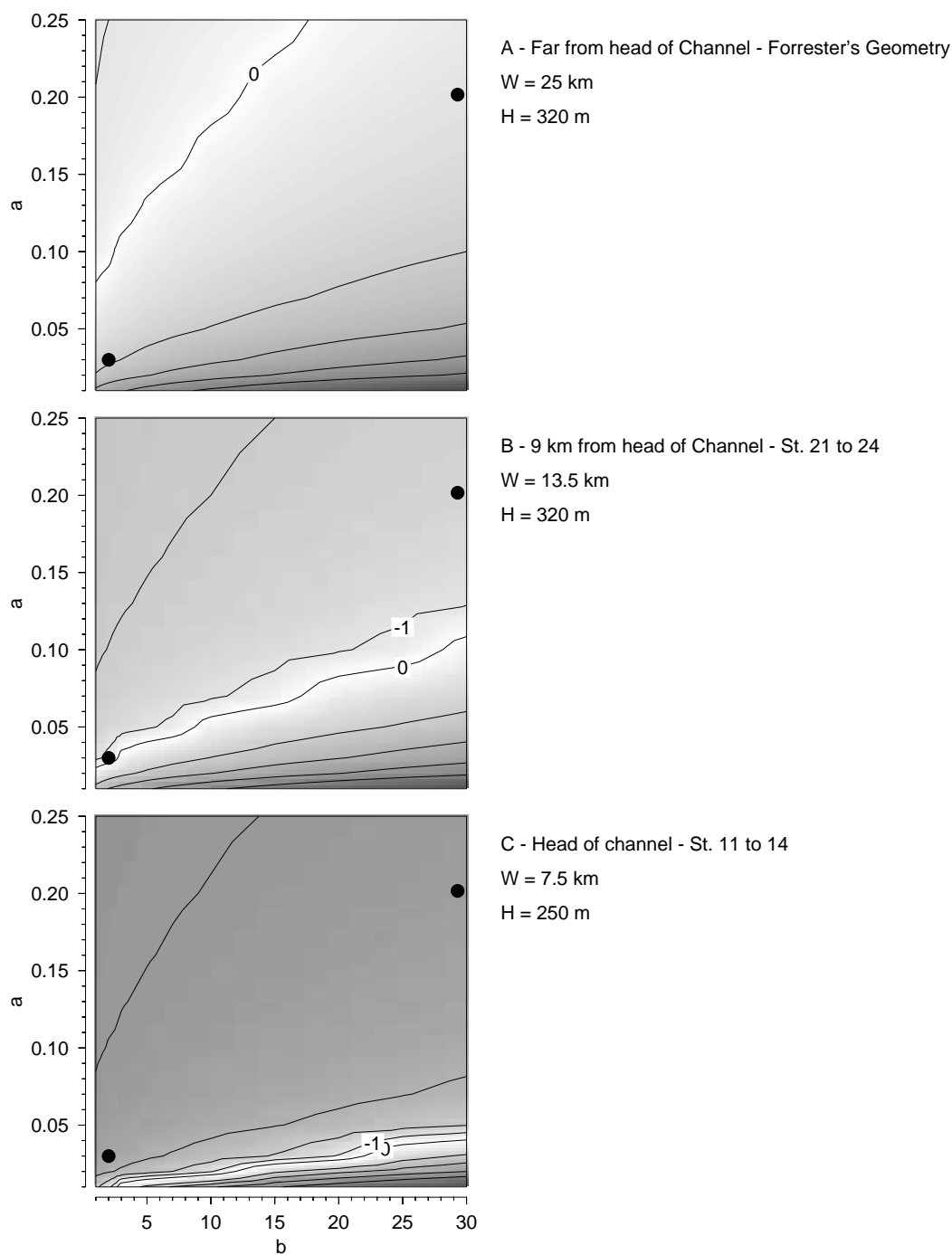
Figure 7.5: Wavenumber k_{21} ($\times 10^4$) for various a and b values. Negative values—found above the zero line—are in fact imaginary (e-folding decay wavenumber). Dots indicate both Forrester's choice for a and b and the alternate choice with second mode node depth of 20 m. **A-** $W = 25$ km and $H = 320$ m, corresponding to the far field geometry of the channel used by Forrester; **B-** $W = 13.5$ km and $H = 320$ m, corresponding to the channel geometry at stations 21–24; **C-** $W = 7.5$ km and $H = 250$ m, corresponding to the channel geometry at stations 11–14.

Unfortunately, to confuse the issue, it is possible that the approximation of a rectangular channel shape is erroneous, and that accommodating a proper (wider) shape would yield better results. The width of the deep part of the channel varies from 7 km at the head, to 25 km further down-channel. But the channel opens out to the South bank at approximately 60 m at the head and at 30 m further Northeast. The extended width of the head of the channel, taken at the 50 m isobath, is 16 km (compared to 7 km in the deep channel). The second vertical mode would be free to propagate in a channel of that width.

Also, a propagating Poincaré wave is not symmetric in the cross-channel direction (I have not worked out the cross-channel modulation of the evanescent modes of a Poincaré wave). In the first cross-channel mode, isopycnal displacements should have a node usually closer to (in this case) the South side of the channel. The isopycnal displacements should be observed to change sign from side-to-side of the channel. This is not observed in Figure 7.4, nor are displacements at least reduced on the South side. It is possible that the cross-channel structure of the evanescent modes would predict this. It is also possible that the full estuary width should be used, in which case Station 24 would be close to the channel center rather than close to the edge. In that case the observed cross-channel phase of isopycnal displacements would be consistent with theory.

7.3.4   Observed Shears

Figure 7.6 shows observed isopycnal displacements and shears at Station 14. Data were sampled while the ship drifted in proximity of the station. Sampling was interrupted and the ship was repositioned after a drift of 0.5 nautical miles along-shore or 0.25 nautical miles across-shore from the station. The empty bands in Figure 7.6C are re-positioning intervals. All finestructure data presented here have these gaps.

Strongest shears were expected near the surface (from Figure 7.6B). Although this pattern is somewhat observed in panel C, there is a lot more structure than expected, including some unexpected rotation of the shear vectors. Shear structure appears

layered along isopycnals (panel D). The average of the surface density slice is taken in panel E ($\sigma_t < 21$) and a shear vector rotating clockwise at tidal frequency provides an adequate fit, as seen by low residuals of unorganized patterns in panel F. Note that along and cross-channel components of shear were independently fitted for phase and amplitude; both were fitted best with the same phase, such that the shear ellipse is aligned along the axis of the channel. The fitted near-surface clockwise-rotating shear vector is consistent with a Poincaré wave. Its phase is along-channel simultaneously with maximum isopycnal displacements (near high tide, indicated with an 'H' between panels A and C). This is also consistent with a Poincaré internal tide anywhere across the channel, with the possibility of a sign change of the shear.

While some of the observed shear seems consistent with a Poincaré internal tide, the cross-channel modulation was not compared to theory, nor were amplitudes (because of the evanescent mode). Some of the shear variability does not compare well with predictions in panel B. There is no reason to believe that observed gradient Richardson numbers should compare well to those predicted from theoretical shears and the idealized density profile. Even if the onset of mixing could be predicted, theory would then have to account for the density profile evolving into layers.

7.3.5   Summary of the Internal Tide

In this section, it was observed that

- Forrester's mean density profile does not match the large gradients near the surface.

- A wide range of analytical density profiles with various parameters a and b in (7.2) can fit observations with similar errors.

- The depth of the node of the second vertical mode depends greatly on b. It is at 72 m for Forrester's profile ($b = 29.29$), and at 20 m for $b = 2$.

- Isopycnal displacements at Stations 21 and 24 are consistent with $b = 2$, rather than with $b = 29.29$.
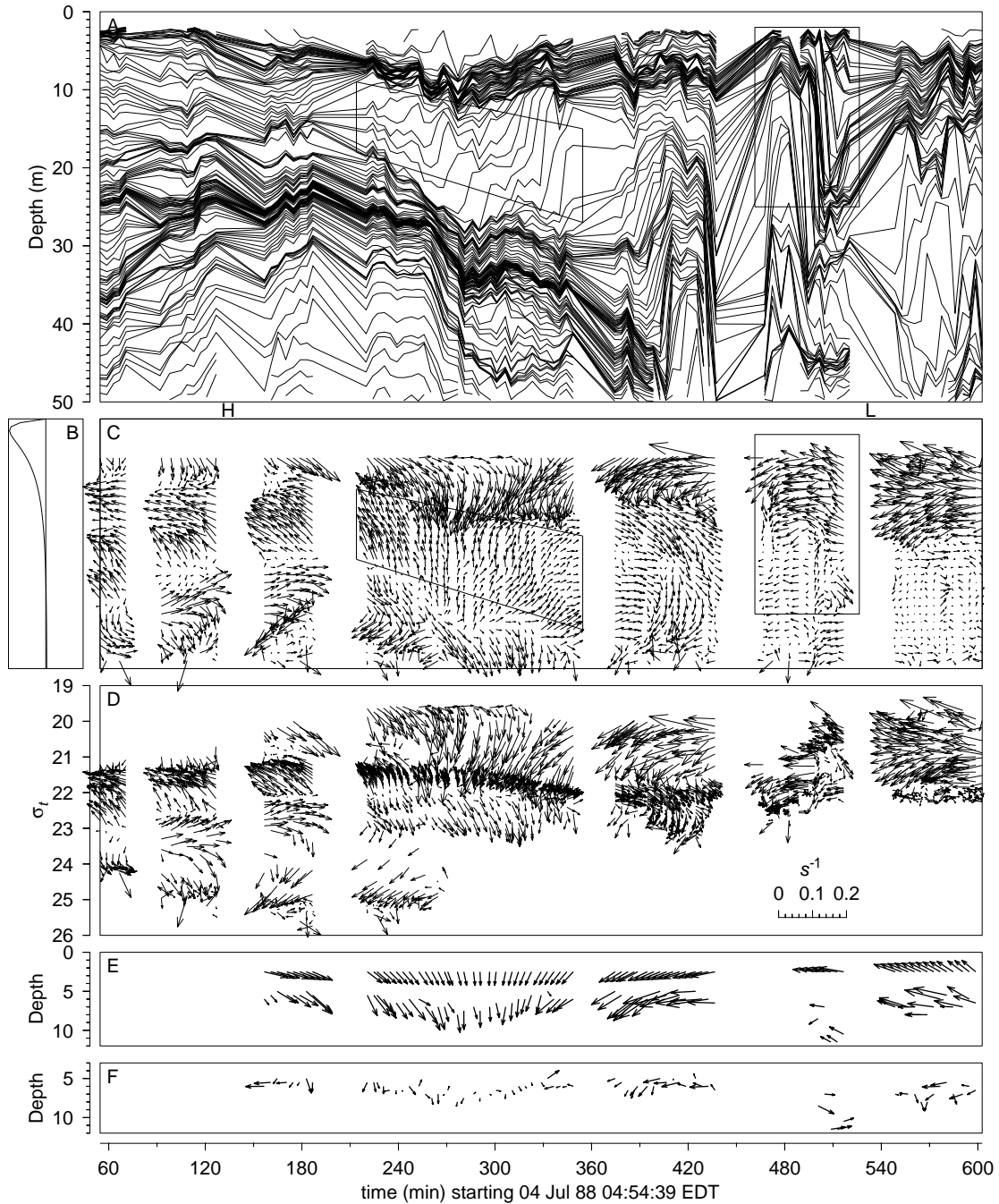
Figure 7.6: Shear and isopycnal displacements at Station 14. **A-** Isopycnal displacement obtained from CTD casts sampled approximately every 4 minutes, collected at the same time as the shear vectors of panel C; **B-** Theoretical Poincaré shear depth-modulation for $n = 2$, $b = 2$ m and $H = 250$ m; **C-** Shear vectors from 0 to 32 m. Towards the right is down-channel and downwards is toward the South side of the channel. Scale indicated in panel D; **D-** Shear plotted against density; **E-** Bottom arrows: average shear for $\sigma_t < 21$. Top arrows: Tidal-frequency rotating vector least-squares fit to bottom arrows; **F-** Difference between average shear and fit in panel E; Boxed areas in A and C indicate mixing layers described in later sections. Letters H and L between panels A and C indicate high and low tide.

- The observed second mode may be evanescent at the head of the channel due to the narrow width of the deep channel. The e-folding distance varies quickly from 3 km to 10 km between stations 14 and 11, less than 10 km apart. Thus large shears measured at the head may only be typical at the head due to a non-propagating wave. Alternatively, the second mode is free to propagate if the full width of the estuary is used instead of the deeper Laurentian channel.

- Surface shears are consistent with a Poincaré internal tide at tidal frequency (M_2), but there are some inconsistent deeper large shears that seem homogeneous in isopycnal layers.

These observations add to the body of knowledge of the internal tide at the head of the Laurentian channel. They also raise questions that future investigators should consider. Modal fits are not a viable solution to predicting mixing because of the variability of the shear and of stratification so that Ri_g cannot be modelled well by a simple analytical form, and because of the effect of mixing itself on the shear and density profile. The internal tide must be considered as a measured but mostly unpredicted forcing, and go on from there to compare it with observed overturning. It is unclear if mixing rates measured here will be applicable to areas further down-channel because it is uncertain if measured shears are representative of down-channel forcing (evanescent or propagating wave?). The mixing area could be limited to only a few kilometers from the head, or it could extend further down-channel.

7.4   A Mixing Layer with a Tight T–S relation

Density stratification above the temperature minimum of the Laurentian channel is controlled by the salinity gradient. The effect of the salinity gradient is close to 6 times greater than that of the temperature gradient. In spite of this, temperature fluctuations can be used directly as tracers of density fluctuations on the North side of the channel in the tightest parts of the T–S relation (See station 11 on Figure 7.1).

An example is shown on Figures 7.7 and 7.8 showing 5.5 hours of data collected at station 11 (a shorter and different series than those presented on Figure 7.1). Figure 7.7A shows the temperature difference between observed temperature and the temperature at the observed density on the main surface T–S water mass in Figure 7.1; this shows how far off the main T–S characteristics the water is. Data gaps are from ship repositioning. All CTD profiles were taken from the surface to 50 m, at approximately 4 minute intervals. The sea state was usually calm, with very little ship pitch and roll to influence CTD drop velocity (typically 50 cm s^{-1}, with 25 Hz sampling yielding over-resolved samples at 2 cm vertical intervals). Figure 7.7B shows isopycnal displacements. Figure 7.8A shows gradients Richardson numbers, calculated as described in section 7.1.1, Figure 7.8B and C shows gray scales of ξN values calculated over individual overturns by re-ordering density and temperature profiles respectively, using the unfiltered raw CTD data.

Even on a broad scale, it is difficult to establish a clear relation between Ri_g and ξN in Figure 7.8. Some areas where $Ri_g < 1/4$ have little mixing activity (*e.g.* between hours 4.5 and 5 and at about 10 m depth). Many reasons could account for this, such as the volume averaging of the ADCP or the difference in sampling location. However some higher intensity mixing layers do appear related to low gradient Richardson numbers. This section will focus on one layer where there appears to be a relationship between these quantities. It is an example of a best-case scenario where temperature measurements are used to observe overturning events.

The boxes in Figures 7.7 and 7.8 encompass what appears to be the beginning of a mixing layer in an environment of tight T–S relation. Figure 7.9A shows the
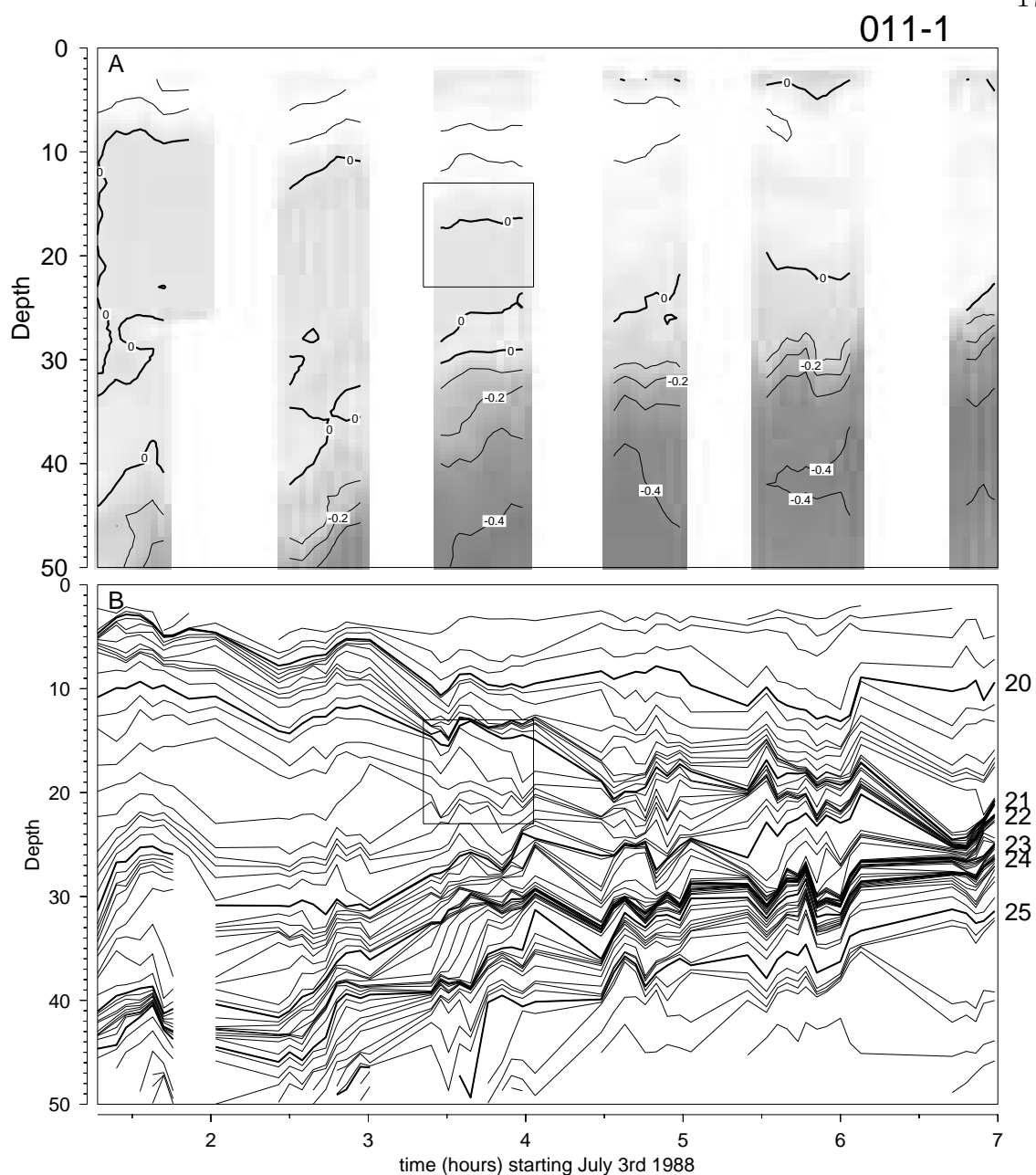
Figure 7.7: Isopycnal displacements and temperature anomaly at station 11. **A-** Temperature anomaly versus depth, where temperature anomaly is defined as $T = 37.284 - 1.445\,\sigma_t$, the difference between observed temperature and that calculated for observed σ_t from least-squares fit between 0 and 6 °C for station 011 on Figure 7.1; **B-** Isopycnal displacements; The box indicates a mixing layer discussed in the text. The gaps in A are due to ship repositioning; contours are constructed from vertical profiles typically separated by 4 minutes in time.
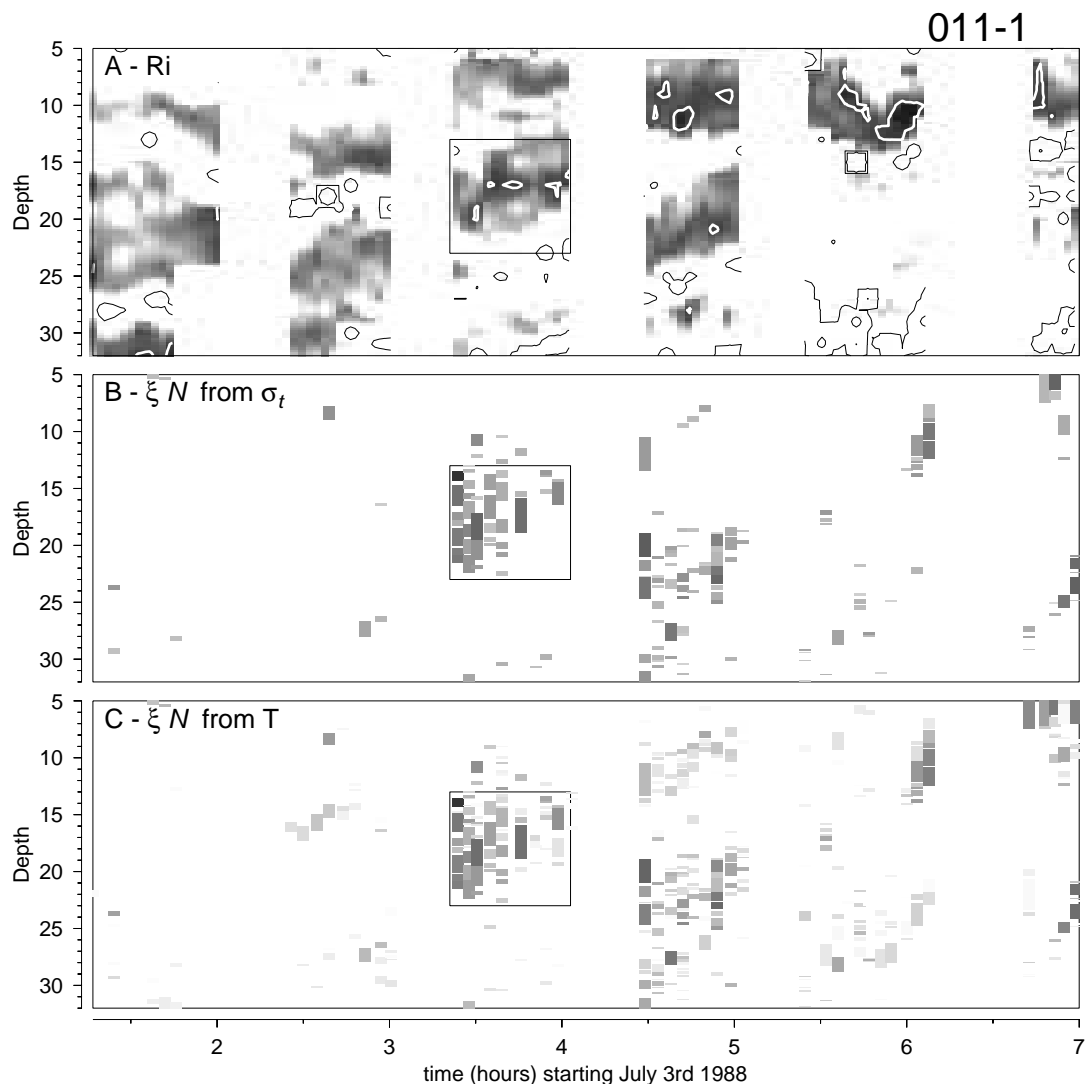
Figure 7.8: **A-** Gradient Richardson numbers at station 11. Black on white contour line is for $Ri_g = 10$, shaded areas for $Ri_g < 1$ and white on black contour is for $Ri_g = 1/4$; **B-** Quantity ξN calculated for each overturn measured using density. Only overturns with rms $\rho' > 0.005$ kg m^{-3} are shown. Gray scale is log-linear from 10^{-8} W kg^{-1} (white) to 10^{-4} W kg^{-1} (black); **C-** ξN calculated for each overturn measured using temperature as density tracer. Gray scale same as B. The box on all panels indicates a mixing layer discussed in the text. The gaps correspond to sampling interruption due to ship repositioning.

10 temperature profiles in this patch. Notice the richness in finestructure in the first few profiles compared to the last. This could suggest the evolution of a mixed layer, but the difference in velocity between 3 m and 12 m is of order 15 cm s^{-1}, and is up to 45 cm s^{-1} between 3 m and 22 m (velocities are not shown). These velocities translate to an advection distance of ≈ 400 m and ≈ 1250 m between the ship and the top and bottom of the layer during the 46 minute time span of the sampling. Thus an energy budget would require assumptions about the horizontal structure and will not be pursued here.

Only temperature profiles are shown in Figure 7.9A but density profiles would be fairly close to mirror images. The tight T–S relation in Figure 7.9B shows this. As a further example, Figure 7.9C shows the T–S relation for a part of the first profile shown in Figure 7.9A. There are several overturns with temperature excursions of 0.1 °C which are difficult to see because their deviations from the main T-S line are small (more about this below). As a consequence, temperature inversions can be related to density inversions by a proportionality constant which includes both temperature and salinity effects in density. Figure 7.8 shows both ξN calculated using temperature and density fluctuations.

The T–S characteristics of Figure 7.9C can be related to the measurements of an overturn with a 'perfect' CTD. Assuming that the T–S relation is linear in the water column, then a CTD sampling overturned water will record T and S on the same T–S line as would were the water not overturning. If only points are plotted, a T–S diagram from a perfect CTD would show nothing out of the ordinary. If the measurements are connected by a line, then that line should oscillate between denser and lighter waters found within the overturn on the T–S diagram. This resembles what is seen in Figure 7.9C, with very little deviation off of the main T–S line. When deviations are found, they can be due to enhanced temperature and salinity gradients within the overturn highlighting any sensor mismatch between temperature and conductivity sensors. If the deviations are isopycnal, rather than on the main T–S line, then it is likely that an isopycnal water intrusion was measured rather than
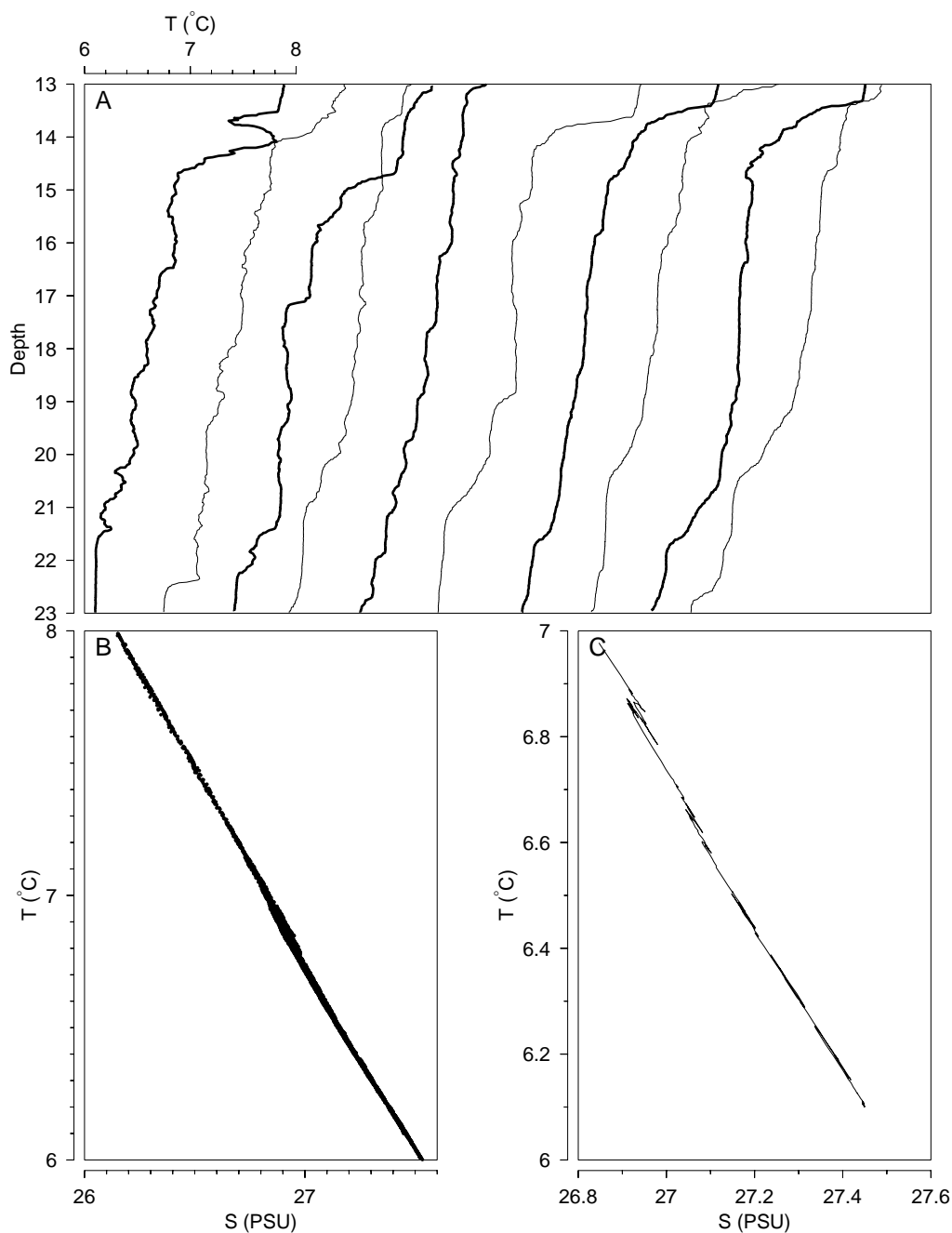
Figure 7.9: **A-** Temperature profiles for the 10 profiles of the mixing layer at station 11 discussed in the text and shown in the box in Figure 7.7. Only down traces of the CTD profiles are used. The profiles are shown alternatively with thin and thick line to better identify them; **B-** T–S diagram for the same 10 profiles; **C-** T–S diagram for part of the first profile. Note the tight relation even within overturning events.

an overturn.

7.4.1 Mixing Rates

Forty-three percent of the length of the profiles in Figure 7.9A is overturning. The average value of $J_b = \xi N$ for the layer is 3.4×10^{-7} W kg^{-1}. Difficulties arise when evaluating a value of the turbulent Froude number to yield an estimate of buoyancy flux from the isotropic growing turbulence model using $J_b = (2/3)\,\xi N Fr_t$. Since the eye picks up some correspondence between ξN and Ri_g in Figure 7.8, some sort of patch averaging seems most appropriate for that layer, if somewhat arbitrary. Values of ξN and Ri_g were time-averaged for the 46-minute time span in each 1-m bin, and averages of ξN were further filtered with a $(\frac{1}{4},\frac{1}{2},\frac{1}{4})$ vertical moving average as Ri_g was in the processing of N^2 and shear-squared. The layer-average value of $J_b = (2/3)\xi N Fr_t \approx (2/3)\xi N \,(0.4\,Ri_g^{-1/2})$ is 1.2×10^{-7} W kg^{-1}, using (7.1) to relate Fr_t to Ri_g. However, if the minimum Ri_g in each 1-m 45-minute bin is used to estimate the Froude number, then the buoyancy flux is estimated as 1.8×10^{-7} W kg^{-1}, 50% greater than by using a mean value of Ri_g. It could be argued that the minimum Ri_g observed is dynamically more important than more average because the overturning can be caused by the lowest Ri_g measured. This factor can perhaps be used as a rough estimate of the error in Fr_t.

The average stratification in the layer is $N^2 = 10^{-3}$ s^{-2}. Combined with the buoyancy fluxes from both models two and three, this yields an eddy diffusivity of $K_\rho = J_b N^{-2} \approx 1$ to 3×10^{-4} m^2 s^{-1} (Which model should be most suitable will be discussed in section 7.7). Some averaging is required to compare this value to Ingram's mean value along the channel ($K_\rho = 2 \times 10^{-5}$ m^2 s^{-1}). If only one such layer occurs every tidal cycle, mixing for 40 minutes, then the time-averaged K_v would be 5.3% of the layer K_ρ. This is very similar to Ingram's result of 2×10^{-5} m^2 s^{-1}. Considering that Ingram calculated the mixing of a layer (not the entire water column) due to the mixing forcing of the internal tide, it seems reasonable to compare these time-averaged values of K_ρ. Since sampling was only for half a tidal cycle, and that a few

other mixing layers are observed in Figure 7.8, mixing is slightly more intense during this 6-hour observation period at the head of the channel than the average mixing further down the channel (assuming N^2 is comparable in both cases such that K_ρ is an appropriate measure of mixing).

Of course, this is only the mixing from one of the patches on Figure 7.8, which shows only one 6-hour observation. It cannot be assumed that this observation is typical; a few more observations follow.

7.5   A Mixing Layer in a Loose T–S relation

In the previous section, a mixing layer with tight T–S was shown where temperature inversions always correspond to overturning. In this section, a time-series from the South side of the Laurentian channel is presented. It is used to demonstrate how intrusive water masses are the main difficulty in identifying overturns with a CTD, even when one uses density to find inversions.

Figures 7.10 and 7.11 show isopycnals, temperature anomaly, Richardson numbers and the mixing parameter ξN for station 14, as Figures 7.7 and 7.8 did for station 11. The data shown from station 14 is simultaneous with shear measurements shown on Figure 7.6 and with the T–S diagram of station 14 on Figure 7.1. The warm intrusion at $\sigma_t \approx 25$ described in Section 7.2 and observed on Figure 7.1 is evident on the temperature anomaly plot, rising to 30 m at 31 hours. The use of either density or temperature from CTD measurements to identify overturns will not be attempted within this feature. It will be shown here that more subtle T–S features, which are not as evident, also cause problems.

The deep data gap in Figure 7.10A is caused by the processing cut-off of the profiles at 0 °C, above the temperature minimum of the water column.
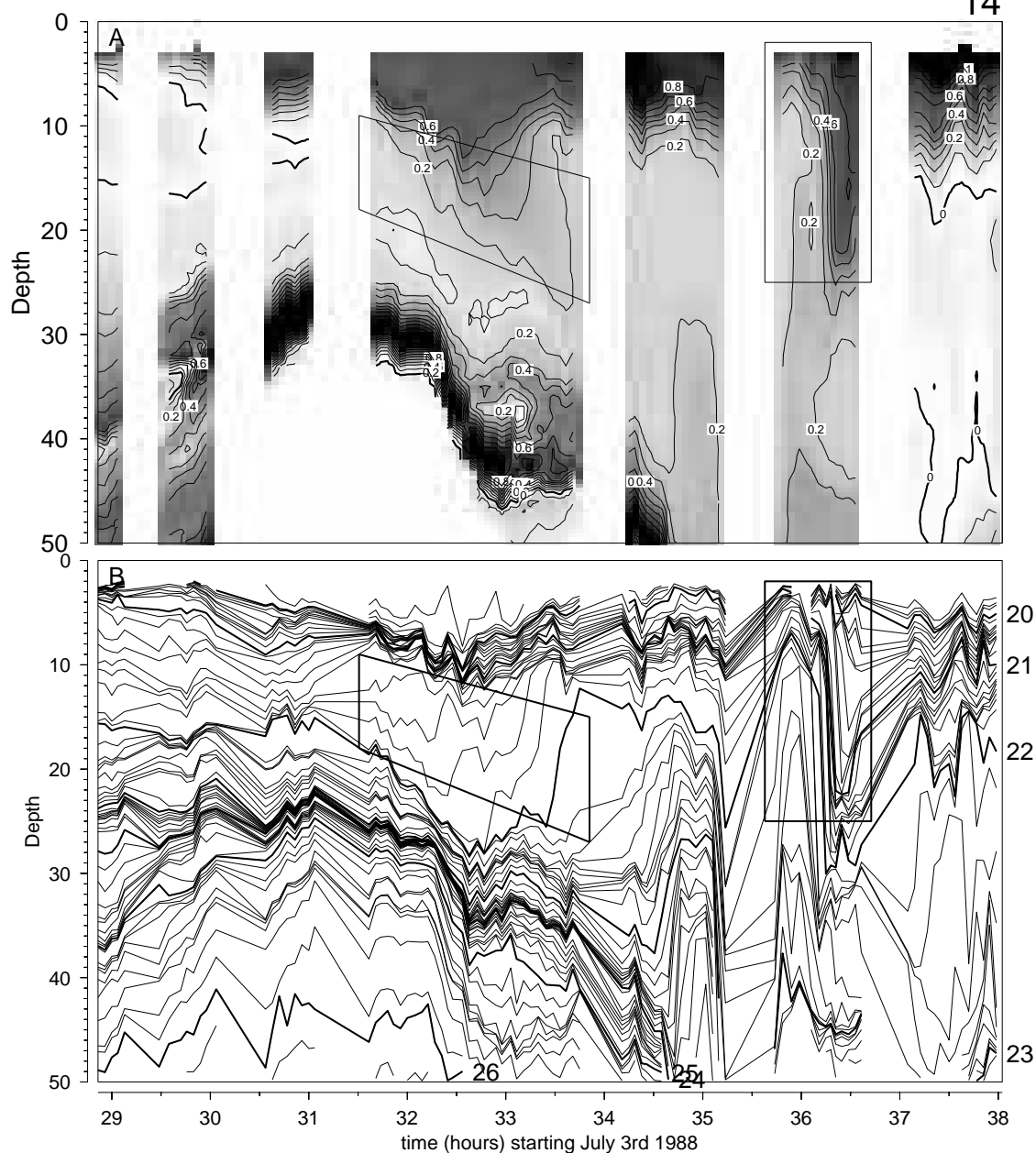
Figure 7.10: Isopycnal displacements and temperature anomaly at station 14. **A-** Temperature anomaly versus depth, where temperature anomaly is defined as $T = 37.2838 - 1.44494\sigma_t$, the difference between observed temperature and that calculated for observed σ_t from least-squares fit between 0 and 6 °C for station 011 on Figure 7.1; **B-** Isopycnal displacements; The boxes indicate a mixing layer and soliton discussed in the text.
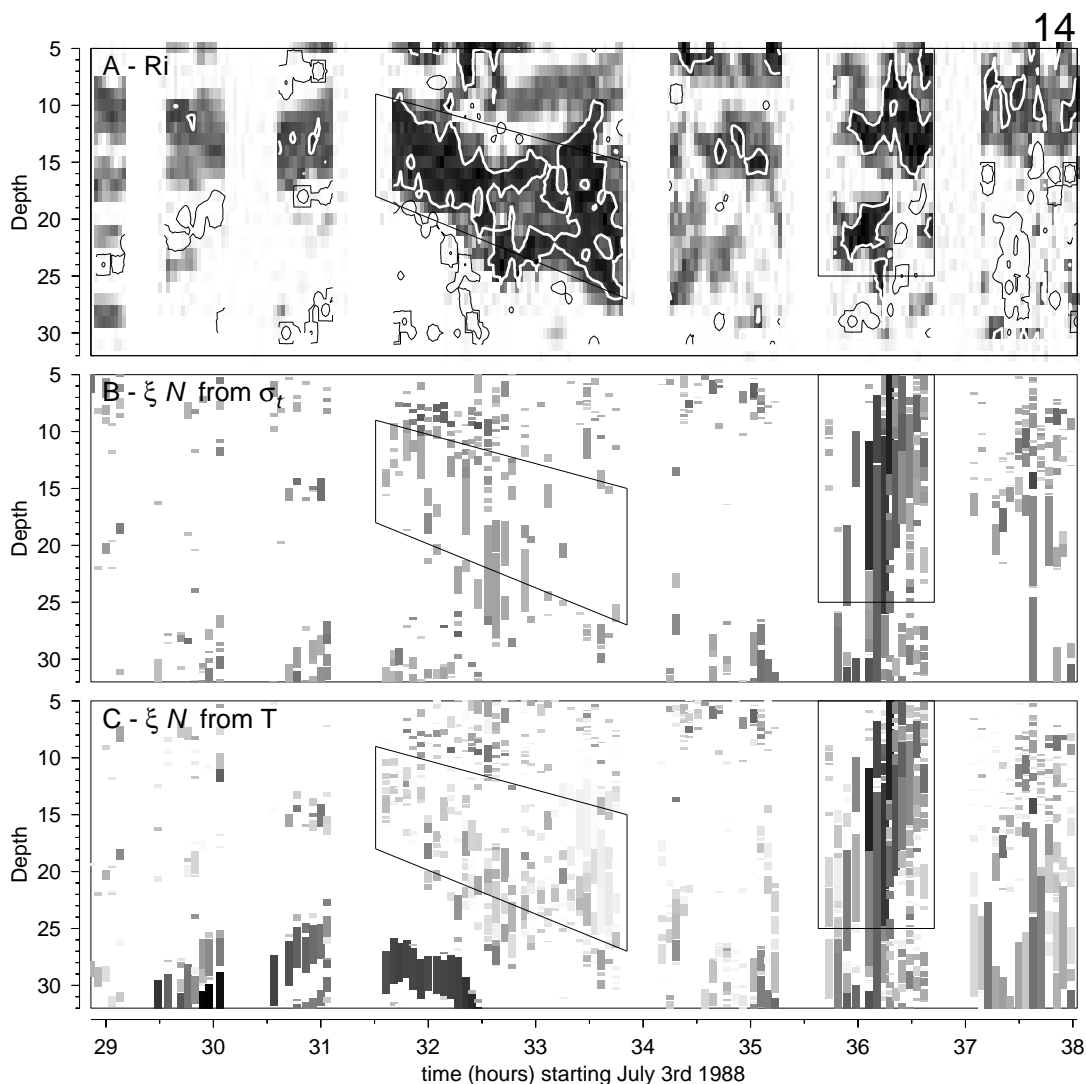
Figure 7.11: **A-** Gradient Richardson numbers at station 14. Black on white contour line is for $Ri_g = 10$, shaded areas for $Ri_g < 1$ and white on black contour is for $Ri_g = 1/4$; **B-** Quantity ξN calculated for each overturn measured using density. Only overturns with rms $\rho' > 0.005$ kg m^{-3} are shown. Gray scale is log-linear from 10^{-8} W kg^{-1} (white) to 10^{-4} W kg^{-1} (black); **C-** ξN calculated for each overturn measured using temperature as density tracer. Gray scale same as B. The boxes on all panels indicates a mixing layer and a soliton discussed in the text.

7.5.1 Intrusive Layers

The first striking feature on Figures 7.10 and 7.11 is the mixing layer shown boxed between 31.7 and 33.7 hours, consisting of 31 CTD casts. Stratification is very low for that depth range, gradient Richardson numbers are mostly below $\frac{1}{4}$ and the layer appears to be overturning throughout. Overturning energy, as measured by ξN, seems rather low. Most of the overturns that occur near the end of the layer are not seen by re-ordering on density because of the high density fluctuation threshold selected[4]

The density range within the first half of the layer is fairly constant, but the layer gets denser during the second half (see Figure 7.10). The T–S relation of the profile of the first half are shown in Figure 7.12A; the T–S relation of the second half is denser and is therefore not in the same T–S parameter space. The water gets progressively warmer with successive CTD casts in Figure 7.12A. It appear that a family of water masses are present, each on a T–S line going from warm-fresh to cold-salty. Within each casts, these water masses are seen intruding into each other. However, the warm-salty to cold-fresh lines joining up these water masses do not lie on isopycnals; the isopycnal for $\sigma_t = 21.6$ is shown on Figure 7.12B.

Figure 7.12A shows what appear to be intruding stratified water masses, with the top water mass denser than the one underneath! Figure 7.12B illustrates this; only parts of the T–S lines which are unstable in density are shown. Instabilities correspond to overturns when they lie on a unique T–S water mass; in this case, it it difficult to determine if these are sampling artifacts or real structure.

Temperature and Conductivity Sensor Mismatch

A possible explanation for the density inversions of Figure 7.12B is time-response mismatch between the CTD conductivity and temperature sensors. This is known

---

[4]Only overturns with an rms density fluctuation of 0.005 kg m^{-3} or greater are shown. Perhaps this limit could be lessened if density were calculated to a forth significant decimal place. With the current density values calculated to three significant decimals, it is difficult to establish a good estimate of the noise level. I opted to err on the side of caution by select only overturns having an rms density fluctuation of 0.005 kg m^{-3} or greater.
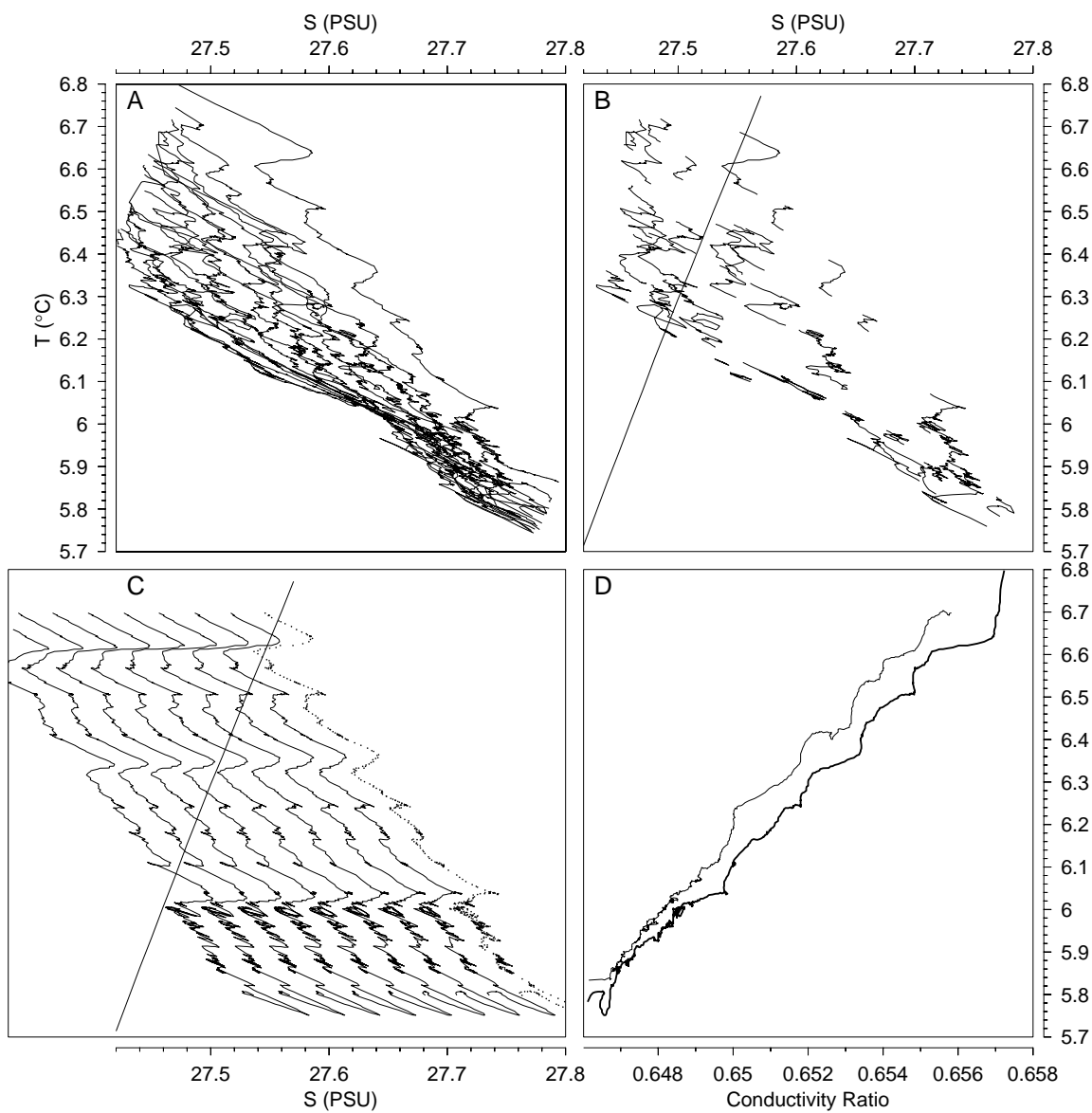
Figure 7.12: **A-** T–S diagram for first 15 profiles of mixing layer described in text; **B-** T–S diagram showing only depth-spans where the density profile is statically unstable. Solid line is isopycnal for $\sigma_t = 21.6$; **C-** T–S diagram for right-most profile in A (dots). T–S lines offset to the left are obtained by using conductivity measurements offset in depth with respect to temperature as explained in the text; **D-** Conductivity ratio versus temperature for profile in C (thick line) and its preceeding profile (thin line).

to result in what is commonly referred to as 'spiking'. Such mismatch is discussed in Perkin *et al.* (1982) and is summarized here. The 14 cm long conductivity cell has approximately instantaneous response to new water when it has penetrated the cell 7 mm past mid-point (although the response is to an average property of the water found between the two electrode pairs, separated by 4 cm). The thermometer is quoted as having a 50 ms response; its time response is said to be adequately represented by a simple exponential decay (Perkin and Lewis, 1982) if the drop speed is held constant. At the descent rate of 50 cm s^{-1}, this corresponds to a length-scale of 2.5 cm. Since ship pitch and roll were minimal on our cruise, this representation is thought to be adequate. Thus time-response mismatches could be reduced by calculating salinity and density by combining conductivity with temperature measured 2 cm later, by which time the sensor has caught up with most of the temperature changes as it can.

Figure 7.12C shows the right-most profile in Figure 7.12A and B with dots. Most of the density inversions consist of many points and so cannot be dismissed as random error. The profiles offset to the left are T–S calculated by offsetting temperature and conductivity by 1 sample ($\approx$ 2 cm), and then 2, and so on to 8 samples of offset. This is much more than could be accounted for from the known sensor mismatch, and none of these offsets resulted in eliminating—or even significantly reducing—the density inversions.

Therefore, time-response mismatch of CTD sensors cannot account for the unusual T–S structure observed in Figure 7.12A, at least using single-pole transfer functions for the temperature sensor and instantaneous but delayed response of the conductivity cell as suggested by Perkin *et al.* (1982).

Conductivity Cell Flushing

Another explanation for the density inversions of Figure 7.12B involves flushing of the CTD conductivity cell. This is a narrow tube 14 cm long within which 2 electrode pairs measuring conductivity are separated by 4 or 5 cm. It is conceivable that the

overturning circulation would be strong enough at low gradient Richardson numbers (which is the case here) to prevent proper circulation through the conductivity cell. However, I will show here that this is unlikely.

While is it true that turbulent velocities increase with decreasing values of Ri_g, a brief look at Figures 7.10B and 7.6C indicates that low values of Ri_g must be mostly due to low N^2. Turbulent velocities are in fact proportional to the inverse of the shear. From (7.1), the originating relation $u' = 0.4NL_T Ri_g^{-1/2}$ is back-tracked. Using $Ri_g \approx 0.15$ and N^2 in the range of 10^{-3} to 10^{-4} s^{-2}, the turbulent velocity is $u' \approx (0.02\text{s}^{-1} \pm 0.01)L_T$. Overturning scales would have to be about 10 m for turbulent velocities to become comparable to the descent rate of the CTD instrument of 50 cm s^{-1}. Overturning scales are typically less than 1 m.

It is also not obvious that the turbulent velocity field preventing proper flushing of the conductivity cell would result in the T–S characteristics of Figure 7.12A. The conductivity ratio between *in-situ* water and standard sea-water is plotted versus temperature in Figure 7.12D. The figure includes the profile shown in Figure 7.12C and the preceeding profile. The curves have a stair-case shape, as might be expected from interrupting the flushing of the conductivity cell. However, simultaneously with conductivity remaining constant, temperature would be expected to quickly decrease and then increase again if the sensor were going through an overturn. This expected signature is not observed.

In summary, then, it remains a puzzle as to whether the density inversions observed in Figure 7.12A are artifacts. A simple scheme of turbulent velocities associated with overturns inhibiting proper flushing of the conductivity cell cannot cause mis-sampling similar to observations.

7.5.2 Mixing Rates

Density inversions found in this intrusive layer do not all occur between different water masses. Most of the inversions found on the left-hand side of Figure 7.12B stay mostly along a single water mass. Also, while mixing intensity appears to wane in

the second half of the layer, the overturns are mostly along a single water mass T–S line (not intrusive). An example is shown in Figure 7.13 where the second last profile is plotted in a T–S diagram. Note how inversions in temperature and salinity stay on the T–S line of the water mass, representative of overturning of the same T–S water mass. Temperature is a good density proxy in this case.

The mixing rates are computed using the last 11 CTD profiles of the layer in 1-m bins in a manner described in Section 7.4.1. The layer-average value of $J_b = (2/3)\xi N F r_t \approx 0.27\, \xi N R i_g^{-1/2}$ is 1×10^{-8} W kg^{-1}. Using the minimum Ri_g observed in each 1-m time-averaged bin to estimate Fr_t leads to $J_b \approx 1.7 = \times 10^{-8}$ W kg^{-1}, 70% higher than with the average Ri_g.

The turbulent Froude number averaged equally over all bins is 0.85. The average of the maximum turbulent Froude number found in each bin is 1.51.[5]

The averaged N^2 was 10^{-4} s^{-2}. The layer-averaged $K_\rho = J_b N^{-2} = 1$ to 1.7×10^{-4}m^2 s^{-1}. These mixing rates will be compared to those of the previous layer in section 7.7, after a last mixing layer (forced by solitons) is presented

7.6 Solitons

In this section, the observations of what are thought to be solitons are discussed. The mixing they induce is estimated and translated to a decay time.

7.6.1 Observations

Most of the isopycnal displacements at station 14 show fairly low frequency oscillations (see Figure 7.10B). However, there is a deep and fast depression of the surface isopycnals before sampling was interrupted at 35.25 hours, and again at 36.25 hours.

---

[5]We can define an overturn-averaged turbulent Froude number weighted by overturning intensity as $\sum(\xi N F r_t L)/\sum \xi N L$, where L is the size of each overturn, and the sums are over all overturns. This would yield the average Fr_t in energetic areas. Surprisingly, the result is 0.83 using the average value of Fr_t in each 1-m time-averaged bin, and 1.45 using the minimum Fr_t in each bin; These are very similar to the bulk averages.
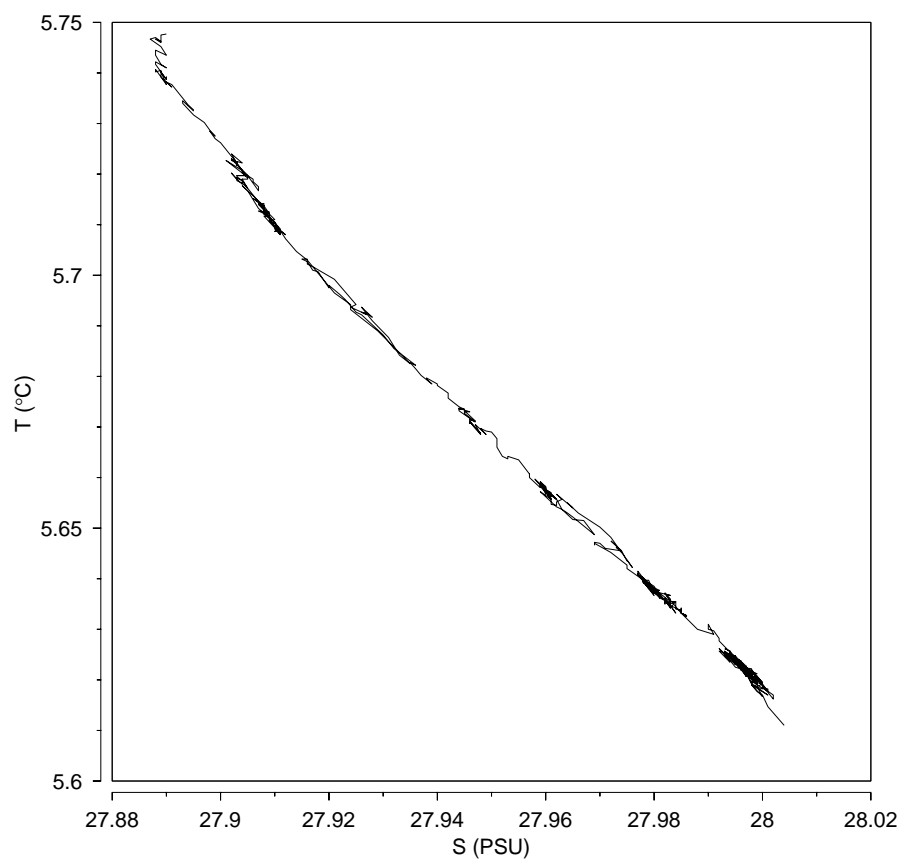
Figure 7.13: T–S relation at the second from last profile of the first mixing layer at station 14. The mixing layer is discussed in the text. Note here how inversions stay on the T–S water mass line.

This is also seen in Figure 7.10A where anomalously warm water plunges to 25 m deep. These isopycnal excursions are thought be solitons passing by.

Two facts support the interpretation of the isopycnal depressions as solitons. First, similar CTD data were collected the following summer, in July of 1989, and the same pattern was observed and is shown in Figure 7.14A. In a series of three CTD casts the isopycnals were depressed and restored. Simultaneous 200 kHz acoustic echo-sounding reveals a very smooth motion resembling the observations of a "sech^2" shape by Sandstrom and Elliott (1984) on the Scotian shelf. The second reason why these observations are consistent with solitons is that they are always observed within 1 hour of low tide. Such motions were observed on all five occasions when that phase of the tide was sampled, on both sides of the channel. This is consistent with tidally generated solitons.

There are some variations. Sometimes the depression extends to isopycnals deeper than 50 m, sometimes to only 15 m deep. Usually two or three solitons consecutive are observed, sometimes only one.

7.6.2   Generation Point

Ingram (1978) observed solitons in the shallower South channel, 15 km up the channel and to the South of station 14. The solitons Ingram observed were travelling down-channel 3.5 hours after high tide. To travel the 15 km separating station 14 from Ingram's observation point in 1.5 hours, solitons would have to propagate at 2.8 m s^{-1}./footnoteLow tide at Station 14 in Figure 7.10 occurs at 36:50 hours, such that the first soliton appears approximately 1.5 hours before low tide.. Since Ingram observed them to be travelling at $\approx$ 0.8 m s^{-1}, they are unlikely to be the same solitons originating from a tidally-timed event.

Shear was measured at station 14 simultaneously with the passage of the soliton using the ADCP (See Figure 7.6C). One of the periods where shear is poorly fitted by the rotating-vector of the internal tide in Figure 7.6E and F corresponds to the passage of the soliton. It is argued now that the shear measured during that time
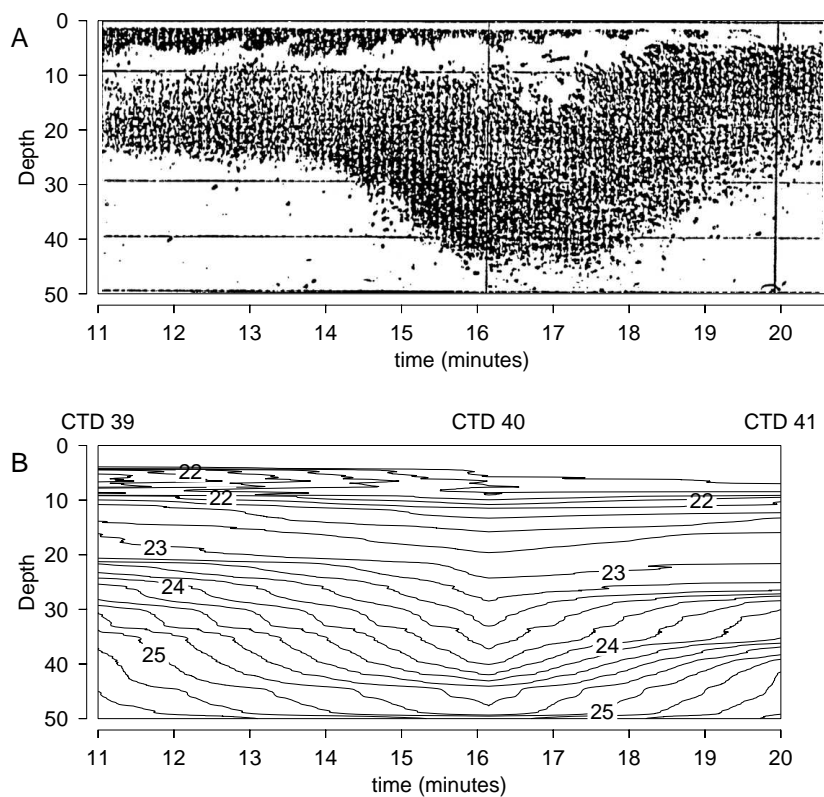
Figure 7.14: **A-** Acoustic echo-sounding taken between stations 11 and 14 on July 7th 1989 showing a soliton. Time in minutes starts at 23:11 EDT; **B-** Isopycnals constructed using 3 CTD casts taken at the times indicated by the lines in A and the labels between the panels. Note the correspondence between isopycnal excursions and the acoustic backscatter of zoo-plankton.

should not be associated with the internal tide, but rather with the soliton. In the presence of additional strain, I argue that that internal tide shear should not be a conserved, but that rather the transport (volume flux) between isopycnals should be conserved; the vertical derivative of transport velocities leads to shear. If isopycnals are strained by a soliton by a factor γ, the velocities associated with internal tide transport are reduced by γ. Furthermore, shear—already reduced because velocities are smaller—should be reduced by another factor γ from spreading of the isopycnals. Since isopycnals around 5 m in depth plunge to more than 20 m with the soliton, the shear signature of the internal tide should be reduced to noise level, and the shear should be due to the soliton itself.

Shear during the passage of the soliton is such that it was was travelling down-channel (toward the mouth of the estuary). The generation point is thus probably the sill. This, and the soliton's passing at low tide, is consistent with models of soliton generation as lee-waves. Tidal flood could create a lee-wave on the other side of the sill. As ebb flow starts, the lee-waves are free to propagate off the sill and evolve into solitons. A delay of 5 hours before their observation at station 14 would put the generation point at 18 km up-channel using an approximate propagation velocity of 1 m s^{-1}. This is an approximately correct distance to the other side of the sill. While this generation process of the solitons remains only a guess, the timing of their arrival provides an important clue for future investigators. These solitons appear unrelated to those observed by Ingram (1978).

7.6.3 Mixing Rates

Overturning events and overturning potential energy are maximum at the onset of isopycnal deepening (see Figure 7.10). Deep isopycnals plunge before ones close to the surface. Mixing seems to follow this pattern as well, starting at depth and progressing toward the surface. A very energetic overturn is also observed at the leading edge of another soliton in Figure 7.14, but the overturn is close to the surface this time.

Mixing at the leading edge of solitons is consistent with Bogucki's (1991) simple 2-layer model, separated by a pycnocline, for the propagation of a soliton. In Bogucki's model, the interface is thickened by the soliton's shear until the layer Richardson number reaches an upper limit when mixing stops.

Figure 7.15A shows a temperature profile with two of the most energetic overturns observed associated with the soliton. The profile was taken at 36.18 hours. The vertical lines in Figure 7.15A delimit the extent of the 2 overturns. The T–S relations for each of these are shown in Figure 7.15B and C. The top overturn is 5 m in size, and has big temperature fluctuations ($\approx 0.8°$C). The second is 19 m in size, but has lower rms temperature fluctuations of 0.025°C, which is still an order of magnitude above noise level. Both overturns have good tight T–S relations and there is no doubt that they are real. Upon close examination of the temperature profile, it could be argued that the top overturn is actually made up of two. If that is the case, there is a temperature overlap of 0.15°C between the two features which is due to mis-sampling. This is much greater than noise level (a few millidegrees). In any case, the potential energy of the overturns, ξ, would not be significantly different for a 'corrected' case if one choose to 'correct' the temperature profile to eliminate the overlap.

Using either density or temperature fluctuations to evaluate ξ results in a 20% difference in Figure 7.15B, mostly because the overturn extends 1 m deeper evaluated on density. The difference is only 6% for Figure 7.15C. Density fluctuations will be used for this series, but either would do.

The mixing rates are computed for all 13 CTD profiles in the same manner as described in Section 7.4.1. The layer-average value of $J_b = (2/3)\xi N Fr_t \approx 0.27\,\xi N Ri_g^{-1/2}$ is 1.6×10^{-6} W kg^{-1}. Using the minimum Ri_g observed in each 1-m time-averaged bin to estimate Fr_t leads to $J_b \approx 3.7 \times 10^{-6}$ W kg^{-1}, 125% higher than with the average Ri_g.

The averaged N^2 was 4×10^{-4} s^{-2}. The layer-averaged $K_v = J_b N^{-2} = 6 \times 10^{-3}$ m^2 s^{-1}.

Assuming that the total energy of the soliton scales like $N^2 A^2$, where A is the
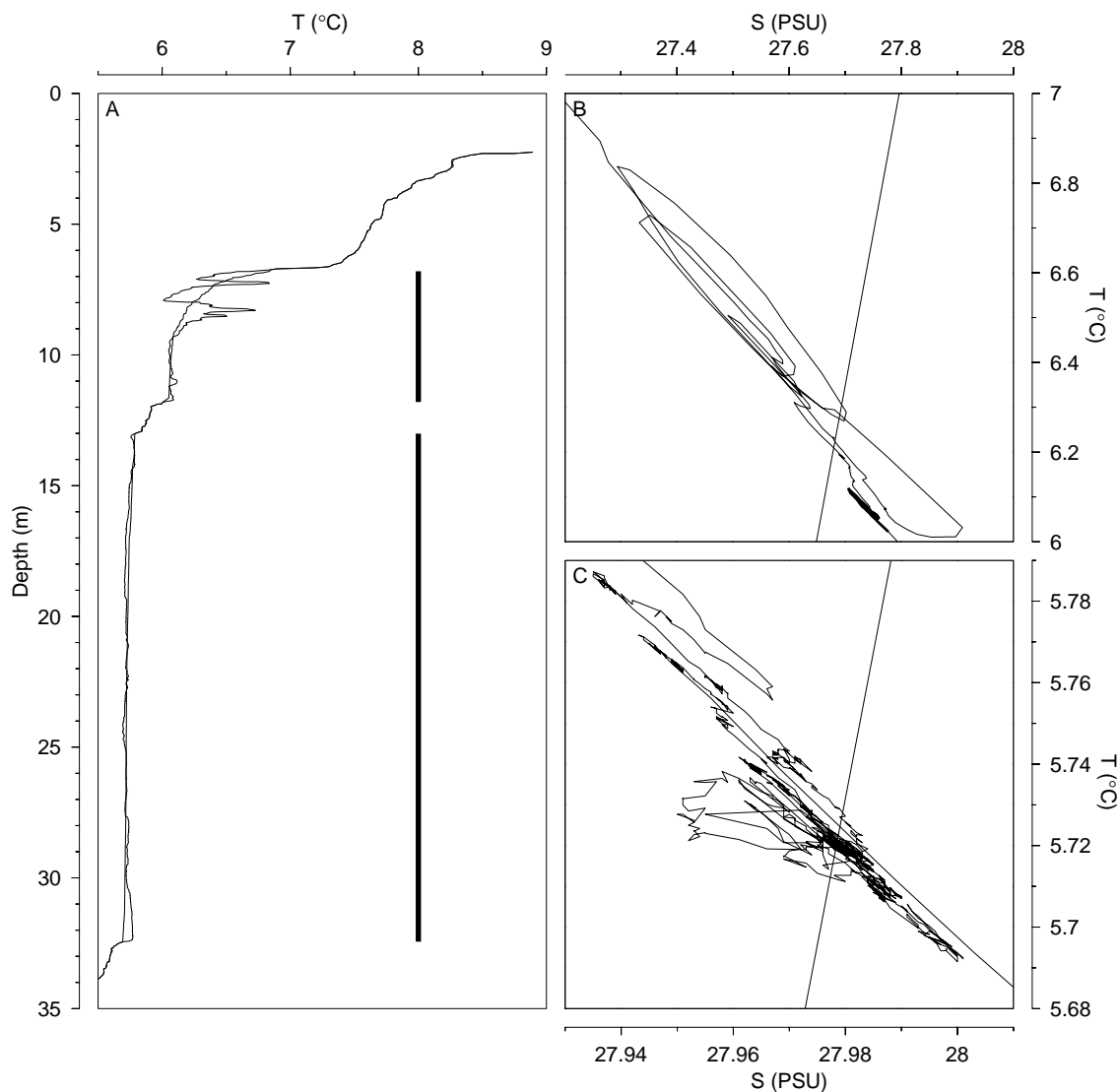
Figure 7.15: **A-** Measured and re-ordered temperature profile at 36.18 hours in Figure 7.10. The two vertical lines show the intervals of two overturns. **B-** T–S relation for top overturn in A. Oblique line is the $\sigma_t = 21.75$ isopycnal. **C-** T–S relation for bottom overturn in A. Oblique line is the $\sigma_t = 22.04$ isopycnal.

		New layer	Well mixed	Soliton
N^2	[s^{-2}]	10^{-3}	10^{-4}	4×10^{-4}
$J_b \approx \xi N$	[W kg^{-1}]	3.4×10^{-7}	1.7×10^{-8}	2.4×10^{-6}
$J_b \approx (2/3)\,\xi N(0.4\,\overline{Ri_g^{-1/2}})$	[W kg^{-1}]	1.2×10^{-7}	1×10^{-8}	1.6×10^{-6}
$J_b \approx (2/3)\,\xi N(0.4\,\overline{Ri_{g\min}^{-1/2}})$	[W kg^{-1}]	1.8×10^{-7}	1.7×10^{-8}	3.7×10^{-6}
$\overline{Fr_t}$		0.47	0.85	0.59
$\overline{Fr_{t\max}}$		0.73	1.51	1.46
K_ρ	[m^2 s^{-1}]	1 to 3 $\times10^{-4}$	1 to 1.7 $\times10^{-4}$	4 to 9 $\times10^{-3}$
Calculation Depth		12 to 22 m	variable	5 to 25 m
Duration		45 minutes	2 hours	53 minutes

Table 7.2: Summary of mixing layers

amplitude, the energy is ≈ 0.8 m^2 s^{-1} using $N^2 = 4 \times 10^{-4}$ s^{-2} and $A = 45$ m. Considering that the turbulent Froude number inferred from Ri_g is approximately equal to 1, an inertial-buoyancy balance may hold. In this case, let us assume conservatively that there is an equal amount of dissipation of turbulent kinetic energy as there is buoyancy flux ($\Gamma = 1$). This is a lower bound on the rate of dissipation of turbulent kinetic energy. The total dissipation rate (TKE plus potential) is then $> 5 \times 10^{-6}$ W kg^{-1}. It would take 44 hours to dissipate all the soliton's energy at this rate. The soliton would travel 160 km at a typical propagation velocity of 1 m s^{-1}.

7.7 Comparison of the Mixing Layers

The mixing rates obtained for the three mixing layers are summarized in Table 7.2. A brief discussion follows.

New Mixing Layer

The first mixing layer was observed in the beginning stages of mixing: The first temperature profiles had very high stratification and much overturning finestructure (see Figure 7.9). As the mixing progressed, stratification decreased while overturning

length scale increased such that the APEF remained about constant.

The average Fr_t over all bins and the average of the maximum Fr_t in each 1-m thick layer were both the lowest of the three mixing layers. The average maximum Fr_t is evaluated using the minimum gradient Richardson number in each 1-m thick layer. Perhaps this value is more indicative of the dynamics; the minimum Ri_g reached should be more relevant than some mean value. The averaged-maximum Fr_t is 0.73, which is very close to the maximum value of $(Fr_t)_{isoIB} = 0.8$ estimated in chapter 4 for growing isotropic turbulence reaching inertial-buoyancy balance. This value of Fr_t seems to indicate that overturns created at the onset of mixing are in an inertial-buoyancy balance. Note, however, that this is an average value of Fr_t. Many lower values are found and it is possible that the turbulent Froude number is under-estimated by a factor of 2 because the critical Richardson number where overturning starts is ≈ 1 instead of $1/4$ (see Figure 7.16A).

The buoyancy flux obtained using model two's $J_b \propto \overline{Ri_{g\min}^{-1/2}}$ or model three's $J_b = \xi N$ are both relevant at isotropic inertial buoyancy balance. They give a similar buoyancy flux within a factor of 2 (although the coefficient for model three is adapted to higher values of Fr_t for which anisotropy is greater; its buoyancy flux formulation overestimates slightly for isotropy because the TKE is under-estimated). Thus while model two or three should apply to this layer, because it appears to be at critical Richardson number (isotropic inertial-buoyancy balance where both models converge), model two would be applied were it not at critical Richardson number (as it may be if Ri_g is under-estimated) because there is evidence that the layer is newly mixing, and thus that turbulence may be growing; if Ri_g is not under-estimated, the overturning appears to be created already at inertial-buoyancy balance, perhaps through K-H instability.

Well Mixed Layer

The second layer observed had K_ρ about the same as the first layer, but the buoyancy flux estimates are one order of magnitude smaller because of the smaller stratification.

The turbulent Froude number is estimated to be twice the value of the previous case, meaning that this layer has a lower mixing efficiency.

Since the layer has unusually low stratification, it has probably been mixing for a long time. To illustate this, note that using $K_\rho = 1.5 \times 10^{-4}$ m^2 s^{-1} and a thickness of $H \approx 10$ m, the time to mix to completion is $H^2/(12\,K_\rho) \approx 15$ hours. The layer may have been mixing for a few hours, unless its low density gradient is caused by strain from the internal tide. It seems reasonable to assume that the third model should apply, describing anisotropic steady-state turbulence at inertial-buoyancy balance. In this case the buoyancy flux is 1.7×10^{-8} W kg^{-1} (the same result is obtained with the second model) and the isotropy is estimated as $L_h/L_T = Fr_t = 1.51$.

Soliton

The mixing associated with the soliton occurs mostly at its leading edge. The eddy diffusivity K_ρ is nearly 2 orders of magnitude higher than for the other two layers described. The buoyancy flux is 20 times higher than the average of the first layer. The averages listed in Table 7.2 are for one or two solitons (the trailing edge of one is sampled before the leading edge of the main one sampled), but over nearly an hour. This leads to the unexpected result that solitons are a very important source of mixing at the head of the Laurentian channel. Solitons are probably more important than the internal tide, which is thought to be generated there. This is a new result.

For this layer, the turbulent Froude number based on minimum Ri_g is 1.46, which is as high as for the well mixed layer previously discussed. In this case the mixing is known to be new because of the sudden appearance of the soliton. Since there is no reason for the overturning to be created at inertial-buoyancy balance in this case, it is assumed that the turbulence is growing. In this case, the second model is appropriate and the buoyancy flux is estimated as $J_b \approx 3.7 \times 10^{-6}$ W kg^{-1}.

7.7.1 Comparison to Wind Mixing

Oakey *et al* (1982) measured approximately 1% of the work done by wind stress below 10 m, E_{10}, as dissipation of turbulent kinetic energy, where E_{10} is

$$E_{10} = \rho_a C_{10} U_{10}^3 \tag{7.7}$$

and ρ_a is the density of air (≈ 1.2 kg m^{-3}), C_{10} is a drag coefficient (1.3×10^{-3}) and U_{10} is the wind speed measured at a height of 10 m. Most of E_{10} is dissipated in the atmosphere above the water.

If buoyancy flux is approximately equal to a quarter of the rate of dissipation within the water (assuming that mixing efficiency in this possibly high Fr_t flow is below the maximum inertial-buoyancy balance value), then a 10 m s^{-1} wind corresponds to a depth-integrated buoyancy flux of 4×10^{-3} W m^{-2}. If this mixing occurs in the top 20 m of the water column, the buoyancy flux is 2×10^{-7} W kg^{-1}. This is an order of magnitude lower than instantaneous buoyancy flux from solitons. In addition, shear layers mix water (and nutrients) up without unduly disturbing the surface waters like wind mixing does. Thus nutrients may be mixed up into surface waters with little mixing of plankton down below the photic zone.

7.8 Relating Mixing to Shear

Recent work by Gregg (1989) has shown promising results in relating the shear forcing the mixing directly to the dissipation of turbulent kinetic energy, ϵ. This effort is very worthwhile because mixing could be inferred by simple measurements of shear rather than the more technical difficult task of measuring microstructure, or even finestructure. All three models of finestructure which have been compared in this thesis will be tied to Gregg's shear-dissipation relation. This will gives three predictions for ξN as a function of shear which can tested tested with our data.

7.8.1 Background of the Gregg Model

In order to understand and quantify fluxes of heat and mass in the ocean, and to provide numerical modellers a basis on which to set eddy diffusivities, theories for the scaling of turbulent kinetic energy dissipation rate as a function of stratification and energy level have been derived. These include scalings like $\epsilon \propto N^{1-1.5}$ (Gargett and Holloway, 1984), $\epsilon \propto f^{\frac{1}{2}} N^{\frac{3}{2}} E_{GM}^{\frac{3}{2}} e^{-c/E_{GM}}$ (Munk, 1981) where E_{GM} is the energy level associated with the Garrett-Munk model, $\epsilon \propto N^2$ (McComas and Muller, 1981) and more recently $\epsilon \propto E_{GM}^2 N^2 \cosh^{-1}(N/f)$ (Henyey $et\ al.$, 1986) based on the rate of energy transfer from low to high wavenumber by wave-wave interactions.

These theoretical formulations typically use a constant energy level of internal waves, but over periods of days to weeks the true energy level E_{IW} can vary by factors of 2-3 relative to E_{GM}. Gregg (1989) therefore assumed $\epsilon \propto E_{IW}^2 N^2$ (dropping the small $\cosh^{-1}(N/f)$ variation in Henyey $et\ al.$ (1986)) and used the integrated shear variance of the Garrett-Munk spectrum to obtain $E_{GM} \propto S_{GM}{}^2$. Assuming that the variable energy level still follows the Garrett-Munk spectral shape, an estimate of E_{IW} can be obtained by measuring the $in\ situ$ shear. The estimated dissipation is

$$\epsilon = 3.5 \times 10^{-10} \frac{N^2}{N_{GM}} \frac{S_{10}^4}{S_{GM}^4} \tag{7.8}$$

in units of W kg^{-1}, where S_{10} is the shear measured on a scale of 10 m..

The dissipation relation can be further simplified. The Garrett-Munk shear is related to a reference stratification of $N_{GM} = 0.0052$ s^{-1} as (Gregg, 1989)

$$S_{GM}^2 = 1.91 \times 10^{-5} \frac{N^2}{N_{GM}^2} \tag{7.9}$$

Defining a 10 m Richardson number Ri_{10} as N_{10}^2/S_{10}^2, dissipation becomes

$$\epsilon = 2.6 \times 10^{-5} Ri_{10}^{-1} S_{10}^2 \tag{7.10}$$

in W kg^{-1} using S_{10} in s^{-1}.

This relation for dissipation in the main thermocline (which assumes a Garrett-Munk spectral shape), has surprisingly been shown to hold to within a factor of 2 in

four different sites. In fact Gregg (1989) adds the factor of 2 which better collapses the data. The relation becomes $5.2 \times 10^{-5} Ri_{10}^{-1} S_{10}^2$ in W kg^{-1} (Gregg, 1989).

7.8.2 Relating Gregg's Model to ξ

Gregg's model can be written in terms of mixing intensity $\epsilon/\nu N^2$ as

$$\frac{\epsilon}{\nu N^2} = \frac{52}{Ri_{10}^2} \tag{7.11}$$

using (7.10), $\nu \approx 10^{-6}$ m^2 s^{-1} and incorporating the factor of 2.

This relation (7.11) cannot be compared directly to the finestructure measured from the St. Lawrence, except for the first model. However, the two other models from chapter 3 relate ϵ to ξN for known values of Ri_{10}. The Gregg model will be linked to each model via ϵ–ξN conversions such that measured values of $\xi N/\nu N^2$ can be compared to Gregg's predictions coupled to the models. It most be noted that Gregg's model yields an average predicted value of ϵ, which will be compared to instantaneous measurements of overturning.

Model One

In the first model, the relation $L_o = L_T$ leads to a direct estimate of dissipation from measurements of ξN. Combined with (7.11), $\epsilon \approx 2\xi N$ simply becomes

$$\frac{\xi N}{\nu N^2} = \frac{26}{Ri_{10}^2} \tag{7.12}$$

Model Two

In the second model, the ratio $\xi N/\epsilon$ is related to $Ri_t \approx 6.2 \, Ri_g$ using (3.23) Linked with (7.11), this becomes becomes

$$\frac{\xi N}{\nu N^2} = \frac{\epsilon}{\nu N^2} \frac{\xi N}{\epsilon} \approx \frac{52}{Ri_{10}^2} \frac{1}{2} \left(6.2 \, Ri_{10}\right)^{3/2} \approx 400 \, Ri_{10}^{-1/2} \tag{7.13}$$

Model Three

In the third model, the ratio of $\xi N/\epsilon$ is simply the mixing efficiency $\Gamma = Ri_t/2 = 3.1\,Ri_{10}$. Combined with Gregg's model, this gives

$$\frac{\xi N}{\nu N^2} = 160 Ri_{10}^{-1} \tag{7.14}$$

The Comparison

Values of $\xi N/\nu N^2$ are shown in Figure 7.16 for the three mixing layers discussed in this chapter. The values are 1-m thick time-averages and are shown versus both the time-average gradient Richardson number of each 1-m layer (calculated in logarithmic space) and versus the minimum value of Ri_g found in each 1-m. Gregg's prediction for $\epsilon/\nu N^2$ is shown in relation to each of the three model by the three lines.

The use of the minimum Richardson number leads to slightly better fits. The soliton data have approximately the proper slope for model two of growing turbulence, but have values of $\xi N/\nu N^2$ an order of magnitude higher than expected. This should not really come as a surprise because there is no reason why mixing should follow internal wave transfer rates. This was also the most intense case of mixing encountered in this data set.

Well-mixed layer data are scattered in Figure 7.16A and have values of $\xi N/\nu N^2$ too low to fit the third model. The new mixing layer data could be argued to fit any of the three models.

The data from the three mixing layers do not collapse under Gregg's turbulence scaling. It would be difficult to determine if the ξN to ϵ conversion models are not correct, or if Gregg's model does not apply to these circumstances. The latter seems the most reasonable. Gregg's dissipation dependence on shear is a function of internal wave energy transfer rates. The only mixing layer described here which could be argued to be forced by internal waves (although not the typical Garrett-Munk spectrum) is the newly-created mixing layer, which appears to have overturns created at inertial-buoyancy balance. Perhaps this is a factor affecting the success
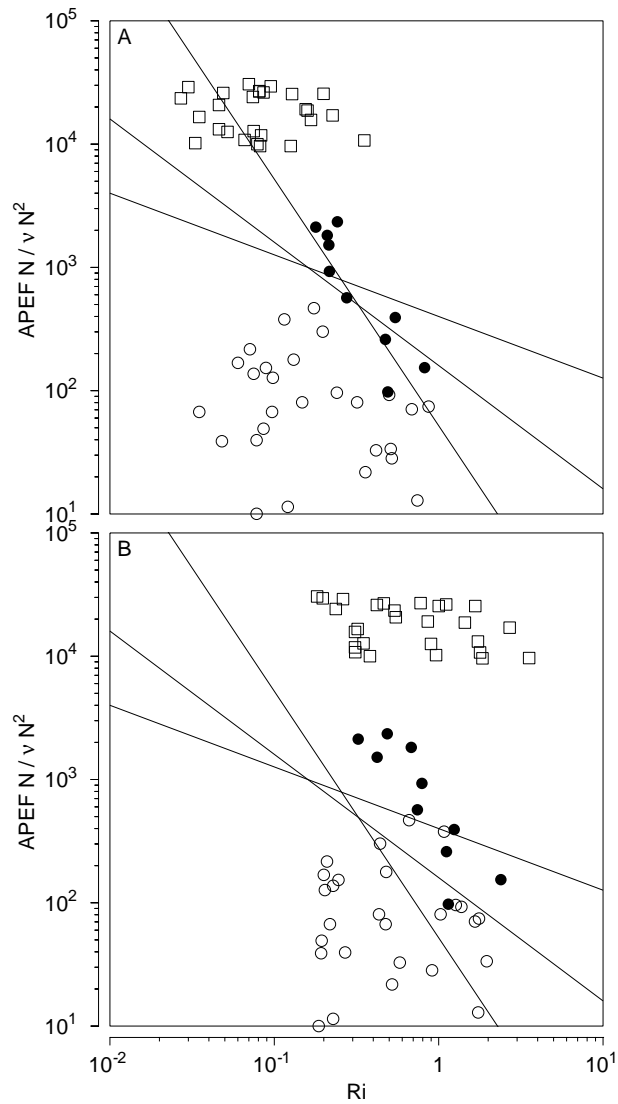
Figure 7.16: Comparison of Gregg's model with observed finestructure. **A-** ξN versus minimum Ri_g in each 1-m thick time-average layer; **B-** ξN versus log-averaged Ri_g in each 1-m thick layer; Data are from ($\bullet$) new mixing layer, ($\circ$) well-mixed layer and ($\square$) soliton. The lines are, from the steepest, combination of Gregg's model with the first model ($\epsilon = \xi N$), with the third model ($J_b = \xi N$) and with the second model ($J_b = (2/3)\xi N Fr_t$).

of the Gregg model in that case. Perhaps a comparison with more averaging would yield closer results.

7.9   Summary

In this chapter, CTD and ADCP data were combined to study mixing layers at the head of the Laurentian channel. The main results are as follows

- The T–S characteristics at the head of the channel were observed to change quickly in space. Two different water masses are found above the temperature minimum at station 24. The warmer water masses may be formed by deep water—usually below the temperature minimum—put into contact with shallower water from above the temperature minimum. Large internal tide isopycnal displacements could do this by 'upwelling' water over the bank or the sill. The water mass formed by the mixture of the two end members is seen mostly on the South side of the channel, but it also intrudes into the North side.

- The internal tide was studied following Forrester (1974). It is unclear if the internal tide, thought to originate from the head of channel, is evanescent. If so, then the large shears observed at the head are only typical of the first few kilometers away from the generation point, and mixing rates described here cannot be applied further downstream. Results are summarized in section 7.3.5.

- The gradient Richardson number was used to infer the turbom tt Froude number as suggested in chapter 3, and verified in chapter 4. Figure 7.16 shows that the minimum observed Ri_g in 1-m layers varies by a factor of 10 in each of the 3 mixing layers observed. The highest value of $Ri_{g\min}$ which still produces mixing is about 1, instead of 1/4. This means that the turbulent Froude numbers may be under-estimated by a factor of 2. Buoyancy fluxes quoted using Fr_t are thus lower bounds.

- Three mixing layers were examined, summarized in Table 7.2.

– The first appears to be starting to overturn. The lowest average values of Fr_t were observed in this layer, for which overturning is thought to occur at inertial-buoyancy balance. Stratification is very high. The T–S relation is very tight, even within overturns. Temperature can be used as a density proxy without worry about intrusions. Model two for growing turbulence is a good choice for this layer, since it appears to be new, growing turbulence. Buoyancy flux from model three is only two times higher, because of the proximity to inertial-buoyancy balance.

– The second layer has very low stratification and low Ri_g. The corresponding high Froude numbers and the low N^2 indicate that model three is appropriate to describe this layer as steady-state turbulence at inertial-buoyancy balance, but slightly anisotropic because the layer is thought to have been mixing for some time. The first half of the layer has a loose T–S relation in which unusual density-unstable features are found. Different water masses, between which the measured density profile is unstable, are layered. I do not think that they are overturns but cannot explain them.

Although these structures cannot be explained, they have been detected and can be disregarded in mixing quantification. This shows that a conventional CTD, used in low wave conditions from a stable platform and in shallow depth with strong gradients of temperature and salinity, can sample T and S adequately to measure overturns and differentiate them from even slight intrusions in most cases.

– The third layer is associated with the passing of solitons. Mixing is maximum at the leading edge of the soliton. The eddy diffusivity and buoyancy flux are respectively 100 and 20 times higher than the first layer described. Since overturning is new, model two is appropriate. If Fr_t is under-estimated by a factor by two, model two predicts buoyancy fluxes three times higher than model three for this layer. This is the largest difference between models observed between the three layers.

- Although mixing was never measured at the head of the channel, many authors have anticipated that the larger shears associated with this generation area of the internal tide is responsible for high mixing rates. I have shown here that solitons may in fact be more important. Buoyancy flux averaged over an hour was 20 times higher than the second highest buoyancy flux (the new layer), which was a 45-minute average. Since solitons pass by at each low tide, this is also a 'steady' source of mixing, like the internal tide.

  More solitons and internal tide-forced mixing layers need to be quantified before solitons are positively demonstrated to be more important for mixing, but this research clearly points in that direction.

- Further mixing studies should focus on the possibility of deep waters overflowing onto the shallower South channel or the sill, where it can mix with the shallower waters. This mechanism may be responsible for the intrusions we have observed. This internal tide effect may also be more important than mixing forced by the large scale shears of the internal tide.

- The data from the three mixing layers were compared to chapter 3's three models linked to Gregg's (1989) relation of ϵ to shear. Only the new mixing layer was consistent with Gregg's model.

Chapter 8

Discussion and Conclusions

In one sentence, the conclusion to this thesis is that "Buoyancy flux can be inferred in a shear-stratified flow by the measurements of the APEF, of the density gradient and of the shear". Let us now use a few more words to qualify and quantify this sentence.

8.1 New Ideas In Mixing Models

Microscale measurements of the rate of turbulent kinetic energy dissipation ϵ and of the rate of dissipation of temperature variance χ_θ are most often used to infer buoyancy flux.

The assumptions of *i)* constant mixing efficiency and of *ii)* a duration time of order N^{-1} for the mixing associated with an overturn, lead to what I have termed "the traditional model" relating overturning length scales L_T to the dissipation of turbulent kinetic energy ϵ. It is **the first model** used in the thesis, as a comparison to new ideas.

The first model is perhaps misleading, relating a length scale constructed from dissipation ϵ and stratification N^2, *i.e.* the Ozmidov scale $L_O = (\epsilon/N^3)^{1/2}$, to overturning scales. Albeit L_O has a physical interpretation as the largest still isotropic overturn size in the presence of stable stratification, it is obtained from microscale

measurements. The inference is that Thorpe scales are related directly to the rate of dissipation of turbulent kinetic energy, and then only to buoyancy flux through a constant mixing efficiency. This implies a balance between inertial and buoyancy forces.

Buoyancy flux should be thought of as an overturn-scale quantity; Moum (1990) has shown that the largest contributions to the the correlation $\overline{w'\rho'}$ are at overturning scale. I have argued in chapter 3 that the buoyancy flux and potential energy dissipation are both related directly to the APEF, ξ. The presumption is that buoyancy flux accumulates into a stock-pile of ξ, which in turn is usually dissipated as fast as it is being produced (i.e. Buoyancy flux adds potential energy to the APEF; that energy is then dissipated and raises the center of mass of the water column). If the fluxes in and out of the APEF increase, the APEF must also increase. The buoyancy flux can be inferred from ξ if the decay time of an overturn, and therefore of ξ, is known. In this view, Thorpe scales—related to the APEF—are linked to buoyancy flux directly beacuse the APEF is potential energy created by buoyancy flux. The APEF is then related to ϵ through a mixing efficiency, which can be predicted from the ratio of kinetic to potential energy of the overturn. This is in contrast to the first model. In this new view, the potential energy of the overturn (APEF) is argued to be proportional to potential energy flows J_b and dissipation of potential energy; this holds for any ratio of inertial to buoyancy forces, and is argued to be a more general assumption than model one.

The assumption that the dissipation of potential energy at microscales, $3N^2\kappa_T C_x$, is equal to the buoyancy flux J_b which may occur at larger scales is used for models two and three described in chapter 2. Dillon *et al.* (1987) assume that $3N^2\kappa_T C_x$ is an upper bound to buoyancy flux. Perhaps if turbulence is growing (*e.g.* model two) then this is a better assumption; however it is assumed that the rate of change of the APEF during growth is smaller than either buoyancy flux or the dissipation of potential energy.

Some of the pertinent questions addressed in this thesis are then

- What is the decay time of an overturn, and therefore the decay time of ξ from dissipation of potential energy, or equivalently the growth time of ξ through J_b?

- Do the mixing efficiency and decay time vary sufficiently that the distinction between overturning scales being related to J_b rather than to ϵ matters?

- Can this method be used with conventional CTD instruments? What are the difficulties?

8.2   Decay Time

Rather than picking a decay time of N^{-1} as in the first model, the decay time for the APEF is taken to be the decay time of the turbulent kinetic energy by ϵ. The turbulent kinetic energy decay time scale is implicit to the Kolmogorov spectrum. If ϵ is constant at all scales of a cascading energy spectrum, then it must scale like $\epsilon \approx u^3/L$. If the turbulence is not isotropic and the Kolmogorov spectrum still holds, then L is the energy containing scale: the horizontal turbulent scale. The assumption that $\epsilon \approx u^3/L$ was shown to hold very well in slightly anisotropic grid-turbulence data in chapter 4. The decay time of the turbulent kinetic energy $3u'^2/2$ by dissipation u'^3/L is then $(2/3)L/u'$.

8.2.1   Second Model

If the overturns are isotropic, the ratio of the decay time scale (without the coefficient) L/u' to the buoyancy time scale of N^{-1} yields a turbulent Froude number $Fr_t = u'/NL_T$. This is often written as a turbulent Richardson number $Ri_t = N^2 L_T^2/u'^2$, describing the ratio of ξ to one horizontal component of turbulent kinetic energy.

In grid-turbulence, the decay time can be very short such that $u' \gg NL$ ($Fr_t \gg 1$). In this case, buoyancy forces are much smaller than inertial forces. Furthermore, the mixing efficiency is low because, in spite of the high kinetic energy, the buoyancy flux and APEF are limited by the small overturning scales, because density fluctuations

associated with the turbulence are proportional to the vertical overturning scale. Turbulent scales then grow without feeling the effects of buoyancy, until $u' \approx NL$ ($Fr_t \approx 1$). At this stage, mixing efficiency is maximum, and the decay time scale is $\approx N^{-1}$, determined by the balance of inertial and buoyancy forces.

The above description is of the **second model** for growing isotropic turbulence. Using Fr_t and Ri_t to parameterize the decay time, its buoyancy flux is written $J_b \approx \left[\frac{3}{4} \pm \frac{1}{4}\right] \xi N Fr_t$, and its mixing efficiency is $\Gamma \approx \left[\frac{3}{4} \pm \frac{1}{4}\right] Ri_t/3$. This model was shown to hold within a factor of two for $Fr_t > 0.8$, using grid turbulence data in chapter 4. Unfortunately the inertial-buoyancy balance stage of maximum mixing efficiency was not sampled because turbulence dies-out before reaching it.

In the presence of shear, a third time scale is possible in addition to N^{-1} and L/u': the inverse of the shear $(\partial \overline{U}/\partial z)^{-1}$. It was postulated in chapter 3 that turbulent velocity fluctuations derived from the shear must be proportional to it as $u' = a L_T \partial \overline{U}/\partial z$. In chapter 4, this was tested using published grid-turbulence results in the presence of shear; we find $a \approx 0.4$. The decay time scale $(2/3)L/u'$ is then also parameterised by the large scale flow as $(5/3) (\partial \overline{U}/\partial z)^{-1}$. The turbulent Richardson number—and hence mixing efficiency—is then proportional to Ri_g. We obtain $Ri_t \approx 6.2 Ri_g$. The coefficient is important. The maximum value of Ri_g which still promotes instability and overturning corresponds to the inertial-buoyancy balance values of Ri_t and Fr_t. This critical value determines the maximum ξ/TKE ratio for overturning, setting the maximum value of mixing efficiency. The current estimate, from chapter 4, is $Ri_t \approx 1.55$ at $Ri_g = 1/4$; this corresponds a maximum mixing efficiency of $\Gamma \approx 0.52$. This value is tentative. None of the decaying grid-turbulence experiments have sampled the inertial-buoyancy balance stage. Future experiments should focus on it.

The inference of Fr_t from Ri_g was attempted in chapter 7 using acoustic Doppler current profiler data sampled at 1 m intervals. The main difficulties were *i)* to average N^2 to match the implicit filtering of shear from the ADCP sampling and *ii)* to bin-average Ri_g and ξ on time and depth scales such that the two quantities are

correlated. The first difficulty is rather straightforward, the second is less. The choice of the bin-averaging of ξ and Ri_g was arbitrary. A much better scheme would look at evolution of the cross-correlation of ξ with Ri_g with increasing averaging. However, best results could come from future instruments measuring both the density and meter-scale shear profile from the same vehicle. Present data showed that a dependence between ξ and Ri_g could not always be found, but encouraging correspondence was found for the most active mixing layers. The correspondence was better when using the minimum Ri_g observed in each bin rather than a logarithmic average. The critical gradient Richardson number was approximately 1, higher than in grid-turbulence in the presence of shear. The buoyancy fluxes derived from the second model using Fr_t are possibly under-estimated by a factor of 2 because of this. New technology broad-band ADCPs should do much better in resolving the small scale shear with lower errors, and yield better gradient Richardson numbers. It was found in chapter 7 that Gregg's (1987) model relating ϵ to shear did not collapse all $(\xi/\nu N^2)$—Ri_g data from three different mixing layers. While the slope of the dependence resembles Gregg's model, the intensity varied by an order of magnitude either way.

8.2.2 Third Model

A **third model** is derived in chapter 3, describing steady-state mixing layers for which overturning scales have out-grown the layer thickness, *e.g.* a surface mixed layer. If vertical overturning scales reach the layer thickness before inertial-buoyancy balance, horizontal scales are still free to grow, leading to anisotropy. Horizontal scales are still linked to vertical scales through continuity. It was argued in chapter 3 that horizontal growth stops when the vertical kinetic energy is balanced by buoyancy forces. The steady-state horizontal length scale is the Ozmidov scale L_O for steady-state turbulence at inertial-buoyancy balance; the ratio L_T/L_O describes the level of isotropy. The decay time is $\approx N^{-1}$, but the mixing efficiency is affected by the isotropy described by $\Gamma \approx (L_T/L_O)^2$. The ratio L_T/L_O also describes the energy

separation between kinetic and potential, which affects the mixing efficiency. The buoyancy flux is $J_b \approx \left[\frac{3}{4} \pm \frac{1}{4}\right] \xi N$ and the mixing efficiency is $\Gamma \approx \left[\frac{3}{4} \pm \frac{1}{4}\right] Ri_t/2$.

8.3   Mixing Efficiency

The second and third models make very similar predictions about mixing efficiency; only the coefficient changes. But the models describe quite different turbulence for low mixing efficiencies. In the second model, low mixing-efficiency is characterized by isotropic turbulence with small overturning scales relative the inertial-buoyancy scale $\approx L_O$, turbulence does not feel the effect of buoyancy. In the third model, low mixing-efficiency is characterized by anisotropy and turbulent velocities limited by buoyancy forces. In both models, the turbulent Richardson number Ri_t quantifies mixing efficiency because it describes the ratio of potential to kinetic energy. The generalized form of Ri_t in terms of length scales combining both the inertial-buoyancy balance and isotropy factors is $Ri_t \approx L_T^2/(L_O^{4/3} L_h^{2/3})$ (using $\epsilon \approx u'^3/L_h$).

Both the second and third models predict a wide range of mixing efficiency for various turbulent conditions possible. This is in contrast to the first model which uses a constant mixing efficiency. The only oceanic data set reviewed in this thesis, with sufficient information about mixing (e.g. ϵ and J_b estimates) to distinguish between the models, was Dillon's (1982) oceanic and freshwater data. The mixing efficiency varies by an order of magnitude within each of Dillon's three data sets, and by two orders of magnitude within all three data sets. This is incompatible with the first model. The variation of the mixing efficiency is consistent with both models two and three (because of error bounds). Models two and three are thus preferable to model one in energetic mixing regions.

The new APEF approximation $\xi \approx (g/2\overline{\rho})L_T\overline{\rho'^2}^{1/2}$ found in chapter 2 was used with Dillon's data because the APEF was not tabled. This improved our ability to test the models because the usual approximation $N^2 L_T^2/2$ was shown to over-estimate by a factor of more than 2 for Dillon's data. The layer-averaged N^2 include

non-overturning parts of the water column where stratification is higher than within overturns. I also used a buoyancy flux formulation for the second model using a decay time parameterisation not sensitive to the N^2 over-estimation. Dillon's oceanic data were consistent with the third model describing steady-state anisotropic turbulence at inertial-buoyancy balance. His freshwater data set was marginally consistent with the second model, describing growing isotropic turbulence. The consistency between models and data stops with the coefficient. Dillon's data has values of χ_θ a factor of 3 higher than models two and three account for, leading to an average mixing efficiency greater than 1. Apart from this difference, Dillon et $al.$'s (1987) empirical relation for buoyancy flux as $J_b = 4.8 \, \xi \, N$ is the same as model three (assuming J_b is equal to the dissipation of potential energy, measured by Dilon et $al.$). Caution is adviced using Dillon et $al.$'s (1987) relation which is possibly an over-estimate by a factor of 3, as well as not being a general result.

8.4   Difficulties

If only layer-averaged Thorpe quantities are available to calculate $J_b \approx \xi N$ or $J_b \approx (2/3) \, \xi N F r_t$, then one needs to worry about APEF approximations as discussed in chapter 2. This difficulty disappears when all original data are available, as in chapters 6 and 7. The APEF and the density gradient can be calculated over each separate overturn. This leads to non-approximated values of ξN. If turbulent kinetic energy dissipation rate measurements are not available, then $F r_t$ must be evaluated from Ri_g as discussed above. The other problem is that salt-compensated inversions must not be mis-interpreted as overturns if temperature is used to find overturns. This mostly occurs from intrusions of different water masses.

In chapter 6, finestructure data from Emerald basin were compared to ϵ data. Most of the data were again consistent with a relation of the APEF to buoyancy flux (testing of individual models was not done because measurements of χ_θ from which buoyancy flux could also be estimated were not used). Most of the dissipation

rates were consistent with buoyancy flux models if the mixing efficiency varies by an order of magnitude, up to about 1. This is slightly high, but would be lower with some time-averaging. The data that were not consistent with the models had high ξN values and low ϵ values. CTD casts taken before and after the sequence of EPSONDE drops show that the ship had moved between two water masses during the EPSONDE sampling. It is likely that intrusions between these water masses caused the mis-interpretation of temperature inversions as overturns.

The main difficulty with the use of this technique in areas where salinity controls the density gradient is the possibility of salt-stabilized inversions being mis-interpreted as overturns. Obviously, temperature measurements alone cannot be trusted in such circumstances. In chapter 7, data from the St. Lawrence estuary showed that even slight T–S differences in water masses could cause mis-interpretation. This is very problematic because the apparent APEF of these intrusions is very high. However, it was also shown in chapter 7 that a conventional CTD used in the absence of surface waves (heaving the winched instrument up and down) produced T–S relations sufficiently reliable to determine if temperature inversions were overturns. In the presence of waves, overturning within the surface mixed layer could escape the sensitivity of the instrument. Overturning below the mixed layer could be sampled if ship motion can be de-coupled from the instrument. There are at least three ways of doing this: *i)* using a motion-compensating winch, *ii)* using a free-falling instrument and *iii)* using a parachuted instrument. In these ideal measuring conditions, an ordinary CTD can be used to record energetic overturns, and these measurements can be used to infer buoyancy flux.

Appendix A

Validity of the Determination of the Transition Dissipation Rate

Grid-turbulence experiments by Stillinger *et al.* (1983) and Itsweire *et al.* (1986) were used to determine the transition dissipation rate, ϵ_{tr}. This quantity defines the minimum bandwidth available to overturning scales needed to produce a buoyancy flux.

The bandwidth is defined as the ratio of the Ozmidov scale $L_O = (\epsilon/N^3)^{1/2}$ to the Kolmogorov scale $L_K = (\nu^3/\epsilon)^{1/4}$. The Ozmidov scale is the maximum overturning scale in the presence of stratification and the Kolmogorov scale is the length scale at which viscous forces equal inertial forces and viscosity dissipates energy. Raised to the 4/3 power, the ratio becomes

$$\left[\frac{L_O}{L_K}\right]^{4/3} = \frac{\epsilon}{\nu N^2} \tag{A.1}$$

where $\epsilon/\nu N^2$ is often referred to as the turbulent intensity. The transition dissipation rate is defined as the minimum multiple of νN^2 required to sustain a buoyancy flux.

Itsweire *et al.* (1986) estimate the transition dissipation rate as

$$
\begin{aligned}
\epsilon_{tr} &= (15 \pm 1.2)\,\nu N^2 \quad \text{for } M = 1.905 \text{ cm} \\
\epsilon_{tr} &= (21 \pm 1.4)\,\nu N^2 \quad \text{for } M = 3.81 \text{ cm}
\end{aligned}
\tag{A.2}
$$

It is reasonable to assume that some minimum inertial force may be required to overcome viscous force to create overturning. The ratio $\epsilon/\nu N^2$ can be interpreted as a Reynolds number because it describes the ratio of inertial to viscous forces (although it is different than a Reynolds number based on turbulent scales as $Re_t = u'L_T/\nu$). Thus Itsweire et $al.$'s (1986) interpretation appears reasonable.

I believe these numbers to be suspect. Consider Figure 4.10 showing the parameter space for L_t/L_O versus $\epsilon/\nu N^2$. Many data points that were used by Itsweire et $al.$ (1986) are shown to contain significant amounts of internal wave energy by a new scaling analysis done in chapter 4 (see Figure 4.4). Some data with turbulent intensity as high as $\epsilon/\nu N^2 = 100$ are mostly internal waves.

Further, consider Figure A.1 showing the isotropy of turbulent velocities w'/u' against turbulent intensity $\epsilon/\nu N^2$. The solid symbols indicate the presence of internal wave energy from the criterion derived in chapter 4. The top two panels have a grid spacing of $M = 3.81$ cm, the bottom ones have $M = 1.905$ cm. The transition dissipation rate was calculated by Itsweire et $al.$ (1986) as $21\,\nu N^2$ for the top panels. Note most of the data at that energy level contain internal waves. The transition dissipation rate was calculated as $15\,\nu N^2$ for the bottom panels. In both these cases anisotropy increases with decreasing energy, as expected (Gargett et $al.$, 1984), until at $\epsilon/\nu N^2 \approx 25$ where w'/u' increases. The increase is most certainly due to internal wave energy. The increase begins before my criterion classifies data as internal waves, suggesting the criterion could be tighter.

Itsweire et $al.$ (1986) argue that the internal wave energy is created by the grid at a low level, and only becomes perceptible when the turbulent kinetic energy has sufficiently decayed. Considering that Itsweire et $al.$ (1986) calculated different transition dissipation rates for the two grid size, and because it is more reasonable to assume that such a value should be universal, it then seems likely that the internal wave energy interfered with their calculation of the cross-correlation $\overline{\rho'w'}$. Values of w' are probably internal wave energy for $\epsilon/\nu N^2 < 25$. The correlation $\overline{\rho'w'}$ from the much less energetic turbulent fluctuations may then be drowned out by the mostly
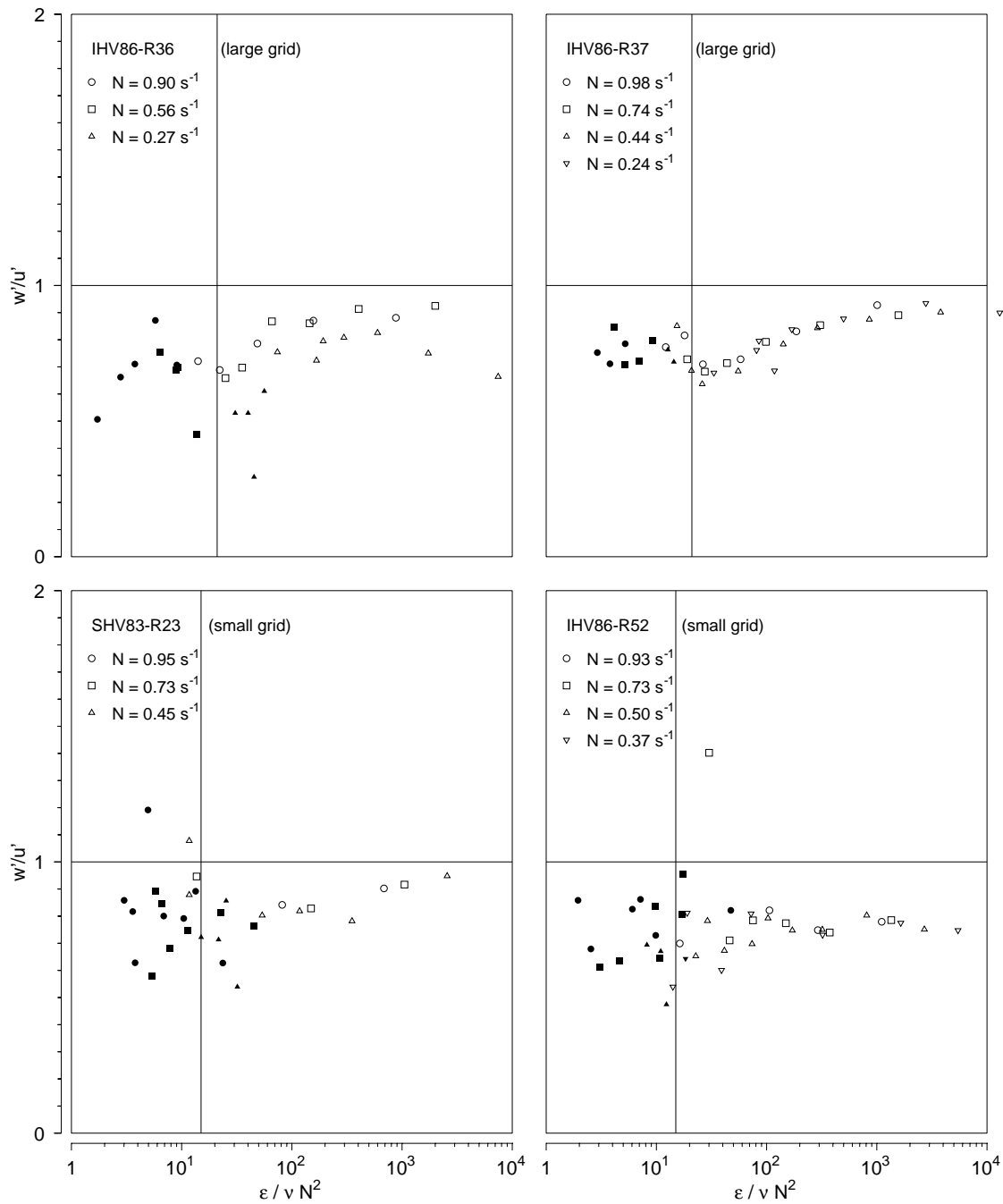
Figure A.1: Isotropy of rms turbulent velocities w'/u' versus turbulence intensity $\epsilon/\nu N^2$. Values in the legend are for N in s^{-1}. Open symbols are for $q/(\epsilon L_t)^{1/3} < 2.2$ (turbulence) and solid symbols for $q/(\epsilon L_t)^{1/3} \geq 2.2$ (internal waves). The vertical lines are for $\epsilon/\nu N^2 = 15$ (small grid mesh size) and $\epsilon/\nu N^2 = 21$ (large grid mesh size). They are the values quoted by Itsweire *et al.* (1986) at which buoyancy flux ceased.

uncorrelated product of $\rho'w'$ associated with the internal waves.

Until further experiments are done without internal waves, or until the technique Itsweire *et al.* (1986) used is shown to be sensitive enough to pick up weak cross-correlation amongst stronger internal wave energy, I would suggest that $\epsilon_{tr} = 15\,\nu N^2$ be viewed as an upper bound on the transition dissipation rate. Perhaps future experiments without internal waves but with a range of Fr_t will show that the important non-dimensional number is Re_t rather than $\epsilon/\nu N^2$.

Appendix B

Interpretations of the Grid-Turbulence Experiments

This appendix reviews the interpretions of Ivey & Imberger (1991) and Gargett (1988) of the grid-turbulence experiment results used in chapter 4. Ivey & Imberger obtain an empirical result similar to my isotropic model. It is then important for me to illustrate where their contribution and mine differ. Gargett (1988), on the hand, has a completely different interpretation of the experiments as evolving from anisotropy towards isotropy as sluggish low-Reynolds-number turbulence. Since her interpretation could invalidate my results, I will contribute new evidence to support my point of view.

B.1   Ivey and Imberger's Empirical Relations

Ivey & Imberger (Ivey and Imberger, 1991; Imberger and Ivey, 1991) use the SHV, IHV and other lab results to derive an empirical prediction to the flux Richardson number as function as turbulent parameters, assuming full isotropy. The resulting form is similar to my second model. Their work is first summarized. A discussion about our differing view points follows.

Ivey & Imberger (1991) describe the experiments in the Fr_t–Re_t parameter space

where the turbulent Froude number is written in various forms as

$$Fr_t \equiv \frac{u'}{NL_t} \tag{B.1}$$

$$= \left[\frac{\epsilon}{L_t^2 N^3}\right]^{1/3} \tag{B.2}$$

$$= \left[\frac{L_O}{L_t}\right]^{2/3} \tag{B.3}$$

$$= \left[\frac{\epsilon}{g_e' w'}\right]^{1/2} \tag{B.4}$$

using $w' = u' \approx (\epsilon L_t)^{1/3}$, and defining $g_e' = g\rho_e'/\overline{\rho} = N^2 L_t$. The turbulent (overturning) Reynolds number is

$$Re_t \equiv \frac{u' L_t}{\nu} = \frac{\epsilon^{1/3} L_t^{4/3}}{\nu} = \left[\frac{L_t}{L_K}\right]^{4/3} \tag{B.5}$$

Additionally, the small-scale Froude number was defined as

$$Fr_\gamma \equiv \frac{\gamma}{N} = \left[\frac{\epsilon}{\nu N^2}\right]^{1/2} = \left[\frac{L_O}{L_K}\right]^{2/3} \tag{B.6}$$

where γ is the rate of strain of the small-scale fluctuations or high wavenumber components of the turbulence defined by:

$$\epsilon = \nu \gamma^2 \tag{B.7}$$

The small-scale Froude number is interpreted as the ratio of the rate of strain of the small-scale fluctuations, γ, to the rate of adjustment by buoyancy of overturn scale fluctuations, N.

The three parameters Fr_t, Re_t and Fr_γ are related by

$$\frac{\epsilon}{\nu N^2} = Fr_\gamma^2 = Fr_t^2 \, Re_t \tag{B.8}$$

written here in terms of the more commonly used turbulent intensity parameter $\epsilon/\nu N^2$. Only two of the three parameters are thus needed to describe the turbulence.

Ivey & Imberger suggest that viscosity suppresses the turbulence when $Re_t < 15$ and the combined effects of buoyancy and viscosity suppress overturning for $Fr_\gamma < 15^{1/2} = 3.9$ (from Ivey & Imberger's average of data from SHV, IHV and other data sets.)

B.1.1 Flux Richardson number, R_f

Ivey & Imberger define a generalized flux Richardson number as the buoyancy flux divided by the net mechanical energy required (or available) to sustain the turbulent motions. For the decaying grid-turbulence, this is

$$R_f = \frac{J_b}{J_b + \epsilon} = \frac{1}{1 + (\epsilon/J_b)} \tag{B.9}$$

Taking advantage of the direct measurements of buoyancy flux, they introduce the correlation coefficient (following Luketina *et al.* (1989))

$$R_{\rho w} = \frac{\overline{\rho'_e w'}}{\left(\overline{\rho'^2_e}\right)^{1/2} \left(\overline{w'^2}\right)^{1/2}} \tag{B.10}$$

for which the dependence on turbulent parameters can be obtained. It allows them to write the flux Richardson number as

$$R_f = \frac{1}{1 + \epsilon/J_b} = \left[1 + \frac{\epsilon}{(g/\overline{\rho})\rho'_e w' R_{\rho w}}\right]^{-1} = \left[1 + \frac{Fr_t^2}{R_{\rho w}}\right]^{-1} \tag{B.11}$$

from $J_b = (g/\overline{\rho})\rho'_e w' R_{\rho w}$ and using (B.4).

Ivey & Imberger then proceed to test (B.11) by first finding the dependence of $R_{\rho w}$ as a function of Fr_t, shown in Figure B.1A. They find that $R_{\rho w}$ tends to an asymptotic value between 0.2 and 0.5 for $Fr_t > 1.2$ such that

$$R_f = 1/(1 + 3Fr_t^2) \quad \text{for } Fr_t > 1.2 \tag{B.12}$$

without dependence on Re_t so long as $Re_t > 30$. For $Fr_t < 1.2$, they find a quick decrease of $R_{\rho w}$ towards lower Fr_t, reaching zero when motion is made up predominantly of internal waves. They find this behaviour entirely consistent with

the result of SHV and IHV[1] who found that effects of buoyancy are first felt at $Fr_t = (L_O/L_t)^{2/3} \approx 1.1$. Ivey & Imberger then proceed to find a functional form for R_f which satisfies three constraints: $R_f = 0$ when $Fr_t = (Re_t/15)^{-1/2}$ from (B.8) and that the solution patches with (B.12) smoothly, which sets the second and third constraints as $R_f = 0.19$ and $\partial R_f/\partial Fr_t$ = -0.25 at $Fr_t = 1.2$. The resulting dependence of R_f on Fr_t is shown in Figure 4.6A compared to data without internal wave contributions (Note that Ivey & Imberger included these internal waves data).

B.1.2   Discussion of Ivey and Imberger's Interpretation

There are several problems with the empirical fit that Ivey and Imberger have chosen and with the way in which they have done it. On physical grounds, they argue that for $Fr_t > 1$ the velocity is greater than the buoyancy adjustment velocity NL_t such that turbulence is possible. By contrast, for $Fr_t < 1$ velocities cannot break the hold of gravity and only internal wave motion is possible. Therefore, they expect a decrease in R_f for $Fr_t < 1$ because of the expected internal wave motions in that Froude number range. However, when (3.26) is verified in Figure 4.5A, it is seen that although L_t/L_O continues to increase after the transition to internal wave motion (using my new classification scheme), the measured Fr_t increases instead of decreases, and is still greater than unity for internal wave dominated data. Therefore, since Ivey and Imberger chose to show both R_f and $R_{\rho w}$ variations as functions of Fr_t, rather than as a function of L_t/L_O, their transition to internal wave occurs at a higher Fr_t, and considerable scatter is added in their plots. Removing internal wave data takes out much of the scatter, as shown in Figure 4.6B.

---

[1]In the experiments, L_t initially grows at the same rate for all stratifications, matching the growth rate in un-stratified experiments. The overturning scale L_t deviates from the un-stratified case when the effects of buoyancy are first felt. The ratio L_t/L_O at this transition was debated by SHV and IHV because they felt it represented the inertial-buoyancy balance, so that the ratio should be directly comparable with Dillon's (1982) oceanic result of $L_T/L_O = 1.25$. SHV obtained $L_t/L_O = 0.7$, but IHV obtained $L_t/L_O = 0.85$ which they thought to be more accurate. Interestingly, IHV noted that their result of $L_t/L_O = 0.85$ (equal to $L_T/L_O = 0.7$ using $L_T/L_t \approx 1.2$ from Itsweire (1984), Figure 4.9 here) was well correlated with Dillon's (1982) result of 0.8. In fact, Dillon's result was $L_O/L_T = 0.8$, not $L_T/L_O = 0.8$.
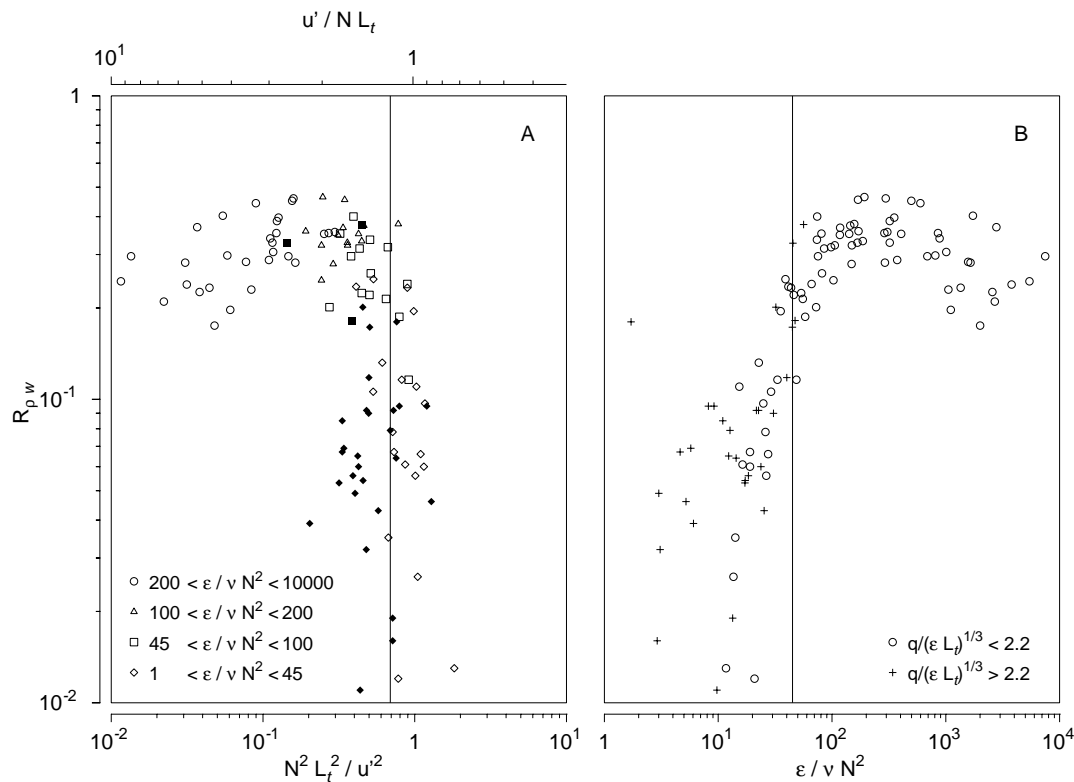
Figure B.1: Correlation coefficient $R_{\rho w}$ versus turbulent parameters (A) Fr_t, Ri_t; and versus (B) $\epsilon/\nu N^2$ for data with $R_f > 0$ (not re-stratifying). Note that most data with $R_f < 0$ are also classified as internal waves ($q/(\epsilon L_t)^{1/3} < 2.2$). **A:** The vertical line is $Fr_t = 1.2$, to the right of which $R_{\rho w}$ decreases (data with $q/(\epsilon L_t)^{1/3} > 2.2$, classified as internal waves, decreases at a higher value of Fr_t). This was interpreted by Ivey & Imberger (1991) as being due to the onset of buoyancy effects. The data are shown coded for various values of $\epsilon/\nu N^2$. The solid symbols are classified as internal waves ($q/(\epsilon L_t)^{1/3} > 2.2$); **B:** The same R_f data are shown versus $\epsilon/\nu N^2$, coded for the presense of internal waves. The vertical line is $\epsilon/\nu N^2 = 45$. Note that the decrease of $R_{\rho w}$ for $\epsilon/\nu N^2 < 45$ or so is much tighter when only internal wave free data are considered ($q/(\epsilon L_t)^{1/3} < 2.2$). Data from Stillinger $et\ al.$ (1983) and Itsweire $et\ al.$ (1986).

Second, their scaling suggests $\Gamma = R_{\rho w}/Fr_t^2$ so they verified the behaviour of $R_{\rho w}$ as function of Fr_t, shown in Figure B.1A, finding a dramatic decrease at the onset of buoyancy effects. Further arguments in their paper point to a maximum mixing efficiency corresponding to $R_f = 0.19$ at the inertial-buoyancy balance. They compare this value to oceanic results, thus assuming that ocean mixing occurs at inertial-buoyancy balance.

I have argued in chapter 4 that the inertial buoyancy-balance is not at $Ri_t = 0.7$ ($Fr_t = 1.2$), but rather at $Ri_t \approx 1.55$. I have shown in chapter 4 that the dramatic decrease in mixing efficiency in these experiments is due to low turbulent intensity ($\epsilon/\nu N^2 < 45$) toward the end of the experiments. I believe that the turbulence never reaches inertial-buoyancy balance. Figure B.1B shows the variation of $R_{\rho w}$ versus $\epsilon/\nu N^2$. It is consistent with my interpretation.

Lastly, a minor point. Their empirical fit for small Fr_t uses the condition that R_f only goes to zero only when $Fr_t = 3.9\,Re_t^{-1/2}$ from the combined effects of buoyancy and viscosity. Their graph did not include predictions for oceanic values of Re_t. As an extreme example, Gargett (1988) reports values of $\epsilon/\nu N^2$ of up to 50000 in the ocean. Assuming $Fr_t \approx 1$, this value of $\epsilon/\nu N^2$ yields $Re_t = 50000$ for which their prediction is included on Figure 4.6. How useful is this Ad Hoc parameterization? It predicts high R_f for very low Fr_t for which no data are shown to produce overturning either in the lab or in the ocean. Oceanographers measure ϵ rather than Re_t and so an empirical result based on $\epsilon/\nu N^2$ would have been more useful.

In summary, Ivey & Imberger's empirical fit of R_f as function of Ri_t is in agreement with my second model, but only for $Fr_t > 1.2$. Ivey & Imberger associate the observed flux Richardson number of $R_f \approx 0.20$ at $Fr_t = 1.2$ to expected values for Kelvin-Helholtz billows which presumably occur at inertial-buoyancy balance. This implies that ocean mixing occurs at this inertial-buoyancy balance.

I believe that (1) turbulence at the inertial-buoyancy balance was never sampled in the laboratory experiments described because of the presence of internal waves.

Therefore the maximum mixing efficiency quoted is an under-estimate. Ivey & Imberger misinterpreted the decrease of mixing efficiency, which I attritute to low turbulent intensity ($\epsilon/\nu N^2 < 45$) (2) Comparing only the maximum mixing efficiency to oceanic values implies that all oceanic mixing occurs at near-inertial balance. This assumption may not be correct. I believe that average oceanic mixing efficiency is lower than the inertial-buoyancy value, but that the oceanic average represents a mix of conditions. (3) The extrapolation that they have made for R_f at $Fr_t \gg 1$ are not useful. Why even defines a mixing efficiency for a turbulent Froude number for which overturning cannot occur (as shown by Figure 4.8)?

B.2 Gargett's Alternative Interpretation

Gargett (1988) provides an alternative interpretation of the SHV and IHV experiments as low $Re_w = w'L_t/\nu$ flows with $Fr_t \approx 1$ throughout their evolution. The overturning would be initially anisotropic, evolving towards isotropy during decay. This interpretion led to a debate between Van Atta (1990) and Gargett (1990). Since her interpretation could invalidate my use of the data to verify my model, I will add new evidence to the discussion.

B.2.1 Review

Gargett presents a scaling of the TKE equations for $Fr_h \equiv u'/NL_h \approx 1$ where L_h is a horizontal overturning scale which differs from the overturn height when aniostropic. Assuming $Fr_h \approx 1$, she equates L_h to the Ozmidov scale L_O, which is reasonable when an inertial-buoyancy balance holds. The isotropy is then described by the ratio $L_t/L_h = L_t/L_O$. She defines a vertical fluctuations Reynolds number $Re_w = w'L_t/\nu$ and uses continuity, $u'/L_O \approx w'/L_t$, and $u' = (\epsilon L_h)^{1/3}$ to write a relation similar to

Ivey and Imberger's (B.8)[2] as

$$\frac{\epsilon}{\nu N^2} = \frac{u'^3/L_h}{\nu N^2} = \left[\frac{u'^2}{L_h^2 N^2}\right]\left[\frac{L_h u'}{\nu}\right] = Fr_h^2\,Re_h = \left[\frac{u'^2}{L_t^2 N^2}\frac{L_t^2}{L_h^2}\right]\left[\frac{L_t w'}{\nu}\frac{L_h^2}{L_t^2}\right] = Fr_t^2\,Re_w$$

(B.13)

The turbulent Froude number Fr_t was said to be related to the mixing efficiency via $\Gamma = R_{\rho w}Fr_t^{-2}$ by Ivey & Imberger[3]. Gargett writes a similar relation (dropping the correlation coefficient $R_{\rho w}$) which is independent of Re_w and isotropy[4] as

$$\Gamma = \frac{J_b}{\epsilon} \approx \frac{N^2 L_t w'}{u'^3/L_h} = \left[\frac{N^2 L_t^2}{u'^2}\right]\left[\frac{w' L_h}{u' L_t}\right] = Fr_t^{-2}$$

(B.14)

Gargett argues from scaling the TKE equations for $Re_w \gg 1$ that the turbulent velocity field must be nearly isotropic. In this case (B.13) collapses to (B.8).

In the case where $Re_w \approx 1$, the velocities may be anisotropic and (B.13) reduces to

$$\frac{\epsilon}{\nu N^2} = Fr_t^2$$

(B.15)

where turbulence is characterized by the same horizontal scales as for $Re_w \gg 1$, but vertical scales should scale with ν and N as

$$w' \approx (\nu N)^{1/2}$$

(B.16)

$$L_t \approx (\nu/N)^{1/2}$$

(B.17)

Combining (B.15) and (B.14), the turbulence intensity is related to the mixing efficiency; additionally using $Fr_t = Fr_h(L_h/L_t)$ and $Fr_h \approx 1$ (by assumption) we get

$$\frac{\epsilon}{\nu N^2} = \Gamma^{-1} \approx \left[\frac{L_h}{L_t}\right]^2$$

(B.18)

---

[2]although there was no relation between the paper. I point out the similarity to help the reader.

[3]Note that this relation was derived using $Fr_t = (\epsilon/g'w')^{1/2}$, which can be shown to not require isotropy, as long it can be assumed that the relation $u' = (\epsilon L_h)^{1/3}$ holds, where L_h is the horizontal turbulent length-scale. Even for the anisotropic inertial-buoyancy balance case of the third model, it can easily be shown that $Fr_t = (\epsilon/g'_e w')^{1/2}$ still holds for $Fr_t = L_O/L_T$. Using $\epsilon = L_O^2 N^3$, $g' = N^2 L_T$ and $w' = NL_T$, we obtain $Fr_t = (L_O^2 N^3/N^2 L_T\,NL_T)^{1/2} = L_O/L_T$.

[4]This also confirms my result in chapter 4 that isotropy does not matter for this formulation of the mixing efficiency

The main point is that while the two regimes, $Re_w \approx 1$ and $Re_w \gg 1$, describe quite different types of turbulence, they may both be characterized by $\epsilon/\nu N^2 \gg 1$ from (B.18) and (B.15). The turbulence intensity cannot be used to distinguish the two types of turbulence.

If the turbulence is isotropic, $\epsilon/\nu N^2 \gg 1$ is interpreted as $Re_w = Re_t \gg 1$ from (B.13) since Fr_h is of order 1. If the turbulence is not isotropic, Gargett assumes $Re_w \approx 1$ such that $\epsilon/\nu N^2 \gg 1$ must be interpreted as $\Gamma \ll 1$. from (B.18).

B.2.2 Discussion of Gargett's Interpretation

Gargett interprets the SHV and IHV experiments as the $Re_w \approx 1$ case because Re_w is relatively low compared to ocean values (from 160 near the grid to 20–30 at the transition to internal waves) and assumes Fr_h is close to unity throughout the experiment. Indeed, I have found support for this point of view comes from Figure 4.10 if L_O is interpreted as L_h; the prediction from (B.18) is very good. Gargett argues that the evolution in Figure 4.2 must be interpreted as always feeling the effects of buoyancy, with sluggish vertical turbulence. The Ozmidov scale L_O must be interpreted as the horizontal scale of the turbulence, initially much greater than the vertical scale L_t. The turbulence thus starts out being very anisotropic, evolving towards isotropy as the vertical scale remains more or less constantly proportional to (B.17) and L_O decreases with the decay. If this were the case, our results concerning the mixing efficiency, which are also predicted by Gargett independently of Re_w, would only validate the prediction for cases which do not apply to the ocean and where the decreased efficiency is interpreted as caused by anisotropy. Of course, Van Atta holds the opposite view that the turbulence is created at isotropy without buoyancy effects, and evolves towards inertial-buoyancy balance.

Estimating the Horizontal Length Scale; An Inconsistency

Gargett assumes that L_O represents the unmeasured horizontal turbulent length scale L_h and, at the same time, that the continuity relation for turbulence $u'/L_h \approx w'/L_t$

holds. However, L_O/L_t varies from 10 to 100 near the grid to less than 1 at the end of the experiments (see Figure 4.2). At the same time w'/u' is shown in Figure A.1 start close to unity, decreasing as the turbulence decays. This is consistent with Van Atta's interpretation; indeed Gargett (1988) points out the inconsistency with her interpretation. If the continuity relation does not hold, then neither does her $\Gamma = Fr_t^{-2}$ scaling which was shown to hold very well for the lab data.

I will exploit this inconsistency here with a new test to verify if Gargett's or Van Atta's interpretation is correct. Since the assumption that $L_O = L_h$ is incompatible with $L_h \approx L_t(u'/w')$, let us test which best fits Kolmogorov scaling $\epsilon = u'^3/L_h$. Gargett's assumption leads to

$$u' = (\epsilon L_h)^{1/3} = \left[\frac{\epsilon}{N}\right]^{1/2} = L_O N \qquad (B.19)$$

while Van Atta's leads to

$$u' = (\epsilon L_h)^{1/3} = \left[\epsilon L_t \frac{u'}{w'}\right]^{1/3} \qquad (B.20)$$

Figure B.2 provides a new test of Gargett's and Van Atta's interpretations. The predictions (B.19) and (B.20) are compared versus L_t/L_O. Gargett's assumption that L_O is the appropriate horizontal turbulent length scale would imply horizontal velocities near the grid three times larger than those measured ($u'/NL_O \approx 1/3$ in Figure B.2A at lowest values of L_t/L_O which occur at the beginning of the experiments). The length scales from turbulent continuity (and Van Atta's interpretation of near-isotropy near the grid) are consistent with turbulent scaling for most of the early part of the evolution, where Gargett predicted they would not be. Turbulent scaling fails far from the grid where velocities are smallest and internal wave are thought to be important. Thus the SHV and IHV experiments cannot be interpreted as Gargett's low vertical Reynolds number flow at inertial-buoyancy balance.
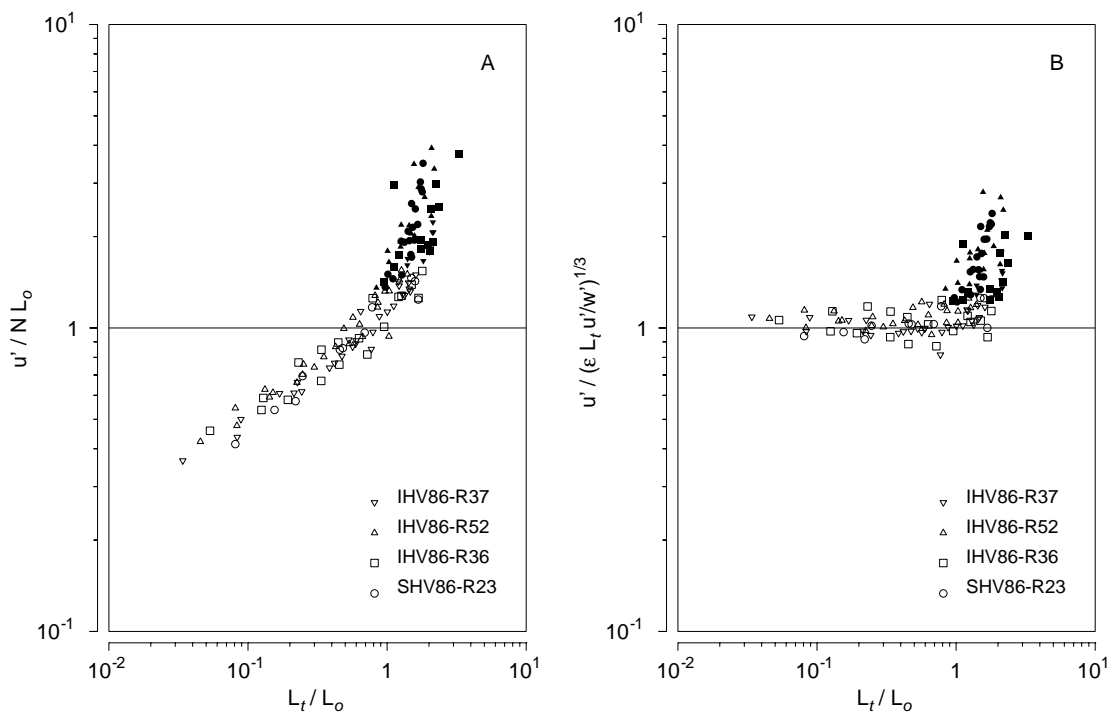
Figure B.2: Two models of turbulent scaling $u'/(\epsilon L_h)^{1/3} = 1$ are tested vs L_t/L_O. **A:** For Gargett's low Re_w turbulence, assuming the horizontal eddy scale L_h is equal to L_O makes $u'/(\epsilon L_t)^{1/3}$ scales like u'/NL_O. **B:** The horizontal eddy scale L_h is inferred from continuity as $L_t(u'/w')$.

Appendix C

Review of Dillon's Relations of Finestructure to Mixing

Dillon (1982) was first to verify Thorpe's (1977) proposal that the Thorpe scale L_T is related to the Ozmidiv scale L_O. In this appendix, we review Dillon's (1982; 1984) and Dillon *et al.*'s (1987) work relating overturn-related quantities such as Thorpe scales L_T and the Available Potential Energy of the density Fluctions ξ to dissipation and buoyancy flux. The data sets used in chapter 5 are briefly described.

C.1   Data Sets

Dillon (1982) tabled data obtained at Ocean Station P during the MILE experiment (Series A and B) and at Green Peter Reservoir (Series C). For all cases, temperature mainly determines density such that $\rho'/\overline{\rho} = -\alpha T'$ and $J_b = -\alpha g \, \overline{w'T'}$. The oceanic data were taken in two periods; series A was sampled during winds of 5 $\mathrm{m\,s^{-1}}$, but winds were greater than 15 $\mathrm{m\,s^{-1}}$ five hours before then. Series B were sampled in strong winds (>15 $\mathrm{m\,s^{-1}}$). These two oceanic series (A and B) were deep in the interior of wind-forced layers and in the seasonal thermocline. The reservoir data (Series C) were taken in winds of 8.5 $\mathrm{m\,s^{-1}}$ and a portion were taken in the near-surface zone. In all, 102 mixing layers of order 1–5 m thick were used. Only layers

where all quantities are well resolved are used.

C.1.1 Relation of Thorpe Scale to Ozmidov

Dillon (1982) expected L_T to be highly correlated with $L_O = (\epsilon/N^3)^{1/2}$ when the gradient Richardson Ri_g was constant in time. To demonstrate this he started with the steaty-state TKE balance equation (with the advective terms neglected)

$$-\overline{u'w'}\frac{\partial \overline{U}}{\partial z} = \epsilon + J_b \tag{C.1}$$

and assumed the Thorpe scale to be proportional to the size of an eddy, defined as $(-\overline{u'w'})^{1/2}(\partial \overline{U}/\partial z)^{-1}$. Then using $Ri_g = N^2(\partial \overline{U}/\partial z)^{-2}$, $N^2 = -g\rho^{-1}(\partial \rho/\partial z)$ and $R_f = J_b/(J_b + \epsilon)$ and some manipulation, (C.1) reduces to

$$L_T \propto Ri_g^{3/4}\left[\frac{\epsilon + J_b}{N^3}\right]^{1/2} = Ri_g^{3/4}(1 - R_f)^{-1/2}L_O \tag{C.2}$$

Thus the L_T–L_O relation was expected to hold for nearly constant gradient and flux Richardson numbers[1].

Dillon's comparison between Thorpe Scale and Ozmidov Scale is reproduced in Figure C.1. Dillon obtained his much-quoted ratio of $L_T/L_O = 1.25$ by first performing a regression of the form $L_O = aL_T^n$ on series B (the high wind case) where (C.2) is expected to hold better for the more strongly driven turbulence; Dillon thought that turbulence could be decaying in the other cases. Dillon obtained $n = 0.98$, close to unity, and thus evaluated a from the mean ratio $\overline{L_O/L_T} = 0.8$. The value of L_O/L_T can be evaluated many different ways, a sample of which is provided in Table C.1 for comparison with Dillon's calculation. I obtain $\overline{L_O/L_T} = 0.885$ rather than 0.8 using all points of series B; this could be due to transcription errors in the table.

The data probably have a log-normal distribution suggesting that a regression in logarithmic space is appropriate. In this case, the L_T/L_O ratio is 1.17 $^\times\!/_\div$ 1.14 from the

[1]In Chapter 3, it was noted that $L_T \propto u'(\partial \overline{U}/\partial z)^{-1}$ led to $Ri_t \propto Ri_g$. Here we note that $L_T \propto (-\overline{u'w'})^{1/2}(\partial \overline{U}/\partial z)^{-1}$ leads to $L_T/L_O \propto Ri_g^{3/4}$, consistent with $L_T/L_O \propto Ri_t^{3/4}$ for isotropic turbulence from Chapter 3.
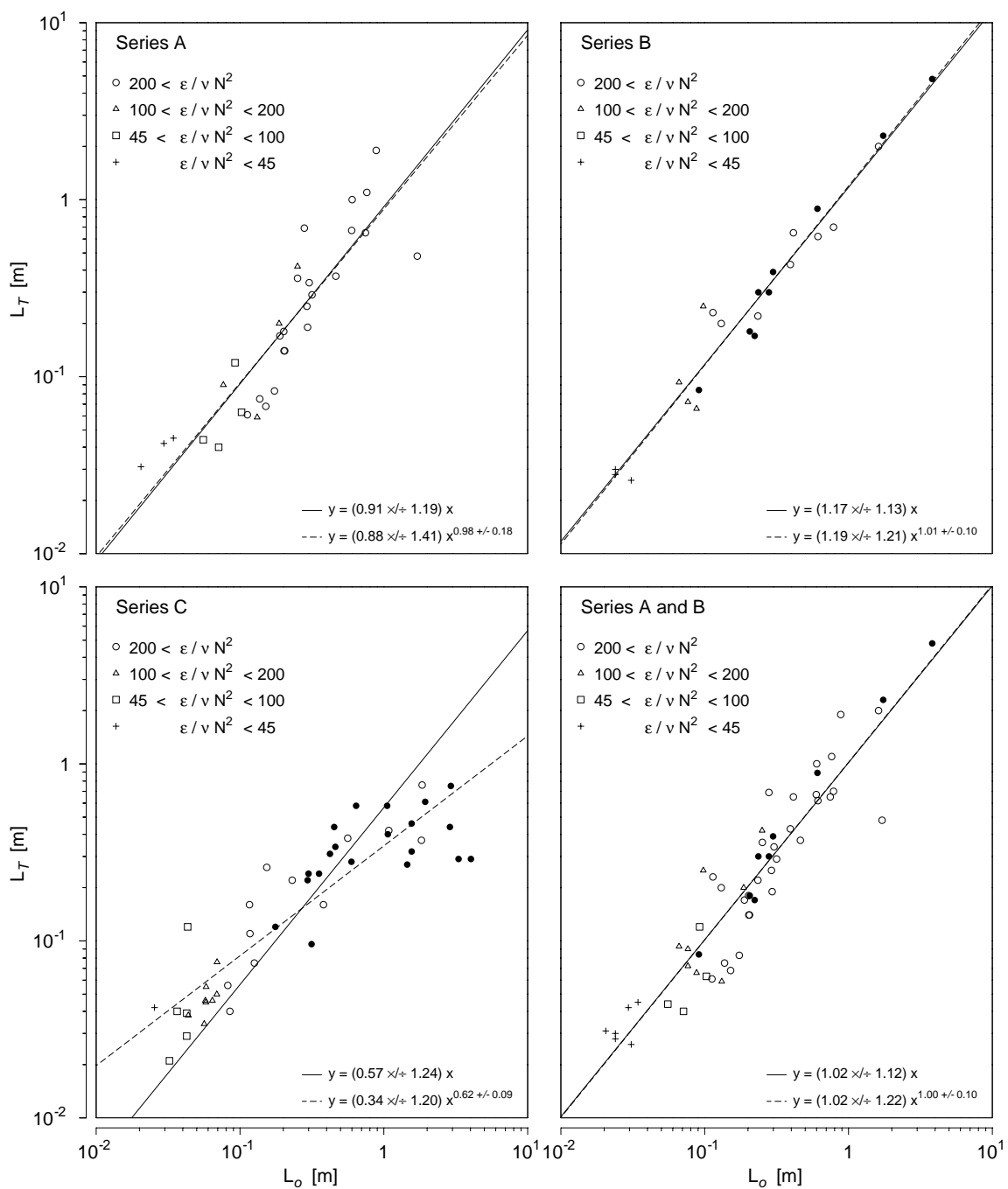
Figure C.1: Comparison of Thorpe scales L_T versus Ozmidov scales L_O for two oceanic cases (Series A and B) and a fresh water reservoir (Series C). Data are classified by turbulent intensity $\epsilon/\nu N^2$. Open symbols are well resolved; filled symbols are marginally resolved. Data are from tables in Dillon (1982). This figure corresponds to Figures 8, 9 and 10 in Dillon (1982).

	Series A		Series B		Series A and B	
	All pts	$\epsilon/\nu N^2 > 200$	All pts	$\epsilon/\nu N^2 > 200$	All pts	$\epsilon/\nu N^2 > 200$
Linear						
$\overline{L_T/L_O}$	1.04	1.04	1.23	1.23	1.15	1.15
$\overline{L_T}/\overline{L_O}$	1.03	1.00	1.23	1.21	1.11	1.09
$(\overline{L_O/L_T})^{-1}$	0.81	0.76	1.13	1.14	0.92	0.89
Log						
$L_T = aL_O$	0.91	0.87	1.17	1.17	0.99	1.02
	$^\times\!/_\div 1.19$	$^\times\!/_\div 1.27$	$^\times\!/_\div 1.14$	$^\times\!/_\div 1.13$	$^\times\!/_\div 1.15$	$^\times\!/_\div 1.12$

Table C.1: Calculation of the L_T/L_O ratio for oceanic data series A and B. In the logarithmic regression, $L_T = aL_O$ is used because $L_T = aL_O^n$ was tried and n was never statistically different than 1.

more strongly forced mixing of series B. This ratio remains unchanged whether all data are used, or only those for which $\epsilon/\nu N^2 > 200$ associated with isotropic turbulence (Gargett *et al.*, 1984). While the ratio is numerically different from Dillon's result of 1.25, the two are not statistically different.

C.1.2   Thorpe Scale Relation to Buoyancy Flux

The reservoir data (series C) has more scatter; Dillon attributed this to the smaller segments, averaging 1.6 m instead of 3.5 m. Nevertheless, the L_T/L_O ratio was consistent with the oceanic cases at the base of the mixing layer, but was much larger near the surface where Richardson numbers can be much lower.

Dillon expected both a gradient and flux Richardson number on the L_O/L_T relation from (C.2), and so attributed the disparity near the surface to decreasing Richardson numbers. A new length scale $L_B = (J_b N^{-3})^{1/2}$ was introduced, estimating the buoyancy flux J_b from $\alpha g \chi_\theta / 2(\partial \overline{T}/\partial z)$. A weaker dependence on R_f was predicted for the ratio L_B/L_T assuming $R_f \approx Ri_g$ by rewriting (C.2) as

$$L_T \propto Ri_g^{1/4} \left[\frac{Ri_g}{R_f} \right] L_B \tag{C.3}$$

The correlation between L_T and L_B is better than between L_T and L_O for all mixing regimes (See figure C.2). This includes the near-surface zone where the L_O/L_T ratio failed to hold, although L_T/L_B still decreases there. This is Dillon's first indication that the Thorpe scale may be in fact more closely related to the buoyancy flux than to dissipation.[2]

C.1.3 The APEF linked to buoyancy flux

As discussed in section 3.2.2, Dillon (1982) used the temperature variance equation (3.8) to look at the decay time of temperature fluctuations by χ_θ, using Thorpe fluctuations as the stock of temperature variance to dissipate. Dillon (1984) multiplied the temperature variance equation (3.8) by $\alpha g/(2\partial T_o/\partial z)$ to obtain a potential energy equation (3.10). He defined the Available Potential Energy of the density Fluctuations ξ as the potential energy difference between the measured and re-ordered profile. The re-ordered profile represents the base state from which an overturn has evolved from. As I have argued in chapter 3, Dillon (1984) noted that (3.10) suggests an intimate relation between the APEF and the potential energy dissipation rate $3N^2\kappa_T C_x$.

Dillon *et al.* (1987) end with an empirical relation between the APEF and the dissipation of potential energy as

$$3N^2\kappa_T C_x = 4.8\,\xi\,N \tag{C.4}$$

They suggest that this is the prime relation, but that $L_T \approx L_O$ follows from this if $3N^2\kappa_T C_x/(\epsilon + 3N^2\kappa_T C_x)$ is fairly constant[3].

C.1.4 Discussion

There are many similarities between Dillon's (C.4) and my own models. Indeed Dillon's work was a great inspiration to me. The differences are mostly in the decay

---

[2] Although Dillon obtains $\overline{L_B/L_T} = 0.93$, I prefer $L_T/L_B = 1.2$ from a log-space regression.

[3] If $3N^2\kappa_T C_x = J_b$ and there is a steaty-state, then this is the flux Richardson number R_f, related to the mixing efficiency.
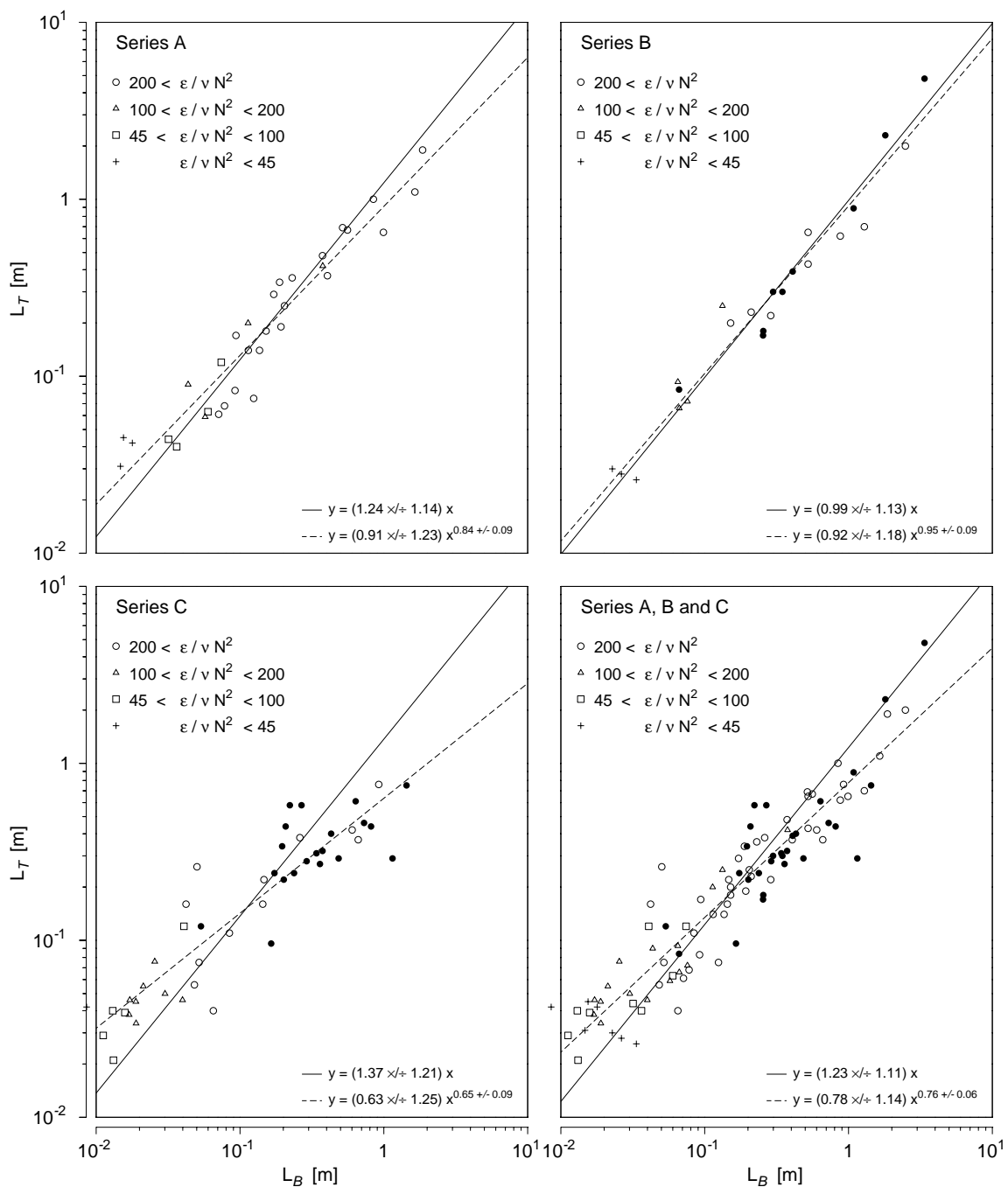
Figure C.2: Comparison of L_T vs L_B for two oceanic cases (Series A and B) and a fresh water reservoir (Series C). Data are classified by turbulent intensity $\epsilon/\nu N^2$. Open symbols are well resolved; filled symbols are marginally resolved. Data are from tables in Dillon (1982). This figure corresponds to Figure 11 in Dillon (1982).

time and mixing efficiency. Dillon (1984) compared terms in the total energy equation (3.13) by approximating the total kinetic energy as 3 times ξ, and assumed a decay time proportional to N^{-1}. These assumptions are only consistent with my isotropic model at inertial-buoyancy balance (see chapter 3).

Dillon et $al.$'s (1987) empirical result relates ξ to $3N^2\kappa_T C_x$ again using a decay time proportional to N^{-1}. Their decay time is 4.8 times faster than my predictions; This is discussed in chapter 4. Their only prediction regarding the relation of ϵ to ξN is through $L_T \approx L_O$. Squaring this latter relation gives $L_T^2 = \epsilon/N^3$ and thus $\epsilon \propto \xi N$. They predict the relation $L_T \approx L_O$ to hold for a constant mixing efficiency (see above), but make no prediction as to what the mixing efficiency should be, or how it should vary. My main contribution is to relate the APEF to buoyancy flux through a simple kinematical model, and explain why and how mixing efficiency should vary through anisotropy.

Appendix D

The Run-Length Method To Determine Temperature Noise Level

In this appendix, I briefly describe a new technique to estimate the temperature noise level. No example is shown; only a brief description is given.

The aim is to determine the noise level of the temperature sensor. The technique assumes that the real temperature profile is generally monotonic such that any measured inversions are either intrusions, overturns or noise. It is also assumed that temperature is recorded with enough digits such that noise actually produces inversions. The technique is then simply to identify which of the inversions are caused by noise; the noise level is then the rms Thorpe fluctuation T' of the noise-related inversions, where T' is the temperature difference between the measured and re-ordered profiles.

Let us denote the temperature sensor noise level as δT. Noise will create inversions unrelated to physical features in low stratification: where noise δT is greater than the temperature difference between successive points of the re-ordered profile $\delta z \, (\partial T_o / \partial z)$, where δz is the sampling interval and T_o is the re-ordered profile.

These inversions have differences with those created by overturns: their Thorpe

fluctuations T' are approximately equal to the noise level δT, and the overturns are not 'very' top-heavy. This second point is explained by contrasting it to the case of an overturn. The top half or so of an overturn is heavy water that originates from the bottom half. Thus it is top heavy, in the sense that most Thorpe fluctuations in the top half are positive and most of those in the bottom half are negative (for a stable profile with increasing temperature with pressure). When noise creates inversions this pattern does not occur. Noise might add to a point and subtract from the next. Re-ordering the points moves them randomly upwards and downwards, and a series of Thorpe fluctuations of random sign follows.

The temperature noise level δT is estimated by the amplitude of Thorpe fluctuations which have a random sign distribution. These are identified by a run-length analysis. The run-length is the number of consecutive points of the same sign. For a random population of numbers, equally divided between positive and negative, the fraction of run lengths of length n is $(1/2)^n$. If the distribution is random, half of the run lengths should have a length of 1, a quarter should have a length of 2, and so on. Noise can statistically produce very few run lengths of long length (say $n > 5$). This is where the overturns come into play: since overturns are top-heavy they will have long run-lengths, uncharacteristic of noise-related inversions. Thus, the run lengths distribution calculated on a temperature profile containing both noise inversions and energetic overturns has a decreasing number of run lengths with increasing size, until the run length size where overturns starts to be observed. A run-length size cut-off can then be chosen to separate noise from overturn, and the amplitude of Thorpe fluctuations of noisy inversions can be calculated as an estimate of δT. An application of this method is shown in Galbraith and Kelley (1992).

This method succeeds best with a short sampling interval and small instrument least count. This increases both the occurrence of noise inversions and the difference between the high run lengths of overturns and the low run length of noise. When very few noise-related inversions occur it is impossible to apply the technique.

Bibliography

BLACFORD, B. L. (1978). On the generation of internal waves by tidal flow over a sill—a possible nonlinear mechanism. *J. Mar. Res.*, 36:529–549.

BOGUCKI, D. (1991). Shear induced decay of internal solitary waves. *M.Sc. Thesis, Dalhousie University, Halifax.*

BROWAND, F. K. AND HOPFINGER, E. J. (1985). The inhibition of vertical turbulent scale by stable stratification. In HUNT, J. C. R., editor, *Turbulence and diffusion in stable environments.*

CRAWFORD, W. R. (1986). A comparison of length scales and decay times of turbulence in stably stratified flows. *J. Phys. Oceanogr.*, 16:1847–1854.

DILLON, T. M. (1982). Vertical overturns: a comparison of Thorpe and Ozmidov length scales. *J. Geophys. Res.*, 87:9601–9613.

DILLON, T. M. (1984). The energetics of overturning structures: implications for the theory of fossil turbulence. *J. Phys. Oceanogr.*, 14:541–549.

DILLON, T. M. AND PARK, M. M. (1987). The available potential energy of overturns as an indicator of mixing in the seasonal thermocline. *J. Geophys. Res.*, 92:5345–5353.

EL-SABH, M. I. (1979). The lower St. Lawrence estuary as a physical oceanographic system. *Naturaliste Can.*, 106:55–73.

FORRESTER, W. D. (1974). Internal tides in the St. Lawrence estuary. *J. Mar. Res.*, 32:55–66.

GAGNON, M. AND EL-SABH, M. I. (1980). Effets de la marée interne et des oscilations de basse fréquence sur la circulation côtière dans l'estuaire du Saint-Laurent. *Naturaliste Can.*, 107:159–174.

GALBRAITH, P. S. AND KELLEY, D. E. (1992). Identifying overturns in finestructure. In revision for *J. Geophys. Res.*

GARGETT, A. E. (1988). The scaling of turbulence in the presence of stable stratification. *J. Geophys. Res.*, 93:5021–5036.

GARGETT, A. E. (1990). Reply. *J. Geophys. Res.*, 95:11675–11677.

GARGETT, A. E. AND HOLLOWAY, G. (1984). Dissipation and diffusion by internal wave breaking. *J. Mar. Res.*, 42:15–27.

GARGETT, A. E., OSBORN, T. R., AND NASMYTH, P. W. (1984). Local isotropy and the decay of turbulence in a stratified fluid. *J. Fluid Mech.*, 144:231–280.

GARRETT, C. (1984). Parameterizing the effects of internal waves: simple ideas and things we need to know. In MULLER, P. AND PUJALET, R., editors, *Internal gravity waves and small-scale turbulence*, pages 171–181. Hawaii Inst of Geophysics.

GARRETT, C. (1989). Are diapycnal fluxes linked to lateral stirring rates? In *Internal gravity waves and small-scale turbulence*. Hawaii Inst of Geophysics.

GIBSON, C. H. (1982). Alternative interpretations for microstructure patches in the thermocline. *J. Phys. Oceanogr.*, 12:374–383.

GREGG, M. C. (1987). Diapycnal mixing in the thermocline: a review. *J. Geophys. Res.*, 92:5249–5286.

GREGG, M. C. (1989). Scaling turbulent dissipation in the thermocline. *J. Geophys. Res.*, 94:9686–9698.

GREGG, M. C., D' ASARO, E. A., SHAY, T. J., AND LARSON, N. (1986). Observations of persistent mixing and near-inertial internal waves. *J. Phys. Oceanogr.*, 16:856–885.

HENYEY, F. S., WRIGHT, J., AND FLATTÉ, S. M. (1986). Energy and action flow through the internal wave field: An eikonal approach. *J. Geophys. Res.*, 91:8487–8495.

IMBERGER, J. AND IVEY, G. N. (1991). On the nature of turbulence in a stratified fluid. Part II: Application to lakes. *J. Phys. Oceanogr.*, 21:659–680.

INGRAM, R. G. (1975). Influence of tidal-induced vertical mixing on primary productivity in the St. Lawrence estuary. *Mémoires Societé Royale de Liège*, 6e série, tome VII:59–74.

INGRAM, R. G. (1978). Internal wave observations off Isle Verte. *J. Mar. Res.*, 36:715–724.

INGRAM, R. G. (1979). Water mass modification in the St. Lawrence estuary. *Naturaliste Can.*, 106:45–54.

INGRAM, R. G. (1983). Vertical mixing at the head of the Laurentian Channel. *Estuar., Coast. and Shelf Sci.*, 16:333–338.

ITSWEIRE, E. C. (1984). Measurements of vertical overturns in a stably stratified turbulent flow. *Phys. Fluids*, 27:764–766.

ITSWEIRE, E. C., HELLAND, K. N., AND VAN ATTA, C. W. (1986). The evolution of grid-generated turbulence in a stably stratified fluid. *J. Fluid Mech.*, 162:299–338.

IVEY, G. N. AND IMBERGER, J. (1991). On the nature of turbulence in a stratified fluid. Part I: The energetics of mixing. *J. Phys. Oceanogr.*, 21:650–658.

JONES, J. H. (1973). Vertical mixing in the Equatorial undercurrent. *J. Phys. Oceanogr.*, 3:286–296.

LUKETINA, D. A. AND IMBERGER, J. (1989). Turbulence and entrainment in a buoyant surface plume. *J. Geophys. Res.*, 94:12619–12636.

MARMORINO, G. O. (1991). Observations of small-scale mixing processes in the seasonal thermocline. Part II: Wave breaking. *J. Phys. Oceanogr.*, 17:1348–1355.

McCOMAS, C. H. AND MULLER, P. (1981). The dynamic balance of internal waves. *J. Phys. Oceanogr.*, 11:970–986.

MOUM, J. N. (1990). The quest for kρ – preliminary results from direct measurments of turbulent fluxes in the ocean. *J. Phys. Oceanogr.*, 20:1980–1984.

MUNK, W. H. (1981). Internal waves and small-scale processes. In WARREN, B. A. AND WUNSCH, C., editors, *Evolution of physical oceanography*, pages 264–291. MIT Press, Cambridge, Mass.

OAKEY, N. S. (1982). Determination of the rate of dissipation of turbulent energy from simultaneous temperature and velocity shear microstructure measurements. *J. Phys. Oceanogr.*, 12:256–271.

OAKEY, N. S. (1985). Statistics of mixing parameters in the upper ocean during JASIN phase 2. *J. Phys. Oceanogr.*, 15:1662–1675.

OAKEY, N. S. (1990). Cruise report 90-014. Technical report, Beford Institute of Oceanography.

OAKEY, N. S. AND ELLIOTT, J. A. (1982). Dissipaton within the surface mixed layer. *J. Phys. Oceanogr.*, 12:171–185.

OSBORN, T. R. (1980). Estimates of the local rate of vertical diffusion from dissipation measurements. *J. Phys. Oceanogr.*, 10:83–89.

OSBORN, T. R. AND COX, C. S. (1972). Oceanic fine structure. *Geophys. Fluid Dyn.*, 3:321–345.

OZMIDOV, R. V. (1965). On the turbulent exchange in a stably stratified ocean. *Izv Acad Sci USSR Atmos Ocean Phys*, 1:853–860.

PERKIN, R. G. AND LEWIS, E. L. (1982). Design of CTD observational programmes in relation to sensor time constants and sampling frequencies. Technical Report 7, Institute of Ocean Sciences, Patricia Bay, B.C., Canada.

RICKER, W. E. (1973). Linear regressions in fishery research. *J Fisheries Res Board of Canada*, 30:409–434.

ROHR, J. AND VAN ATTA, C. (1987). Mixing efficiency in stably stratified growing turbulence. *J. Geophys. Res.*, 92:5481–5488.

ROHR, J. J., ITSWEIRE, E. C., HELLAND, K. N., AND VAN ATTA, C. W. (1988). Growth and decay of turbulence in a stably stratified shear flow. *J. Fluid Mech.*, 195:77–111.

ROHR, J. J., ITSWEIRE, E. C., AND VAN ATTA, C. W. (1984). Mixing efficiency in stably stratified decaying turbulence. *Geophys. Astrophys. Fluid Dyn.*, 29:221–236.

SANDSTROM, H. AND ELLIOTT, J. A. (1984). Internal tide and solitons on the Scotian shelf: A nutrient pump at work. *J. Geophys. Res.*, 89:6415–6426.

STEVEN, D. M. (1974). Primary and secondary production in the Gulf of St. Lawrence. Technical Report 26, McGill University, Montreal, Quebec, Canada.

STILLINGER, D. C. (1981). *An experimental study of the transition of grid turbulence to internal waves in a salt-stratified water channel.* Ph.D. thesis, University of California, San Diego.

STILLINGER, D. C., HELLAND, K. N., AND VAN ATTA, C. W. (1983). Experiments on the transition of homogeneous turbulence to internal waves in a stratified fluid. *J. Fluid Mech.*, 131:91–122.

TAVOULARIS, S. AND CORRSIN, S. (1981). Experiments in nearly homogeneous turbulent shear flow with a uniform mean temperature gradient. Part 1. *JFM*, 104:311–347.

TENNEKES, H. AND LUMLEY, J. L. (1972). *A first course in turbulence.* MIT Press, Cambridge, MA.

THERRIAULT, J.-C. AND LACROIX, G. (1976). Nutrients, chlorophyll, and internal tides in the St. Lawrence estuary. *J. Fish. Res. Board Can.*, 33:2747–2757.

THORPE, S. A. (1973). Experiments on instability and turbulence in a stratified shear flow. *J. Fluid Mech.*, 61:731–751.

THORPE, S. A. (1977). Turbulence and mixing in a Scottish loch. *Phil Trans Roy Soc London A*, 286:125–181.

THORPE, S. A. (1982). On the layers produced by rapidly oscillating a vertical grid in a uniformly stratified fluid. *J. Fluid Mech.*, 124:391–409.

THORPE, S. A. (1984). The transition from kelvin-helmholtz instability to turbulence. In MULLER, P. AND PUJALET, R., editors, *Internal gravity waves and small-scale turbulence*, pages 65–76. Hawaii Inst of Geophysics.

VAN ATTA, C. W. (1990). Comment on "The scaling of turbulence in the presence of stable stratification" by A. E. Gargett. *J. Geophys. Res.*, 95:11673–11674.

YAMAZAKI, H. AND OSBORN, T. (1992). Direct estimation of heat flux in a seasonal thermocline. To appear in *J. Phys. Ocean.*, december 1992.